DEVELOPMENT AND STUDY OF NANOCRYSTALLINE AND AMORPHOUS SOFT-FERROMAGNETIC ALLOYS

Jordi Bonastre i Muñoz

Universitat de Girona

Doctoral Thesis

Development and study of nanocrystalline and amorphous soft-ferromagnetic alloys

Jordi Bonastre Muñoz

2017

Universitat de Girona

DOCTORAL THESIS

DEVELOPMENT AND STUDY OF NANOCRYSTALLINE AND AMORPHOUS SOFT-FERROMAGNETIC ALLOYS

JORDI BONASTRE MUÑOZ

2017

Doctoral Program in Technology

Thesis supervisor: Joan Josep Suñol

Thesis submitted in fulfillment of the requirements to obtain a doctoral degree in the University of Girona

Universitat de Girona

El sotasignat doctor J.J. Suñol Martínez, professor de la Universitat de Girona

DECLARA

Que el treball titulat DEVELOPMENT AND STUDY OF NANOCRYSTALLINE AND AMORPHOUS SOFT-FERROMAGNETIC ALLOYS, que presenta Jordi Bonastre Muñoz per a l'obtenció del títol de doctor, ha estat realitzat sota la meva direcció.

El meu informe és favorable a la presentació d'aquesta tesi.

I, perquè així consti i tingui els efectes oportuns, signo aquest document,

Signatura,

Girona, 6 de setembre de 2017.

A la meva família, la meva guia en el que he estat,
a l'Ari, la meva guia en el que soc,
i a en Biel, la meva guia en el que seré.

Acknowledgements

Aquest treball inclou algunes caracteritzacions realitzades amb equips específics que han estat possibles gràcies a la col·laboració d'altres departaments i universitats. Agraeixo l'ajuda i serveis del personal dels Serveis Tècnics de Recerca (STR) de la UdG en els experiments de microscòpia electrònica de rastreig (SEM) i difracció de raigs X (XRD), del Grup de Caracterització de Materials (GCM) de la UPC i del Département de Physique de la Universitat d'Annaba (Algèria) en les caracteritzacions per espectroscòpia Mössbauer (TMS), i del Departamento de Física de la Universidad de Oviedo, del Materialen Fisika Saila de l'Euskal Herriko Unibertsitatea (EHU) i de la Facultat de Física de la Universidad de Sevilla en les mesures magnètiques.

Voldria agrair també l'ajuda, col·laboració i suport dels membres del Departament de Física de la UdG, i en especial dels companys de batalles i de no-batalles (Jesús, Xavi, Lluïsa, Marianna, Joseps, Laura, Dani, Àlex, Imma, Jordi, Javis, Toni, Francesc, Eduard, i d'altres que segur que em deixo), i per descomptat del Dr. Joan Josep Suñol.

Per últim, però no per això menys important, agrair a nivell personal el suport i paciència de tots aquells que he tingut la sort de tenir al voltant i que d'una manera o altra m'han ajudat o han patit les conseqüències de tenir-me a prop durant tots aquests anys. Ha estat un procés molt més llarg i intermitent del que m'esperava en començar-lo, i durant el qual he fet quatre mudances, he publicat tres discos i tres llibres, he perdut tres persones molt properes i n'he guanyat dues de molt especials. Després de la tesi i el fill, ja puc dir que només em queda plantar l'arbre, i esperem no haver d'esperar tant de temps per fer-ho! :-)

Contents

List of Publications

The following is a list of publications derived from the contents of this thesis:

J Bonastre, JJ Suñol, P Bruna, Kiminori Sato, JD Santos, B Hernando. "Influence of a magnetic field applied during the quenching process on the spin density and nanoscale structure of an amorphous Fe-B ribbon". *Materials letters* 87 (2012), 131-134. DOI: 10.1016/j.matlet.2012.07.072

T Sánchez, J Bonastre, JD Santos, ML Sánchez, A Chizhik, J González, JJ Suñol, B Hernando. "The effect of field-quenching fabrication on the magnetoimpedance response in Co66Fe4Ni1Si15B14 amorphous ribbons". *Journal of Applied Physics* 111.5 (2012), -053913. DOI: 10.1063/1.3687417

L González, J Bonastre, T Sánchez, JD Santos, ML Sánchez, A Chizhik, L Domínguez, M Ipatov, V Zhukova, A Zhukov, J González, JJ Suñol, B Hernando. "Magnetoimpedance response in Co-based amorphous ribbons obtained under the action of a magnetic field".
IEEE Transactions on Magnetics 48.11 (2012), 4375–4377. DOI: 10.1109/TMAG.2012.2198623.

J Bonastre, L Escoda, B Hernando, JM Sánchez-Llamazares, JJ Suñol. "Amorphous metal nanocrystallization changes due to mechanical alloying".
Physica Status Solidi (C) 7.11-12 (2010), 2660- 2662. DOI: 10.1002/pssc.200983790

J Bonastre, L Escoda, J Saurina, JJ Suñol, JD Santos, ML Sánchez, B Hernando. "Non-isothermal approach to crystallization process of a Co-rich alloy".
Journal of Non-Crystalline Solids 354.47 (2008), 5126-5128. DOI: 10.1016/j.jnoncrysol.2008.05.060

List of Figures

List of Tables

Abstract

This thesis deals with the study of the mechanical alloying (MA) technique as a method of production of soft-ferromagnetic nanocrystalline alloys. Several Fe-Cr and Fe-Co based alloys produced by this technique from commercial powders are analyzed and their structural and magnetic properties are discussed. In addition, some Fe and Co-based alloys produced by milling of amorphous ribbons previously quenched by the melt-spinning technique (MS) are also studied and their structural and magnetic properties analyzed and compared, including the effects of the addition of an external magnetic field during the production process itself.

The alloys produced directly by MA are found to show generally nanocrystalline properties even in the very early stages of the process and the resulting alloys seems to have achieved a significant reduction of the grain size with magnitudes in the range 5-15 nm. The milling process is also observed to induce a significant amount of stress and structural defects in the alloys. On the other hand, the alloys produced by milling of previously quenched MS amorphous ribbons seem to show different behaviors between them, with the Co-based alloys retaining some of the amorphous features of the precursors whereas the Fe-based appearing to have been recrystallized during the milling process.

All the powder alloys produced show good soft ferromagnetic properties, although with coercivities more in agreement with other reported nanocrystalline materials and still higher than the desired low coercivities found in amorphous ribbons. The magnetic saturations are found to be also generally higher than the low values featured in the amorphous ribbons, with some exceptions. Furthermore, the alloys produced with the addition of an external magnetic field during the quenching process feature induced magnetic anisotropy the effects of which are noticeable in the respective magnetic hysteresis cycles and magnetoimpedance.

Resum

Aquesta tesi tracta sobre l'estudi de la tècnica de l'aliatge mecànic (*mechanical alloying*, MA) com a mètode de producció d'aliatges ferromagnètics tous d'estructura nanocristal·lina o amorfa. S'analitzen alguns aliatges de base Fe-Cr o Fe-Co produïts amb aquesta tècnica a partir dels elements en forma de pols de gran puresa disponibles commercialment i es discuteixen les seves característiques i propietats estructurals i magnètiques. Per altra banda, també s'estudien alguns aliatges de base Fe i Co produïts per mòlta de cintes amorfes prèviament produïdes per solidificació ràpida mitjançant la tècnica del *melt spinning* (MS), i es comparen les seves respectives propietats estructurals i magnètiques, incloent-hi també un estudi dels efectes de la presència d'un camp magnètic extern durant el procés de refredament.

Els aliatges produïts directament per MA mostren característiques nanocristal·lines fins i tot en les fases més inicials del procés i s'assoleix una gran reducció de la mida de gra fins a magnituds en el rang 5-15 nm. S'observa també que el procés de mòlta indueix una quantitat significativa de defectes estructurals. Els aliatges produïts per mòlta de cintes amorfes, per altra banda, mostren algunes diferències no només respecte els anteriors sinó també entre ells: mentre els aliatges de base Co retenen part de les característiques amorfes dels precursors, els de base Fe revelen clarament que hi ha hagut una recristal·lització durant el procés de mòlta.

Tots els aliatges produïts en forma de pols mostren propietats magnètiques toves, tot i que les coercivitats observades estan properes a les d'altres materials nanocristal·lins i encara lluny de les baixes coercivitats desitjades que es poden trobar en les cintes amorfes. En contrapartida, les magnetitzacions o polaritzacions de saturació també s'allunyen dels valors baixos observats a les cintes, tot i que amb algunes excepcions. Els aliatges produïts amb presència d'un camp magnètic extern durant el procés de refredament presenten anisotropia magnètica, els efectes de la qual es poden apreciar en la comparació dels cicles d'histèresi i les magnetoimpedàncies respectives.

Resumen

Esta tesis trata sobre el estudio de la técnica del aleado mecánico (*mechanical alloying*, MA) como método de producción de aleaciones ferromagnéticas blandas de estructura nanocristalina o amorfa. Se analizan algunas aleaciones de base Fe-Cr o Fe-Co producidos con esta técnica a partir de los elementos en forma de polvos de gran pureza disponibles comercialmente y se discuten sus características y propiedades estructurales y magnéticas. Por otro lado, también se estudian algunas aleaciones de base Fe y Co procesadas por molienda de cintas amorfas previamente producidas por solidificación rápida mediante la técnica del *melt spinning* (MS), y se comparan sus respectivas propiedades estructurales y magnéticas, incluyendo también un estudio de los efectos de la presencia de un campo magnético durante el proceso de enfriamiento.

Las aleaciones producidas directamente por MA muestran características nanocristalinas incluso en las fases más iniciales del proceso y se logra una gran reducción del tamaño de grano hasta magnitudes en el rango 5-15 nm. Se observa también que el proceso de molienda induce una cantidad significativa de defectos estructurales. Las aleaciones producidas por molienda de cintas amorfas, por otro lado, muestran algunas diferencias no sólo respeto las anteriores sino también entre ellas: mientras las aleaciones de base Co retienen parte de las características amorfas de las cintas precursoras, las de base Fe revelan claramente que ha habido una recristalización durante el proceso de molienda.

Todas las aleaciones en forma de polvo muestran propiedades magnéticas blandas, aunque los campos coercitivos observados están más bien cercanos a los de otros materiales nanocristalinos y todavía lejos de las bajas magnitudes que se pueden encontrar en las cintas amorfas. En contrapartida, las magnetizaciones o polarizaciones de saturación también se alejan de los valores bajos observados en las cintas, con algunas excepciones. Las aleaciones producidas con presencia de un campo magnético externo durante el proceso de enfriamiento presentan anisotropía magnética, cuyos efectos se pueden apreciar en la comparación de los respectivos ciclos de histéresis y magnetoimpedancias.

1 Introduction

> *Conscience is our magnetic compass. Reason, our chart.*
>
> — **Joseph Cook**
> (Politician)

Contents

The technological progress of civilizations have been historically linked to advances in the knowledge and control of materials. A clear example for this is that historians use to name the three prehistoric ages after the most recent discovered or developed material mainly used: Stone Age, Bronze Age and Iron Age, respectively. Even in recorded history, civilizations who first achieved the knowledge of certain new materials with superior properties generally became the hegemonic in that time [1].

This general pattern may also be applied to the modern era, with well-known examples such as the information and communication technology (ICT) revolution -linked with previous discoveries on semiconductors- or the huge advances in fields such as aeronautics, construction or transport -linked to the development of new alloys and composites-. More recently, the irruption of nanostructured materials has meant a significant step forward and has allowed the creation of new disciplines in the nanoscience and nanotechnology fields such as nanomedics or nanoelectronics.

Scientific investigations in the area of materials have been continuously directed towards improving the properties and performance of materials, and the understanding of their structure and composition has proved to be the key for this. The introduction of very powerful analytic techniques such as X-ray diffraction -which might be considered a milestone in history of materials science- and high-resolution electron microscopy allowed the description of materials in the microscopic scale and its direct relation with the macroscopic properties. After this, significant improvements in mechanical, chemical, and physical properties of materials have been achieved through chemistry modifications and conventional thermal, mechanical and thermomechanical processing methods.

In parallel to the technological development, socioeconomic progress of mankind has carried an increasing demand for better, specific and attractive properties, and has led to the design and development of novel microstructures, the so-called *advanced materials*. This group of materials may be defined as those where first consideration is given to the systematic synthesis and control of the structure of the materials in order to provide a precisely tailored set of properties for demanding applications [2].

1.1 Non-equilibrium materials

It is generally accepted that conventional processing methods, which are generally based on equilibrium states, are limited to constraints and usually found unsuitable for the development of most of the desired advanced materials. On the other hand, it is now well recognized that their structure and constitution can be better controlled by processing them under non-equilibrium conditions [3], giving access to a wider range of structures which can form the basis of interesting advanced materials as either the final or an intermediate product.

The microstructural magnifications of the departures from equilibrium can be achieved by several processing routes commercial or industrially available, such as rapid solidification [4, 5], mechanical alloying [6–9], plasma processing [10] and vapor deposition [11].

The central underlying theme in all these techniques is to synthesize materials in a non-equilibrium state generally by a two-step process: 1) energization -i.e., bringing the material into a highly non-equilibrium metastable state by some external dynamical forcing such as melting, evaporation,

irradiation, application of pressure or storing of mechanical energy by plastic deformation [12])[1]- and 2) quenching -i.e., bringing it into a configurationally frozen state, which can then be used as a precursor to obtain the desired chemical constitution and/or microstructure by subsequent heat treatment/processing.

The ability of the different processing techniques to synthesize metastable structures can be conveniently evaluated by measuring or estimating the departure from equilibrium -i.e., the maximum energy that can be stored in excess of that of the equilibrium/stable structure-, and materials processed this way generally show improved physical and mechanical characteristics in comparison with conventionally processed materials.

The correct knowledge of the microstructural characteristics of these solid materials is crucial for the determination and control of their mechanical, electrical and magnetic properties. Depending on the resulting atomic arrangement, a first general division can be made into two basic types: crystalline and amorphous solids.

- *Crystalline materials*:

  Crystalline materials are solids with a long-range order in which their atoms are arranged in an orderly repeated pattern (a lattice) extended in all three spatial dimensions. A region where this long-range order spreads without interruption is called a crystallite or grain. Multiple grains of varied size, orientation or even different composition and/or crystal lattice may be featured in a single sample, with the regions of separation between different ones forming what are called *grain boundaries*. This is the case of polycrystalline solids, which are indeed the most common case in metals, as opposed to monocrystalline solids, where the crystal lattice of the entire sample is continuous and unbroken and with no grain boundaries[2].

  The number of total grains in a sample, their crystalline structure and their average size, which can vary from a few nanometers to several meters, and their diversity are generally determined not only by the chemistry of the material but also strongly by the conditions under which it has been processed.

- *Amorphous materials*:

  Commonly known also as *glasses*, amorphous materials are solids that do not show the long-range atomic order characteristic of crystalline solids, although they do show a short-range order due to the nature of chemical bonding. Amorphous metals are metallic materials (mostly alloys) which shows this non-crystalline structure (in contrast to most “normal” metals, which are polycrystalline, as mentioned above).

  The term *glass* is often used when referring to all amorphous materials. However, in a strict sense, this term can only be applied when the material shows a glass transition temperature.

[1] Such materials have been often referred to as *driven materials* [13]

[2] In a monocrystalline solid, the absence of crystallographic defects associated to the grain boundaries generally give these materials mechanical, electrical or optical unique properties which are industrially used in technological applications, especially in optics and electronics.

Analogously, the term *metallic glass* is commonly used, especially in materials science, when referring to amorphous metals.

1.1.1 Nanocrystalline metals

Metals processed under "normal" equilibrium conditions are generally crystalline solids with relatively big average crystal sizes. However, as it has been mentioned at the beginning of this section, non-equilibrium processing techniques allow the formation of materials with smaller average sizes (or even without any crystalline structure, as is the case of amorphous metals).

When the average crystal sizes in a solid shows magnitudes below the 100 nm in at least one dimension, it is classified as a *nanocrystalline solid*. Nanocrystalline materials seem to be of interest because they exhibit atomic structures and properties which differ from both those of glasses and/or crystals with the same chemical composition and also due to their ability to from alloys of conventionally insoluble components [14].

These peculiar and interesting features are mainly due to the fact that in nanocrystalline materials the grain boundaries may represent up to the 50% of the total volume of the solid. It is well known that grain boundaries play a decisive role in structural behavior, due to their significantly lower atomic density compared with the rest of the material and also due to the different coordination between neighboring atoms, resulting in a higher density of crystallographic defects. Both high defect number and low atomic density help increasing diffusivity [15].

Atoms located in the crystal borders are in a metastable state, since their energy is always superior to those of the inner crystal (which are in a minimum energy state). This causes a tension field that moves out the inner atoms from their equilibrium positions [16]. Therefore, grain boundaries disrupt the motion of dislocations, modify atomic diffusion and electronic flux, as well as can act as preferential sites for the onset of corrosion and the precipitation of new phases [17].

1.1.2 Metallic glasses

As mentioned above, amorphous metals -commonly known as *metallic glasses*- are solid metallic materials -mostly alloys- which show a disordered atomic-scale structure.

Due to their non-crystalline structure, amorphous metals have different physical properties with regard to their crystalline counterparts [18, 19]. Specifically, the absence of crystalline defects such as dislocations gives amorphous metals in general higher tensile yield strengths and higher elastic strain limits, and the lack of grain boundaries and the compositional homogeneity of the alloys lead to better resistance to corrosion [20]. On the other hand, metallic glasses at room temperature are not ductile enough and tend to fail suddenly when loaded in tension [21, 22], which limits the material applicability in reliability-critical applications, as the impending failure is not evident.

The most common way for the production of amorphous metals is rapid cooling from a liquid state, although other ways have been used such as physical vapor deposition, solid-state reaction, ion irradiation and mechanical alloying. It is known that when heat from a melt is released and the temperature drops to a certain point, the Gibbs free energy of the liquid state becomes higher than

that of the crystalline solid phase and hence a phase transition begins through the nucleation and subsequent growth of the solid into the liquid. However, this process require a certain time, so when the process of cooling down is made at a significantly high speed, the atoms may not have time to form the crystalline phase. When this happens, the undercooled melt may freeze while avoiding the nucleation-and-growth process mentioned above and keeping the same atomic configuration than the previous liquid state, thus forming a glass.

The critical cooling rate that allows a glass formation depends on the nature of the atomic bonding. This bonding imposes limitations to the ability of atoms to rearrange themselves in order to maintain thermodynamic equilibrium during cooling. In typical examples of common glasses, such as normally polymeric materials or silica (SiO_2), critical cooling rates are small enough (about 10^{-2} K/s) and the glassy state is easily achieved. However, for the formation of amorphous metals, higher cooling rates (typically about $10^4 - 10^7$ K/s) are necessary.

In addition to these extremely high cooling rates, three empirical rules have been historically reported to be essential for an optimal metallic glass formation by rapid solidification [23–25]:

1. *Multicomponent alloy system*. Alloys with 3 or more different components require more complex crystal units with higher potential energy, meaning a lower chance of formation, which helps preventing the formation of the crystalline phase.

2. *Significant atomic size mismatch*. The main constituent elements should contain atoms of significantly different sizes (typically >12%). Atomic mismatch (or mismatch entropy) generates micro strain, leads to low free volume and therefore to higher viscosity, which prevents the atoms moving enough to form an ordered lattice and would result in the formation of a glassy structure [26, 27].

3. *Negative heat of mixing*. In order to inhibit crystal nucleation and prolong the time the molten metal stays in supercooled state. A more negative ΔH_{mix} encourages the stability of the liquid phase and impedes the atomic diffusivity and crystallization during cooling [28].

Although the first metallic glasses were developed in early 1960s with the development of amorphous ribbons produced by rapid solidification [29], it was not until the development of the melt-spinning technique that production at large scale became possible. A wide variety of multicomponent alloys had been cast since then, but in all cases the high cooling rates needed limited one of the dimensions of the samples to less than 50 μm, thus limiting the applications range.

In the 1990s, new alloys were produced with critical cooling rates low enough to allow the formation of amorphous structure in thick layers over 1 millimeter, known as *bulk metallic glasses* (BMG). Many of these alloys were developed by exploiting a phenomenon called the “confusion” effect. When certain alloys contain so many different elements and are cooled at sufficiently fast rates, the constituent atoms simply cannot coordinate themselves into the equilibrium crystalline state, resulting in a locked-in random disordered state.

These bulk amorphous alloys exhibit unique softening behavior above their glass transition, allowing an easy processing like polymers, but with the superior electronic, thermal and mechanical properties of the metal alloys.

1.2 Soft-ferromagnetic materials

One particular group of advanced materials, from the point of view of their application, is the one that comprises magnetic advanced materials. Research on this kind of materials showed a dramatic grow during the 1970s and 1980s, mainly due to the jump from the laboratory to the industrial production scale. But before entering into the specifics, which will be detailed in the next section, it is important to understand the basics behind the different magnetic behaviors found in materials.

1.2.1 Overview of magnetic behaviors

The physical cause of magnetism of objects is the atomic magnetic dipole. This magnetic dipole produces a magnetic moment $\vec{m}$ which has three non-excluding sources or contributions:

1. *Orbital magnetic dipole moment*: due to the orbital motion of the electrons around the nucleus, which can be considered as a current loop.

2. *Electron magnetic dipole moment*: caused by the intrinsic property of spin of the electrons.

3. *External magnetic field*: magnetic dipole induced by an externally applied magnetic field.

In a single atom, the overall magnetic moment is the vector sum of the first two own contributions (orbital and electron spin) plus any variation induced by the third one (the external magnetic field).

Macroscopically, the magnitude used for the quantitative measurement of the magnetic response of materials is the magnetization $\vec{M}$, which is the net magnetic moment per volume unit:

$$\vec{M} = \frac{\mathrm{d}\vec{m}}{\mathrm{d}V} \tag{1.1}$$

It is obvious that the atomic magnetic moment $\vec{m}$ differs significantly between different materials, and is also modified by the presence of an external magnetic field in several different ways. The resulting magnetization $\vec{M}$ is thus strongly dependent on the intensity of this external field $\vec{H}$, and this dependence can be quantitative explained with a dimensionless parameter called **magnetic susceptibility** (χ):

$$\chi = \frac{\partial \vec{M}}{\partial \vec{H}} \tag{1.2}$$

As one can deduce from the latter equation, the magnetic susceptibility χ measures the relative amount of "response" of a certain material to an external magnetic field. Its meaning is indeed directly related to another well known and commonly used parameter: the relative magnetic permeability μ_r (sometimes represented by K_m), with a simple mathematical expression[3]:

$$\mu_r = 1 + \chi \tag{1.3}$$

[3]The simple expression in equation 1.3 is due to the fact that both parameters explain the same physical phenomenon, with the magnetic permeability μ_r taking into account both the external field H and the magnetization M induced by it and the magnetic susceptibility χ measuring only the amount "modified" by the presence of the material.

Table 1.1 shows the physical meaning of χ according to equations 1.2 and 1.3.

Value of χ	Physical meaning
$\chi > 0$	The magnetization $\vec{M}$ induced in the material has the **same direction** as the external field. The presence of the material tends to **increase** the overall magnetic field ($\mu_r > 1$).
$\chi < 0$	The magnetization $\vec{M}$ induced in the material **opposes** the external field. The presence of the material tends to **decrease** the overall magnetic field ($\mu_r < 1$).
$\chi \approx 0$	The magnetization $\vec{M}$ is very weak or almost non-existent. The presence of the material **does not affect** significantly the overall magnetic field ($\mu_r \approx 1$).

Tab. 1.1: *Physical meaning of the magnetic susceptibility χ*

The specific value of χ may drastically change not only between different materials but also between samples of the same material or even in a single sample when measured under different conditions. This is due to differences in the electronic configurations producing variations in the nature of their atomic magnetic moments $\vec{m}$ that consequently change the overall magnetization $\vec{M}$.

In order to analyze the magnetic behavior of a certain material, there are basically two characteristics that must be taken into account:

1. How the atomic moments $\vec{m}$ of each atom in the material behavior *individually*.
2. How these individual behaviors affect or are affected by the *neighboring atoms*.

Whereas the first point affects all materials, this is not the case of the second one, since not all atoms interact magnetically with their neighbors. According to this, two groups of magnetic behaviors can be made, with the most common of each group listed and described in table 1.2[4].

Some of the magnetic behaviors listed are non-exclusive and can be shown simultaneously although usually the orders of magnitude involved lead one behavior to overwhelm the others. As a general rule, the materials are classified according to the dominant magnetic mechanism, with paramagnetic materials, for example, being those where paramagnetism prevails over diamagnetism (and vice versa)[5], ferromagnetic those where ferromagnetism prevails, etc.

The first group, diamagnetism and paramagnetism, generally involve extremely weak magnetizations ($\chi \sim 10^{-6} - 10^{-4}$) and their effects are usually overwhelmed by other behaviors[6].

[4] Besides the magnetic behaviors described in the table, there are several other more specific kinds of magnetism whose explanations are beyond the scope of this work, such as *superdiamagnetism*, *superparamagnetism*, *superferromagnetism*, *metamagnetism*, *spin glasses*, etc.

[5] In most diamagnetic and paramagnetic materials there is usually a "competition" between diamagnetism and paramagnetism, and it is often not trivial to deduce *a priori* when a certain material will end behaving in one way or the other.

[6] This is the reason why these materials are usually informally labelled as "non-magnetic", due to their magnetic behavior being almost undetectable in most applications of every-day life. For example, the magnetic susceptibilities of copper or aluminum are around $\chi \sim 10^{-5}$, which means that their magnetic permeabilities μ are just a $0{,}001\%$ lower or higher than that of the vacuum.

Main magnetic behaviors with no interaction between neighboring atoms	
Diamagnetism 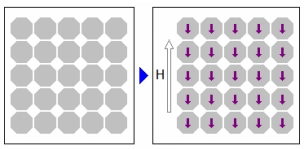	The electrons in the atoms are paired and the atomic moment is zero ($\vec{m} = 0$), resulting in a default zero net magnetization ($\vec{M} = 0$). Under the presence of an external magnetic field their electron orbitals are affected in such a way that a slightly non-zero magnetization ($\vec{M} \neq 0$) is observed **opposing** to the applied field. When the magnetic field is removed, the induced magnetization disappears.
Paramagnetism 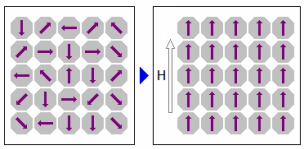	The atomic magnetic moments are not completely canceled out ($\vec{m} \neq 0$), but the atoms are randomly oriented, resulting again in a default zero net magnetization ($\vec{M} = 0$). Under the presence of an external magnetic field, the atomic moments tend to align with it, producing a non-zero overall magnetization $\vec{M} \neq 0$ in the **same direction** as the applied field. When the magnetic field is removed, the atomic moments spontaneously return to their normal random orientation due to thermal agitation.
Main magnetic behaviors with interaction between neighboring atoms	
Ferromagnetism 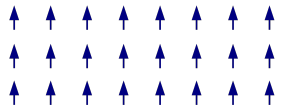	There is energy exchange with the neighboring atoms intense enough for allowing the formation of short-range regions with the respective magnetic moments aligned in the same direction (parallel alignment). These short-range regions are called **magnetic domains** (or Weiss domains) and produce a significant departure in the macroscopic effects with respect to the other magnetic orderings.
Antiferromagnetism 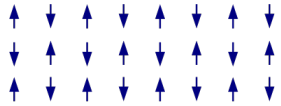	As in ferromagnetism, there is also energy exchange between neighboring atoms, but in this case the tendency is to align in opposite directions, leading to a magnetically ordered state that can be visualized as the combination of two magnetic sublattices, with the atomic moments parallelly coupled within each of the two sublattices, but with any two atomic magnetic moments belonging to different sublattices set in an antiparallel orientation and canceled each other out ($\vec{M} = 0$).
Ferrimagnetism 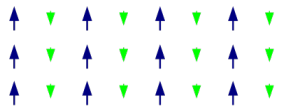	Like in antiferromagnetism, the neighboring atoms tend to align in opposite directions, effectively behaving as a combination of two opposite magnetic sublattices. However, as opposed to antiferromagnetism, in ferrimagnetism the sublattices are formed by **different** crystallographic environments and each of the sublattices is occupied by one of the magnetic species with either different magnetic moments or different number of atoms per unit cell, resulting in an spontaneous non-zero magnetization ($\vec{M} \neq 0$).

Tab. 1.2: *List of the most common magnetic behaviors*

Ferromagnetic, ferrimagnetic and antiferromagnetic materials, on the other hand, are the result of a magnetic structure and therefore their magnetic behaviors are usually not only noticeable but also directly affected by their crystalline structure and temperature.

Since the scope of this work is the study of soft ferromagnetic alloys, only ferromagnetism will be discussed in detail here.

1.2.2 Ferromagnetism and magnetic hysteresis

Ferromagnetism is probably one of the most interesting and useful magnetic behaviors, due to the presence of the magnetic domains mentioned in table 1.2). These magnetic domains are the result of the spontaneous parallel alignment between neighboring atoms, as opposed to the antiparallel alignment found in anti- and ferrimagnetism.

The domain structure produces a peculiar non-linear dependence of the magnetization M with the magnetic field intensity H known as **hysteresis cycle** or hysteresis loop (fig. 1.1), which is common to all ferromagnetic materials although with variations in the shape and magnitudes involved.

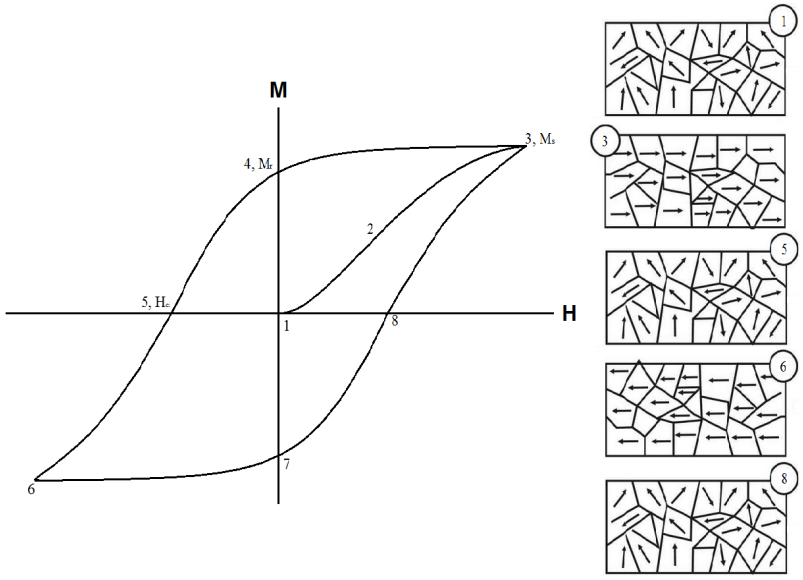

Fig. 1.1: *Typical ferromagnetic hysteresis cycle in a M-H diagram (left) and evolution of the magnetic domain structure (right)*

A typical hysteresis curve is the result of several stages (1-9 in the figure):

1. A balanced or non-magnetized ferromagnetic material already shows the magnetic domain structure, but without the presence of any external magnetic field ($H = 0$), every domain is randomly aligned with respect to the neighboring domains, resulting in an overall zero magnetization ($M = 0$).

2. Under the presence of an external magnetic field ($H > 0$), the alignment already observed in paramagnetic materials is dramatically enhanced by the domain structure, resulting in a huge increase in the overall magnetization ($M > 0$). As the magnetic field is intensified, more domains join the alignment and the magnetization keeps growing ($M \gg 0$). The consequence of this effect is a steep slope in the M-H magnetization graph, which means a high magnetic susceptibility χ.

3. The increase in the magnetization value finish when all magnetic domains have already been aligned. When this point is reached, the overall magnetization cannot keep growing even if the external field is still increasing. The maximum value achieved for the magnetization is

called the **saturation magnetization** (M_s) and is one of the main parameters to take into account when characterizing the magnetic properties of a certain material.

4. Arguably the most singular characteristic of a ferromagnetic material is exhibited when the external field H is turned off after reaching the saturation point. Contrary to what one would expect, some of the magnetic domains remain oriented even without the presence of the external field which first produced the alignment. This means that the system does not return to the initial zero-magnetization state but stays at a certain value called remanent magnetization or **remanence** (M_r). Although this state of aligned domains is not a minimal-energy configuration, it is extremely stable and has been reported to persist for even millions of years (in seafloor magnetite aligned with older Earth's magnetic field, for example).

5. In order to eliminate this non-zero magnetization, a field must be applied in the opposite direction in order to force the still-aligned domains to the opposite direction and return to the initial zero magnetization by creating a perfect balance between domains aligned in opposite directions. The necessary field intensity to make this happen is called the coercive field or **coercivity** (H_c), which is specific for every material and depends strongly on its microstructure and primarily on its domain structure.

6-9. One can easily deduce that increasing again the magnetic intensity beyond this balance point and repeating exactly the same procedure in the opposite direction will produce an identical response in the ferromagnet behavior. Indeed, the continuous repetition of this process of increasing/decreasing the external magnetic field in alternative and opposite directions, results in a periodic cycle in the magnetization.

The exact ferromagnetic behavior, and specially the shape and the magnitudes involved in the magnetic hysteresis loop, is specific for each material and for the given conditions. As an example, figure 1.2 shows the first stages of the magnetization curves for pure iron, cobalt and nickel, the only three pure elements which are ferromagnetic at room temperature.

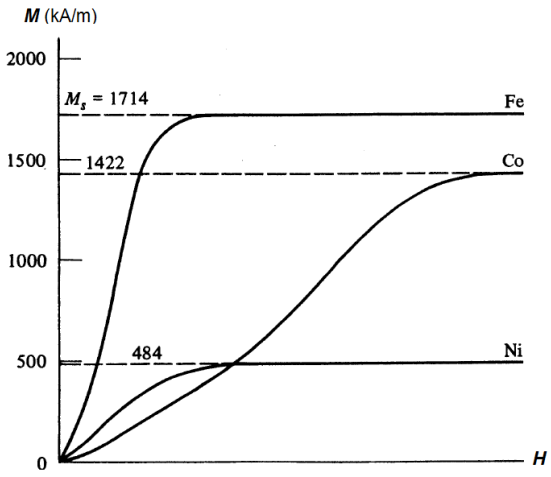

Fig. 1.2: *Magnetization curves of Fe, Co and Ni at room temperatures* [30].

1.2.3 Thermomagnetic behavior of ferromagnetic materials

One of the primary parameters affecting the magnetic properties of the materials is their temperature. This is because the tendency of the atomic magnetic dipoles to align due to the presence of an external magnetic field, as described above, has to compete with the default tendency to randomness due to thermal oscillation. As the temperature increases, this thermal agitation becomes stronger and consequently the effective overall magnetization M and magnetic susceptibility χ are affected.

In the particular case of ferromagnetic materials, when a certain temperature is reached, the thermal agitation is strong enough to overpower the ferromagnetic tendency to a parallel alignment of the neighboring atoms and the system can no longer maintain its characteristic magnetic order. For higher temperatures, the atomic magnetic moments continue to align with the external magnetic fields although now individually and without interaction between neighboring atoms. The resulting magnetization M becomes linear linear with the external magnetic field, as in paramagnetism.

This point is known as the Curie temperature T_C (named after Pierre Curie [31]), and is considered a second-order phase transition (from a ferromagnetic to a paramagnetic phase, see fig. 1.3). Its value is specific for each material and is an important characteristic in ferromagnetic materials, because it marks their maximum working temperature.

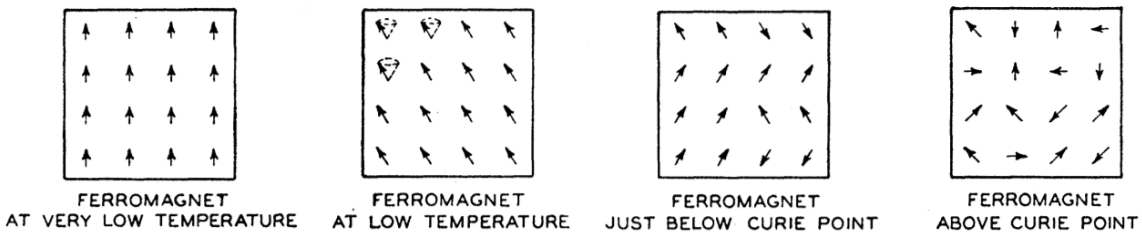

Fig. 1.3: *Evolution of the magnetic moments with the temperature in a ferromagnetic material* [32].

Figure 1.4 shows the evolution of the magnetic susceptibility χ with the temperature in ferromagnetic and antiferromagnetic materials and their similarity with paramagnets above the Curie/Néel point.

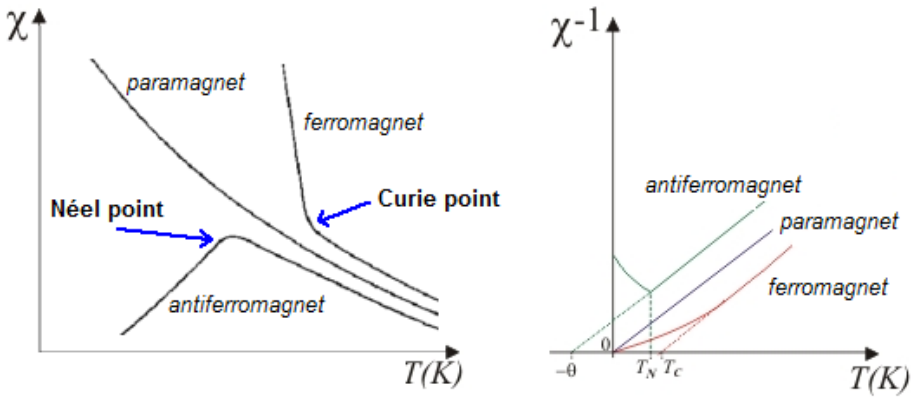

Fig. 1.4: *Magnetic susceptibility χ as a function of the temperature T for different magnetic behaviors.*

The figure also includes a χ^{-1} vs T plot in order to show the inverse-law behavior (named Curie-Weiss law) of the ferromagnetic materials above the Curie point:

$$\chi = \frac{C}{T - T_C} \tag{1.4}$$

where C is a material-specific constant.

The same thermal agitation responsible of the paramagnetic behavior above the Curie point is also responsible of a reduction in the effective saturation magnetization M_s below T_C, as can be seen in 1.5, which also shows the specific cases of Fe, Co and Ni.

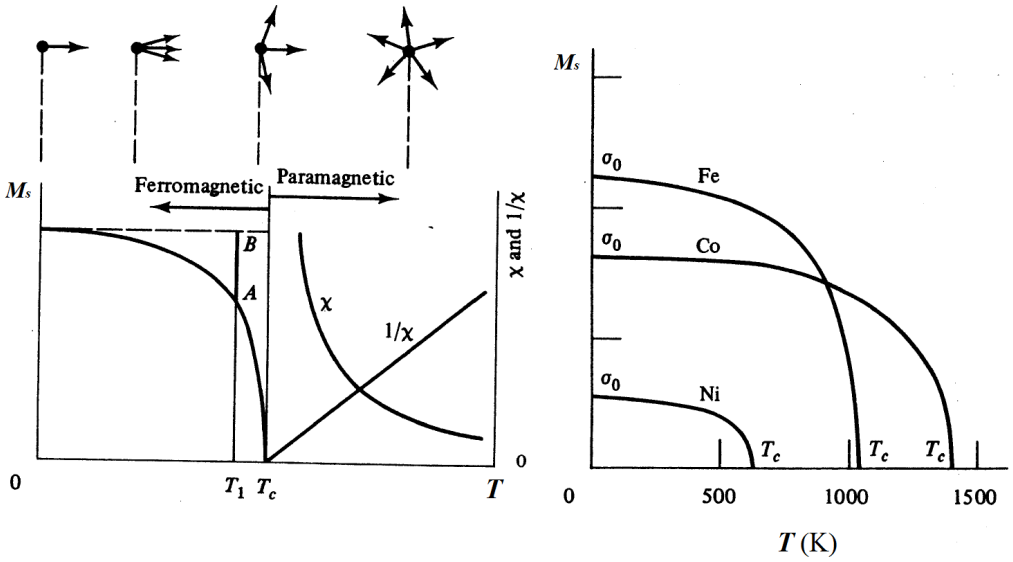

Fig. 1.5: *General evolution of the magnetic behavior with the temperature T in ferromagnetic materials and specific features for Fe, Co and Ni* [30].

The specific value of T_C gives an idea of the amount of energy necessary to break up the magnetic ordering. For example, the Curie temperature for pure iron is T_c = 1043 K and corresponds to an energy of $E \approx 13$ kJ/mol, which is significantly higher than the energy associated to the same material at room temperature (about 3.8 kJ/mol).

Table 1.3 shows the Curie temperature for several crystalline ferromagnetic materials.

element	T_c (K)	*alloy/compound*	T_c (K)
Co	1388	MnBi	630
Fe	1043	MnSb	587
Ni	627	CrO_2	386
Gd	292	MnAs	318
Dy	88	EuO	69

Tab. 1.3: *Curie temperatures for some crystalline ferromagnetic materials (L: pure elements, R: alloys/compounds)* [33]

1.2.4 Soft vs hard ferromagnetism

The correct determination of the magnitudes involved in the magnetic properties of a certain material is a crucial issue in the study of its suitability for a specific application.

One particular interesting magnitude to be measured is the area enclosed inside the magnetic hysteresis cycle, since it is proportional to the energy losses due to common dissipative processes in magnetic materials such as magnetostriction or domain wall motion.

According to the magnitude of this area, a common division of ferromagnetic materials is usually made between hard ferromagnetic -those with the largest area- and soft ferromagnetic -those with the smallest area- (fig. 1.7).

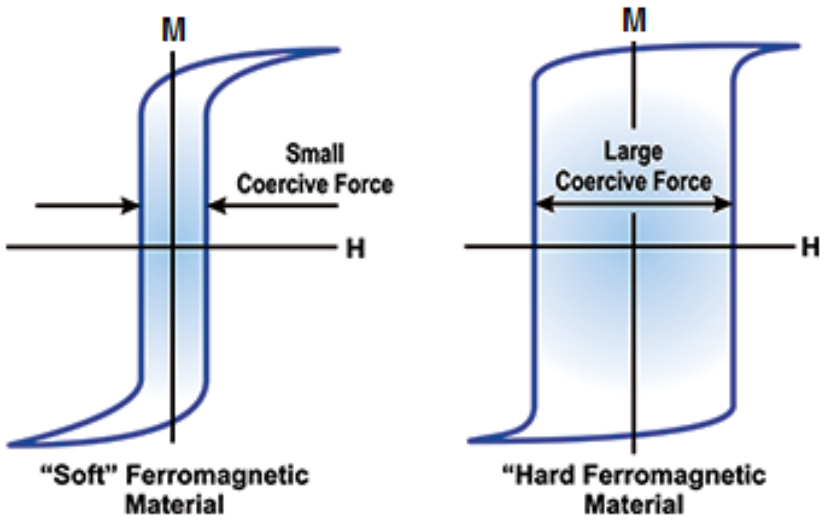

Fig. 1.6: *Comparison between the hysteresis cycles of a soft and a hard ferromagnetic material*

Hard magnetic materials show higher energy losses and are generally used for DC applications such as permanent magnets, components of electric motors, magnetic recording media (e.g. hard drives, floppy disks, magnetic tapes...) and magnetic separation. Their study is out of the scope of this work.

On the other hand, soft magnetic materials show lower energy losses and are mostly used in AC applications such as microwave devices, magnetic shielding, transformers or recording heads, and is the main focus of this work.

1.3 Development of optimal soft-ferromagnetic alloys

The following properties are required to constitute a good soft magnetic material [34, 35]:

1. *Small coercivity* H_c

   Coercivity is probably the parameter most directly related to the energy losses in a complete hysteresis cycle, since it affects directly to the magnitude of the enclosed area drawn by the hysteresis curves. A lower coercivity value means a smaller area between the upward and downward curves and hence lower energy loss per cycle.

2. *High magnetic susceptibility* χ *and permeability* μ

   Larger values of χ and μ mean higher slopes, which means that less magnetic field intensity H is required to increase or decrease a certain amount of magnetization M in the material. This is crucial in order to achieve the low coercivity and large saturation searched in the previous points.

3. *High saturation magnetization* M_s *and polarization* J_s

   High magnetic saturation values allow the development of a strong magnetic field, enabling control devices such as solenoids and fuel injectors to function with as little input energy as possible. In addition, high saturation magnitudes enable the design of smaller and lighter components without loss in performance.

4. *High Curie temperature* T_c

   As explained above, T_c marks the point where the second-order phase transition between ferromagnetic and paramagnetic states is produced and is also a measure of the thermal stability of the alloy and its suitability for high temperature applications.

5. *High electrical resistivity* ρ *(or low electrical conductivity* σ*)*

   A high electrical resistivity ρ is desired because it reduces the intensity of eddy currents in AC or rapidly pulsed DC applications. Low eddy current loss also results in a more responsive device.

The specific ferromagnetic properties of a certain material are determined mainly by its chemistry and microstructure. In particular, the magnetic domain structure is arguably one of the key factors to affect them.

1.3.1 Magnetic domain structure

The advances, developments, discoveries and innovations on non-equilibrium materials have improved the understanding and control of the magnetic domain structure in ferromagnetic materials, contributing intensely to several technologies and allowing the production of optimal soft ferromagnetic alloys, which in turn has meant a significant step in the development of some quotidian applications.

One of the key issues in this magnetic domain structure is the fact that between two neighboring magnetic domains there is no sharp change in the orientation but a progressive transition in the alignment of the atomic magnetic moments which extends in a generally narrow region at the boundary between the two domains. These regions, where the magnetization changes progressively from its value in one domain to that in the next, are called *domain walls*, and may come in some different configurations (see figure 1.7):

Bloch wall: named after the physicist Felix Bloch [36], in a Bloch wall the magnetization rotates through the plane of the domain wall. These type of domain walls generally appear in bulk materials, i.e. when sizes of magnetic material are considerably larger than domain wall width [37]. In this case, energy of the demagnetization field does not impact the micromagnetic structure of wall.

Néel wall: named after the French physicist Louis Néel [38], in a Néel wall, the magnetization rotates within the plane of the domain wall. It consists of a core with fast varying rotation and two tails where the rotation logarithmically decays. These type of walls are the common magnetic domain wall type in very thin film where the exchange length is very large compared to the thickness.

cross-tie wall: complex two-dimensional magnetic domain wall structure often found experimentally in thin soft ferromagnetic films with thicknesses of about several exchange lengths. The structure of such walls can roughly be imagined as a sequence of magnetic vortices and anti-vortices, arranged along a straight line [39].

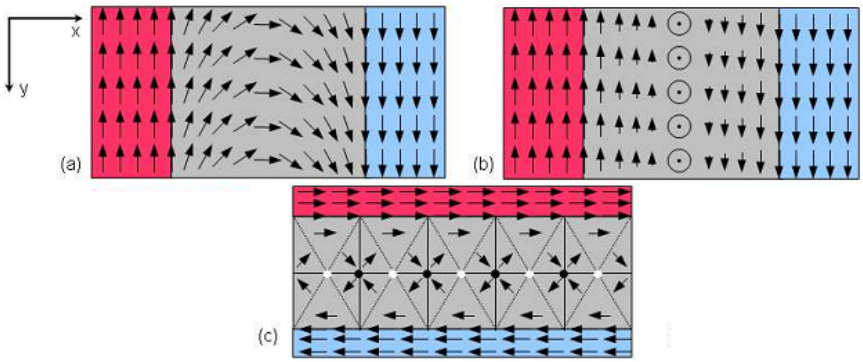

Fig. 1.7: *Schematic of the magnetization in the most common types of domain wall: (a) Néel wall, (b) Bloch wall, (c) cross-tie wall* [40]

When an external magnetic field is applied, the domains oriented in the same direction tend to growth at expenses of the others, and two mechanisms are involved in this growth: the domain growth or domain wall movement, and the rotation of domains. Therefore, the average width (δ_w) of the magnetic domain walls in a certain material is determined by an energy balance between the exchange energy and the anisotropy energy.

The coercivity H_c of a material is controlled by its magnetic anisotropy K, which can be defined as the dependence of magnetic energy on the orientation of the magnetization vector with respect to the crystal axes [41]. Although the most common are the magnetocrystalline and magnetoelastic anisotropies, some different anisotropies may be induced by magnetic annealing, plastic deformation, irradiation and magnetostatic shape anisotropy [42, 43]. The presence or absence of magnetostriction is another factor affecting the overall magnetic anisotropy [44].

The magnetic anisotropy represents a barrier to switching the magnetization [44]. Therefore, for soft magnetic materials, a small magnetic anisotropy is desired in order to minimize the hysteretic losses and maximize the magnetic susceptibility χ and permeability μ. Cubic crystalline phases of Fe, Co, Ni or alloys such as Fe-Co, Fe-Ni, etc. are good choices due to their low magnetocrystalline anisotropy [45].

The fact that the magnetic exchange length is typically in the order of magnitude of a few nanometers illustrates the underlying importance of this length scale in magnetic systems [34]. Figure 1.8 shows the general dependence of the coercivity H_c with the gran size D.

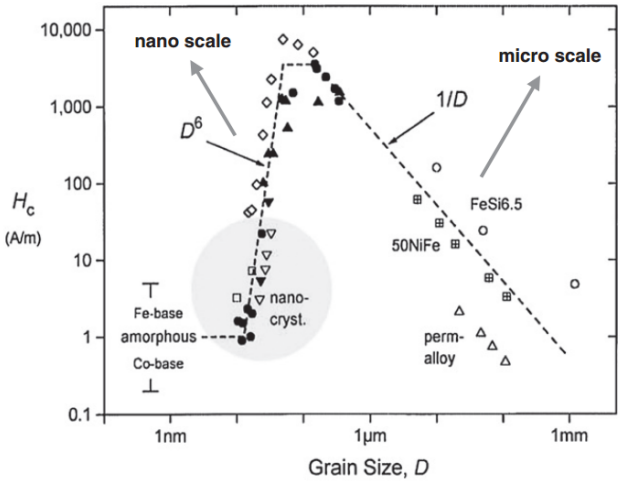

Fig. 1.8: *Dependence of the coercivity H_c with the grain size D. Two different tendencies can be clearly seen above and below 100 nm* [28, 34, 46–48]

As can be seen in the graph, for grain sizes above 100 nm, the classical rule for crystalline alloys shows an increase of H_c with the reduction of the grain size following approximately an inverse law ($H_c \propto D^{-1}$), which can be explained by the grain boundaries being the main contribution to the coercivity, hindering the domain wall motion [49]. However, for values lower than 100 nm the trending is reversed and the coercivity rapidly decreases with a D^6 dependence [47]. Therefore, amorphous materials or nanocrystalline with grain sizes below 10 nm are generally excellent soft magnets.

The D^6 dependence described above can be explained by the Random Anisotropy Model, schematized in figure 1.9, in which the magnetic anisotropy is statistically averaged over the exchange correlation length L_{ex}. Although his model was originally proposed for grain sizes smaller than the exchange correlation length, L_{ex}, it was later successfully extended to nanocrystalline materials [46, 50, 51].

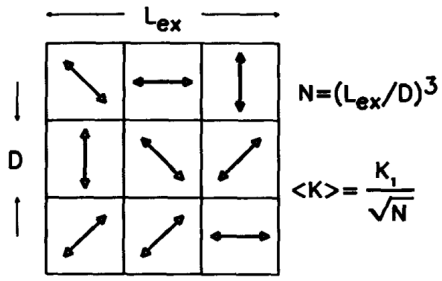

Fig. 1.9: *Schematic representation of the random anisotropy model* [47].

1.3.2 History and current status

The subject of nanoscale magnetic materials has been a topic of study for several decades in several different fields ranging from the obvious physics, material science and engineering to chemistry or biology [52]. These materials have shown potential for various applications such as ferrofluids [53], high-frequency electronics, high performance permanent magnets, magnetic refrigerants and catalytic systems [54] as well as interesting biomedical applications such as improving the quality of magnetic resonance imaging (MRI), hyperthermic treatment for malignant cells, site-specific drug delivery, and manipulating cell membranes [55, 56].

The first theoretical predictions for ferromagnetic amorphous alloys were done by Gubanov in the early 1960s [57], on the basis that ferromagnetism is a short range-order phenomenon. Nevertheless, Duwez et al. [58] were the first to experimentally obtain a ferromagnetic amorphous FePC alloy, opening a way to several alloy-type families based in ferromagnetic Fe, Co or Ni.

Some developed metallic alloys with soft-magnetic properties were FINEMET™ (Fe-Si-B-Nb-Cu) [59], NANOPERM™ (Fe-B-M-Cu, with M = Nb, Hf, Zr...) [60] or, more recently, HITPERM™ ((Fe,Co)-M-B-Cu with M = Nb, Zr, Hf) [61]. This advances were possible thanks to the use of thermal processing for the control of crystallization kinetics in previously amorphous materials and relied in the addition of boron (B), silicon (Si), phosphorus (P) and other metalloids to ferromagnetic alloys with iron (Fe), cobalt (Co) or nickel (Ni) [62].

Traditionally, the crystallization of Fe-B-Si glasses leaded to the formation of crystals of typical sizes from 0.1 to 1 μm, considerably deteriorating the resulting soft ferromagnetic properties. Nevertheless, the addition of small amounts of Cu and Nb to the alloy compositions was observed to produce a finer microstructure with size grains of about 10-15 nm, which showed very good soft ferromagnetic properties such as very low coercivities (H_c) and conductivities (σ), or improved permeabilities (μ) and saturations (M_s), which could compete with traditional Fe-Si crystalline steels for applications such as inductors, power transformers, etc.

These alloys, however, initially needed very high cooling rates and could only be prepared in form of ribbon about 30 μm thick and hence had a limited usability. Since the beginning of the 1990s [63–65] and until present day, there have been several researches upon alternative paths for their development, which has been possible thanks to the use of mechanical alloying (MA) -explained in detail in next chapter- on the production of powder alloys and their subsequent compression.

Recent investigations in bulk amorphous alloys have driven to the casting of rods of several millimeters obtaining good soft ferromagnetic materials of compositions Fe-(Cr,Mo,Ga)-(P,C,B) [66–68] and Fe-Si-B-P [69] and Fe-M-B [70]. This investigation field has been very active in the last two decades and several works were devoted to enhance and understand all the physical aspects related to these materials. The most important features are summarized in the review by McHenry et al. [34] published in 1999. However, the research on these materials is still going on nowadays and some questions related to the physical mechanisms of crystallization and to the magnetism involved still remain open.

Amorphous and nanocrystalline soft magnetic alloys share the same actual and potential applications than their crystalline counterparts, with uses related with the electrical power distribution and transformers being their main target. Furthermore, these alloys can also be used as inductors or chokes, switches, magnetic sensors or transducers. More recently these materials have been proposed as very good candidates for magnetic refrigerants at room temperature [71].

For DC applications, the most important properties are generally high saturation magnetization and permeability. In this case, although amorphous and nanocrystalline alloys have lower coercivity than Si steels, they cannot reach their saturation. In AC applications, on the other hand, the small hysteresis area and low eddy current losses make these materials even more suitable than crystalline materials.

The first amorphous Fe and Co-based alloys such as the METGLAS™, VITROVAC™and VITROPERM™families were seen to be very favorable for most of the applications from the point of view of energy saving and economic costs. However, nanocrystalline materials such as FINEMET™, NANOPERM™or HITPERM™have the advantage that can be used for high frequency applications because they combine higher saturation polarization and higher permeability, with NANOPERM™alloys showing power losses at high frequency even lower than silicon steels and Fe-based amorphous alloys [72].

Figure 1.10 shows a comparison of some common soft magnetic alloy families.

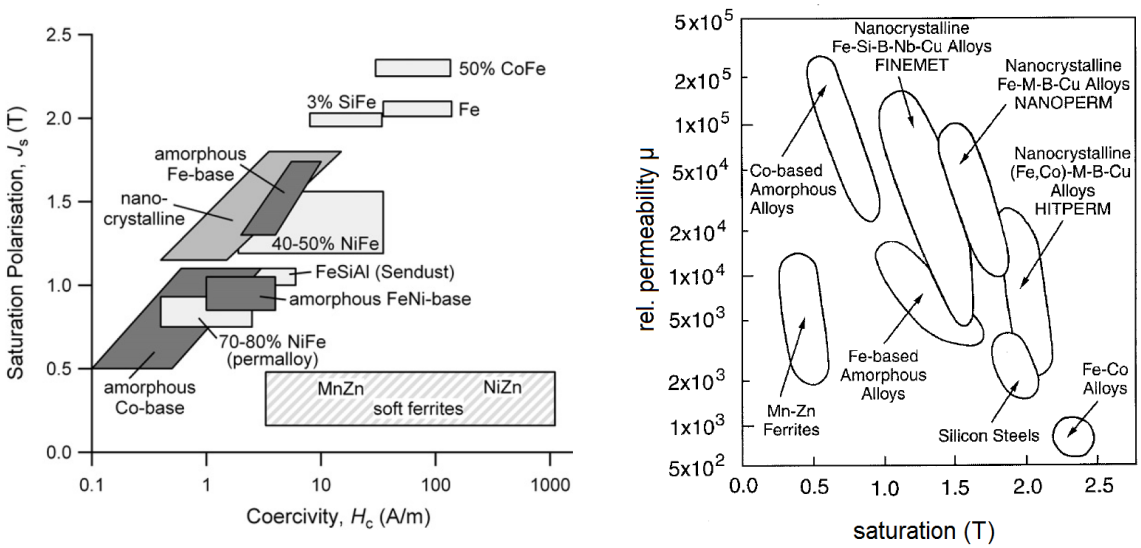

Fig. 1.10: *Comparison of some common soft magnetic alloy families* [34, 72–75]

Lastly, one particular subgroup of magnetic materials to be mentioned are those based on single-domain particles, where magnetization reversal can only occur via rotation of the magnetization vector from one magnetic easy axis to another overcoming a magnetically hard direction. Although these particles generally carry high coercivities and are not suitable for soft-magnetic applications, the fact that they also carry the ability to control the specific overall coercivity value has led to a number of significant technological applications, particularly in the field of information storage, where small magnetic particles are promising candidates for a further increase in the density of magnetic storage devices [76, 77]. The magnetic behavior of the single-domain particles can be explained by the well-known Stoner-Wohlfarth model [78], which can also be interestingly extended to materials with uniaxial magnetic anisotropy.

1.4 Aims of this thesis

The overall focus of this work is on the study of the mechanical alloying (MA) technique as a method of production of soft ferromagnetic nanocrystalline alloys.

This general objective can be further divided into several more specific goals:

1. Study of the MA process of production of Fe-Cr and Fe-Co nanocrystalline powder alloys.
2. Study of the effects of the MA process on Co-based and Fe-based amorphous ribbons previously produced by MS.
3. Analysis of the soft ferromagnetic properties of the alloys and their dependence on the processing method and the alloying elements.
4. Analysis of the magnetic anisotropy induced during the production process and its effects on the magnetic properties of the resulting alloys.

As a complement, the development of this thesis also allowed the familiarization with several analytical techniques and their applications in the characterization of materials in general and soft-ferromagnetic nanocrystalline or amorphous alloys in particular.

1.5 Methodology

The experimental contents of this thesis can be divided in four parts:

1. *Production of Fe-Cr and Fe-Cr-B nanocrystalline powder alloys by MA and subsequent characterization*. This part is described and detailed in chapter 4 and includes the following stages:
    - Production of the alloys by MA from high purity commercial powders using the equipment available and under milling conditions in concordance with previous works. The compositions were selected in order to allow the analysis of the possible effects of the alloying elements (Cr and B in this group of alloys) and, for every alloy, several batches

were produced with the same milling conditions but different milling times in order to allow the analysis of the evolution of the milling process.

- Characterization of samples processed with different milling times by means of Scanning electron microscopy (SEM), X-ray diffraction (XRD), transmission Mössbauer spectroscopy (TMS) and differential scanning calorimetry (DSC).

- Magnetic characterization of the final alloys. In this group of alloys, this magnetic analysis was limited to the obtaining of the respective M-H hysteresis cycles, also detailed in chapter 3, which allowed the determination of the respective coercivity and saturation magnitudes.

2. *Production of Fe-Co-B and Fe-Co-Ni nanocrystalline powder alloys by MA and subsequent characterization*. This part is described and detailed in chapter 5 and includes the following stages:

   - Production of the alloys by MA from industrial powders. The compositions were again selected in order to allow the analysis of the possible effects of the alloying elements, Co, B and Ni in this case. Like in the previous group of alloys, several batches with different milling times were produced.

   - Characterization of the alloys by Scanning electron microscopy (SEM), X-ray diffraction (XRD), transmission Mössbauer spectroscopy (TMS) and differential scanning calorimetry (DSC). As opposed to the previous study, these analyses were focused mainly on the final alloys, including several DSC experiments under different heating times needed for the structural analysis by the Kissinger method. A notable exception are the XRD analyses, which were performed for all milling times, like in the previous group.

   - Magnetic characterization of the final alloys. In addition to the M-H experiments, thermomagnetic (TM) experiments were also carried out for this group of alloys.

3. *Production of Co-based and Fe-based amorphous or nanocrystalline powder alloys by MA of previously melt-spun (MS) ribbons and subsequent characterization*. This part is described and detailed in chapter 6 and includes the following stages:

   - Production of the alloys by MA using ribbons previously produced by the MS technique as precursors. Unlike the previous groups, these alloys were produced after short milling times in order to avoid excessive processing of the alloys, with the specific settings not freely selected but determined by a particle size criterion.

   - Production of alloys with identical compositions by MA of industrial powders for comparison purposes.

   - Characterization of the alloys by x-ray diffraction (XRD) and differential scanning calorimetry (DSC). The analyses were carried out not only on the alloys produced from the ribbons but also on the ribbon precursors themselves and on the MA powders parallely produced from industrial powders, in order to compare them.

- Magnetic characterization of the final alloys by means of their respective M-H hysteresis cycles. Like in the structural characterizations, the experiments were carried out on the alloys produced by all the different production methods, for comparison.

4. *Characterization of some samples of the previous group produced under the application of an external magnetic field during the MS quenching process*. This part is described and detailed in chapter 7 and includes the following stages:

    - Characterization of the selected alloys by differential scanning calorimetry (DSC). Two samples of every allow were analyzed, one produced under the presence of the magnetic field and the other without it, in order to compare the results.

    - Complementary characterization by transmission Mössbauer spectroscopy (TMS) of one of the alloys due to the inconclusive previous DSC results. Several TMS experiments were performed using different geometric configurations in order to obtain information about the magnetic anisotropy of the samples. Complementary observations of the domain structure by means of the Bitter colloid method were also carried out.

    - Magnetic characterizations of the samples produced by both with and without the field. In addition to the common M-H experiments, measurements of the respective magnetoimpedance responses were also carried out, in order to study the possible effects of the magnetic anisotropy induced.

Likewise, descriptions and details about the alloy processing methods (MA and MS) and the characterization techniques (SEM, XRD, DSC, TMS, etc.) used in this work can be found in chapters 2 and 3, respectively.

Alloy production techniques

2

> *However far modern science and techniques have fallen short of their inherent possibilities, they have taught mankind at least one lesson: nothing is impossible.*
>
> **— Lewis Mumford**
> (Sociologist)

Contents

This chapter is an introduction to two non-equilibrium alloy production techniques: mechanical alloying (MA), which is the principal method used for the production of most of the alloys studied in this work, and melt spinning (MS), used for the production of alloys studied in chapters 6 and 7.

2.1 Mechanical alloying (MA)

Mechanical alloying (MA) is a solid-state powder processing technique involves repeated welding, fracturing, and rewelding of powder particles in a high-energy ball mill [79].

Two different terms are commonly used in the literature to denote the processing of powder particles in high-energy ball mills: mechanical alloying (MA) and mechanical milling (MM). MA describes the process when mixtures of powders (of different metals or alloys/compounds) are milled together and material transfer is involved in this process to obtain a homogeneous alloy. On the other hand, MM refers to milling of uniform (often stoichiometric) composition powders, such as pure metals, intermetallics, or pre-alloyed powders, where material transfer is not required for homogenization. However, the term MA is often used as a generic denomination for both types.

2.1.1 Introduction

Originally developed around 1966 by John Benjamin and his colleagues at the International Nickel Company (INCO) as an alternative path to produce oxide-dispersion strengthened (ODS) nickel-based superalloys for applications in the aerospace industry [80, 81], this relatively simple but effective processing technique has been applied to metals, ceramics, polymers, and composite materials and has been shown to be capable of synthesizing a wide variety of both equilibrium and non-equilibrium alloy phases starting from blended elemental or pre-alloyed powders.

The MA processing allows the extension of solid solubility limits and the possibility of alloying of combinations of elements which are difficult at normal conditions, the refinement of grain sizes down to the nanometer range, the synthesis of novel metastable crystalline and quasicrystalline phases, the development of amorphous (glassy) phases, the disordering of ordered intermetallics, the inducement of chemical reactions at low temperatures, etc. [79]

The background work that led to the development of the present process can be summarized to the following characteristics [82, 83]:

- Use of a high energy mill to favor plastic deformation required for cold welding and reduces the process times.
- Use of a mixture of elemental and master alloy powders (the latter to reduce the activity of the element, since it is known that the activity in an alloy or a compound could be orders of magnitude less than in a pure metal),
- Elimination of the use of surface-active agents which would produce fine pyrophoric powder as well as contaminate the powder,

- Relying on a constant interplay between welding and fracturing to yield a powder with a refined internal structure, typical of very fine powders normally produced, but having an overall particle size which was relatively coarse, and therefore stable.

Since the formation of an amorphous phase by mechanical grinding of a Y-Co intermetallic compound in 1981 [84] and in the Ni-Nb system by ball milling of blended elemental powder mixtures in 1983 [85], MA has been recognized as a potential non-equilibrium processing technique [86] and has been widely employed to produce a variety of commercially useful and scientifically interesting materials.

2.1.2 Diffusion as the main mechanism

The main physical mechanism which alloys true alloying in MA is diffusion, although the diffusion process in MA differs from thermally induced diffusion process in the fact that is also controlled by mechanical energy [8].

During MA, heavy deformation is introduced into the particles. This is manifested by the presence of a variety of crystal defects such as dislocations, vacancies, stacking faults, and an increase in the proportion of grain boundaries. The presence of this defect structure, which help decreasing the diffusion distances, and the slight rise in temperature during the milling process enhance the diffusivity of the solute elements into the matrix and aid the diffusion behavior. Consequently, true alloying takes place among the constituent elements. Figure 2.1 shows an schematic of some diffusion mechanisms.

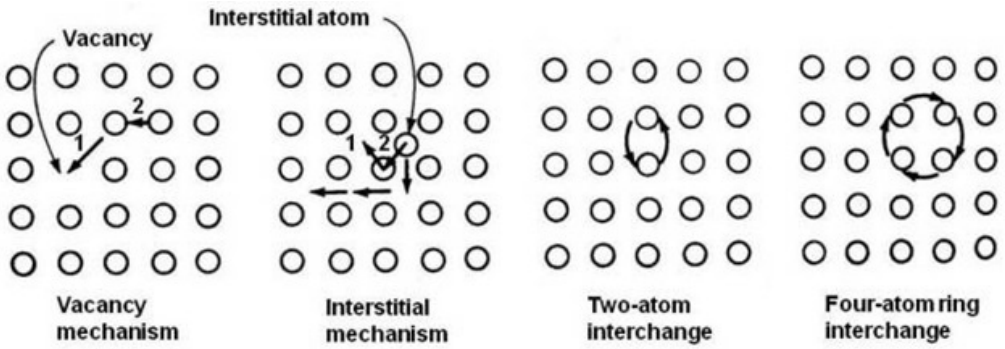

Fig. 2.1: *Schematic of some different diffusion mechanisms* [87].

Diffusion is mathematically described by the well-known Fick's laws of diffusion:

$$J = -D\frac{\partial \phi}{\partial x} \tag{2.1}$$

$$\frac{\partial \phi}{\partial x} = D\frac{\partial^2 \phi}{\partial x^2} \tag{2.2}$$

where J is the diffusion flux and ϕ is the concentration.

The parameter D in equations 2.1 and 2.2 is the diffusion coefficient or diffusivity, which describes the diffusion rate: the higher the diffusivity, the faster one substance will diffuse into another. D is generally well estimated by an Arrhenius-type equation:

$$D = D_0 \cdot e^{\frac{-E}{RT}} \tag{2.3}$$

As can be seen, the speed of diffusion depends on two main parameters: temperature (T) and activation energy (E).

- *Temperature*

  It is well-known, and easily deduced from equation 2.1, that temperature favors diffusion. An increase in its value means more energy for the atoms movement and therefore faster diffusion. During MA process, an increase in the temperature is produced due to friction during collisions and plastic deformation [88].

- *Activation energy*

  A transfer of a certain amount of energy is required for any diffusion mechanism. This energy is generally obtained after heating the sample, but in MA it is obtained from the kinetic energy of the movement of the balls and stored in the crystallographic defects enhanced by the MA process itself. Lower values of E mean faster diffusion, whereas higher values mean slower diffusion. The magnitude of the required energy varies from one diffusion mechanism to the other. For example, volume diffusion shows very high values for E, whereas surface diffusion shows lower values. In MA, the predominant mechanism is surface diffusion [8].

  The amount of energy that may be stored in the defects depends dramatically on the grain size although two regimes can be observed below and above the nanometric limit [89], with the region with small grain sizes being where the dependence is stronger (fig. 2.2), due to the increase of crystallographic defects induced by the MA process.

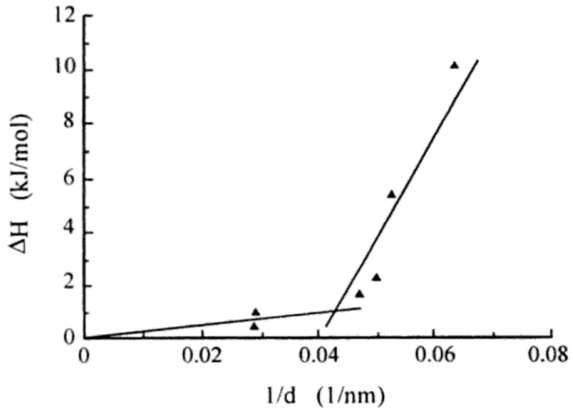

Fig. 2.2: *Dependence of the stored enthalpy ΔH with the grain size d. Two regimes can be observed: weak dependence for grain sizes above approx 25 nm (left) and strong dependence for sizes below (right)* [8]

Consequently, alloys with nanometric crystals show a significant higher diffusivity. This can be explained by the fact that their grain boundaries represent a large proportion of the total size, and hence diffusion mechanisms are enhanced [90].

2.1.3 Process of alloying

During the milling process, the powder particles are frequently and repeatedly trapped between the balls or between the balls and the container and are therefore repeatedly flattened, cold welded, fractured and rewelded. Typical figures of the amount of material trapped in each collision lie around 1000 particles and an aggregate weight of about 0.2 mg [79]. The force of the impacts plastically deforms the powder particles leading to work hardening and fracture. The new surfaces created, along with the fact that in the early stages of milling the particles are relatively soft, enable the particles to weld together and this leads to an increase in particle size, although with a broader range of sizes. The composite particles at this stage have a characteristic layered structure consisting of various combinations of the starting constituents.

With continued deformation, the particles get work hardened and fracture by a fatigue failure mechanism and/or by the fragmentation of fragile flakes. Fragments generated by this mechanism may continue to reduce in size in the absence of strong agglomerating forces. At this stage, the tendency to fracture predominates over cold welding. Due to the continued impact of grinding balls, the structure of the particles is steadily refined, but the particle size continues to be the same. Consequently, the inter-layer spacing decreases and the number of layers in a particle increases.

After milling for a certain length of time, steady-state equilibrium is attained when a balance is achieved between the rate of welding, which tends to increase the average particle size, and the rate of fracturing, which tends to decrease the average composite particle size. Smaller particles are able to withstand deformation without fracturing and tend to be welded into larger pieces, with an overall tendency to drive both very fine and very large particles towards an intermediate size [80]. At this stage each particle contains substantially all of the starting ingredients, in the proportion they were mixed together and the particles reach saturation hardness due to the accumulation of strain energy. The particle size distribution at this stage is narrow, because particles larger than average are reduced in size at the same rate that fragments smaller than average grow through agglomeration of smaller particles [91].

As mentioned in the last section, the ductility of the raw materials is crucial for the characteristics of the final alloy, and it has been suggested [80] that it is necessary to have at least 15% of a ductile component for achieving alloying, due to the necessity of the cold welding to occur for true alloying.

According to the ductility of the materials, three possible combinations arise:

- *Ductile-ductile systems*

  The ductile-ductile combination has been usually considered the ideal for MA [79], and a large number of elemental blends that are mechanically alloyed so far fall indeed in this category [9].

In the early stages of MA, the ductile components get flattened to platelet/pancake shapes by a micro-forging process [92].

In the next stage, these flattened particles get cold welded together and form a composite lamellar structure of the constituent metals. An increase in particle size is also observed at this stage.

With increasing MA time, the composite powder particles get work hardened. As hardness and consequently brittleness increase, the particles get fragmented, resulting in more equiaxed dimensions [93]. Later on, the elemental lamellae of the welded layer and both the coarse and fine powders become convoluted rather than being linear. This is due to the random welding together of equiaxed powder particles without any particular preference to the orientation with which they weld. Alloying begins to occur at this stage due to the combination of decreased diffusion distances (interlamellar spacing), increased lattice defect density, and any heating that may have occurred during the milling operation. The hardness and particle size tend to reach a saturation value at this stage, called the steady-state processing stage.

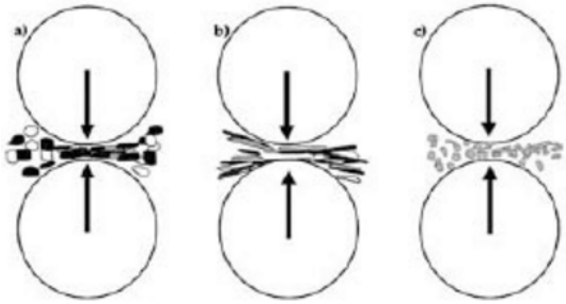

Fig. 2.3: *Schematic of different stages during MA: (a) starting powder, (b) flattened, layered, composited particles, (c) homogeneous equiaxed particles* [94]

With further milling, true alloying occurs at the atomic level resulting in the formation of solid solutions, intermetallics, or even amorphous phases. The layer spacing becomes so fine or disappears at this stage that it is no longer visible under an optical microscope.

- *Ductile-brittle systems*

  In ductile-brittle systems, MA usually results in a homogeneous dispersion of brittle phase in the ductile matrix [93], but whether alloying occurs or not in a ductile-brittle system mainly depends on the solid solubility of the brittle component in the ductile matrix. If a component has a negligible solid solubility then true alloying is unlikely to occur (e.g. boron in iron), but if the brittle phase is soluble enough (e.g. silicon in iron), alloying occurs and chemical homogeneity can be achieved. Thus, alloying of ductile-brittle components during MA requires not only fragmentation of brittle particles to facilitate short-range diffusion, but also reasonable solid solubility in the ductile matrix component.

  In the initial stages of milling, the ductile (generally metal) powder particles get flattened by the ball-powder-ball collisions, whereas the brittle (usually oxide or intermetallic) particles get fragmented/comminuted. The latters tend to become occluded by the ductile constituents and

trapped in the ductile particles. The brittle constituent is closely spaced along the interlamellar spacings.

With further milling, the ductile powder particles get work hardened, the lamellae get convoluted, and refined (as described for ductile-ductile combination). Later on, the lamellae get further refined, the interlamellar spacing decreases, and the brittle particles get into the ductile matrix either interstitially (if they are insoluble) or substitutionally (if they are soluble).

- *Brittle-brittle systems*

  It should seem intuitively unlikely that alloying might occur in a system consisting of two or more brittle components -at least at low temperatures-, due to the absence of any ductile component preventing fast welding and to the longer diffusion distances required in the brittle-brittle granular geometry in comparison with the ductile-ductile laminar geometry, and/or the enhanced diffusion paths provided by severe plastic deformation in ductile-ductile systems.

  However, it must be considered that, as the brittle components get fragmented during milling, their particle size gets reduced continuously until reaching a point where further reduction in size is generally not possible [95], thus showing a more ductile behavior.

  Alloying has been reported to occur in brittle-brittle component systems such as Si-Ge and Mn-Bi [96, 97], and milling of mixtures of some brittle intermetallics has been also reported to produce amorphous phases [98]. In these cases, the harder (more brittle) component generally gets fragmented and embedded into the softer (less brittle) component [79].

  Possible factors that may contribute to material transfer during milling of brittle components may include local temperature rise, microdeformation in defect-free volumes, surface deformation or hydrostatic stress state of powders during milling [97], all of them enhancing plastic deformation.

2.1.4 Procedure and parameters involved

The typical procedure for MA processing starts with mixing of the powders in the right proportion and loading the powder mix into the mill along with the grinding medium (generally steel balls). This mix is then milled for the desired length of time until a steady state is reached when the composition of every powder particle is the same as the proportion of the elements in the starting powder mix. The milled powder can be then consolidated into a bulk shape and heat treated to obtain the desired microstructure and properties.

There are several elements and parameters which may modify the final result of the milling process. An adequate combination of these variables improves control of the final product and its microstructural properties. The most significant parameters are:

- *Properties of the raw materials*

  The evolution of the alloying process depends strongly on the characteristics and properties of the raw materials used, and especially on their ductility or ability of sustaining plastic deformation without fracturing. For ductile materials, welding will be the predominant mechanism, whereas for fragile materials, fracturing will.

- *Type of mill*

  Different types of high-energy milling equipment are used to produce mechanically alloyed powders. They differ in their capacity, efficiency of milling and additional arrangements for cooling, heating, etc:

  – Shaker mills. Shaker mills such as SPEX mills, which mill about 10-20 g of the powder at a time, are most commonly used for laboratory investigations and for alloy screening purposes. The common variety of the mill has one vial, containing the sample and grinding balls, secured in the clamp and swung energetically back and forth several thousand times a minute. The back-and-forth shaking motion is combined with lateral movements of the ends of the vial, so that the vial appears to be describing a figure of an eight or an infinity sign as it moves. With each swing of the vial the balls impact against the sample and the end of the vial, both milling and mixing the sample. Because of the amplitude (about 5 cm) and speed (about 1200 rpm) of the clamp motion, the ball velocities are high (on the order of 5 m/s) and consequently the force of the ball's impact is unusually great. Therefore, these mills can be considered as high-energy variety.

  – Planetary mills. This is arguably one of the most popular group of mills, and includes the devices used for the purpose of this work. The planetary ball mills owe their name to the planet-like movement of its vials, which are arranged on a rotating support disk and a special drive mechanism causes them to rotate around their own axes (fig. 2.4).

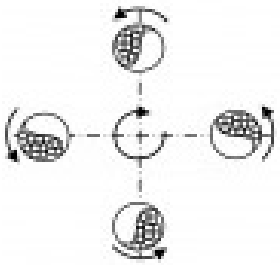

Fig. 2.4: *Movement of the vials in a planetary mill* [99].

The centrifugal force produced by the vials rotating around their own axes and that produced by the rotating support disk both act on the vial contents and the grinding balls (fig. 2.5). Since the vials and the supporting disk rotate in opposite directions, the centrifugal forces alternately act in like and opposite directions. This causes the grinding balls to run down the inside wall of the vial (the friction effect), followed by the material being ground and grinding balls lifting off and travelling freely through the inner chamber of the vial and colliding against the opposing inside wall (the impact effect).

In a planetary mill, a few hundred grams of the powder can be milled at a time.

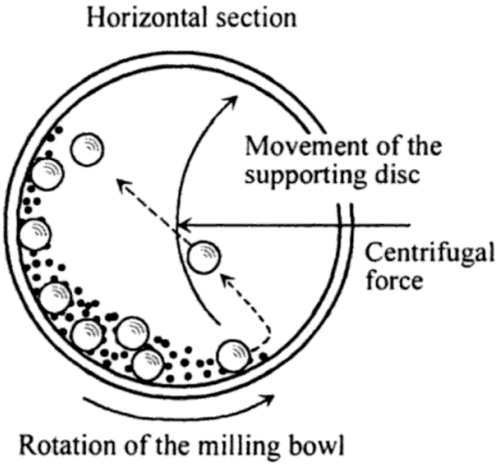

Fig. 2.5: *Schematic diagram of the internal movements in a planetary mill container* [8].

- Attritor mills. A conventional ball mill consists of a rotating horizontal drum half-filled with small steel balls. As the drum rotates, the balls drop on the metal powder that is being ground; the rate of grinding increases with the speed of rotation. At high speeds, however, the centrifugal force acting on the steel balls exceeds the force of gravity, and the balls are pinned to the wall of the drum. At this point the grinding action stops. An attritor (a ball mill capable of generating higher energies) consists of a vertical drum with a series of impellers inside it. Set progressively at right angles to each other, the impellers energize the ball charge, causing powder size reduction because of impact between balls, between balls and container wall, and between balls, agitator shaft, and impellers. Some size reduction appears to take place by interparticle collisions and by ball sliding. A powerful motor rotates the impellers, which in turn agitate the steel balls in the drum.

- Commercial mills. Commercial mills for MA are much larger in size than the mills described above and can process several hundred pounds at a time. Mechanical alloying for commercial production is carried out in ball mills of up to about 1250 kg capacity.

- *Milling speed*

  It is easy to realize that the faster the mill rotates the higher would be the energy input into the powder. However, depending on the design of the mill there are certain limitations to the maximum speed that could be employed. For example, in a conventional ball mill increasing the speed of rotation will increase the speed with which the balls move. Above a critical speed, the balls will be pinned to the inner walls of the vial and do not fall down to exert any impact force. Therefore, the maximum speed should be just below this critical value so that the balls fall down from the maximum height to produce the maximum collision energy.

  Another limitation to the maximum speed is that at high speeds (or intensity of milling), the temperature of the vial may reach a high value. This may be advantageous in some cases where diffusion is required to promote homogenization and/or alloying in the powders. But, in some cases, this increase in temperature may be a disadvantage because the increased temperature accelerates the transformation process and results in the decomposition of supersaturated solid solutions or other metastable phases formed during milling [100].

- *Milling time*

  The time of milling is arguably the most important parameter [79]. Normally the time is so chosen as to achieve a steady state between the fracturing and cold welding of the powder particles. As said before, the times required vary depending on the type of mill used, the intensity of milling, the ball-to-powder ratio, and the temperature of milling. These times have to be decided for each combination of the above parameters and for the particular powder system. But, it should be realized that the level of contamination increases and some undesirable phases form if the powder is milled for times longer than required [7]. Therefore, it is desirable that the powder is milled just for the required duration and not any longer.

- *Grinding medium*

  The material used for the milling -balls and container- is important due to impact of the balls on the inner walls of the container, which may force some material to be dislodged and get incorporated into the powder. This can contaminate the powder or alter the chemistry of the powder. If the material of the grinding medium is different from that of the powder, then the powder may be contaminated with it. On the other hand, if the two materials are the same, then the chemistry may be altered unless proper precautions are taken to compensate for the additional amount of the element incorporated into the powder.

  Hardened steel, tool steel, hardened chromium steel, tempered steel, stainless steel, WC-Co, etc. are some of the most common types of materials used [101]. Furthermore, the density of the grinding medium should be high enough so that the balls create enough impact force on the powder. It is always desirable, whenever possible, to have the grinding vessel and the grinding medium made of similar material as the powder being milled to avoid cross contamination.

  The size of the grinding medium also has an influence on the milling efficiency. Generally speaking, a large size (and high density) is useful since the larger weight of the balls will transfer more impact energy to the powder particles.

- *Ball-to-powder weight ratio* (BPR)

  The ratio of the weight of the balls to the powder (BPR) is an important variable in the milling process. The BPR has a significant effect on the time required to achieve a particular phase in the powder being milled. The higher is the BPR, the shorter is the time required, since when increasing in the weight proportion of the balls, the number of collisions per unit time increases and consequently more energy is transferred to the powder particles and so alloying takes place faster.

  Nevertheless, an excessively high BPR value may diminish the effectiveness of the milling, because an excessively full container reduces the free path for the milling balls and hence the collision energy. For a better optimization of the milling time, an equilibrium point should be found between the number of balls and the amount of material.

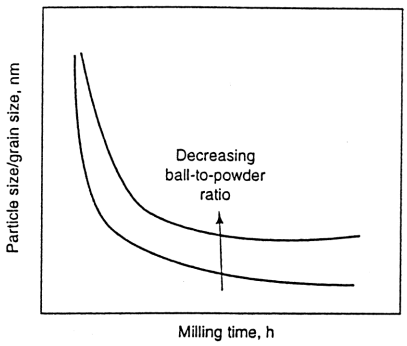

Fig. 2.6: *General dependence of the evolution of milling process with the BPR [79]*

The typical values for BPR differ with the type of mill. For a planetary mill, it may range from 4:1 to 20:1. For the other types, it may range from the 10:1 of low-capacity mills (such as SPEX) [102] to the 50:1 or 100:1 of high-capacity mills [103].

- *Milling atmosphere*

  The major effect of the milling atmosphere is on the contamination of the powder. The presence of air in the vial has been shown to produce oxides and nitrides in the powder, especially if the powders are reactive in nature. Therefore, the powders are usually milled in containers that have been either evacuated or filled with an inert gas such as argon or helium, with high-purity argon being the most common ambient to prevent oxidation or contamination of the powder [79].

  On the other hand, several other non-inert atmospheres are often used for some specific purposes where a certain reaction is sought, such as nitrogen or ammonia atmospheres for the production of nitrides [104, 105] or hydrogen for hydrides [106].

- *Process control agents* (PCA)

  The powder particles get cold-welded to each other, especially if they are ductile, due to the heavy plastic deformation experienced by them during milling. True alloying among powder particles can occur only when a balance is maintained between cold welding and fracturing of particles. A process control agent (PCA), also referred to as lubricant or surfactant, may be added to the powder mixture during milling to reduce the effect of cold welding and help the balance [79, 107, 108].

  A wide range of PCAs has been used in practice at a level of about 1-5 % of the total powder charge. Although any solid, liquid or gas which act as a surface-active agent may be used, they are mostly organic compounds such as cyclohexane (C_6H_{12}) [109], hexane (C_6H_{14}) [110], stearic acid ($C_{17}H_{35}CO_2H$) [111], methanol (CH_3OH) [112], ethanol (C_2H_5OH) [113] or polyethylene glycol [114].

  The PCA adsorbs on the surface of the powder particles, lowers the surface tension of the solid material and minimizes cold welding between powder particles and thereby inhibits agglomeration. A reduction in surface energy results in the use of shorter milling times and/or

generation of finer powders [79] (the energy required for the physical process of size reduction is given by $E = \gamma \cdot \Delta S$, where γ is the specific surface energy and ΔS is the increase of surface area).

The use of PCAs may be also a source of contamination. Due to the increase of the temperature during the milling process, some elements of the PCA (mostly C and H) may react and form carbons, hydrides, etc. [108, 115]. The majority of commonly used PCAs show a low boiling temperature and often get volatilized, so reducing its effects on contamination. However, this might also be counterproductive, since the PCA may completely disappear before the end of the process and reduce the effectiveness of the milling process.

- *Temperature of milling*

  The temperature of milling is another important parameter in deciding the constitution of the milled powder. As it will be explained in next section, diffusion processes are involved in the formation of alloy phases irrespective of whether the final product phase is a solid solution, intermetallic, nanostructure, or an amorphous phase. It is thus expected that the temperature of milling will have a significant effect in any alloy system produced. There have been conflicting reports on the formation of an amorphous phase as a function of the temperature of milling, and both enhanced [116, 117] and diminished [118, 119] amorphisation kinetics have been reported.

Most of these variables are not completely independent. For example, the milling time depends strongly on the type of mill, the container dimensions, the milling temperature, the BPR, etc.

Equipment used

Two different planetary ball mill models were used for the production of the alloys in this work (2.7): a Fritsch Pulverissette 7 (P7), used for the the alloys studied in chapters 4 and 5 and the milled ribbons in chapter 6, and a Reitsch PM 400, used for the MA alloys in chapter 6.

Fig. 2.7: *Fritsch Pulverisette 7 (left) and Retsch PM 400 (right) mills* [120, 121]

2.2 Melt spinning (MS)

2.2.1 Introduction

Melt spinning (MS) is one of the most used techniques to cast metallic glasses by rapidly cooling of molten alloys. This technique is based on a wheel which is cooled internally and rotated while a thin stream of liquid is dripped onto it, causing rapid solidification of the molten alloys and allowing the formation of metamaterials which need extremely high cooling rates (in the order of $10^4 - 10^7$ K/s), such as amorphous metallic glasses. Due to the nature of the technique, the resulting alloys are cast in ribbon form.

The complete MS process for the preparation of the final alloys is indeed a two-stages process:

1. Preparation of the master alloys with a complementary technique such as arc-melting.
2. Casting of the final alloys from the molted master alloys prepared in stage 1.

2.2.2 Arc-melting of the master alloys

The preparation of a homogeneous *master alloy* is a crucial stage in the process. The chemical compositions involved are generally complex and consist on three or more elements with often unknown phase diagrams. The working temperature must be higher than that of the element with the highest melting point, in order to achieve a correct alloy. Several problems are usually found and must be solved:

1. If the temperature is just a few degrees beyond the melting point, the chemical reactions between the pure elements may require a significantly long time in order to be completed, during which the crucibles may show corrosion problems.
2. During the heating stage, a certain amount of stable compounds may be formed, which might be difficult to solve into the molten alloy.
3. Even after assuming the constituent elements are completely dissolved and form a high-temperature liquid, a relatively slow cooling process could separate part of the solution and produce a non-homogeneous alloy.

The arc melting technique allows the melting of several materials minimizing some of the problems listed above. It is based on the generation of an electric discharge (plasma) produced by the dielectric breakdown caused by a very high potential difference between two electrodes in the relatively low pressure (around 500 hPa). During the discharge process, a very intense light and heat emanation are produced so the temperature can achieve very high values, thus allowing the melting of different materials, including metals with high melting points.

The arc is generated by two tungsten tips that act as electrodes: a 4-mm diameter tip located in a copper crucible, which is used to generate the first spark of the arc, in contact with a second 2.4-mm

diameter tip, which is also used to maintain the arc all over the material until it is completely melted. This second tip is mounted in a mobile arm, thus allowing the homogenization of the melt.

In the copper crucible there are two holes of different sizes: one for the placement of the metals to be melt and one second hole necessary to place titanium. That is necessary to capture the oxygen that could remain inside the furnace and can cause the oxidation of the samples.

While the arc melting is working it is necessary to refrigerate the copper crucible and the arm independently. The refrigerant liquid is water contained in a tank that flows into the arc melting with the help of a small water pump that gives the sufficient pressure to overcome the difference in height level and to maintain a good refrigeration flow.

A current generator yields the required potential difference between the electrodes and it is controlled by a pedal for switching on and off the current and by a knob for controlling the intensity.

Before starting to work with the arc melting, it is necessary to make the vacuum inside the furnace with a rotatory vacuum pump that reach levels in the order of 10^{-3} hPa. This is necessary to improve the homogeneity of the sample and to minimize impurities, which might cause nucleation of crystals during the melt-spinning stage.

2.2.3 Casting of the final alloys with MS

The second stage of the process is the casting of the final alloys using the *master alloys* produced in the previous stage.

The samples are melt using a coil wounded around a quartz tube where the master alloy is deposited. When the sample reaches the liquid state, is then ejected onto a cooled copper wheel rotating at high speed. The surface of the wheel acts as a heat sink and the liquid solidifies at cooling rates in the order of $10^4 \sim 10^6$ K/s, with the exact value depending mainly on:

- the melting temperature
- the cross-section of the jet ejected,
- the overpressure employed,
- the tangential velocity of the wheel,
- the distance between the pipe quartz and the wheel,
- the pressure of the chamber where the sample is ejected (vacuum, air, inert atmosphere, etc.).

These cooling rates are high enough to obtain amorphous or crystalline ribbons with different grain size. However, due to the high speed, only a few micrometers thick ribbon is formed, which is expelled from the wheel due to the centrifugal force. The typical thickness of the ribbons obtained is 20-40 μm depending on the wheel velocity, and their wideness is 1-50 mm, depending on the crucible hole diameter.

Characterization techniques

3

> *Nearly all men can stand adversity, but if you want to test a man's character, give him power.*
>
> — **Abraham Lincoln**
> (Politician)

Contents

This chapter shows descriptions and physical foundations of the analytical methods used in this work for the characterisation of the samples produced and studied.

Table 3.1 shows an overview of the characterizations carried out and the analytical techniques used in each group. As the table shows, some of the techniques allow several different characterizations.

Morphological and structural analysis
Scanning electron microscopy (SEM) (see section 3.1)
X-Ray diffraction (XRD) (see section 3.2)
Mössbauer spectroscopy (see section 3.3)
Differential scanning calorimetry (DSC) (see section 3.4)
TG-based thermomagnetometry (see section 3.5.2)
Thermal analysis
Differential scanning calorimetry (DSC) (see section 3.4)
TG-based thermomagnetometry (see section 3.5.1)
Magnetic analysis
Mössbauer spectroscopy (see section 3.3)
TG-based thermomagnetometry (see section 3.5.2)
M-H hysteresis cycle measurements (see section 3.5.1)
Bitter colloid method (see section 3.5.3)

Tab. 3.1: *List of the characterization techniques used in this work*

3.1 Scanning electron microscopy (SEM)

Microscopy is a group of techniques that allow the observation of objects with an apparent size higher than the real. In the process of choosing the appropriate microscopy technique to be used, two parameters are of special importance: magnification -the proportionality constant between the real and apparent sizes- and resolution -the minimum distance between two distinguishable objects-.

The optimal resolution of a microscope R is determined by the Rayleigh criterion:

$$R = \frac{0.61\lambda}{n \sin\theta} \tag{3.1}$$

where θ is half the angular aperture, n is the refractive index of the medium between the lens and the specimen and λ is the wavelength of the radiation used.

The Rayleigh criterion means that the maximum resolution achievable by an optical microscope is only about 200 nm and in order to improve (reduce its value), a shorter wavelength must be used. This is the case of electron microscopy, a group of techniques based on the use electrons with de Broglie wavelengths ($\lambda = \frac{h}{p}$) suitable for the desired resolution, with scanning electron microscopy (SEM) as one of the most commonly used techniques.

In a SEM microscope, a beam of electrons with energies between 2 and 40 keV is focused in a certain point of the sample and the response to this interaction is studied and analyzed, as shown schematically in fig. 3.1.

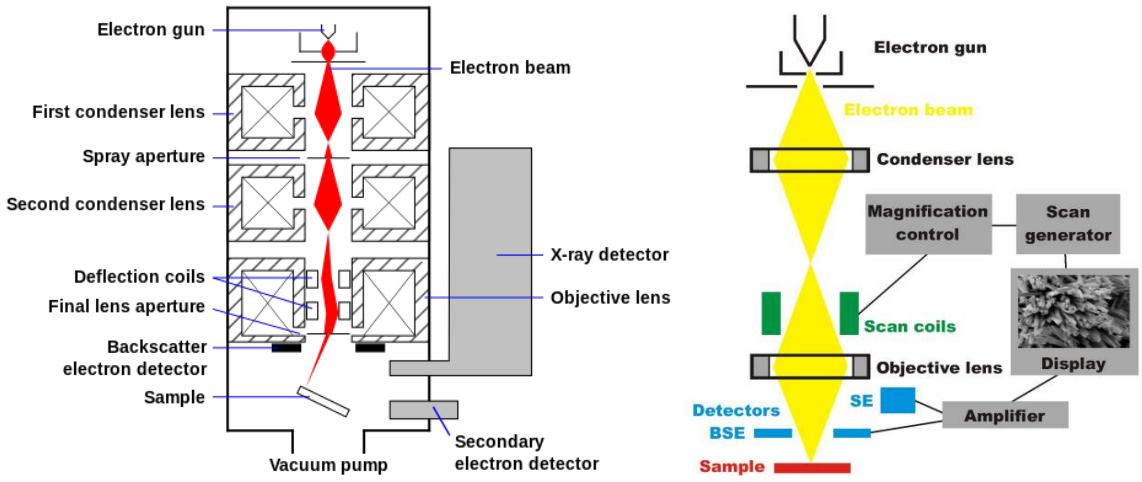

Fig. 3.1: *Schematic representation of a SEM microscope* [122, 123].

Several different kinds of signals are produced during a SEM analysis, as shown in figure 3.2, each one with its own purpose, application, methodology and equipment. The most common products are explained in the list below.

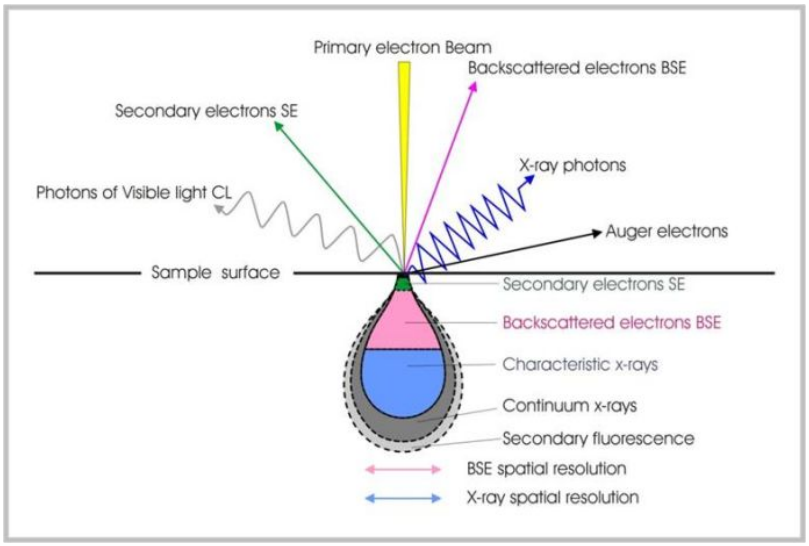

Fig. 3.2: *Signals produced after the interaction of the electrons with a sample in a SEM* [124].

- *Secondary electrons (SE)*

  This is the most common signal analyzed in a SEM and is produced by electrons from the sample excited by the incident electron beam with energy high enough to reach the surface and leave the sample. These are generally low-energy electrons (E < 50 eV).

- *Backscattered electrons (BSE)*

Electrons that interact elastically or quasielastically with the atoms in the sample. The probability of these interactions is related to the atomic number Z of the atoms in the material.

- *Auger electrons (AE)*

  Low-energy electrons produced at the surface of the sample. The amount and energy of these electrons are specific to material of the sample, making this signal useful for elemental analysis. In a simple continuum spectrum, the Auger electrons are easily identifiable as a series of narrow single peaks, as shown in figure 3.3.

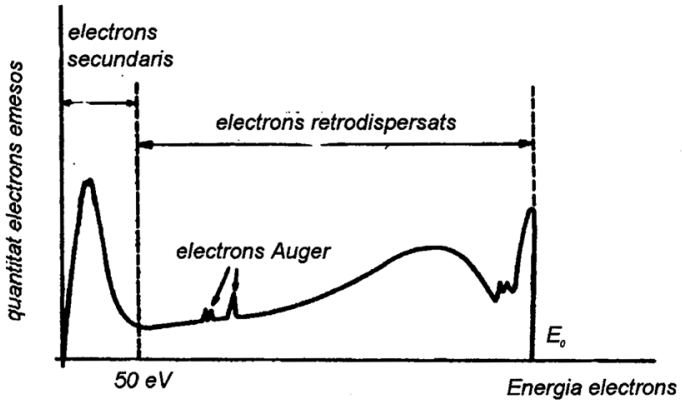

Fig. 3.3: *Electron energy spectrum in a SEM* [125].

- *X-ray photons*

  The production of secondary electrons (SE) in the inner atom layers cause the desexcitation of other electrons from higher energy levels, resulting in the emission of X-ray photons. The wavelength of the emitted radiation is unique for every element, allowing a complementary elemental analysis.

- *Photons of visible light (cathodoluminescence, CL)*

  The inelastic collisions of the incident electrons with the atoms of the sample produce photons of visible light, a phenomenon known as cathodoluminescene (CL). The measurement of this photons allows a non destructive semiquantitative high-sensibility microanalysis with resolutions of the order of the microns.

- *Specimen current*

  Specimen current is defined as the difference between the primary beam current and the total emissive current (backscattered, secondary and Auger electrons)[126]. Therefore, specimens that have stronger emission currents will have weaker specimen currents and viceversa. Imaging from these electrons has the advantage of using the sample as its own detector.

- *Transmitted electrons*

  If the sample is thin enough (typically less than 1μm), a significant amount of primary beam electron may pass through it and produce a suitable signal, as in transmission electron microscopy (TEM).

SEM equipment

The SEM analyses shown in this work were carried out with the equipment, characteristics and working conditions listed in table 3.2.

SEM equipment and working conditions	
equipment	SEM Zeiss DSM-960A (1994) (see fig.3.4)
location	STR - UM (Microscopy Unit) [127] Polytechnic School (EPS), University of Girona (UdG)
resolution	3.5 nm
acceleration voltage	20 kV
magnification	500x and 5000x
detectors	secondary electrons EDX

Tab. 3.2: *Characteristics of the equipment and working conditions used for the SEM experiments*

Fig. 3.4: *The Zeiss DSM-960A microscopy used for the SEM characterizations* [127]

The setting up of the samples consisted in sticking the powder on a metallic stand with a dual-side adhesive paper and a subsequent carbon covering layer, with the purpose of enhancing the sample conductivity and improve the quality of the signal.

3.2 X-Ray diffraction (XRD)

X-Ray diffraction (XRD) is a technique for structural determination of solids through the characteristic diffraction patterns which result from each unique crystal structure. Since X-Ray radiation comprises wavelengths from 10^{-8} to 10^{-12} m ($10^{16} - 10^{20}$ Hz), it is suitable for the studying of diffraction patterns involving interatomic typical distances in a crystal (10^{-10} m).

The X-Ray radiation is produced irradiating with electrons the anode of a cathode ray tube and is composed of two subspectra: the continuum spectrum and the characteristic spectrum. The former, which ranges over a wide part of the spectrum, is due to the *bremsstrahlung*, radiation produced by the deceleration of charged particles. The latter includes a few narrow and sharp peaks which are characteristic of the anode used, and is responsible of the monochromaticity of the X-rays.

The source of the characteristic spectrum are the photons emitted by the anode atoms. When an incident electron collides with an electron of an inner level of the anode and pulls it up, the vacancy is then occupied by another electron of a higher level. This process of desexcitation means the emission of a photon of a specific energy. The specific values for the frequencies of the peaks in the characteristic spectrum will depend on which elements are present in the composition of the anode.

Atomic diffraction theory was first proposed by Max von Laue in 1912 and granted him the 1914 Nobel Prize in Physics [128]. Laue stated that the atoms of the materials act as diffractive centers, following the Huygens principle. The diffracted waves are affected by interferences and produce points of maximum and minimum intensity.

X-Ray diffraction theory was later developed by W.L. Bragg and W.H. Bragg in 1913 [129] in response to their discovery that crystalline solids produced surprising patterns of reflected X-rays. They found that in these crystals, for certain specific wavelengths and incident angles, intense peaks of reflected radiation –the Bragg peaks- were produced. This result was explained by modeling the crystal as a set of discrete parallel planes separated by a constant parameter d and proposing that the incident X-ray radiation would produce a Bragg peak if the reflections of different planes interfered constructively. W.L. and W.H. Bragg were awarded with the 1915 Nobel Prize in Physics for this theory [130].

Mathematically, this explanation can be written by the well-known Bragg's law:

$$n\lambda = 2d_{hkl} \cdot \sin\theta \tag{3.2}$$

where λ is the wavelength of the X-Ray radiation, d_{hkl} is the distance between two consecutive parallel planes with Miller index h, k and l, θ is the angle between the incident ray and the scattering planes and n is an integer number which indicates the order of diffraction.

3.2.1 Powder XRD measurement procedure

Although there are several other kinds of diffraction analysis such as Laue diffraction (where the incident beam is wide in frequency and the incident angle is set constant) and rotating crystal diffraction (the incident beam is monochromatic and the angle is changed by rotating the crystal), only powder diffraction will be described here.

In powder XRD diffraction, the incident beam is monochromatic and, since the sample is in a powder form, the crystals are randomly oriented and the incident angle must be variable. The X-ray source and the detector are placed in a way that a 2θ angle exists between them. A counter is set in the detector, which records the number of photons that reach it for a specific angle. The procedure is repeated for different 2θ values and a spectrum with the intensity –the number of photons detected- as a function of 2θ is obtained.

The obtaining of the XRD spectra can be carried out in either a continuous or discrete operation mode, depending on how the different values for 2θ are set. A discrete operation mode means a stop-and-measure procedure, which generally is more slow and laborious but with significantly better results.

Several other factors affect the amount and quality of the XRD data such as the sweep velocity and acquisition time, the monochromaticity of the radiation or the characteristics of the sample and detector. About the latter, the detection is currently being generally carried out with the use of counters, which sequentially records the intensity for a single angle value.

XRD equipment

The XRD measurements shown in this work were carried out with the equipment, characteristics and working conditions detailed in table 3.3.

XRD equipment and working conditions	
diffractometer	Bruker AXS D8 Advance (see fig.3.5)
location	STR - Chemical Analysis Unit (UAQiE) [131] Polytechnic School (EPS), University of Girona (UdG)
anode	Cu
K_{α_1}, K_{α_2} *and* K_{β} *wavelengths*	0.154060 nm, 0.154443 nm and 0.139222 nm
X-rays voltage and intensity	40 kV, 40 mA
detector	Tl-doped NaI scintillation counter
working temperature	room temperature
working mode	continuous, step time: 4 s
2θ *step*	0.05°

Tab. 3.3: *Characteristics of the equipment and working conditions used for the XRD experiments*

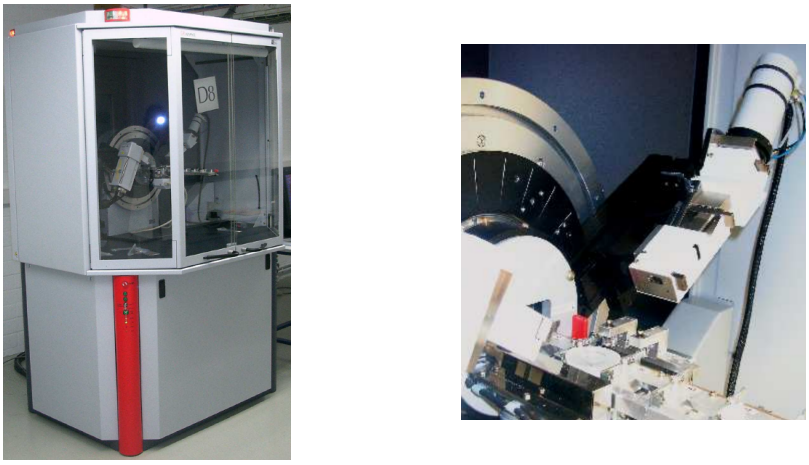

Fig. 3.5: *The D8 diffractometer used for the XRD analyses* [131]

3.2.2 Analysis of the XRD results

The amount of information that can be obtained from a XRD pattern depends on the amount and quality of the data acquired.

Phase identification

One of the primary uses of the XRD analysis is the identification of the solid phases present in the sample. Every single solid phase shows a specific XRD pattern and the spectra of many known phases are commonly stored in large databases. When analyzing a recorded XRD spectrum, the very first step is usually the comparison with patterns of the database and the identification of the best-matched. The most used are the PDF (Powder Data File) databases, edited by the International Centre for Diffraction Data (ICDD) [132], which contain diffraction patterns of several organic and inorganic compounds, minerals, etc. Since pattern databases are huge, phase identification may often be a difficult task and generally requires help from specialized software.

A single diffraction pattern of a certain phase contains information about some of its crystallographic parameters and in particular the positions of the diffraction peaks in a 2θ axis. Some databases may show the equivalent value of d –the interplanar distance- instead of 2θ (It must be remembered that, for a fixed wavelength value, there is a direct equivalence between these two parameters).

Lattice parameters

The lattice parameters are the dimensions and angles in a cell unit of a specific Bravais lattice. The number of parameters required for the complete determination of the lattice depends on the crystal system. In the case of the cubic crystal system ($a = b = c$ and $\alpha = \beta = \gamma = 90°$), this number is reduced to only one (parameter a, which is the length of any single edge of a cell unit). For the tetragonal and hexagonal, two parameters are required (a and c), whereas for the rest of crystal systems the number may vary.

The lattice parameters have a specific geometrical meaning when they are referred to a monocrystal, but when they are referred to amorphous or nanocrystalline materials this meaning is changed and they must be considered as average values. A lattice parameter which differs from the theoretical value for a pure monocrystalline phase may indicate [133]:

- Presence of atoms of a different element in solid solution interstitially
- Presence of atoms of a different element in solid solution substitutionally
- Presence of crystalline defects
- Order-disorder transition

Crystal size and strain

A single ideal monocrystal with theoretical infinite dimensions should show a diffraction pattern consisting of some infinitely narrow peaks in specific positions (only those corresponding to the interplanar distances). Nevertheless, for microcrystalline, nanocrystalline or amorphous powders, rays coming from inner layers and with incidence angles near the Bragg angle are not cancelled, resulting in a non-zero intensity distribution.

A quantitative analysis of the wideness of the peaks can be made adjusting them to either a Cauchy-Lorentz or a Gaussian distribution curve and calculating the parameter β or $FWHM$ (*full-width at half-maximum*), which is the width of the curve at half of its total height. This parameter is strongly related to the average dimension of the crystals, according to the Scherrer formula [134]:

$$< L >= \frac{0.94\lambda}{\beta \cdot \cos\theta} \tag{3.3}$$

where θ is the angle value where the peak is centered at and λ is the wavelength of the X-ray used.

Nevertheless, the whole width of the peak is also affected by other factors such as the presence of deformation microstrain. The sources of this strain may be plastic deformation, dislocations and other crystallographic defects which are mainly concentrated in the grain borders [125]. The wideness due to the deformation microstrain is:

$$\beta_{strain} = 4\varepsilon \tan\theta \tag{3.4}$$

where ε is the average deformation and θ is the angle corresponding to the peak position.

Finally, several other factors related to the instrumental used, such as the non-chromaticity of the X-rays or the detector precision, may modify the width of the peaks detected and must be considered. The contribution due to these sources is generally determined using a spectrum of a perfectly crystalline pattern sample.

Rietveld refinement

Rietveld refinement is a technique devised by H. Rietveld [135] for the analysis of diffraction spectra. This method uses a least squares approach to refine a theoretical line profile until it matches the measured profile. The difference between the experimental and the theoretical curves is quantified with the following expression [136]:

$$R_{wp} = \sqrt{\frac{\sum {y_i}^2 - {y_{i,calc}}^2}{\sum \omega_i {y_i}^2}} \tag{3.5}$$

where y_i and $y_{i,calc}$ are the measured and the calculated intensities, respectively, and ω_i is the weight associated to that intensity.

The quality or goodness of fit of a refinement can be quantified with the parameter χ^2:

$$\chi^2 = \frac{R_{wp}}{R_{exp}} \tag{3.6}$$

where

$$R_{exp} = \sqrt{\frac{N-p}{\sum \omega_i {y_i}^2}} \tag{3.7}$$

N and p are, respectively, the number of measured points and parameters to refine.

The implementation of the Rietveld refinement generally needs help from specialized software, such as FULPROOF™, RIETQUAN™or MAUD™. The latter, created and developed by Luca Lutterotti [137] is one of the most used programs for this purpose and the one used for this work.

3.3 Mössbauer spectroscopy

The Mössbauer spectroscopy is a particular case of nuclear spectroscopy of resonant absorption based on the Mössbauer effect, discovered by R.L. Mössbauer on 1958 [138] after observing a dramatic increase in the resonant absorption of γ rays when the working temperature was decreased.

3.3.1 The Mössbauer effect

The Mössbauer Effect is a process in which a nucleus emits or absorbs gamma rays without loss of energy to a nuclear recoil. R.L. Mössbauer secured the 1961 Physics Nobel Prize [139] for this discovery, which opened some paths in other fields of knowledge, such as the detection of the redshift of light moving in the Earth gravitational field (Pound-Rebka experiment [140]).

During emission or absorption of a gamma ray, conservation of momentum requires the nucleus to recoil. Therefore, there are generally some difference between the energies of the gamma rays emitted and absorbed, because in both cases energy is lost to recoil.

Nuclei in a solid crystal, however, are not free to recoil because they are bound in place in the crystal lattice. When a nucleus in a solid emits or absorbs a gamma ray, some energy can still be lost as

recoil energy, but it always occurs in discrete packets called phonons (quantized vibrations of the crystal lattice). Any whole number of phonons can be emitted, including zero, a event which is known as “recoil-free” (in this case conservation of momentum is satisfied by the momentum of the crystal as a whole, so practically no energy is lost) [141].

Mössbauer found that a significant fraction of emission and absorption events will be recoil-free. This fact is what makes Mössbauer spectroscopy possible, because it means that gamma rays emitted by one nucleus can be resonantly absorbed by a sample containing nuclei of the same isotope, and this absorption can be measured. And since gamma rays are generally very sensitive to small changes in the energies of nuclear transitions, they can be used as a probe to observe the effects of interactions between a nucleus and the electrons of the atom or the neighboring atoms.

The resonant absorption requires the emission and absorption peaks to be wide enough to be able to superpose. In order to increase their normally insufficient natural width, Mössbauer spectroscopy combines the Mössbauer effect with the Doppler effect. The addition of this Doppler term produces an enlargement of the peaks that helps the superposition. One way to produce this is to increase the temperature T, but this reduces the effectiveness of the process. Therefore, Möosbauer spectroscopy uses the relative movement of the emitter respect to the sample to increase the Doppler effect and widens the curves.

Mössbauer spectroscopy requires a suitable gamma-ray source, which consists of a radioactive parent that decays to the desired isotope. For example, the source for ^{57}Fe consists of ^{57}Co, which decays by electron capture to an excited state of ^{57}Fe, which in turn decays to a ground state emitting a gamma-ray of the appropriate energy. The radioactive cobalt is prepared on a foil, often of rhodium.

Ideally the parent isotope will have a convenient half-life and the gamma-ray energy should be relatively low (10-150 keV), otherwise the system will have a low recoil-free fraction resulting in a poor signal-to-noise ratio and requiring long collection times.

^{57}Fe is by far the most common element studied using the technique, although ^{129}I, ^{119}Sn, and ^{121}Sb are also frequently studied.

3.3.2 Nuclear transitions

The analysis of the frequencies of the radiation absorbed by the sample allows the detection of the elements neighboring the elements producing the Mössbauer effect and the phase in which they are arranged, due to the fact that the gaps between different levels is perfectly known for each one.

The hyperphine interactions produce a shift and/or splitting of the nuclear levels. A typical Mössbauer study analyzes the following:

- *Isomeric shift* (IS)

  Also known as chemical shift, is a relative measure describing a shift in the resonance energy of a nucleus due to the transition of electrons within its s orbital. The whole spectrum is shifted in either a positive or negative direction depending upon the charge density, due to

alterations in the electrostatic response between the s electrons and the nucleus they orbit (For example, an increase in s electron density in ^{57}Fe spectrum gives a negative shift while the same increase in ^{119}Sn gives a positive shift). This term can also be affected indirectly by other electrons or by the oxidation state and the chemical environment of the atom (For example, oxidized ferric ions (Fe^{3+}) have lower isomer shifts than ferrous ions (Fe^{2+}), due to a weaker screening effect by d electrons)

The analysis of the IS allows the identification of the atomic charge, the chemical bond and the crystallographic environment.

- *Quadrupole splitting* (QS)

  A splitting in the absorption line, it reflects the interaction between the nuclear energy levels and surrounding electric field gradient due to the asymmetry in the nucleus.

- *Hyperfine splitting*

  Also known as the Zeeman effect, is a result of the interaction between the nucleus and any surrounding magnetic field.

The combined effect of these three interactions define the Mössbauer spectrum, which can be used to identify a particular compound by simple comparison to standards included in databases available in the literature.

For example, in the case of atoms of Fe, there are 6 allowed absorption transitions, shown in figure 3.6, due to the combined effect of the three interactions described, creating the well-known classic "sextet" in their spectra.

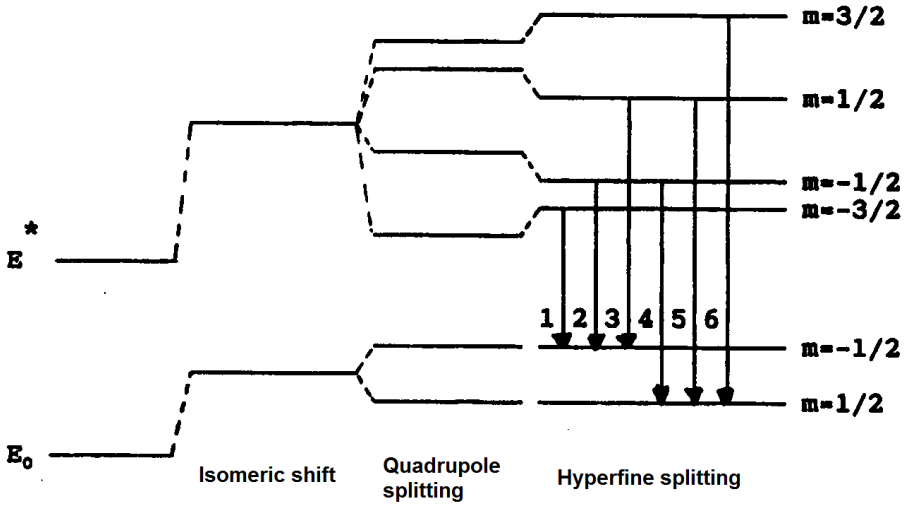

Fig. 3.6: *Magnetic splittings of the nuclear energy levels for ^{57}Fe* [125].

3.3.3 Methodology

The most common Mössbauer spectroscopy methodology is Transmission Mössbauer sepectrocospy, in which the source moves respect to the sample with a speed of the order of mm/s (typically 11 mm/s for ^{57}Fe). Due to the Doppler effect, this movement produces slight variations in the apparent frequency of the radiation. The emitted photons are absorbed by the sample only when the frequency corresponds to the energy gap between specific nuclear levels, and the measured signal is thus reduced. When the frequency does not correspond to any energy gap, the photons are not absorbed and the intensity of the signal is at its maximum. Therefore, a typical Mössbauer spectrum, which shows the % of transmission as a function of the velocity of the source, will consist in a series of depressions corresponding to each of the transition energies.

The obtained experimental spectrum is then adjusted to theoretical curves of the different phases which are supposed to be present in the sample. As in the case of XRD, this adjustment is usually carried out by means of specialized software, such as NORMOS™[142]. This program minimize the distance between the experimental and theoretical points accordin to the Hesse-Rübartsch method[143]. The different hyperfine parameters are then calculated from the adjusted curves.

The measurements carried out for the analyses in this work were performed at room temperature with the equipment of the Universitat Politècnica de Catalunya (UPC) [144], operating in transmission geometry with a 25 mCi source of ^{57}Co in Rh matrix.

3.4 Differential scanning calorimetry (DSC)

IUPAC defines Differential Scanning Calorimetry (DSC) as "*a technique in which the difference in energy inputs into a substance and/or its reaction product(s) and a reference material is measured as a function of temperature whilst the substance and reference material are subjected to a controlled temperature programme*" [145]. DSC is the modern offspring of Differential Thermal Analysis (DTA). Both techniques are based on the comparison between a sample and an inert reference, but in DSC the heat flow is monitored whereas in DTA the difference in temperature is.

This versatile technique allows several practical applications, such as:

- Determination of some relevant temperatures such as crystallization temperature, phase transition temperature, glass transition temperature...
- Phase diagram determination
- Estimation of the crystallized proportion
- Heat capacity measuring
- Reaction heat determination
- Measures on reaction kinetics (activation energy, reaction mechanism...)

In DSC experiments, two kinds of temperature programs are mainly used: isothermal experiments and constant heating/cooling rate experiments. The former ones are generally more accurate, since they are not affected by common dynamic problems such as thermal gradients, thermal delays or hysteresis, but on the other hand they need more process time and number of experiments. The latter ones need less process time but are affected by the problems mentioned above, an also show difficulty for a reliable baseline establishment. Although being complementary methods, these two programs not only are compatible but also are commonly combined.

3.4.1 DSC equipment

Generally speaking, there are two main kinds of DSC equipments:

- *Power compensating DSC*. The sample and the reference are heated/cooled independently but using the same temperature program. Since the heat capacities of both elements are different, so should be their temperature. The DSC device injects or extracts heat flow in order to make both temperatures equal. The amount of heat injected/extracted per time unit is the DSC output signal.

- *Heat flux DSC.* The sample and the reference lie on the same cavity and are heated simultaneously in the same oven and with the same temperature program. The DSC device measures the temperature difference between the two samples and converts it, using specific software and after considering calibration parameters, into the equivalent amount of heat per time unit, which is the DSC output signal.

Both types of DSC devices include the following components:

- *Cell*. This is the cavity where the crucibles are stored. Two crucibles are needed for every experiment: one for the sample to measure and one as a reference. The latter is generally just an empty crucible identical to that of the sample. The cell disposition is symmetrical regarding the centre of the support disk. Each cell is connected to a thermocouple that measures its temperature. The most used kinds of thermocouple are Pt/Pt-Rh, Ni/Cr-Ni and Au/Ni.

- *Ceramic disk*. Disk where the thermocouples are stored. It has to be made of a material with a high thermal resistance.

- *Support*. It is located over the oven and made of a material with high thermal conductivity (usually Ag).

- *Gas flow entrance*. The DSC devices allow the control of the atmosphere during the experiment in order to avoid non-desirable reactions, such as oxidation, and help reaction products in gas or vapour form to be evacuated.

- *Cooling system*. Allows a faster and controlled cooling of both the oven and the sample.

- *Computer*. Used for controlling the DSC device temperature and storing measuring data. It usually contains specific software for data treatment and representation.

The specific DSC experiments performed for the analysis shown in this work were carried out with the equipment, characteristics and working conditions listed in table 3.4.

DSC equipment	
equipment	Mettler-Toledo DSC822 (fig. 3.7)
year	2002
location	STR - Thermal Analysis Unit (UAT) [146] Polytechnic School (EPS), University of Girona (UdG)
temperature range	300-950 K
temperature mode	constant heating rate
heating rates	β = 2.5, 5, 10, 20 and 40 K/min
sample masses	20-30 mg

Tab. 3.4: *Characteristics of the equipment and working conditions used for the DSC experiments*

Fig. 3.7: *Photograph and schematic of the Mettler-Toledo's DSC822 used in this work* [146]

3.4.2 Thermograms

Heat flux DSC devices are based on the measuring of the difference in temperature between the sample and the reference. For the subsequent conversion to the output signal (heat flow per time unit), some approximations and considerations are generally made:

1. Only conduction terms are considered. Radiation terms are negligible for the temperatures involved, and the cell dimensions are not high enough to allow significant convection currents.

2. Heat transmission only happens from the oven to the crucibles and not from/to other parts of the device neither between both crucibles. Accepting this approximation allows considering exclusively the heat capacities of the sample and reference.

3. The measured temperature is the sample temperature. Although the thermocouples measure the temperature at the point where they are located, the thermal resistance between this point and the sample is generally negligible and it can be considered that both temperatures are equal. Furthermore, the temperature is considered homogeneous within the whole sample and the absence of gradients is presumed.

After accepting all these presumptions and approximations, the expression for the heat flux, which is the DSC output signal, can be written as the following:

$$\phi = -\frac{\Delta T}{\mathcal{R}} - \beta(C_s - C_r) - \frac{\tau}{\mathcal{R}} \cdot \frac{d\Delta T}{dt} \tag{3.8}$$

where C_s and C_r are the heat capacities of the sample and the reference, respectively and β is the heating/cooling rate of the temperature program. The parameters $\mathcal{R}$ and τ are, respectively, the overall thermal resistance of the system and the time delay for any heating/cooling process. Both are determined after calibration of the equipment.

The first term of the equation links directly the heat flux with the measured signal (the difference in temperature). The second term is related to the asymmetry of the system due to the differences in the heat capacities of both the sample and the reference. The last term takes into account the thermal inertia of the system.

Thermograms show the heat flux of a DSC experiment as a function of temperature (or as a function of time, in isothermal experiments). Figure 3.8 shows a simple theoretical thermogram: the process of melting of a pure substance.

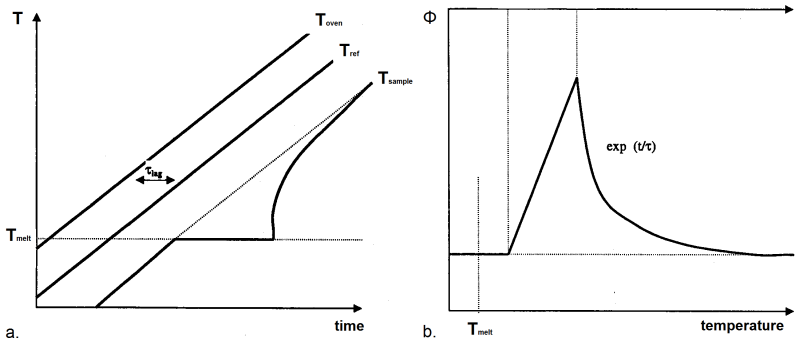

Fig. 3.8: *Example of a simple thermogram: process of melting of a pure substance*

The presence of the peak is due to the fact that the sample temperature does not change during the phase transition. The observed delay or lag corresponds to the necessary time for the heat to be transmitted from the oven to the reference, and is a parameter inherent to the calorimeter. The peak's orientation depends on both the kind of process and the selected sign convention. In the given example, the positive sign has been assigned to absorbed heat and the negative to released heat, and since fusion is an endothermic process, the peak is positive.

The shape and position of the peak are influenced by several parameters, such as the heating/cooling rate (β), the heat capacity (C) and the characteristics of the sample (thermal conductivity, shape, quantity...). The influence of β is highly significant because directly affects the difference between the measured and the real peak temperatures (figure 3.9).

The first step for a correct DSC analysis is the determination and substraction of the baseline, which is the curve that should be observed in a DSC when no reaction or transformation is being produced, in order to obtain the correct heat flow magnitude. Ideally it should be a constant-value line, but

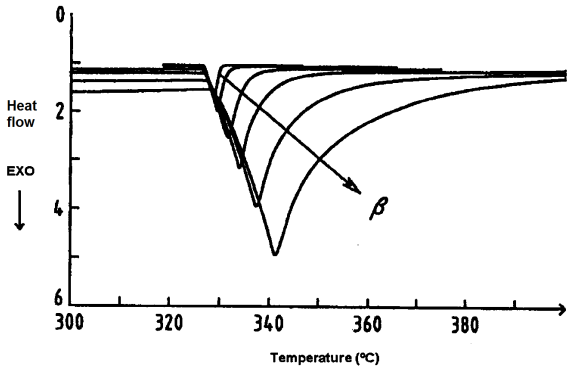

Fig. 3.9: *Temperature shifting as a function of the heating rate* β

in a real calorimeter this is not true and its determination is often a difficult issue. The most usual method to obtain a reliable baseline is submitting the same sample to a second experiment with identical temperature program. The suitability of this second heating/cooling curve as a correct baseline is justified when the reactions or transformations which are expected to be observed are irreversible processes (structural relaxation, crystallization...) that will not be shown in the second curve.

Every significant shifting of the DSC output respect to the baseline is an indication of a possible transformation or reaction in the sample. For the DSC devices used in this work, a positive shifting indicates an exothermic process –heat is absorbed by the sample- whereas a negative shifting indicates an endothermic process –heat is released. Several peaks are commonly observed in a single experiment and are often overlapped. The following are some of the parameters to be determined for each peak:

peak height. Defined as the distance between the peak and the baseline at the same temperature. The distance is measured perpendicularly to the temperature/time axis.

peak width. The temperature/time interval between the points where the DSC and the baseline curves split.

peak area. The area enclosed inside the DSC and the baseline curves. For a isothermal experiment, this total area is is area is proportional to the **transformation enthalpy**.

onset temperature/time. The temperature/time where the process begins. This point is defined as the intersection between the tangent lines of the baseline and of the highest-sloped point before the peak.

offset temperature/time. The temperature/time where the process is considered finished. This point is defined as the intersection between the tangent lines of the baseline and of the highest-sloped point after the peak.

3.4.3 Transformation kinetics analysis

DSC curves allow the determination of the kinetic parameters involved in several transformations, such as crystallization, nucleation, structural analysis...

The transformed fraction of any process can be evaluated from the ratio between the partial and the total enthalpies, which is equivalent to the ratio between the partial area and the total area:

$$\alpha = \frac{\Delta H_{part}}{\Delta H_{tot}} = \frac{S_{part}}{S_{tot}} \tag{3.9}$$

Similarly, an expression for the transformation velocity can be written:

$$\frac{d\alpha}{dt} = \frac{h}{S} \tag{3.10}$$

where h is the height of the curve at a specific point.

As one can deduce from the expression, this transformation velocity begin increasing as the signal shifts from the baseline, reaches a maximum value at the peak position and decreases again until the shifting from the baseline vanishes, so it will depend on the transformed fraction α. In addition, it also depends on the temperature T of the sample.

These 3 parameters (transformed fraction α, transformation velocity $\frac{d\alpha}{dt}$ and absolute temperature T) are linked by a single equation, called the **fundamental equation**:

$$\frac{d\alpha}{dt} = K(T) \cdot f(\alpha) \tag{3.11}$$

$f(\alpha)$ is a function with information about the transformation or reaction mechanism and $K(T)$ is a temperature-dependent velocity parameter which is generally modeled with an Arrhenius-type law:

$$K(T) = K_0 \cdot e^{-\frac{E}{RT}} \tag{3.12}$$

where K_0 is a pre-exponential factor related to the Debye frequency, E is the apparent activation energy of the process, T is the absolute temperature and R is the ideal gas constant ($R \approx 8.31$ J/molK).

The activation energy of a process may be defined as the minimum energy required to start a reaction and the determination of its value can give important information about the nature of the transformation studied. There are several methods to determine its value using DSC thermograms:

Kissinger method. This method was developed by H.E. Kissinger [147] and is based on the fact that the transformation velocity, $\frac{d\alpha}{dt}$, reaches its highest value at the peak maximum, $\frac{d^2\alpha}{dt^2} = 0$. After taking derivative of the fundamental equation, the following equation is obtained for the peak maximum:

$$\frac{d^2\alpha}{dt^2} = K(T)\frac{df(\alpha)}{dt} + \frac{K(T)}{dt} \cdot f(\alpha) = 0 \tag{3.13}$$

After some algebra and approximations, the equation 3.13 can be reduced to the following expression:

$$\ln\left(\frac{\beta}{T^2}\right) = -\frac{E}{RT} + \text{constant} \tag{3.14}$$

which allows an easy calculation of an empirical magnitude of E for every transformation using several different values of T using the following procedure:

1. Repetition of the experiment for different heating rates β. Since the position of the peak maximum depends on the value of β, several values of T_p will be found for the same process, one for every experiment.
2. Graphic representation of $\ln\left(\frac{\beta}{T_{p2}}\right)$ as a function of $\frac{1}{T_p}$, being T_p the peak positions detected on the previous experiments
3. Linear regression of the data from step 2, since the equation 3.14 show a linear behavior with $\frac{1}{T}$. The activation energy magnitude can be estimated from the slope of the regression, which is $-\frac{E}{R}$.

Ozawa method. This second method, first developed by Ozawa in 1965 [148], is almost identical in both the procedure and the results to the Kissinger method, with the following similar equation:

$$\ln(\beta) = -\frac{E}{RT} + \text{constant} \tag{3.15}$$

Similarly to the Kissinger method, the procedure also includes a linear regression -this time with $\ln\beta$ vs $\frac{1}{T_p}$- and the determination of the activation energy from the slope, which again is -$\frac{E}{R}$.

Arrhenius law on isothermal measurements. On isothermal experiments, the activation energy of a process can also be calculated after supposing that an Arrhenius-type law is followed:

$$\frac{1}{t_p} = \frac{1}{t_0} \cdot e^{-\frac{E}{RT}} \tag{3.16}$$

where t_p is the time elapsed for reaching the peak maximum at a specific temperature.

Multiple scans method. This method allows the estimation of the activation energy for both isothermal and non-isothermal experiments without the previous knowledge of the reaction or transformation mechanism [149].

After supposing that f(α) depends only on α and not on T, the fundamental equation can be rewritten as follows:

$$\ln\left(\frac{d\alpha}{dt}\right) = -\frac{E}{RT} + \text{constant} \tag{3.17}$$

and therefore a linear behavior of $\ln\alpha$ versus $1/T$ can be found with a slope equal to -$\frac{E}{R}$.

3.4.4 Transformation mechanism determination

Regarding the fundamental kinetic equation, the information about the reaction or transformation mechanism is included in the function $f(\alpha)$. If the activation energy of a process is known, the expression found for the multiple scans method can be rewritten as follows:

$$\ln\left(\frac{d\alpha}{dt}\right) - \frac{E}{RT} = \ln\left[K_0 \cdot f(\alpha)\right] \tag{3.18}$$

Consequently, a graphic representation of experimental values for $\ln\left[K_0 \cdot f(\alpha)\right]$ as a function of a certain expression of α -usually $\ln(1-\alpha)$- allows, for both isothermal and non-isothermal experiments, the identification of the reaction or transformation mechanism by comparison with pattern curves of existing models.

Several existing models can be found in bibliography for different main mechanisms. Table 3.5 show some specific models commonly used and their respective $f(\alpha)$ function.

Model	$f(\alpha)$
Models driven by diffusion mechanisms [150–153]	
One-dimensional diffusion (D1)	$f(\alpha) = \alpha^{-1}$
Two-dimensional diffusion (D2)	$f(\alpha) = [-\ln(1-\alpha)]^{-1}$
Three-dimensional diffusion (D3)	$f(\alpha) = [-(1-\alpha)^{1/3}\ln(1-\alpha)]^{-1}$
Models driven by propagational mechanisms [154]	
Polanyi-Wigner model (R1)	$f(\alpha) = 1$
Cylindrical contraction model (R2)	$f(\alpha) = (1-\alpha)^{-1/2}$
Spherical contraction model (R3)	$f(\alpha) = 1-(1-\alpha)^{2/3}$
Models driven by nucleation and crystal growth [154–158]	
Exponential law	$f(\alpha) = \alpha$
Johnson-Mehl-Avrami-Erofeév (JMAE) equation (Jn)	$f(\alpha) = n(1-\alpha)[-\ln(1-\alpha)]^{\frac{n-1}{n}}$
Generic models [154]	
Global generic model	$f(\alpha) = \alpha^m(1-\alpha)[-\ln(1-\alpha)]^p$

Tab. 3.5: *Transformation mechanism models*

A single transformation process is often driven by several different mechanisms. Each of these mechanisms can be studied as a generalization of a JMAE equation [159]:

$$-\ln(1-\alpha) = \sum_i \lambda_i t^{n_i} \tag{3.19}$$

where every stage of the transformation is defined by a specific $\lambda_i t^{n_i}$ term.

The exponent n of the JMAE model can be easily found using few isothermal experiments, thanks to the following relation [160]:

$$\ln[-\ln(1-\alpha)] = n\ln t + n\ln K \tag{3.20}$$

Therefore, a graphic representation of $\ln[-\ln(1-\alpha)]$ as a function of $\ln t$ will show a linear behavior with a slope equal to n.

3.5 Magnetic measurements

As explained in section 1.3, in order to study the suitability as soft-magnetic materials of the alloys shown in this work, the correct determination of certain magnetic parameters such as the coercivity H_c, the magnetic saturation M_s (or J_s), the Curie temperature T_c, etc. was needed.

The coercivity H_c and the magnetic saturation M_s (or J_s) could be generally estimated directly from the M-H hysteresis cycle curves. For the estimation of T_c and the study of the dependence with the temperature, however, thermomagnetometry (TM) analyses were required. The TM experiments, along with Mössbauer spectroscopy introduced above, also provided additional information about the magnetic homogeneity of the alloys.

Finally, for the analysis of the influence of a magnetic field applied during the MS quenching process of some alloys of chapter 6, the more specific Bitter colloid method was used.

3.5.1 M-H measurements

For this work, the experimental M-H curves were obtained by applying an external magnetic field with variable field intensity H up to approx 15 kOe in both directions and measuring the evolution of the magnetization M in the samples while H is modified.

The equipment and working conditions used are described in table 3.6.

Equipment and working conditions used for the M-H measurements	
equipment	MPMS-7T (see fig. 3.10)
location	University of the Basque Country (UPV/EHU) (alloys A-B, G-J) University of Sevilla (alloys C-F)
sample masses	100-120 mg (alloys A-B) 13-25 mg (alloys C-F 25-55 mg (alloys G-J)
total experiment time	approx 1.5 h per cycle
step time	1-10 s
H variation rate	5-20 Oe per second
working temperature	300 K

Tab. 3.6: *Characteristics of the equipment and working conditions used for the M-H analyses*

Fig. 3.10: *Images of the equipment used for the M-H measurements* [161, 162]

3.5.2 Thermomagnetometry (TM)

Thermomagnetometry (TM) is defined by IUPAC as "*a technique in which a magnetic characteristic of a substance and/or its reaction product(s) is measured as a function of temperature whilst the substance is subjected to a controlled temperature program*" [145]. Although both the denomination and the definition include several different techniques, only thermogravimetry (TG) based thermomagnetometry is discussed here.

TG-based thermomagnetometry

A simple TG-based TM device can be obtained by superimposing a magnetic field gradient in the vicinity of the sample in a conventional TG device. The presence of the external magnetic field produces an apparent weight gain or loss (depending upon the direction of the field gradient) whenever the sample analyzed shows any magnetic behavior. The study of the variations in this change in the apparent weight determines the magnetic transformation temperature and the formation or demise of magnetic materials [163].

Arguably the most interesting application of TM is the determination of the Curie (or the Curie-Weiss) temperature. As explained in chapter 1, a ferromagnetic material shows ferromagnetic behavior while its temperature is under the Curie point and thus will be affected significantly by the external magnetic field. When the temperature goes beyond this point, the material begins showing a paramagnetic behavior and therefore stops being affected significantly by the field, resulting in an abrupt change in the apparent mass and hence in the TG curve.

TM may also allow the detection of some phase transitions not detected by simple TG if the phases involved show different magnetic behavior. For example, it is possible to detect the oxidation of Co to cobalt oxide (Co_3O_4), since this transformation takes place from a ferromagnetic (Co) to a paramagnetic (Co_3O_4) phase [164]. This transition must not be confused with the Curie point (1388 K for the Co), which is related to thermal agitation.

Generally speaking, the analysis of the thermomagnetic curves allows the study of:

- Homogeneity and heterogeneity of the alloys
- Global and/or local magnetic structures
- Magnetic transition temperatures

TM equipment

The TM experiments carried out in this work were performed by means of TG-based thermomagnetometry, using the equipment, characteristics and working conditions listed in table 3.7.

TM equipment	
equipment	Mettler-Toledo TGA/SDTA851 (fig. 3.11)
year	1997
location	STR - Thermal Analysis Unit (UAT) [146] Polytechnic School (EPS), University of Girona (UdG)
temperature range	300-1500 K
sample masses	25-35 mg

Tab. 3.7: *Characteristics of the equipment and working conditions used for the TM experiments*

Fig. 3.11: *Photograph of the Mettler-Toledo's TGA/SDTA851 used in this work and detail of the crucible support* [146]

Major factors affecting TG-based TM measurements

Several factors affect the TG-based TM measurements and may mean a significant source of error. The majority of them are associated with the potential errors in either measuring the mass or determining the temperature of the sample and have a dependence on the atmosphere, flow and sample properties. The electronic drift problems are relatively minor and only become decisive factors for experiments of duration beyond several hours [163]. The main factors to be considered are buoyancy and atmospheric turbulence:

- *Buoyancy*. As the temperature increases, the mass of the atmosphere displaced decreases, due to changes in its density, giving a slight apparent weight gain as both the sample and its container and suspension system are heated (e.g., one cm^3 of dry air weights 1.3 mg at 25 ºC but only 0.3 mg at 1000 ºC). There are compensation methods based on either instrumental modifications or subtraction by software, with the former mainly based in the duplication of either the weighting or the temperature measure system, and the latter based on storage of a blank run, performed under conditions as identical as possible with an inert dummy sample, and subsequent subtraction from the actual experiment.

- *Atmospheric turbulence*. This factor may become a source of error since it may affect the buoyancy discussed in the previous point. The turbulence is determined by several other factors such as the flow, pressure and even geometrical considerations, and is almost impossible to be reproduced and hence to be completely eliminated from the measurement. List of procedures for the minimization of the effect of turbulences includes waiting for stabilization of both gas

flow and balance-sample system, and working with a tangential –instead of perpendicular– flow. More restrictive operating conditions lead to better optimization (for example, operation in vacuum reduces the aerodynamic noise and the buoyancy corrections whereas high pressures exacerbate these same problems [163]). Nevertheless, a static atmosphere –or the absence of it– carries other collateral problems such as reaction products condensation, contamination between different experiments, or alteration of the oven emissivity [165]. Therefore, a compromise is required to achieve an optimum configuration for a suitable operating range of experimental parameters.

The correct measurement of the mass can be also affected, although in a lower level, by several other factors such as reactions of the atmosphere with the sample holder or between the sample and the holder, contamination from reaction products, the reversibility of chemical equilibria involved, the packing of the sample, electrostatic forces, etc. Furthermore, the correct measurement of the temperature can be also affected by changes in the heating or cooling rate, in the thermal conductivity of either the atmosphere or the device components, and in the enthalpy of the process.

3.5.3 Observation of the domain structure

The observation of the influence of external fields on the domain structure have been carried out by means of the Bitter colloid method [32, 166], a technique that uses ferrofluids for the visualization of the stray fields of the magnetization of the material analyzed .

A ferrofluid consists of an inorganic liquid carrier -usually water- containing magnetic particles -usually Fe_3O_4, γ-Fe_2O_3 or metallic particles of iron, nickel or cobalt with 10-15 nm diameters-, which add a magnetic behavior to the fluid. The particles interact by magnetic forces and by electrostatic and Van der Waals forces. Liquid dispersants are added which surround the particles and lead to a steric repulsion between them, which avoids a particle clustering in the ferrofluid. The equilibrium between repulsive steric forces and attractive van der Waals and magnetic forces is influenced by the stray field of the sample magnetization, leading to differences in colloid particle densities in the ferrofluid [167].

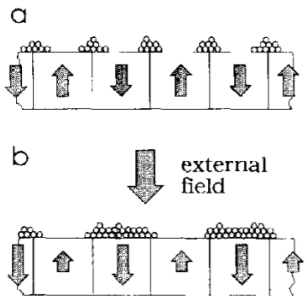

Fig. 3.12: *Schematic of the Bitter colloid method basis. Colloid covering of domain transitions: (a) without an external magnetic field, (b) with an external magnetic field* [167, 168].

4 Study of Fe-Cr nanocrystalline alloys produced by mechanical alloying (MA)

> *The habit of reading is the only enjoyment in which there is no alloy. It lasts when all other pleasures fade.*
>
> — **Anthony Trollope**
> (Author)

Contents

This chapter deals with the analysis of the mechanical alloying (MA) process used for the production of some Fe-Cr based ferromagnetic nanocrystalline powder alloys. The first half will focus in the evolution of the alloys during the milling process while the second half will focus on the final alloys and specially on their magnetic properties.

4.1 Introduction

Fe-Cr based alloys, the basis for stainless steels, are well known for their resistance to corrosion at high temperature [169–171] and interesting soft-ferromagnetic properties. Their applicability has been recently expanded thanks to their optimal magnetocaloric response in magnetic refigeration applications [172] and also due to some interesting specific applications such as their ability to act as a matrix for a cermet compound [173] and their resistance to neutron radiation induced embrittlement and swelling [174, 175], which made them being considered for use in future fission and fusion reactors [174, 176, 177].

Two of the features of the binary Fe–Cr system are the existence of a wide miscibility gap at room temperature[1] in the equilibrium phase diagram [178] and a change in the long-range magnetic order from the ferromagnetic behavior of pure Fe to the antiferromagnetism of pure Cr. About the latter, although this transition is generally located at around 70% Cr [179], depending on the processing technique and the resulting microstructure it might be observed at different compositions or even extend to a broad region where the system might show magnetic frustration (impossibility for some Fe or Cr atoms to assume a ferromagnetic or antiferromagnetic state, respectively, with reference to their neighbors) [174].

Beyond that, this system is characterized by rich non-equilibrium behavior and a chemical arrangement of the atoms in the alloy which can be either random or in clusters among similar atoms [179] with a unique inversion in these tendencies at around 9% and 12% of Cr content, which is related to the magnetic properties [180, 181]. As a result, their processing by techniques such as mechanical alloying (MA) has been widely investigated, generally resulting in final alloys which have been reported to show an extensive metastable behavior with the formation of disordered bcc-based solid solutions [182–186] or paramagnetic amorphous phases at 300K [187], depending on the Cr composition, the preparation procedure and further treatments.

It is also well known that the addition of boron (B) into these systems helps the formation of nanocrystalline and amorphous alloys and also modifies their mechanical properties, generally hardening the resulting alloy, specially if intermetallic phases are formed during the proces [171, 188, 189].

[1] In the middle of the wide miscibility gap there is a small region near equiatomic compositions where the alloys show a tetragonal σ phase but only at higher temperatures (700-1000 K)

4.2 Production of the alloys

The two alloys produced and studied in this chapter have the following atomic compositions:

- Alloy A: $Fe_{80}Cr_{20}$
- Alloy B: $Fe_{80}Cr_{10}B_{10}$

The production of both alloys were carried out in a planetary ball mill with the equipment and the conditions described in table 4.1. The general characteristics and mechanisms involved in the planetary ball mills have been detailed in chapter 2 (see 2.1.1).

equipment	
mill model	Fritsch Pulverisette 7 (see fig. 2.7)
type of mill	planetary ball mill
containers	hardened stainless steel vials (18% Cr, 10% Ni)
balls	hardened stainless steel (18% Cr, 10% Ni)
milling conditions	
raw materials	industrial powders of pure (purity > 99%) elemental B, Cr and Fe in stoichiometric proportions
milling atmosphere	Ar
process control agents (PCA)	1 ml of cyclohexane (C_6H_{12})
quantity of material to process	12 g
ball-to-powder mass ratio (BPR)	4:1
milling speed	700 rpm
milling times	1, 5, 20 and 80 hours
operation program	30-min cycles with 15 min pause between them in order to to minimize excessive temperature rise [190], alternating clockwise and counter-clockwise rotation

Tab. 4.1: *Equipment and milling conditions used for the production of alloys A and B*

An inert atmosphere of argon gas during the production was chosen in order to avoid undesirable reactions between the material and the atmosphere such as oxidations. The containers with the raw materials inside were placed in a vacuum vessel, where they were subjected to a 1 Pa ($\approx 10^{-5}$ atm) vacuum and then refilled with the argon gas. To ensure the inert atmosphere would be preserved, this procedure was repeated 3 times and the containers were subsequently sealed with polytetrafluoroethylene (PTFE, commonly known as *Teflon*). This procedure had been routinely used in previous alloys developed with no reports of noticeable undesired reaction with the atmosphere reported [125, 191–194].

4.3 Analysis of the evolution throughout the milling process

The first half of this chapter is dedicated to the analysis of the evolution of the two alloys throughout the milling process. SEM, XRD, Mössbauer spectrography and DSC measurements were carried out in samples of the alloys after 1h, 5h, 20h and 80h of milling.

4.3.1 Scanning electron microcopy (SEM) analysis

SEM analyses were carried out for both alloys after each different milling time. The generalities and details of the SEM technique have been introduced in section 3.1 and the specific equipment and working conditions used for these analyses can be found in table 3.2.

Figure 4.1 shows a collection of SEM micrographs showing the evolution throughout the milling time for both alloys.

$Fe_{80}Cr_{20}$

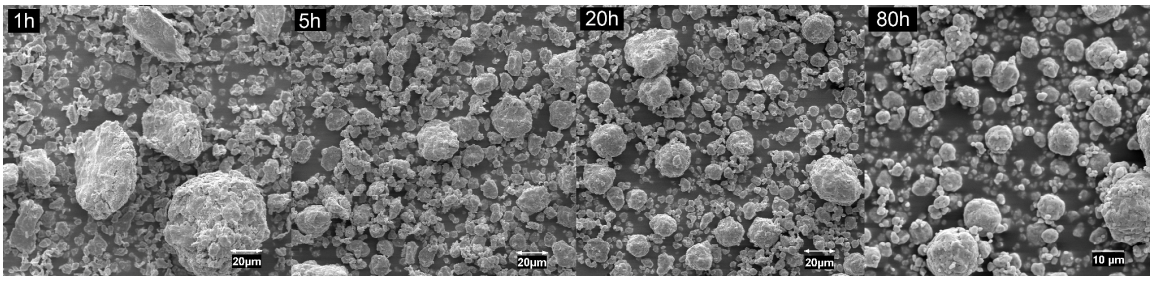

$Fe_{80}Cr_{10}B_{10}$

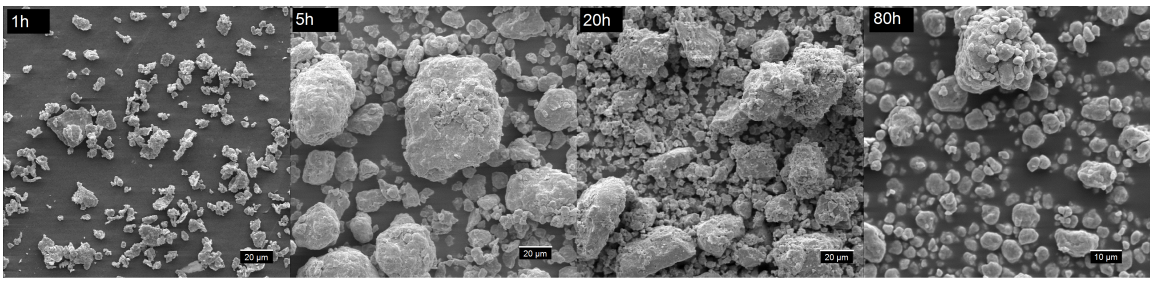

Fig. 4.1: *SEM images for alloys A (top) and B (bottom)*

The images show a continuous decrease in the average particle size throughout the milling process as well as an apparent enhancement in their homogeneity in both shape and size.

A closer observation of the 80h samples (fig. 4.2), reveals slight differences between the two alloys, probably due to the different Cr relative content, a result in agreement with other works [195, 196].

The X-ray microanalysis of the samples milled for 80 hours confirms only slight contamination from the milling tools, with the variation in the Fe contents not higher than 2 at.% in both alloys. Similar

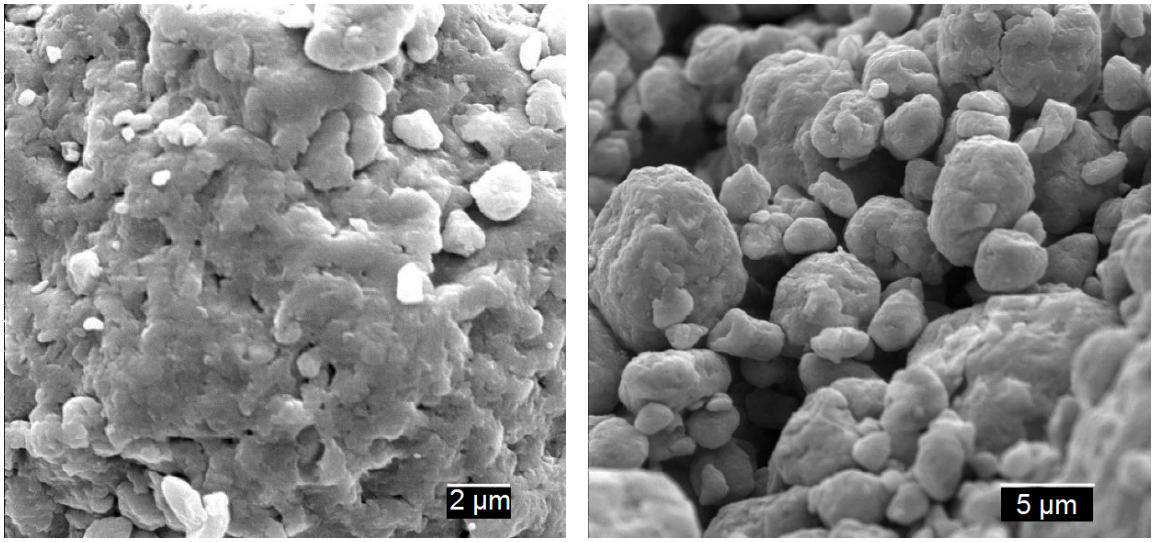

Fig. 4.2: *SEM micrographs for alloy A (left) and B (right) after 80h of milling*

results have been found previously in other Fe-rich alloys produced by mechanical alloying with this very same mill [192–194, 197].

4.3.2 X-ray diffraction (XRD) analysis

XRD experiments were also carried out for both alloys after each different milling time in order to provide information about the structure and the properties from both the interiors and the boundaries of the grains [198]. The details of the XRD technique have been introduced in section 3.2 and the specific equipment and working conditions used have been described in table 3.3.

Previously to any analysis, it must be remembered that the crystallographic structures of pure Fe and Cr at room temperature are almost identical, with both showing a bcc phase with very similar lattice constant a (0.287 nm for Fe and 0.291 nm for Cr). This results in the peaks featured in the respective XRD patterns almost overlapping completely, making difficult the clear identification of either the possible formation of the solid solution or the still presence of the individual phases.

Neverthelss, the obtained spectra (4.3) do show some changes easily identified throughout the milling process:

1. The peaks corresponding to the minor phase were first reduced and later vanished in favor of the main or majoritary phase.

2. The peaks were generally smoothed and broadened.

3. The peak positions were slightly shifted.

4. Peaks corresponding to possible borides (in alloy B) were not detected at any stage.

The first point confirms the formation of a solid solution, where the atoms of the minor phases were introduced into the matrix of the majority phase.

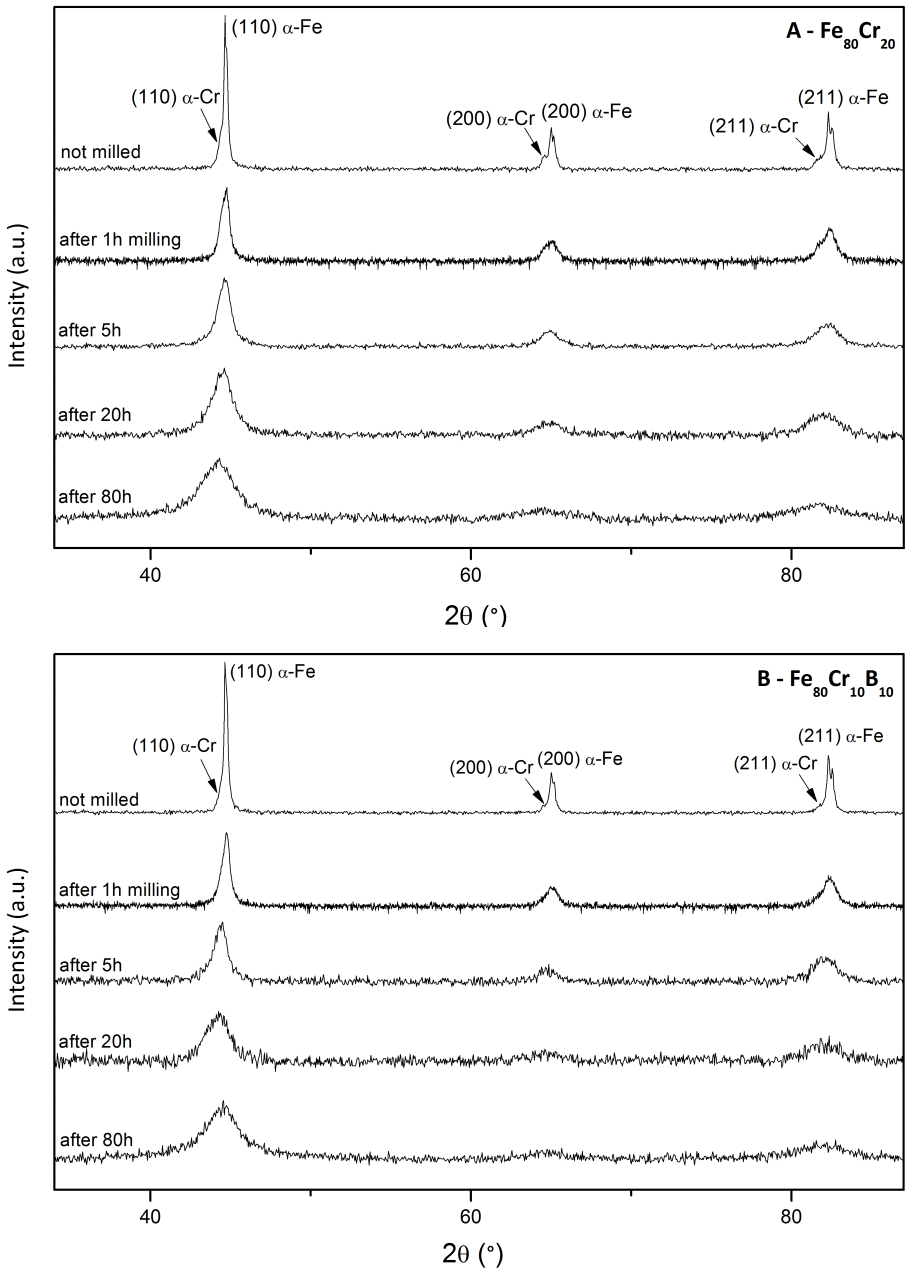

Fig. 4.3: *Evolution of the XRD patterns throughout the milling process for alloys A (top) and B (bottom)*

This is clearly seen when comparing the spectra for the unprocessed raw materials with those of the milled alloys. The spectra for the unprocessed raw materials show clearly the presence of the two separated phases bcc-Fe and bcc-Cr, since the sample is mixed but not milled yet and thus the elements are still in their pure form. Not surprisingly, the weaker peaks correspond to the minority bcc-Cr, which are slightly more intense in alloy A than in alloy B, due to having different relative Cr content.

This contrasts with the disappearance of the peaks of the minor phases after just few hours of milling, indicating that the formation of the solid solution was probably produced in these early stages of the process. However, the exact time reveals difficult to be determined, since the spectra after 1h of milling do not show a clear figure of the possible presence or absence of the secondary peaks. A more

accurate determination of the crystallographic parameters by means of Rietveld refinement -detailed below- shows that some traces of the minoritary phase are still detected at this stage, thus indicating that the solid solutions were only formed partially. After 5h of milling these traces disappear, possible meaning their completion sometime between these two milling times. This result is in agreement with the existing literature for MA processing of similar compositions [136, 199].

Due to both the Fe content being significantly higher and the fact that Cr in Fe diffuses faster than Fe in Cr [190], it seems reasonable that the bcc-Fe acts as the matrix where the Cr atoms are introduced. The introduction of the Cr atoms during the formation of the solid solution was surely produced substitutionally (i.e. by replacing some atoms by the new ones), since the atomic radii of Fe and Cr are very similar (0.126 and 0.128 nm, respectively).

On the other hand, the exact mechanism regarding the introduction of boron atoms is not obvious, according to the literature [200, 201]. Although having atomic radius significantly lower (0.090 nm), boron has also been often found to form substitutional solutions in α-Fe at low temperatures [202, 203]. For higher temperatures, however, diffusion of boron atoms tends to behave like other elements with similar characteristics and the introduction is governed mainly by interstitial (i.e. by fitting into the space of the solvent particles) mechanisms [204, 205]. Due to the nature of the mechanical alloying processing, this is surely the case of the alloy with boron content (alloy B).

The broadening and smoothing of the peaks referred in the second point of the list is mainly related to the reduction of the crystal size [206, 207]. As explained in chapter 2, this refinement is a direct consequence of the mechanical alloying process, and in fact it may be considered its main purpose. The very slight difference between the two last samples analyzed (after 20h and 80h, respectively) indicates that the value had probably reached its lowest limit at this stage, and thus the milling process might be considered finished. The presence of the secondary peaks, which are still slightly detectable, means that the alloys must be considered nanocrystalline rather than amorphous.

The shifting of the positions of the peaks is related to changes in the microcrystalline structure and specifically the lattice parameter and the microstrain index. The general displacement is shown to be towards lower values, indicating that the lattice parameter was increased, probably due to an increase in the defect density and microstrain values produced by the mechanical alloying process [207].

Lastly, in alloy B, the absence of any peaks corresponding to borides, which have been generally reported in other works [189, 208–211], indicates that they were not formed during the milling process or, in case they were, limited or reduced to below the detectability threshold. This is a surprising fact, since it is known that the B solubility in Fe-based alloys containing Cr is generally low [212] and the formation of Fe and Cr borides should be expected.

Evolution of the crystalline parameters

As explained in chapter 3, Rietveld refinements allow a quantitative estimation of the relevant crystalline parameters from the XRD results. Table 4.2 shows the phases detected and the quantitative analysis for the majority phase of each stage of the process.

milling time	phases detected	lattice param. $\langle a \rangle$ (nm)	crystalline size $\langle L \rangle$ (nm)	microstrain $\langle \sigma^2 \rangle^{1/2}$ (%)
alloy A ($Fe_{80}Cr_{20}$)				
0 h	bcc-Fe bcc-Cr	0.2868	176 ±8	0.01
1 h	bcc-(Fe,Cr) bcc-Cr	0.2869	70 ±10	0.34
5 h	bcc-(Fe,Cr)	0.2872	26 ±9	0.46
20 h	bcc-(Fe,Cr)	0.2879	18 ±1	0.67
80 h	bcc-(Fe,Cr)	0.2880	6.6 ±0.3	1.05
alloy B ($Fe_{80}Cr_{10}B_{10}$)				
0 h	bcc-Fe bcc-Cr	0.2868	182 ±8	0.00
1 h	bcc-(Fe,Cr) bcc-Cr	0.2866	57 ±2	0.27
5 h	bcc-(Fe,Cr)	0.2876	24 ±1	0.30
20 h	bcc-(Fe,Cr)	0.2877	15 ±1	0.57
80 h	bcc-(Fe,Cr)	0.2879	5.5 ±0.1	1.00

Tab. 4.2: *Crystalline parameters estimated from Rietveld refinements for alloys A and B*

1. Lattice parameters

Figure 4.4 shows the evolution of the average lattice constant $\langle a \rangle$ of the main cubic phase throughout the milling time.

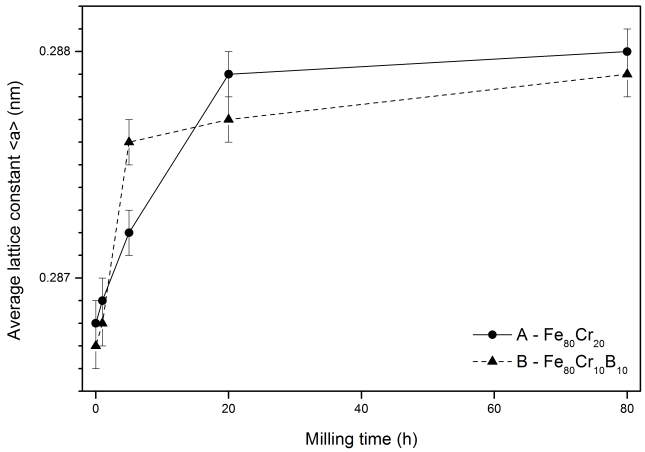

Fig. 4.4: *Evolution of the average lattice constant $\langle a \rangle$ throughout the milling process for alloys A and B*

As can be seen in the figure, both graphs show an increase in the lattice parameter a with the milling time, confirming the previous qualitative analysis. As explained before, this is the consequence of several factors:

- Progressive substitution of atoms in the bcc-Fe matrix by atoms of Cr. As explained above, Cr atoms have slightly higher atomic radius than Fe atoms (0.128 vs 0.126 nm) and tend to form a bcc structure with higher cell parameter (0.291 vs 0.287 nm) [213].

- In alloy B, progressive interstitial introduction of atoms of B into the α-Fe matrix [204, 205].

- Increase in the number of crystalline defects during the alloying process [207].

- Decrease in the grain size, which means that more atoms become part of the grain boundaries and consequently increases the average distance between them [206].

2. Crystalline size

Figure 4.5 shows the evolution of the average crystalline size $< L >$ with the milling time.

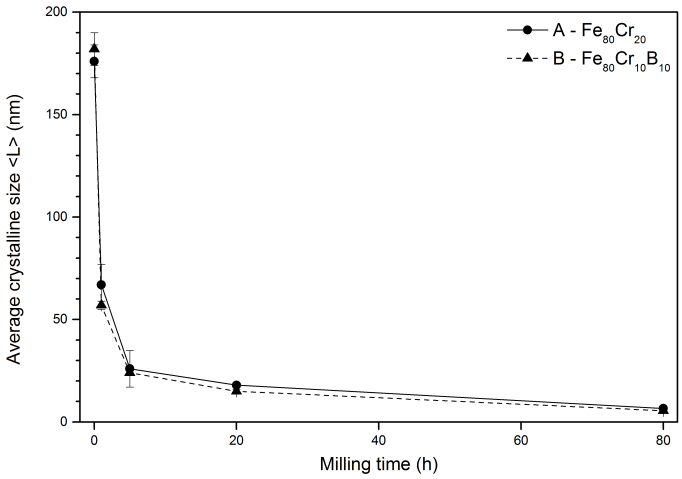

Fig. 4.5: *Evolution of the average crystalline size $\langle L \rangle$ throughout the milling process*

The graph shows the common behavior explained in section 2.1, with the crystalline sizes of the alloys produced by MA decreasing with the milling time and featuring the two-stage process generally found in Fe-based systems: grain refinement during early stages and subsequent grain steady state [198].

In these alloys, the first stage extended up to a certain point between 5 and 20h of milling and produced an abrupt decrease in the crystalline size, while the second stage carried a slow reduction down to 6.6 and 5.5 nm, respectively (for the 80h-milled samples), with the alloy showing the lowest value, which can be attributed to the presence of boron, a similar behavior found in other works [210, 214].

3. Microstrain

As mentioned also in section 2.1, the large plastic deformation induced by the milling process creates a high amount of crystalline defects [8], increasing diffusivity and thus easing true alloying in the powders.

This deformation is generally quantized using the microstrain index (or r.m.s. microstrain) $\langle\sigma^2\rangle^{1/2}$, a magnitude which uses the standard deviation of the strain around the mean value in a crystallite and generalizes the effect of several defect types [215].

For milled samples subjected to severe plastic deformation, where the dislocations are usually the main defects besides grain boundaries [198], a more specific parameter can be also useful: the density of dislocations (ρ). The magnitude of ρ can be estimated from the values of the microstrain $\langle\sigma^2\rangle^{1/2}$ and $\langle L\rangle$ already known, using the following expression [216, 217]:

$$\rho = 2\sqrt{3}\frac{\langle\sigma^2\rangle^{1/2}}{b\langle L\rangle} \tag{4.1}$$

where b is the magnitude of the Burgers vector of dislocations, which for a bcc lattice is [218]

$$b = \frac{a\sqrt{3}}{2} \tag{4.2}$$

Figure 4.6 shows the evolution of this two parameters throughout the milling process for both alloys.

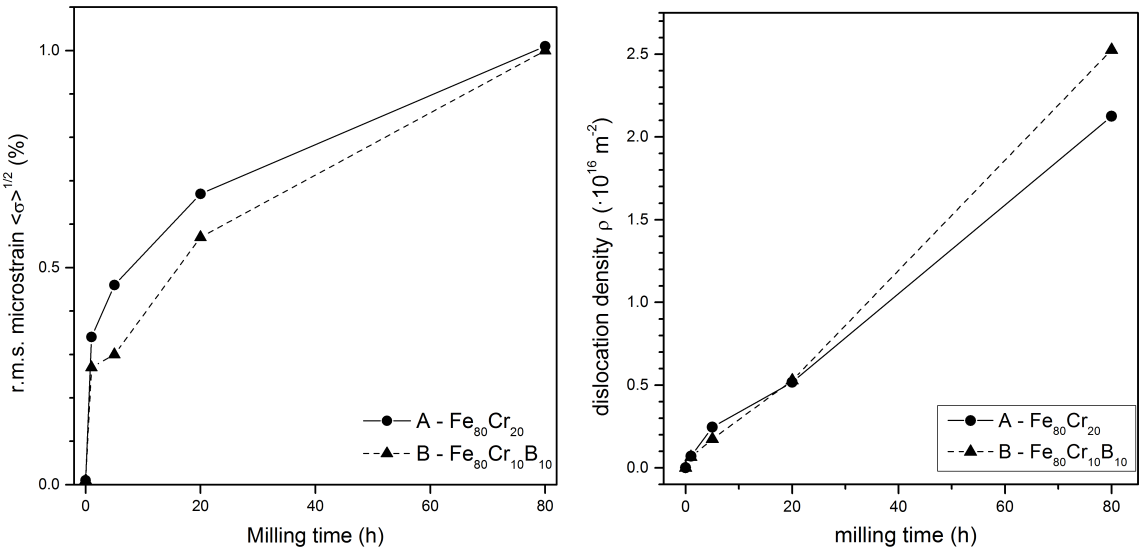

Fig. 4.6: *Evolution of the r.m.s. microstrain $\langle\sigma^2\rangle^{1/2}$ (left) and the dislocation density ρ (right) throughout the milling process for alloys A and B*

As can be seen in the graphs, both the microstrain index and the density of dislocations increased with the milling time, a common feature widely found in other MA-processed alloys [198, 199, 207, 219].

The magnitudes of the estimated dislocation densities are of the order of 10^{16} m^{-2}, which are comparable to the edge dislocation densities limit in metal achieved by plastic deformation [89, 207, 220]. Alloy B shows a slightly higher value than alloy A, due to both the presence of boron and its lower Cr relative content.

The magnitudes found for the r.m.s. microstrain, on the other hand, show lower values in the alloy with boron, although the difference is almost unnoticeable in the final stages and both alloys show similar values and in agreement with the literature [136].

4.3.3 Mössbauer spectroscopy (TMS) analysis

TMS analysis were carried out for both alloys after every different milling time. The fundamentals of TMS and the equipment and working conditions have been detailed in section 3.3. The resulting TMS spectra and their evolution throughout the milling process are shown in figure 4.7. One particular interesting parameter to analyze is the average hyperfine field $\langle B_{hf} \rangle$, the evolution of which is shown in figure 4.8.

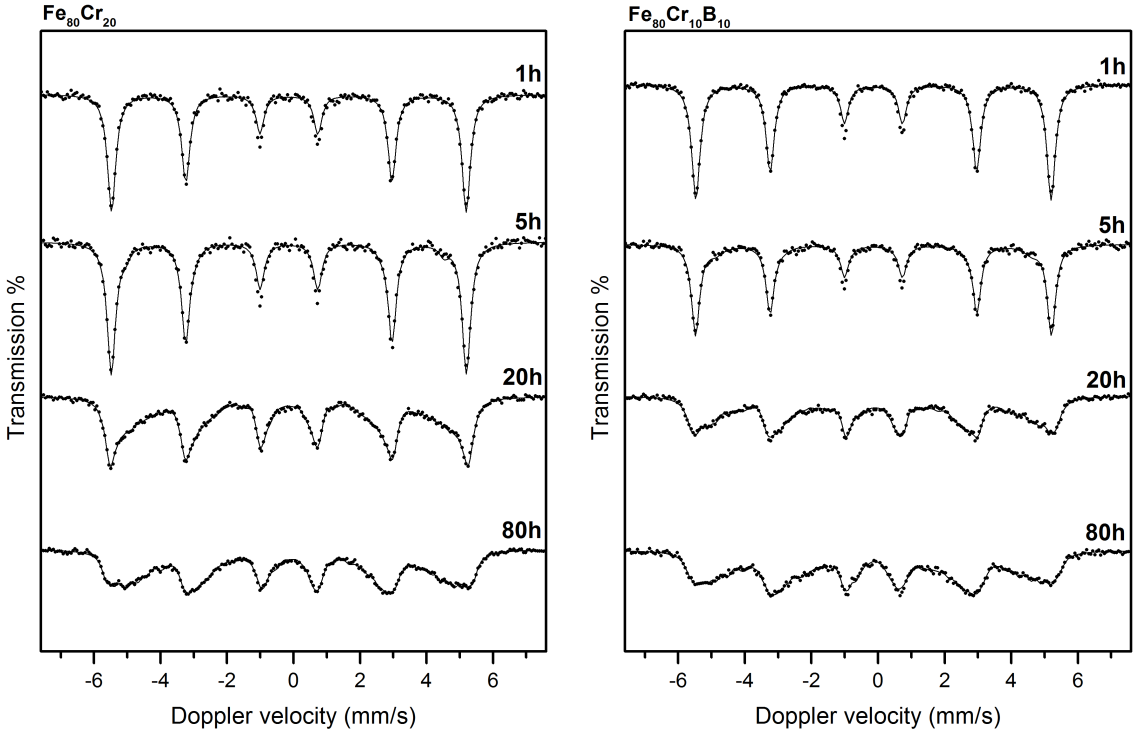

Fig. 4.7: *Evolution of the TMS spectra throughout the milling process for alloys A (left) and B (right)*

The spectra after 1h and 5h of milling are very similar to that of an unreacted α-Fe, and so are the respective average hyperfine fields estimated (fig. 4.8), an indication that the formation of the solid solutions were still in progress at these stages. The XRD refinement did show still some traces of the minority phases in the 1h alloys but not in the 5h alloys, leading to an apparent contradiction between the XRD and the TMS analysis. However, this can be partially explained by the fact that the fitting of the Mössbauer spectra after 5h of milling indeed reveals the existence of two main contributions: a majoritary contribution with an average hyperfine field not very far from the initial 33 T, easily attributed to iron-rich environments with low Cr occupancy in the first neighborhoods, and a secondary contribution with lower field values (31.1 and 29.2 T, respectively), attributed to environments with some Cr atoms.

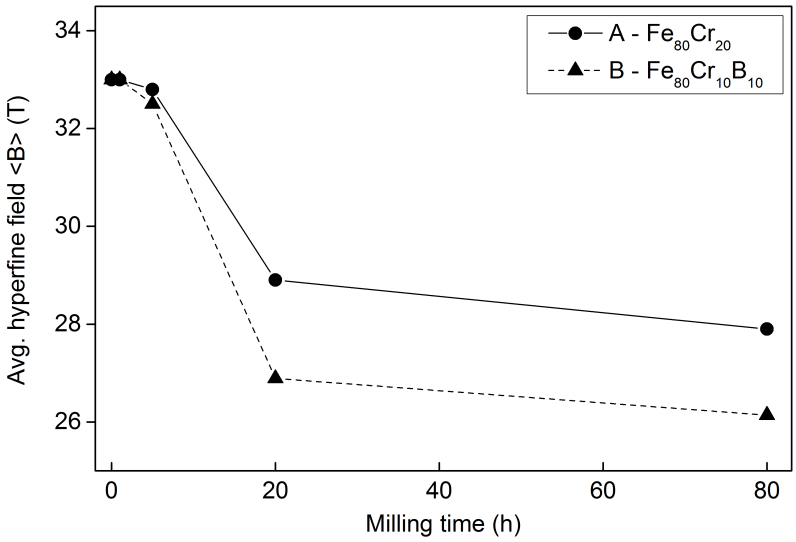

Fig. 4.8: *Evolution of the average hyperfine field $\langle B_{hf} \rangle$ for alloys A and B after 80h of milling*

The broadening of the spectral lines after 20h and 80h of milling can be explained by the alloying process itself and its consequent reduction of the crystallite size accompanied by high lattice strain [221]. This process is also responsible for the reduction of the average hyperfine field observed in fig. 4.8.

About the influence of the Cr content on the average field, its exact determination is complex due to being affected by the method and conditions of production. Nevertheless, it is widely accepted that its increase shifts the average field to lower values and, for mechanical alloyed Fe-Cr alloys, the following linear relation can be used [136, 222]:

$$B(x) = 33.1 - 26.6x \text{ [T]} \tag{4.3}$$

where x is the Cr relative content.

This expression gives the well-known 33 T for unreacted pure Fe [223–225] and the theoretical values of 30.1 T and 27.8 T for the ratios 8:1 and 4:1, respectively.

As can be seen in the figure, the average field reported in the final stages is in agreement with the predicted in alloy A but not in alloy B, where the measurements show a value significantly lower. This can be explained by the presence of boron in the alloy [226].

4.3.4 Differential scanning calorimetry (DSC) analysis

DSC experiments were carried out for every alloy after different milling times in order to complement the previous XRD analysis of above. The fundamentals of DSC have been introduced in section 3.4 and the characteristics of the equipment and working conditions used for the characterization of the samples have been detailed in table 3.4.

Figure 4.9 shows the evolution of the DSC curves throughout the milling process.

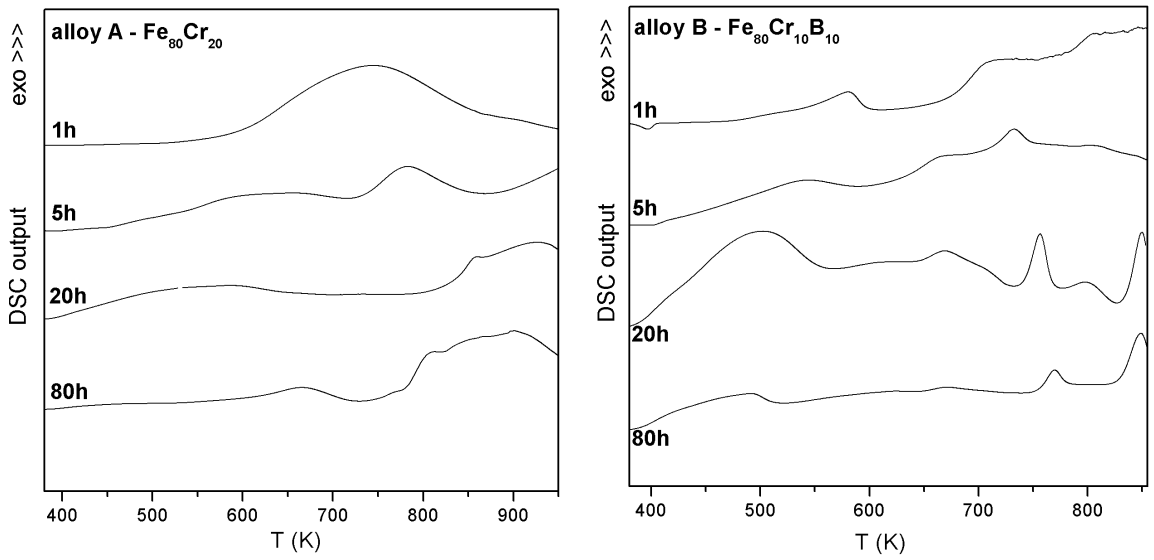

Fig. 4.9: *Evolution of the DSC curves with the milling process for alloys A and B*

The general behavior observed can be summarized in the following points:

1. The curves show two clearly distinguished stages. Below 600-650 K the main peaks detected are only due to structural relaxation processes. Above this point, the main peaks observed can be explained by crystallization and/or nucleation processes. Further analyses including thermograms at different heating rates were needed for a better determination, with the Kissinger method for the 80h sample revealing apparent activation energies of 232±12 and 245±13 kJ/mol, respectively. These values agree with the assumption of a crystalline growth of the nanocrystalline Fe-rich bcc phase [125, 227, 228].

2. The peaks due to structural relaxation become more significant as the milling time increases. This is a normal behavior in MA, since this process introduce a large number of defects in the crystalline matrix. An increase in the number of defects means also an increase in the stress in the material, and hence an increase in the amount of stored energy. Since thermal agitation helps the recovery of stresses, a higher temperature results in a partial or total release of the stored energy and therefore in a presence of exothermic peaks.

3. The onset temperatures of the crystallization peaks shift to higher values with the milling time. This can be again related to the higher stored energy due to the induced defects.

4. The number of peaks and its wideness are reduced with the milling time. This is related to the progressive homogenization of the alloy.

4.4 Analysis of the alloys after 80h of milling

Some samples of the alloys after 80h of milling were analyzed separately in order to study some specific properties and behavior of the final alloys.

4.4.1 Mössbauer spectra

The TMS spectra of both alloys after 80h of milling were analyzed in more depth in order to study the distribution of the Cr atoms in the Fe matrix. The results obtained are shown in figure 4.10 and table 4.3. The table shows the average hyperfine field of each subspectrum used for the computation with the respective relative content compared with the value expected for a hypothetical random distribution.

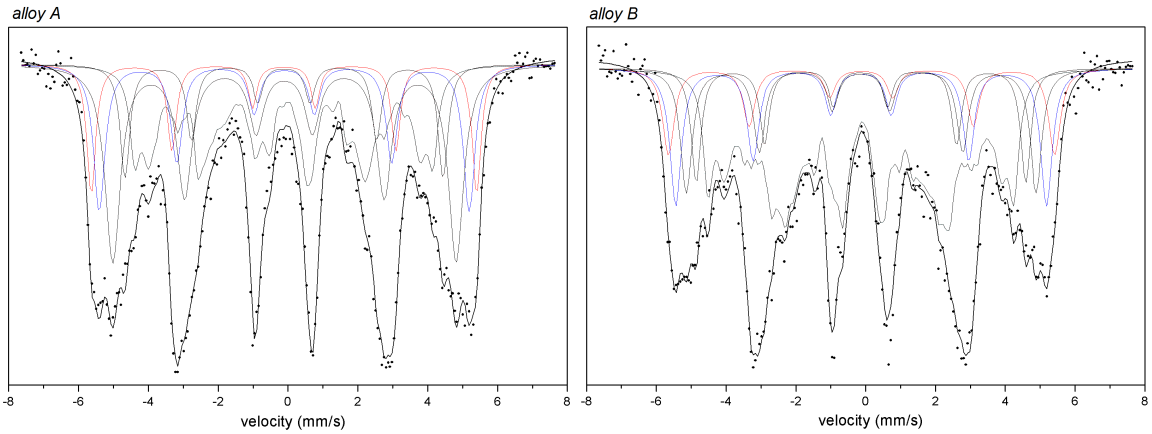

Fig. 4.10: *TMS spectra for alloys A and B after 80h of milling*

alloy A ($Fe_{80}Cr_{20}$)			**alloy B** ($Fe_{80}Cr_{10}B_{10}$)		
hyperfine field	*relative content*		*hyperfine field*	*relative content*	
(T)	observed	random	(T)	observed	random
34.1	11.4%	4-5%	34.2	10.0%	19-20%
32.7	16.8%	6-7%	32.8	15.8%	14-15%
30.4	29.6%	8-9%	31.0	14.4%	19-20%
28.1	11.0%	13-14%	29.1	11.2%	14-15%
26.3	7.9%	7-8%	27.0	10.5%	8-9%
24.0	11.2%	7-8%	24.5	11.2%	2-3%
HFD	12.1%	-	*HFD*	26.9%	-

Tab. 4.3: *TMS subspectra refinement for alloys A and B after 80h of milling*

For the computation of the expected values, a two-shell model has been applied, a model widely used in previous works with Fe-Cr alloys and based in the roughly linear dependence of the hyperfine field value with the number of Cr atoms occupying the neighboring shells around the ^{57}Fe nuclei, as previously explained in section 4.3.3 (equation 8.2). Typical values for bcc Fe-Cr alloys include

a reduction of around 3 T in the average hyperfine field for every Cr atom in one of the 8 nearest neighboring sites and around 2 T for the 6 next-nearest [170, 223, 229]. A hypothetical random distribution would take into account the global proportion of Cr atoms, meaning that the combinations with low number of Cr atoms would be more likely to occur than the ones with high occupancy, specially in alloy A (with higher Cr content).

As can be seen in the table, the observed relative content values do not match with the magnitudes expected for a hypothetical random distribution, a possible indication that the total homogenization was not achieved after 80h of milling. This is consistent with other MA-milled Fe-Cr alloys found in the literature [190, 230, 231].

4.4.2 Magnetic behavior

M-H curves were extracted for both alloys after 80h of milling in order to analyze the hysteresis cycles and estimate their magnetic parameters. The fundamentals and procedure of these analysis have been previously introduced in section 3.5.1, and the equipment and working conditions have been detailed in table 3.6.

Figure 4.11 shows the hysteresis cycles used and table 4.4 lists the magnetic properties estimated from the respective graphs.

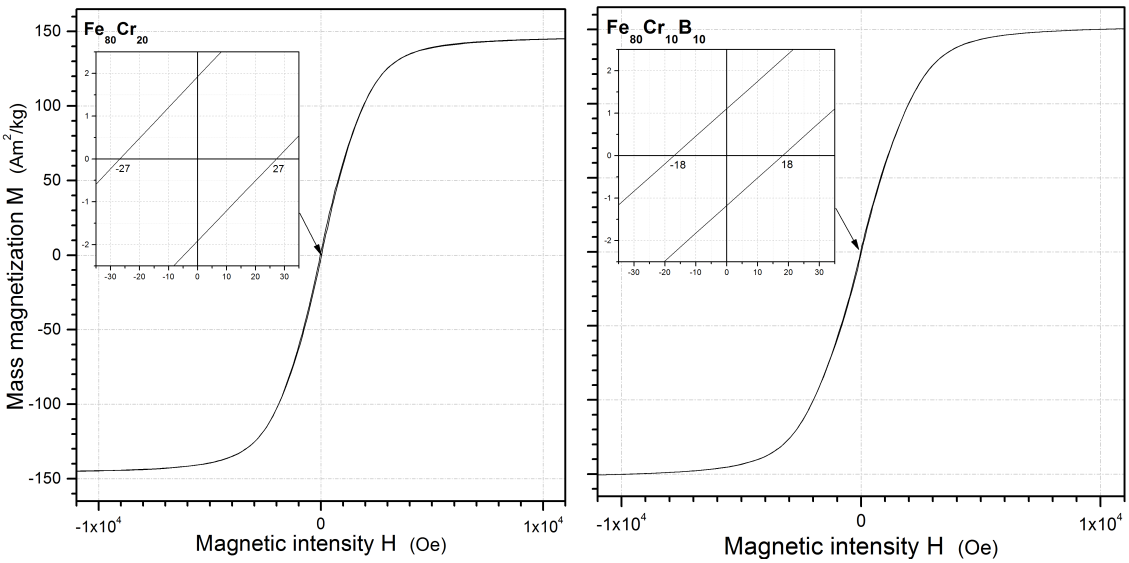

Fig. 4.11: *M-H hysteresis cycles for alloys A (left) and B (right)*

As expected, both alloys show a similar soft-magnetic behavior with relatively low coercivities and high saturation magnetizations.

The observed coercivities H_c of 27 and 18 Oe for alloys A ($Fe_{80}Cr_{20}$) and B ($Fe_{80}Cr_{10}B_{10}$), respectively, are in agreement with the literature dealing with Fe-Cr based nanocrystalline alloys, but still higher than those found in amorphous melt-spun ribbons or in nanocrystalline powders prepared by crystallization of the latter [49, 196, 207, 232, 233].

Estimated magnetic properties

	coercivity	*saturation*		*susceptibility*
	H_c (Oe)	M_s (Am^2/kg)	J_s (T)	χ
alloy A ($Fe_{80}Cr_{20}$)	**27**	146	1.41	540
alloy B ($Fe_{80}Cr_{10}B_{10}$)	**18**	152	1.47	510
	(±1)	(±0.01)	(±0.01)	(±10)

Tab. 4.4: *Magnetic properties estimated from the hysteresis cycles for alloys A and B*

The saturation magnetizations M_s measured, 146 and 152 Am^2/kg respectivelly, also agree with the magnitudes reported in other works [190, 196, 207, 233].

Alloy B seems to show slightly better soft-magnetic properties than alloy A, probably for two reasons:

- Lower relative Cr content. It is known that coercivity tends to increase and saturation to decrease with the Cr relative content [234].
- Presence of B. It has been widely reported that the addition of boron in MA processed alloys helps in the reduction of the coercivity of the final products [125, 165, 193, 194, 235].

4.5 Summary

The two MA-produced alloys analyzed in this chapter have been found to be nanocrystalline even after only 1 hour of milling, with the grain size decreasing at a slower rate as the milling process advanced.

After 80 hours of milling, the average crystalline size has been found to be about 5-6 nm, with alloy B showing a slightly smaller (≈15% lower) value than alloy A. This is probably due to the presence of boron in alloy B, since it is well known that its addition generally reduces the milling time needed for the formation of nanocrystalline or amorphous alloys [171, 236].

In the case of alloy A, there has been reports of other works on MA alloys with identical composition ($Fe_{80}Cr_{20}$) with crystalline sizes of around 12 nm [237]. This noticeable difference is a perfect example of the significance of the specific working conditions in the characteristics of the produced alloy.

The Rietveld refinement of the XRD patterns confirms the formation of a solid solution after only 1 hour of milling. This early disappearance has not been found in other works with higher Cr content, such as in an MA alloys with 31 at%, where the initial Cr-based phase is still detected after this milling time [136].

During the formation of the solid solution, the Cr atoms were introduced substitutionally into the bcc cubic structure of the majority α-Fe phase, due to the fact that pure Cr and Fe have identical crystal structure at room temperature (bcc) and with similar cell parameters (0.291 nm for α-Cr and

0.287 for α-Fe) and atomic radii (0.128 nm for Cr and 0.126 for Fe). It is also known that Cr in Fe diffuses faster than Fe in Cr [190].

In alloy B ($Fe_{80}Cr_{10}B_{10}$) B atoms were also introduced into the main (Fe,Cr) phase, although due to the low atomic radius of the B atoms (0.090 nm), the introduction were likely produced interstitially rather than substitutionally.

As explained in section 4.3.2, the XRD analyses did not show any presence of Fe or Cr borides, which should be expected to be found due to the low solubility of B in Fe-Cr based alloys [212].

The increase in the cell parameter of the Fe-based majority phase throughout the milling time detected in the Rietveld refinements (see details in section 4.3.2) seems to confirm the formation of the Fe-Cr solid solution, based on the higher cell parameter of the bcc-Cr phase. The increase is slightly higher in alloy A, surely explained by its higher relative number of Cr atoms.

There is also an increase in the microstrain index and density of dislocations with the milling time in both alloys, due to defects introduced by the milling process [235].

Although the XRD patterns clearly show the presence of a single crystalline phase in the final alloys, the Mössbauer spectra reveal that this phase is not homogeneous. After following the Dubiel and Cieslak method [178], the results of the analysis indicate that around 10-11% of the Fe atoms do not show having any Cr atom as first or second neighbor, while a similar percentage show a higher number than expected. It is known that a high relative Cr content in any of the environments would have produced a paramagnetic phase [136, 185], as well as in the grain boundaries [238]. Nevertheless, this paramagnetic behavior has not been detected in any of the environments found in the Mössbauer analysis, ruling them out of these alloys, at least above the detectability threshold.

Further annealing of the final alloys as well as an increase of the milling time could help reducing this heterogeneity in the samples. The latter could also produce an amorphization of the alloy [190], which will mean a significant modification of the final properties.

Regarding the magnetic behavior, both final alloys (after 80h of milling) show a clear soft-magnetic behavior. The coercivity was found to be lower in alloy B ($Fe_{80}Cr_{10}B_{10}$), due to both the higher iron relative content and the presence of B. Other previous works with Fe-based alloys showed similar patterns after the introduction of B [125, 165, 189, 193, 194, 235]

5 Study of Fe-Co nanocrystalline alloys produced by mechanical alloying (MA)

> *All experiment is made on a basis of tradition; all tradition is the crystallization of experiment.*
>
> **— Louis MacNeice**
> (Poet)

Contents

This chapter deals with the development and characterization of some Fe-Co based ferromagnetic nanocrystalline powder alloys produced by mechanical alloying (MA).

5.1 Introduction

Fe-Co based alloys, and in particular nanostructured Fe-Co alloys, feature interesting soft magnetic properties such as high permeability at high frequencies, high Curie temperature and the highest saturation magnetization of all known magnetic alloys [239–243], specially in the vicinity of 30 at. % Co [244, 245] and equiatomic compositions [241]. These properties make this nanostructured material family useful in a wide variety of technological and industrial applications such as aerospace motors and generators, electromagnets, high performance transformers, magnetic bearings, saturable reactors, noise filters, miniature inductance elements for abating spike noise, choke coils, zero-phase current transformers or magnetic heads [246–250].

The Fe–Co system shows a small negative heat of mixing (–1 kJ/mol), favoring the formation of nanocrystalline solid solutions rather than amorphous state in MA processing [251], and in particular substitutional alloys based in the α-Fe bcc structure for Co relative contents as high as 80% and the γ fcc for contents higher than 90% Co [224, 252] (see fig. 5.1). Furthermore, the addition of other alloying elements as well as heat treatments may certainly affect the resulting microstructure and the final soft magnetic properties [253].

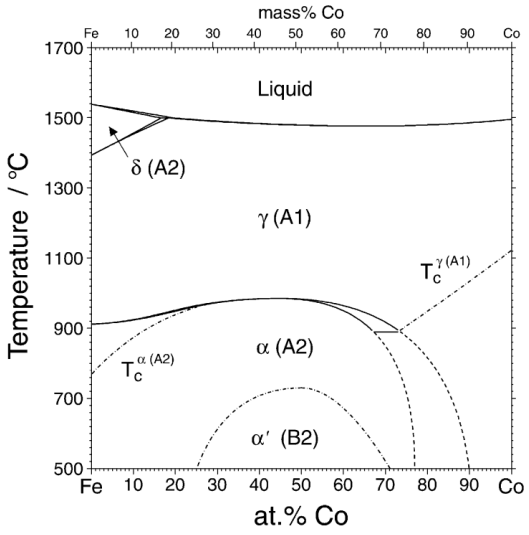

Fig. 5.1: *Fe-Co phase diagram* [239, 254, 255]

Although the significant amount of internal strain introduced during the milling process by the inevitable heavy plastic transformation (see section 2.1) could make this process unsuitable for the production of optimal soft magnetic Fe-Co (and Fe-Co-Ni alloys) [252], some works [256] have shown a regular diminution of the coercivity and the crystallite size as a function of milling time, in good agreement with the theoretical predictions of the random-anisotropy model [257], thus making MA potentially useful in the processing of magnetic materials provided that excessive milling times are avoided [247].

5.2 Production of the alloys

Two groups of alloys were produced for this chapter.

1. $Fe_{90-x}Co_xB_{10}$ alloys:
   - Alloy C: $Fe_{80}Co_{10}B_{10}$
   - Alloy D: $Fe_{45}Co_{45}B_{10}$

   This pair of alloys allows the study of the effects of the relative Co content (1:8 in alloy C and 1:1 in alloy D) on the structure and properties of the alloys.

2. $Co_{50}Fe_{30}X_{20}$ alloys:
   - Alloy E: $Co_{50}Fe_{30}B_{20}$
   - Alloy F: $Co_{50}Fe_{30}Ni_{20}$

   This second pair focus on the differences between the effects of the presence of B or Ni in the alloys. Alloy E also allows the comparison with the previous pair and study of the effects of a higher B content.

Like in the case of the Fe-Cr alloys of chapter 4, the production was carried out in a planetary ball mill (see 2.1.1 for details) with the equipment and conditions described in table 5.1. The vials with the raw materials inside were placed in a vacuum vessel, then refilled with the argon gas and finally sealed with PTFE.

MA production equipment	
mill model	Fritsch Pulverisette 7 (see fig. 2.7)
type of mill	planetary ball mill
containers	hardened stainless steel vials (18% Cr, 10% Ni)
balls	hardened stainless steel (18% Cr, 10% Ni)
milling conditions	
raw materials	Industrial powders of pure (purity > 99%) elemental B, Fe, Co and Ni in stoichiometric proportions
milling atmosphere	Ar
process control agents (PCA)	1 ml of cyclohexane (C_6H_{12})
quantity of material to process	12 g
ball-to-powder mass ratio (BPR)	4:1
milling speed	700 rpm
milling times	1, 5, 20 and 80 hours
operation program	45-minute cycles (30 min running + 15 min pause) alternating clockwise and counter-clockwise rotation

Tab. 5.1: *Equipment and milling conditions used for the production of alloys C, D, E and F*

5.3 Morphological and structural analysis

Several samples of each alloy were extracted and analyzed by means of Scanning Electronic Microscopy (SEM) and X-Ray Diffraction (XRD) in order to study their structure and identify similarities and differences between the alloys throughout the milling process.

5.3.1 Scanning Electronic Microscopy (SEM)

SEM observations for the 80h samples were carried out with the same SEM equipment and under the same procedure and conditions of the Fe-Cr alloys of chapter 4 (see table 3.2 for more details).

$Fe_{90-x}Co_xB_{10}$ alloys

Figures 5.2 and 5.3 show the SEM micrographs for alloys C ($Fe_{80}Co_{10}B_{10}$) and D ($Fe_{45}Co_{45}B_{10}$) after 80h of milling.

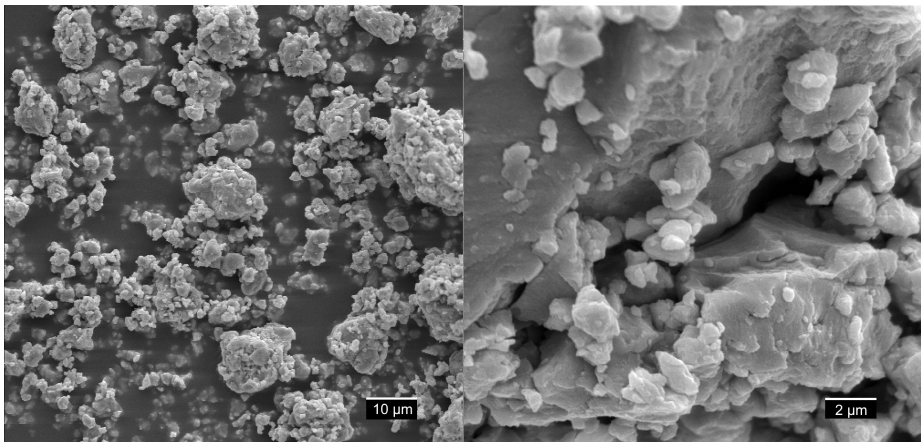

Fig. 5.2: *SEM micrographs for alloy C ($Fe_{80}Co_{10}B_{10}$) after 80h of milling*

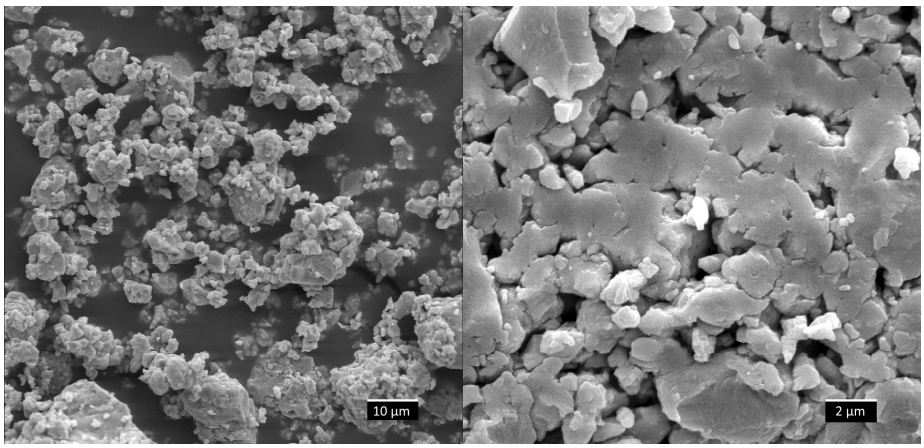

Fig. 5.3: *SEM micrographs for alloy D ($Fe_{45}Co_{45}B_{10}$) after 80h of milling*

According to the SEM micrographs, alloy D seems to feature higher ductility than alloy C, which is surprising since it is known that binary equiatomic Fe-Co alloys are notoriously brittle, particularly in the ordered state [239] and there are no reports of any particular improvement due to the addition of boron [258, 259]. However, it has been also reported that a decrease in the degree of order in the Fe-Co based alloy does improve the ductility [239, 260, 261], which could explain this result.

$Co_{50}Fe_{30}X_{20}$ alloys

Figures 5.4 and 5.5 show the SEM micrographs for alloys E ($Co_{50}Fe_{30}B_{20}$) and F ($Co_{50}Fe_{30}Ni_{20}$) after 80h of milling.

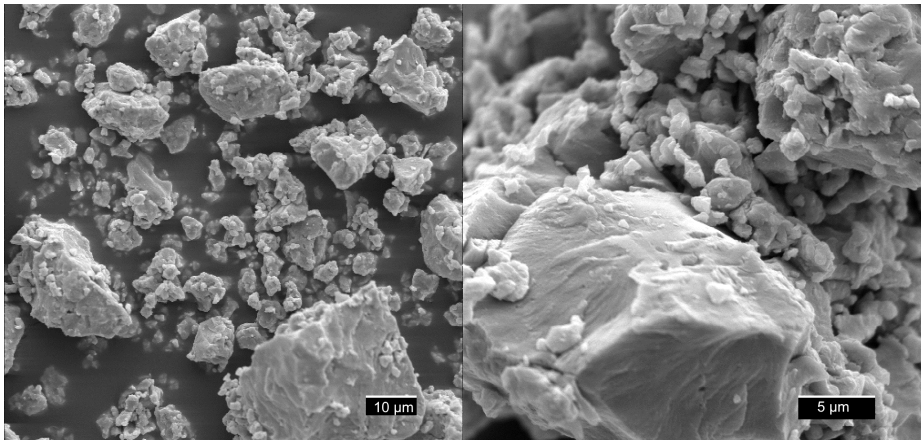

Fig. 5.4: *SEM micrographs for alloy E ($Co_{50}Fe_{30}B_{20}$) after 80h of milling*

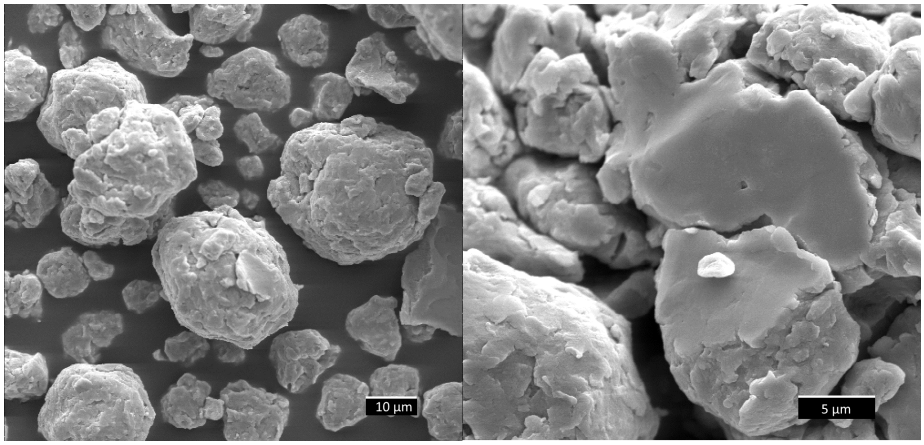

Fig. 5.5: *SEM micrographs for alloy F ($Co_{50}Fe_{30}Ni_{20}$) after 80h of milling*

The micrographs of alloy E ($Co_{50}Fe_{30}B_{20}$) shows similarities with the previous pair of alloys, due to their close compositions. Alloy F ($Co_{50}Fe_{30}Ni_{20}$), on the other hand, features significant differences, and in particular seems to show softened contours and few apparent fractures, indicating a higher ductility in comparison with the other alloys. As it will be explained below in the XRD analysis, this is one of the consequences of the substitution of B for Ni and its effects on the resulting microstructure.

5.3.2 X-ray diffraction (XRD)

Like in the case of the Fe-Cr alloys of chapter 4, XRD analysis were carried out for every alloy and after each different milling time in order to study their evolution throughout the milling process.

$Fe_{90-x}Co_xB_{10}$ alloys

Figure 5.6 shows the evolution of the XRD spectra for alloys C ($Fe_{80}Co_{10}B_{10}$) and D ($Fe_{45}Co_{45}B_{10}$).

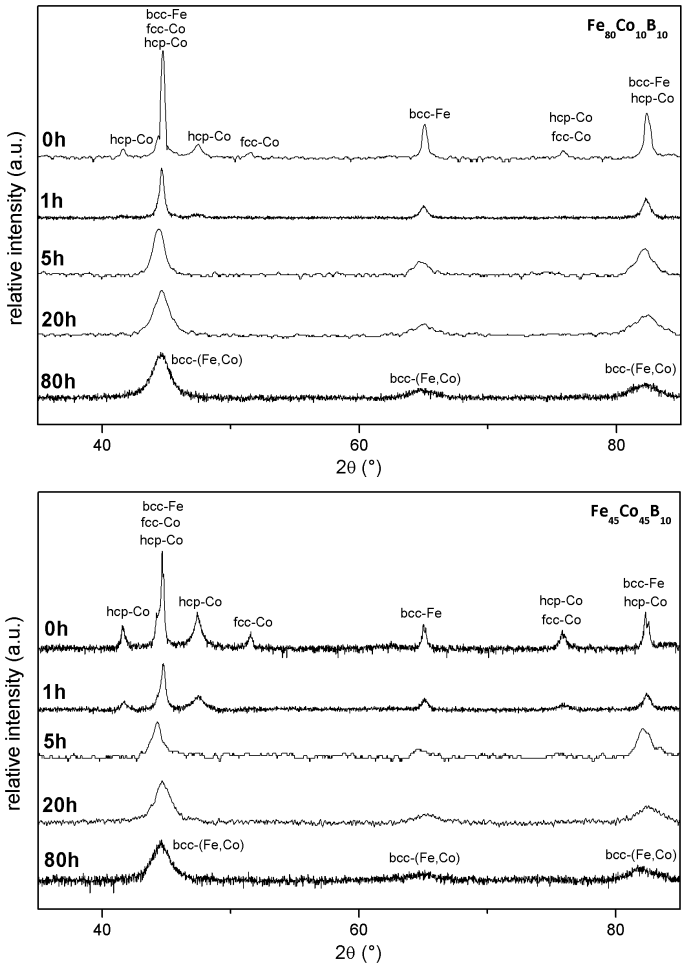

Fig. 5.6: *Evolution of the XRD patterns throughout the milling process for alloys C (top) and D (bottom)*

The XRD patterns of the unmilled alloys show the individual peaks of the bcc-Fe phase of iron and the two coexisting cobalt allotropes, hcp-Co and fcc-Co.

As the milling process advances, the bcc-Fe phase become the main phase and the other peaks are significantly reduced in the samples after 1h of milling and not detected at all in the samples after 5h of milling, a result in agreement with the literature [247, 251], indicating the formation of the solid solution bcc-(Fe,Co) during the stage between these two milling times. The Co atoms, which have atomic radius very close to that of Fe (0.125 and 0.124 nm, respectively), were surely introduced substitutionally in the bcc-Fe phase. This seems to have happened even in the equiatomic case (alloy

B), since the diffusivity of Co into Fe is higher than that of Fe in Co [244, 262, 263]. The B atoms, on the other hand, were probably introduced interstitially such as in the case of the previous Fe-Cr alloys.

One particular case is the fcc-Co phase, whose peaks are already absent even in the 1h samples. Although this could be just attributed to the intensity being reduced below the detection threshold of the XRD equipment, the most reasonable explanation is the allotropic transformation of Co from fcc to hcp form found in other works with similar compositions, since the fcc-Co phase is metastable at room temperature and becomes unstable when an external mechanical or thermal energy is introduced [264, 265]. The accumulation of structure defects and the energy of the energy stored in the materials during the milling process generally accelerates this transformation [224].

The peaks of the remaining solid solution are smoothed and broadened and their position shifted as the milling time increases. This is the same tendency found in the Fe-Cr alloys, as it is related to the reduction of the crystal size and changes in the lattice properties and microstrain values, respectivelly, which is a normal behavior in mechanical alloying processes [134, 266, 267].

In order to quantify all these features and estimate the specific variations of the crystalline parameters involved, Rietveld refinements (see section 3.2.2) of the respective XRD diffractograms had been carried out, with the results shown in table 5.2.

milling time	phases detected	lattice param. $\langle a \rangle$ (nm)	crystalline size $\langle L \rangle$ (nm)	microstrain $\langle \sigma^2 \rangle^{1/2}$ (%)
alloy C ($Fe_{80}Co_{10}B_{10}$)				
0 h	bcc-Fe hcp-Co fcc-Co	0.2868	215 ±5	0.01
1 h	bcc-(Fe,Co) bcc-Fe hcp-Co	0.2867	69 ±2	0.14
5 h	bcc-(Fe,Co)	0.2864	20.8 ±0.6	0.37
20 h	bcc-(Fe,Co)	0.2868	13.8 ±0.6	0.56
80 h	bcc-(Fe,Co)	0.2876	12.5 ±0.3	0.64
alloy D ($Fe_{45}Co_{45}B_{10}$)				
0 h	bcc-Fe hcp-Co fcc-Co	0.2868	200 ±5	0.00
1 h	bcc-(Fe,Co) bcc-Fe hcp-Co	0.2868	106 ±8	0.12
5 h	bcc-(Fe,Co)	0.2865	26.2 ±1.2	0.41
20 h	bcc-(Fe,Co)	0.2859	12.6 ±0.5	0.46
80 h	bcc-(Fe,Co)	0.2877	13.5 ±0.6	0.78

Tab. 5.2: *Crystalline parameters estimated from Rietveld refinements for alloys C and D*

As can be seen, both alloys follow the common behavior found in most MA produced alloys, including the Fe-Cr examples from the previous chapter, and feature nanocrystalline properties after just few hours of milling. The evolution of the grain size (fig. 5.7) shows a drastic reduction during the very early stages of the milling process and an achievement of a relatively steady magnitude of around 12-13 nm in later stages.

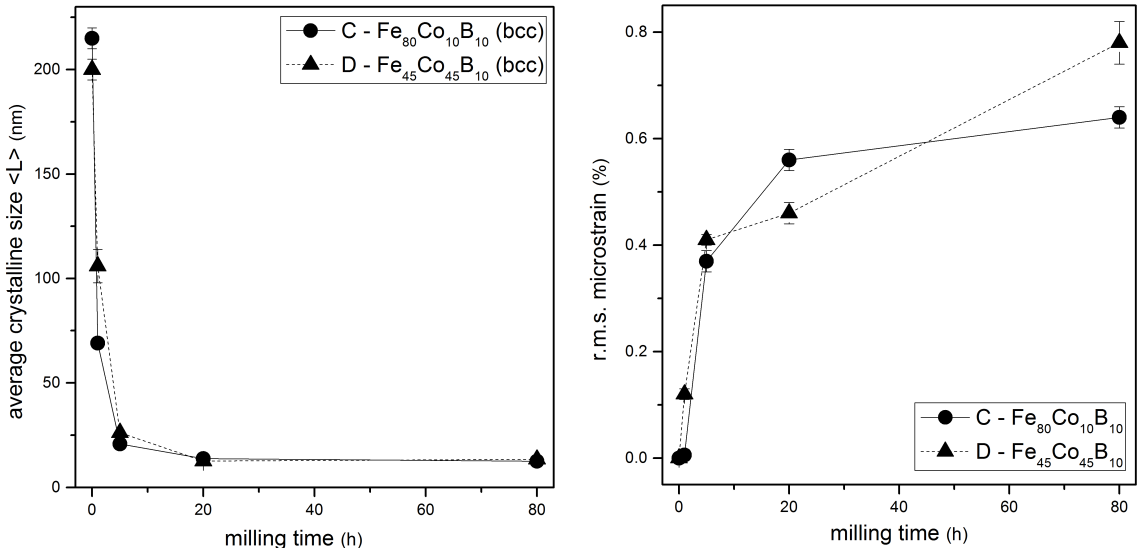

Fig. 5.7: *Average crystalline size (left) and microstrain (right) for alloys C and D*

$Co_{50}Fe_{30}X_{20}$ alloys

Figure 5.8 shows the evolution of the XRD spectra for alloys E ($Co_{50}Fe_{30}B_{20}$) and F ($Co_{50}Fe_{30}Ni_{20}$) throughout the milling process, with some noticeable differences between them.

Alloy E ($Co_{50}Fe_{30}B_{20}$) shows an evolution almost identical to the previous alloys of the other group, including the reduction in the number of peaks, due the formation of the solid solution, and their broadening and shifting, consequence of the crystalline parameters refinement. A bcc crystal structure is again observed in the solid solution formed, which might seem counter intuitive after taking into account the higher Co relative content, but agrees with the equilibrium Co-Fe phase diagram [268–270] and with the results from other works with non-equilibrium alloys with similar compositions found in the literature [271, 272].

In alloy F ($Co_{50}Fe_{30}Ni_{20}$), however, a different evolution is observed, with the solid solution showing a fcc crystalline structure, due to the presence of Ni along with the high Co content. This result agrees with the literature [273, 274] and also confirms the previous SEM analysis, which showed a high ductility of the samples, since materials with the fcc crystal structure generally show higher ductilities than those with bcc, thanks to the fcc being a closely packed structure [275].

Table 5.3 lists the the crystalline parameters for alloys E and F estimated from the Rietveld refinements of the XRD spectra.

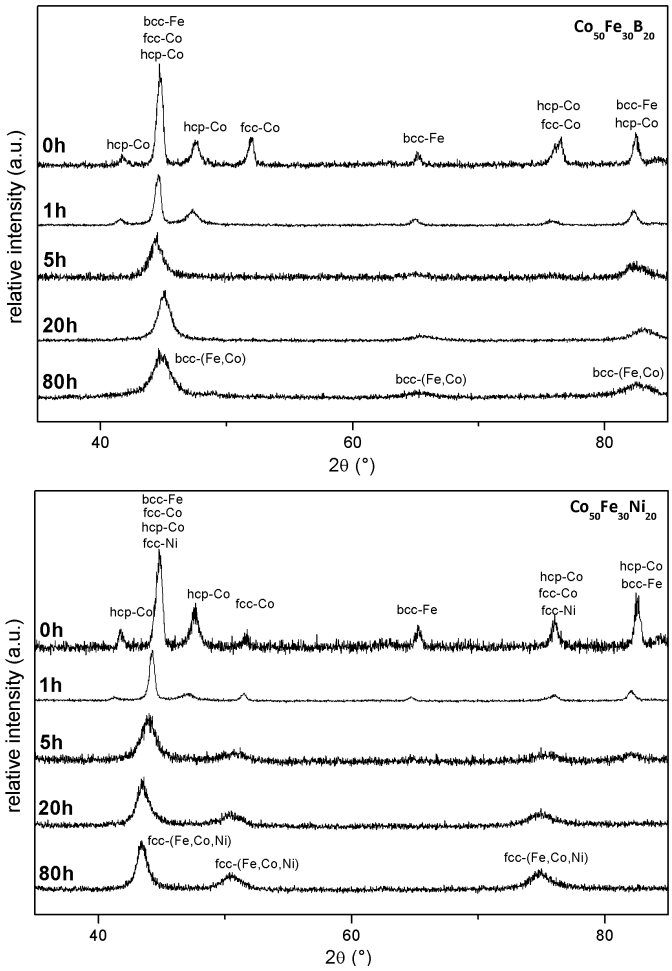

Fig. 5.8: *Evolution of the XRD patterns throughout the milling process for alloys E and F*

Again, like in the previous group, nanocrystalline properties are detected after just few hours of milling, after an initial drastic reduction of the grain size during the early stages. The roughly steady state is also observed during the last stage (fig. 5.9). although this time with lower achieved values.

In the specific case of alloy F, a significant increase in the crystalline size is observed between the 20h and the 80h of milling which might be explained by an excessive rise in the milling temperature. Generally, the temperature of the powders during milling can be high due to either the kinetic energy of the grinding medium itself or the heat generated by exothermic processes occurring during the milling process (or both) [247].

The magnitudes of the lattice parameter in alloy E show an opposite evolution than in alloys C and D. Whereas in the previous pair the tendency was generally to increase, in this case is the opposite: a decreasing tendency. This could be explained by the higher boron content, which might force part of the boron to be introduced into the bcc matrix substitutionally rather than interstitially, producing a true Fe-Co-B ternary solid solution. Alloy F cannot be included in this comparison due to the different fcc crystal structure.

milling time	phases detected	lattice param. $\langle a \rangle$ (nm)	crystalline size $\langle L \rangle$ (nm)	microstrain $\langle \sigma^2 \rangle^{1/2}$ (%)
alloy E ($Co_{50}Fe_{30}B_{20}$)				
0 h	bcc-Fe hcp-Co fcc-Co	0.2867	160 ±40	0.00
1 h	bcc-(Fe,Co) bcc-Fe hcp-Co	0.2867	150 ±40	0.33
5 h	bcc-(Fe,Co,B)	0.2849	10.5 ±0.3	0.40
20 h	bcc-(Fe,Co,B)	0.2849	11.9 ±0.3	0.52
80 h	bcc-(Fe,Co,B)	0.2858	6.9 ±0.1	0.55
alloy F ($Co_{50}Fe_{30}Ni_{20}$)				
0 h	fcc-Ni bcc-Fe hcp-Co fcc-Co	0.3524	43 ±5	0.00
1 h	fcc-(Co,Fe,Ni) bcc-Fe hcp-Co	0.3526	29 ±2	0.11
5 h	fcc-(Co,Fe,Ni)	0.3539	8.8 ±0.6	0.50
20 h	fcc-(Co,Fe,Ni)	0.3584	7.7 ±0.6	0.47
80 h	fcc-(Co,Fe,Ni)	0.3574	11.4 ±0.3	0.56

Tab. 5.3: *Crystalline parameters estimated from Rietveld refinements for alloys E and F*

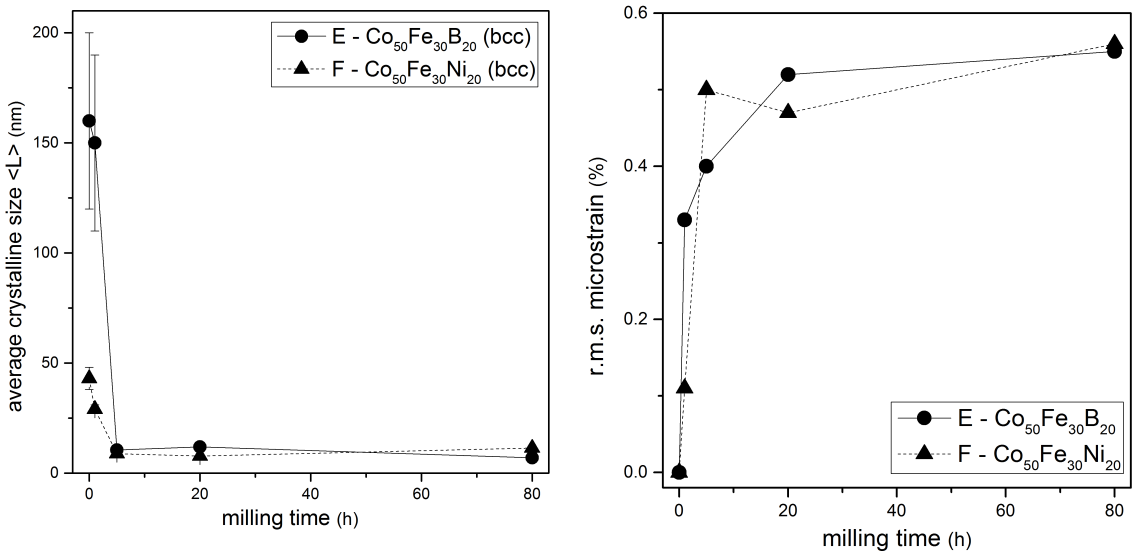

Fig. 5.9: *Average crystalline size (left) and microstrain (right) for alloys E and F*

5.3.3 Mössbauer spectroscopy (TMS) analysis

Structural analysis for each of the 80-hour milled samples were carried out by means of transmission Mössbauer spectroscopy (see sec. 3.3 for details).

$Fe_{90-x}Co_xB_{10}$ alloys

Figure 5.10 shows the Mössbauer spectrum for alloys C and D after 80 hours of milling.

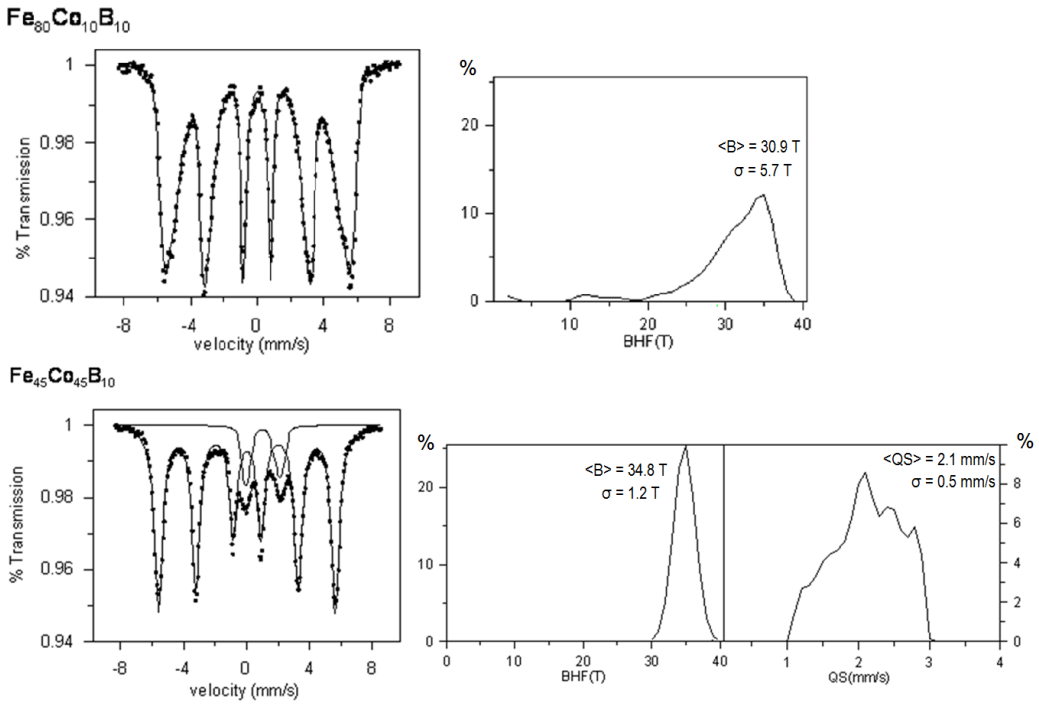

Fig. 5.10: *TMS spectra and estimated hyperfine distributions for alloys C (top) and D (bottom)*

The spectrum for alloy C shows a distribution of hyperfine magnetic field biased to low values with an estimated average value $\langle B_{hf} \rangle = 30.9$ T, which is below the value for an unreacted pure bcc-Fe phase (33 T at room temperature [224, 225]). This fact can be explained by:

- Increase in the number of cobalt neighbors to the iron atoms, due to the formation of the solid solution and the substitution of some of the Fe atoms in the bcc structure by Co atoms [276].
- Introduction of B atoms interstitially within the bcc structure [277].

Similar results can be found in the literature for other Fe-Co MA-processed alloys [251, 276], although with slightly higher average values, probably due to the absence of the interstitial boron found here. Furthermore, the fact that the distribution is significantly wide ($\sigma = 5.7$ T) could be an indication of the presence of a wide variety of different iron environments with a random replacement of iron atoms by cobalt.

The spectrum for alloy D, on the other hand, shows two main contributions: a main (89.6 %) ferromagnetic alloy with an average hyperfine field $\langle B_{hf} \rangle$ = 34.8 T, a value also in agreement with the literature [224, 278], and a a minor (10.4%) paramagnetic alloy, with an average quadrupolar splitting $\langle QS \rangle$ = 2.1 mm/s widely distributed (σ = 0.5 mm/s). It must be noted that the second component was not detected in the XRD spectrum due to the highest sensibility of Mössbauer spectrocopy in the detection of iron environments.

$Co_{50}Fe_{30}X_{20}$ alloys

Figure 5.10 shows the Mössbauer spectra for alloys E and F after 80 hours of milling.

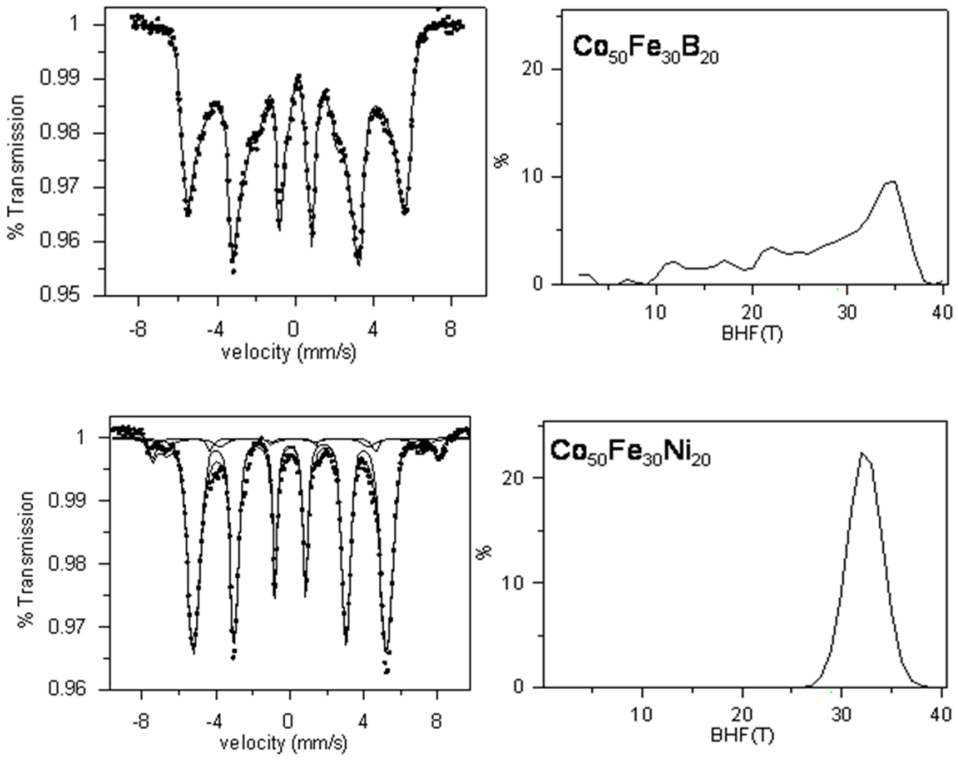

Fig. 5.11: *TMS spectra and estimated hyperfine distributions for alloys E (top) and F (bottom) after 80h of milling*

The Mössbauer spectrum for alloy E reveals, as in alloy C, one single main contribution: a ferromagnetic alloy. Nevertheless, the extremely wide distribution of values (8.10 T) seems to indicate now a highly disordered phase. It must be remembered that the previous XRD analysis showed a reduction in the lattice parameter which was hypothesized to be due to part of the boron being introduced substitutionally into the matrix of the main phase.

On the other hand, the spectrum for alloy F is more similar to alloy D, with two main contributions: a majority (87.3 % in atomic weight) ferromagnetic alloy and some minor (around 6 % each) iron oxides also with ferromagnetic behavior.

5.4 Thermal analysis

The thermal behaviors of the alloys have been analyzed by means of DSC experiments, under the same equipment and working conditions described in chapter 4 and detailed in table **??**.

5.4.1 Evolution of the milling process

Figures 5.12 and 5.13 shows the evolutions of the DSC curves for the $Fe_{90-x}Co_xB_{10}$ and $Co_{50}Fe_{30}X_{20}$ alloys, respectively, throughout the milling processes.

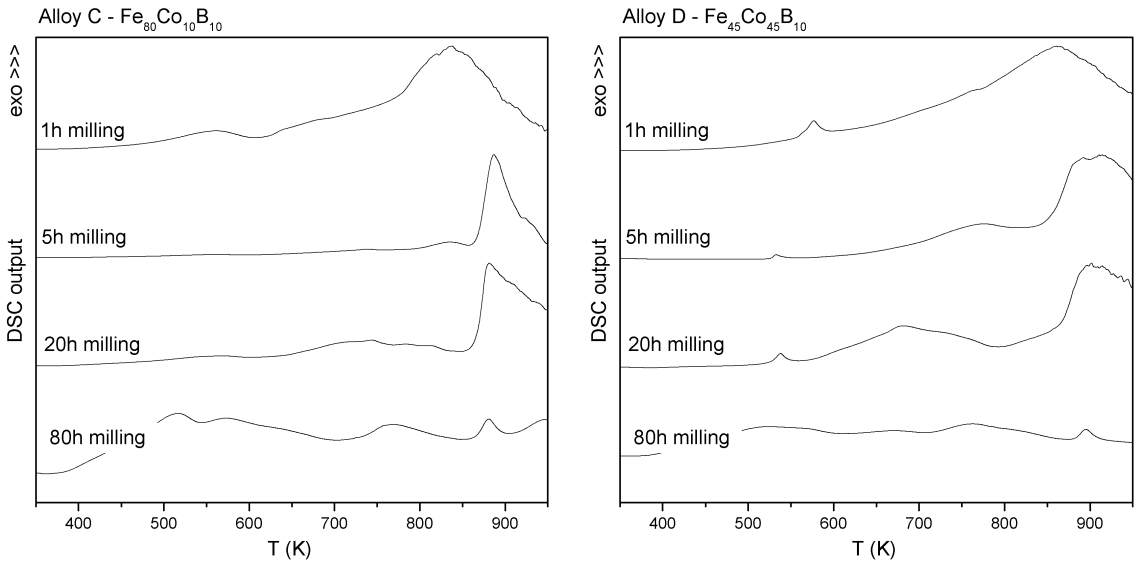

Fig. 5.12: *Evolution of the DSC curves with the milling process for the $Fe_{90-x}Co_xB_{10}$ alloys (C and D)*

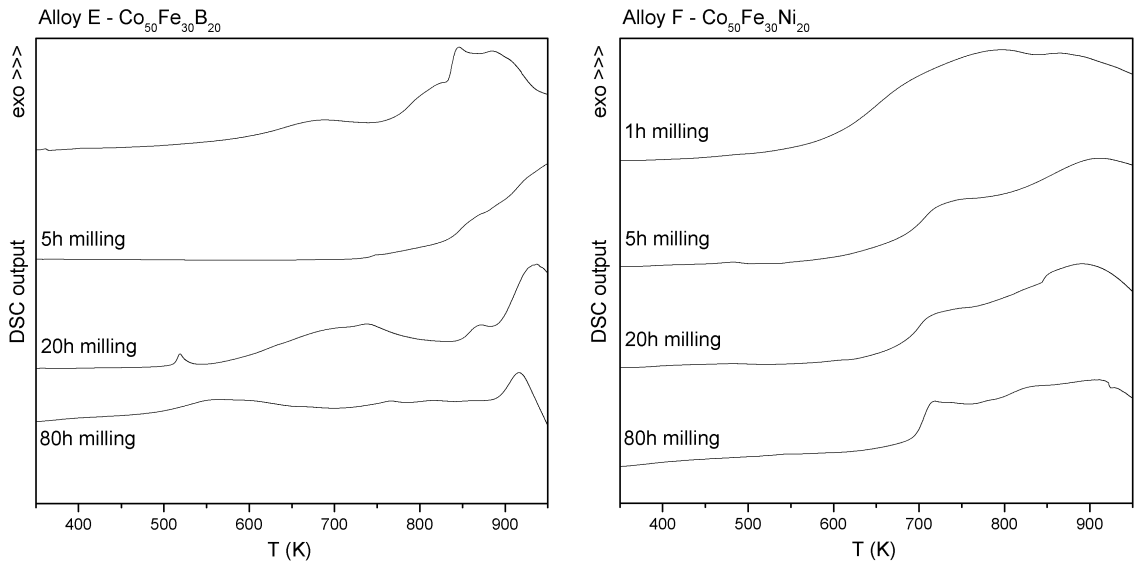

Fig. 5.13: *Evolution of the DSC curves with the milling process for the $Co_{50}Fe_{30}X_{20}$ alloys (E and F)*

The general behavior observed in the DSC curves can be summarized in the following points:

1. The curves show two clearly distinguished stages, with the region below 600-650 K showing mainly structural relaxation processes and the region above showing the most visible peaks, which can be explained by crystallization and/or nucleation processes. The exact nature will be discussed below with the determination of the respective activation energies.

2. The peaks due to structural relaxation become more noticeable and significant as the milling time increases. This is a normal behavior in MA, due to the introduction of a large number of defects in the crystalline matrix. An increase in the number of defects means also an increase in the stress in the material and in the amount of stored energy, and since thermal agitation helps the recovery of stresses, a higher temperature results in a partial or total release of the stored energy, which is reflected in the presence of larger exothermic peaks.

3. The onset temperatures of the crystallization peaks are shifted to higher values throughout the milling process. This reveals an improvement in the thermal stability of the alloys.

4. The number of peaks and its wideness are reduced with the milling time. This is related to the progressive homogenization of the alloy throughout the milling process.

5.4.2 Activation energies in the final alloys

Although the activation energy of a certain process (i.e. the minimum energy required to start the process) may be influenced by several factors, such as the composition and ratio between elements, the magnitude ranges involved are somewhat specific for every kind of reaction or process. According to the bibliography, activation energies for crystalline growth processes in nanocrystalline Fe-based alloys are between about 140 kJ/mol (1.5 eV) [279] and 170 kJ/mol (1.8 eV), with the latter corresponding to a pure iron sample [280]. These energy values are relatively low, since these processes mean the growth of previously created nanocrystals but do not mean the creation of growing nuclei.

On the other hand, amorphous alloys, which require the creation of an initial nucleus -a process called nucleation-, show activation energy magnitudes significantly higher. These values are between about 300 kJ/mol (3.2 eV) [281] and 365 kJ/mol (3.8 eV) [282]. The presence of elements that act as nucleation agents, such as Cu, generally decrease the activation energy values required for the nucleation process. In these cases, the calculated values might be slightly lower [282].

Even the method used for the determination of the activation energy must also be taken into consideration, since it may affect the calculated values [283]. Several methods have been introduced and detailed in section 3.4 of chapter 3, being all of them based on the analysis of several DSC experiments carried out with different heating rates. For the analysis of the alloys in this chapter, the Kissinger method was applied using five different heating rates: 2.5, 5, 10, 20 and 40 K/min.

As mentioned in section 3.4, this method relies on the expected shifting of the peak positions between experiments under different heating rate varies due to the internal lag of the DSC [147]. A plot of $\ln\left(\frac{\beta}{T_p}\right)$) versus the reciprocal temperature ($1/T_p$) will show a good linear correlation with contributions from the two relevant parameters involved, heating rate and peak temperature, and will allow their estimation by linear regression.

$Fe_{90-x}Co_xB_{10}$ alloys

Table 5.4 shows the activation energies for alloys C and D, estimated using the Kissinger method, with the respective graphs shown in figure 5.14.

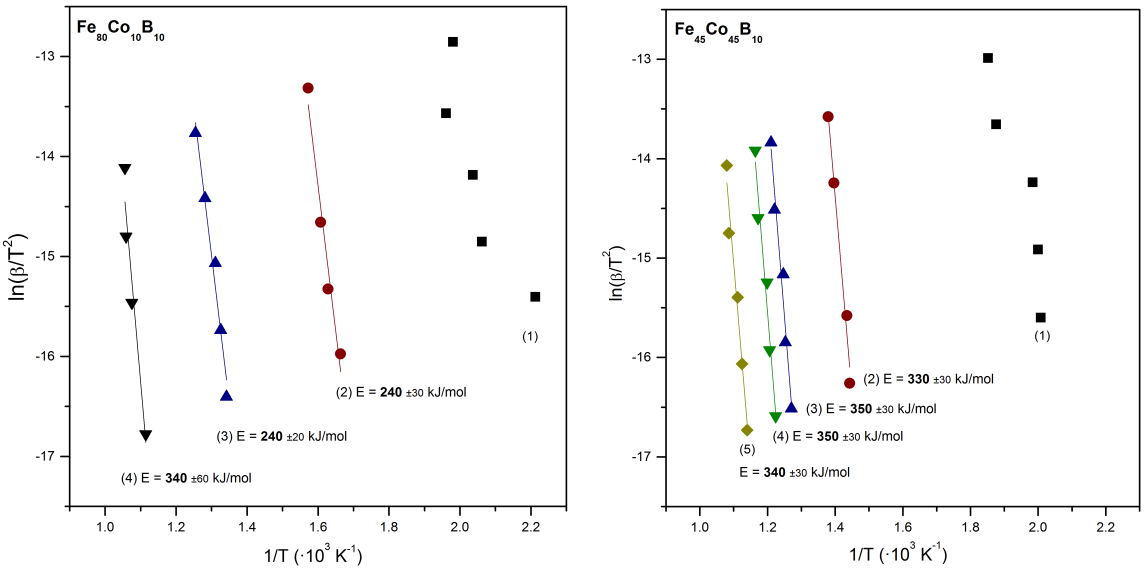

Fig. 5.14: *Kissinger plots for alloys C (left) and D (right)*

process id.	temperature range (K)	activation energy E (kJ/mol)	R^2
	alloy C ($Fe_{80}Co_{10}B_{10}$)		
(1)	450 - 510	*not enough correlation*	
(2)	610 - 640	**240** ±30	0.953
(3)	740 - 800	**240** ±20	0.970
(4)	890 - 950	**340** ±60	0.917
	alloy D ($Fe_{45}Co_{450}B_{10}$)		
(1)	400 - 540	*not enough correlation*	
(2)	560 - 580	**330** ±30	0.979
(3)	600 - 630	**350** ±30	0.960
(4)	740 - 775	**350** ±30	0.957
(5)	860 - 920	**340** ±30	0.960

Tab. 5.4: *Estimated activation energies for alloys C and D*

- The range of 450-550 K shows some difficulties in the determination of the exact peak positions -labelled as (1)-, resulting in an excessive uncertainty and therefore poor correlation. Although no direct activation energy value can be extracted in any case, a simple analogy with the curves observed in several similar alloys might indicate, with high probability, that this processes are related to structural relaxation mechanisms.

- The region beyond 550 K, on the other hand, allows good determination of clear peak positions and the subsequent correlation is high enough to reliable specific activation energies.

  The DSC of the alloy with the lowest Co content (C) reveals the presence of several peaks with a wide distribution in the energy values. According to the literature on nanocrystalline iron-based alloys, the lowest values observed (around 240 kJ/mol) lie in the frontier between the general magnitudes related to crystalline growth and nucleation, and the uncertainty associated to the estimated value ($\pm$20 kJ/mol) adds difficulty to the correct identification. Some Fe-Co-B-Si similar alloys have been reported to show activation energies of 230 kJ/mol associated with crystalline growth processes [284]. However, further complementary analyses are required for a correct classification.

  The last process detected, on the other hand, shows a high energy value similar to those found in alloy D. These processes are probably related to nucleation and crystallization of new phases, although they are still slightly lower than those expected for this kind of mechanism. This could show an indication of the formation of borides.

- The presence of several peaks in some alloys denotes some heterogeneity in the samples. The Mössbauer analyses provided in section **??** showed the presence of minority phases, which might be a possible explanation for that.

$Co_{50}Fe_{30}X_{20}$ alloys

Table 5.5 shows the activation energies for alloys E and F estimated using the Kissinger method, with the respective graphs shown in figure 5.15.

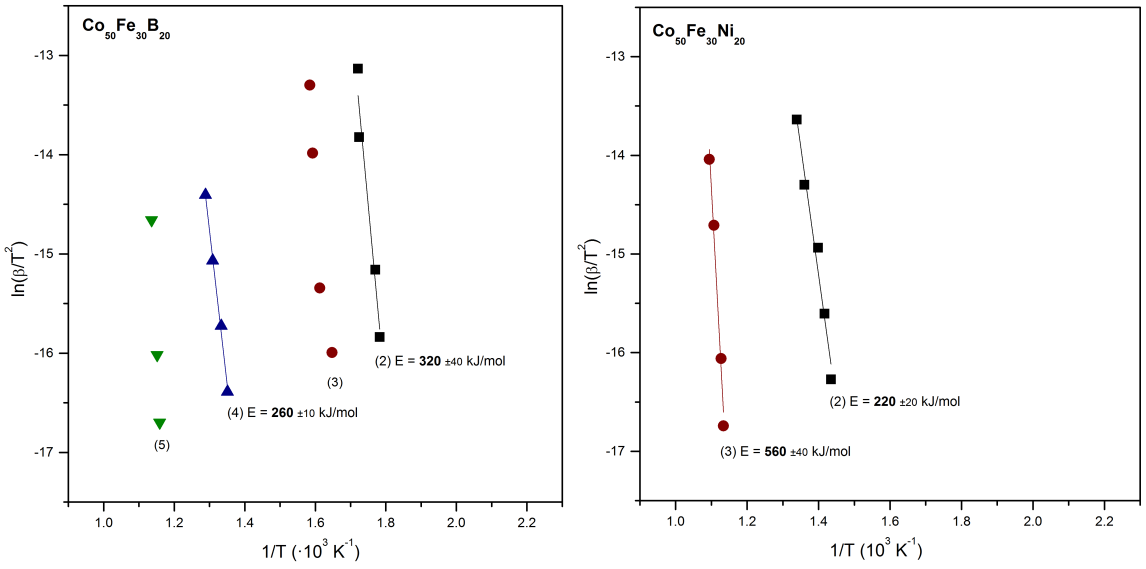

Fig. 5.15: *Kissinger plots for alloys E (left) and F (right)*

The DSC analysis for alloy F shows significant differences with regard to the other Fe-Co based alloys studied. Apart from the first process -which surely can be associated again with structural relaxation

process id.	temperature range (K)	activation energy E (kJ/mol)	R^2
	alloy E ($Co_{50}Fe_{30}B_{20}$)		
(1)	450 - 510	*not enough correlation*	
(2)	560 - 580	**320** $\pm$30	0.939
(3)	600 - 630	*not enough correlation*	
(4)	740 - 780	**260** $\pm$10	0.995
(4)	860 - 880	**260** $\pm$10	0.995
	alloy F ($Co_{50}Fe_{30}Ni_{20}$)		
(1)	400 - 600	-	
(2)	695 - 750	**220** $\pm$20	0.970
(3)	880 - 915	**560** $\pm$40	0.981

Tab. 5.5: *Estimated activation energies for alloys E and F*

mechanisms-, the earliest process was detected beyond the 700 K, which is a temperature value considerably higher than in the other cases.

Two clear peaks were detected in this region, being the first -second in the overall count- related to crystalline growth and the second -third in the overall count- associated with nucleation mechanisms and formation of new crystalline environments.

It must be remembered that in alloys C, D and E almost all the processes detected have been related to the latter type rather than to the former. This probably means that alloy F is either less amorphous in general or shows some significant proportion of crystalline environments.

5.5 Magnetic analysis

The magnetic behaviors of the final alloys were studied using thermomagnetometry and M-H curves.

5.5.1 Thermomagnetometry (TM)

The thermomagnetic measurements were carried out by means of TG-based thermomagnetometry, a technique introduced in section 3.5.2 in which a standard TG device is modified by coupling a permanent magnet to it. Details of the procedure, equipment and working conditions can be found in table 3.7.

$Fe_{90-x}Co_xB_{10}$ alloys

Figure 5.16 shows the thermomagnetic behavior for alloys C ($Fe_{80}Co_{10}B_{10}$) and D ($Fe_{45}Co_{45}B_{10}$).

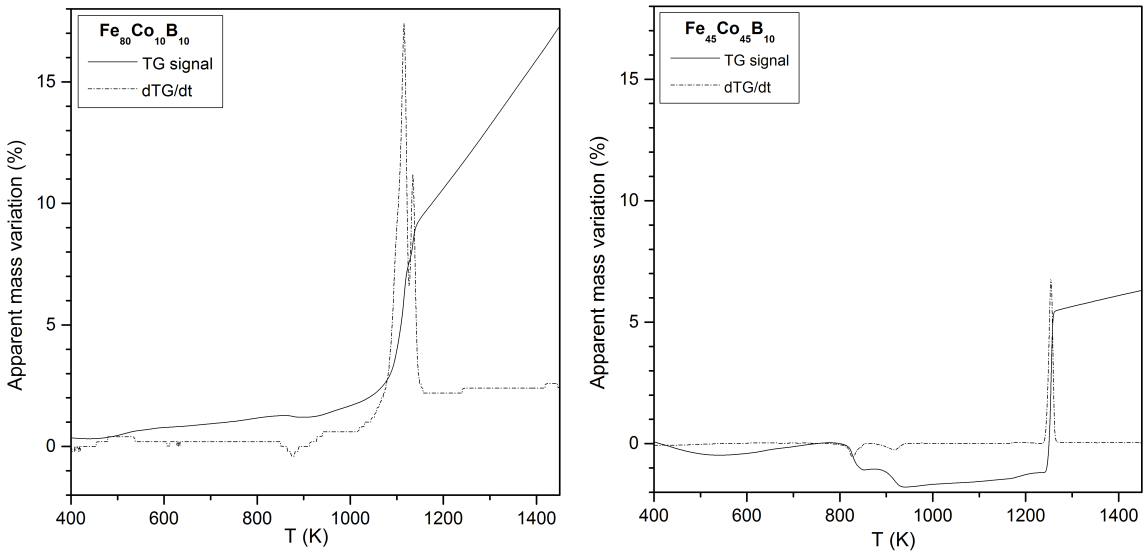

Fig. 5.16: *Thermomagnetic response for alloys C ($Fe_{80}Co_{10}B_{10}$) and D ($Fe_{45}Co_{45}B_{10}$)*

The TM curve for alloy C shows two almost overlapped transitions around 1100 K, which might probably indicate the second-order transformations from ferromagnetic to paramagnetic behavior of two different kinds of environments. This is consistent with the Mössbauer results (see 5.3.3), which showed a significantly wide distribution.

The temperatures involved, with the respective peaks located at 1119 K and 1139 K, are in agreement with the Curie temperature values reported in binary Fe-Co alloys with similar Co relative content. It is known that the Curie temperature tends to increase with the Co content, and in this range of compositions does it significantly, so it is is reasonable to deduce some heterogeneity in the alloy [285, 286].

On the other hand, the curve for alloy D shows a single narrow transition, which is consistent with the corresponding Mössbauer analysis, where the sample showed a considerable homogeneity except for a small presence of a minor phase with a paramagnetic behavior. Furthermore, the analysis also shows some small transitions in the 800-950 K region, probably due to the reordering of paramagnetic environments phase just mentioned.

$Co_{50}Fe_{30}X_{20}$ alloys

Figure 5.17 shows the thermomagnetic behavior for alloys E ($Co_{50}Fe_{30}B_{20}$) and F ($Co_{50}Fe_{30}Ni_{20}$).

The TM analysis for alloy E ($Co_{50}Fe_{30}B_{20}$) shows two narrow not-overlapped transitions, with respective peaks at 1193 K and 1275 K, with the latter being at very similar temperatures than alloy D and the former slightly shifted to lower values. This is probably due to the presence of environments with different Co content, and is in agreement with the Mössbauer results, which showed a wide distribution in hyperfine field values.

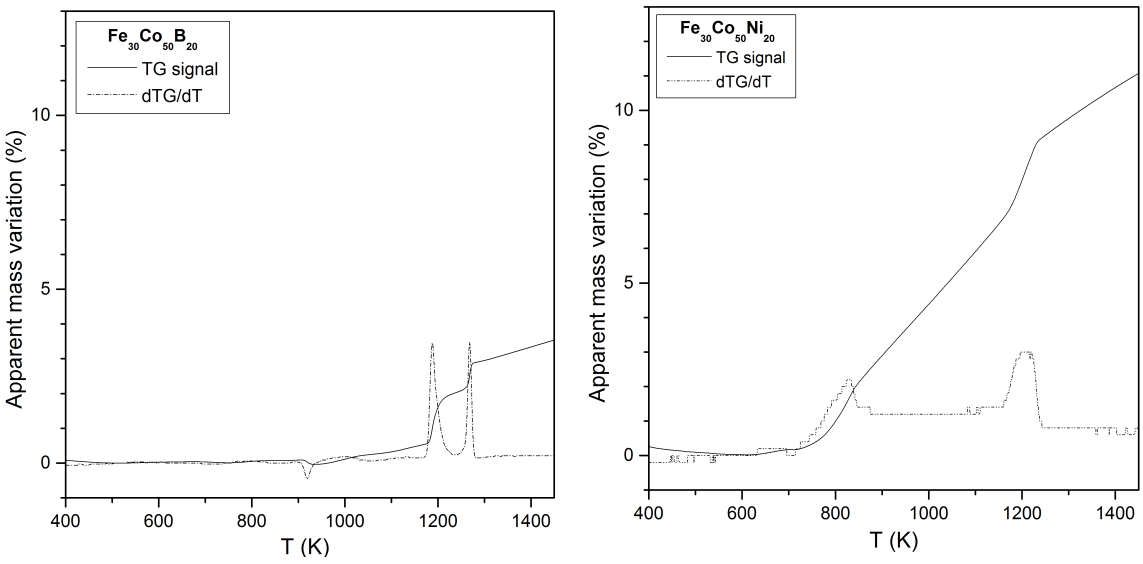

Fig. 5.17: *Thermomagnetic response for alloys E ($Co_{50}Fe_{30}B_{20}$) and F ($Co_{50}Fe_{30}Ni_{20}$)*

Furthermore, like in alloy D, a small reverse transition is detected at around 900 K, also probably due to magnetic reordering.

Lastly, alloy F shows significantly different TM results compared with the other three, surely due to the presence of Ni, which plays an important role in this difference. Two different transitions are found in this case, with their respective ending temperatures at 870 K and 1250 K, which could be associated to different sources. The first reasonable explanation for the lowest transition is that it is related to Ni-rich environments (it must be remembered that pure Ni has a significantly lower Curie temperature than pure Fe and Co). However, Mössbauer analysis showed the presence of some oxides with ferromagnetic behavior, which could also play a role in this first transition. Furthermore, both transitions showed wide curves, so denoting their heterogeneity.

5.5.2 M-H curves

Like in chapter 4, M-H curves were obtained for all four alloys after 80h of milling, with the equipment and working conditions detailed in table 3.6. The curves are shown in figures 5.18 and 5.19, with the respective magnetic parameters extracted from the hysteresis loops listed in table 5.6.

As can be seen in the figures and the table, all alloys show good soft-ferromagnetic properties. The coercivities are in the range of 30-50 Oe, which are in agreement with the literature [241, 242, 245, 247, 287–289]. The lowest value is found in the alloys with the highest Co relative content (E and F) whereas the highest is in the equiatomic case (D). The latter result is consistent with the generally reported increase in the coercivity with the cobalt relative content up to near equiatomic compositions [290–293]. For the alloys with higher Co content, however, conflicting reports can be found of both a decrease [290] and an increase [247, 253, 294], which can be explained by its widely reported strong dependence with the microstructure [240, 295]. In these cases (alloys E and

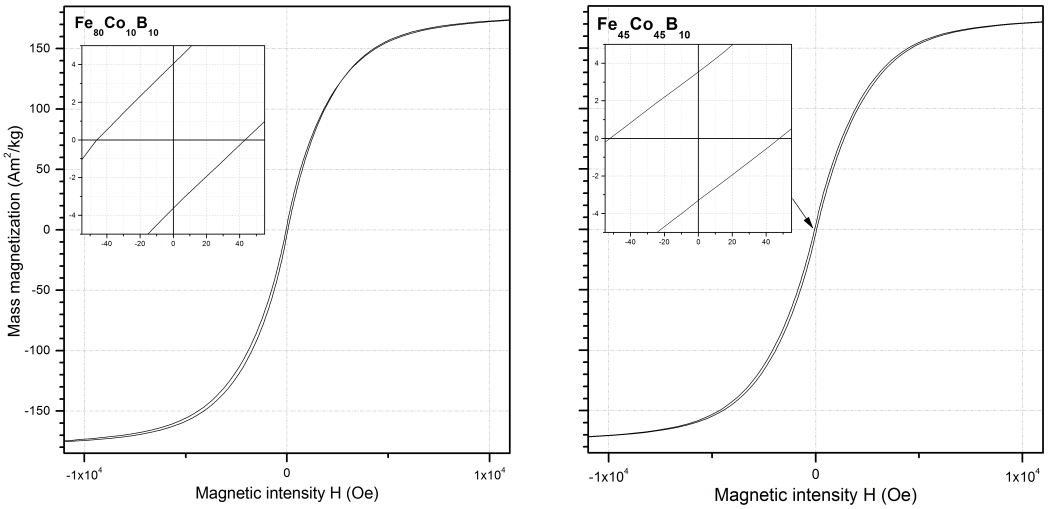

Fig. 5.18: *M-H hysteresis cycles for alloys C (left) and D (right)*

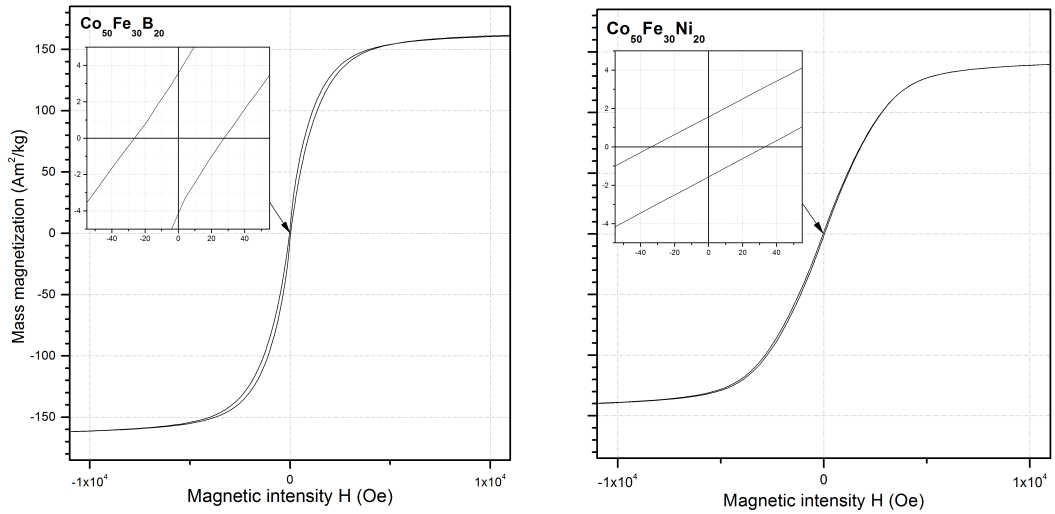

Fig. 5.19: *M-H hysteresis cycles for alloys E (left) and F (right)*

Estimated magnetic properties

	coercivity H_c (Oe)	saturation M_s (Am^2/kg)	J (T)	susceptibility χ
alloy C ($Fe_{80}Co_{10}B_{10}$)	**44**	176	1.79	670
alloy D ($Fe_{45}Co_{45}B_{10}$)	**50**	174	1.79	570
alloy E ($Co_{50}Fe_{30}B_{20}$)	**32**	161	1.75	1340
alloy F ($Co_{50}Fe_{30}Ni_{20}$)	**33**	141	1.50	400
	(±1)	(±0.01)	(±0.01)	(±10)

Tab. 5.6: *Magnetic properties estimated from the M-H loops for alloys C, D, E and F*

F), it must be taken into account the respective higher boron content, which it has been generally reported to lower the coercivity in Fe-C systems [272], and addition of Ni [296].

Regarding the saturation mass magnetization M_s, the lowest value (141 Am^2/kg) is found in the alloy with nickel (F), which is consistent with other works where its addition decreased the saturation [291, 297]. The highest values are found in the alloy with the lowest Co content (C) and also in the equiatomic case (D).

5.6 Summary

The structural analyses of all four alloys reveal an evolution of the crystalline parameters throughout the milling process following the common behavior widely reported in Fe-based MA-processed alloys: steep reduction of the crystal size and formation of a solid solution at the early stages of the milling process [247, 251].

The crystal structure observed in the three Fe-Co-B alloys (C-E) is based on the initial bcc-Fe. This is true even in the alloys with higher Co content, due to the good diffusivity of Co into Fe [244, 262, 263], a feature also found in previously reported results of either equilibrium or non-equilibrium alloys [268–272]. The boron atoms were introduced in the matrix during the milling process interstitially rather than substitutionally, with the exception of alloy E, which features a reduction of the lattice parameter with the milling time that might be an indication of part of the boron being introduced substitutionally.

The Fe-Co-Ni alloy (F), on the other hand, features a fcc structure, in agreement with its location in the ternary Fe-Co-Ni phase diagram (in figure 5.20) and with the literature [273, 274].

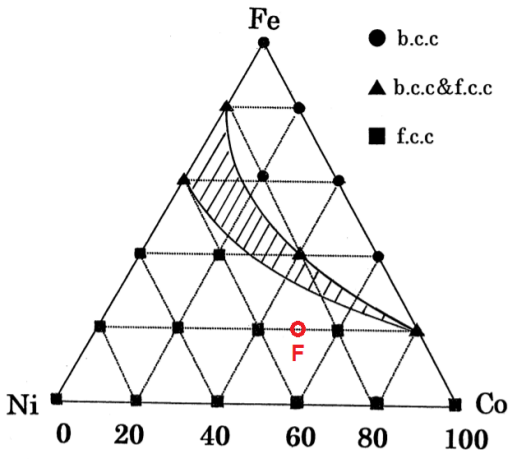

Fig. 5.20: *Phase diagram of the Fe-Co-Ni ternary system* [298]

Later stages of the milling process produced a progressive increase in the strain and further reduction of the crystal size, although the latter achieving a limit at magnitudes around few nanometers and even, in one of the alloys (F), inverting the tendency to a slight increase in the size.

The DSC analyses reveal the presence of some processes below 550 K, which can be attributed to the structural relaxation of the samples subjected to strain during the milling process, but do not show the endothermic transformation associated to the $\alpha' \rightarrow \alpha$ transition (see fig. 5.1), even in the alloys

with high Co content. It is widely known that the milling process hinders the formation of highly ordered phases.

Above 550 K, several processes are detected with a relatively wide distribution of activation energy values. The transformations with the lowest values are probably associated to the crystalline growth of the bcc-(Fe,Co) phase whereas the highest values could be explained by the formation of borides, according to the Fe-Co-B ternary phase diagram at 1200 K shown in figure 5.21.

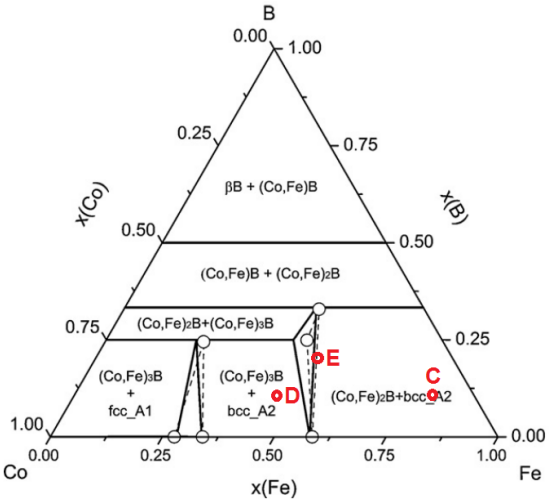

Fig. 5.21: *Calculated phase diagram of the ternary Fe-Co-B system at 1200 K* [299]

Regarding the magnetic characterization, all four alloys seem to show good soft-ferromagnetic properties with coercivities in the range of 30-50 Oe and saturations in the range of 140-180 Am^2/kg, all magnitudes consistent with those found in the literature for similar nanocrystalline alloys [241, 242, 245, 247, 287–289].

The highest coercivity is found in the equiatomic alloy and the lowest in the alloys with higher Co relative content, a behavior consistent with those find in most works [290–293] but conflicting with other reports [247, 253, 294], due to the dependence on the specific microstructure [240, 295]. The higher boron content (alloy E) and the presence of nickel (alloy F) might also add additional explanation to this enhancement in the reduction of the coercivity [272, 296].

The saturation magnetizations observed show an apparent weak dependence with the Co content, although no consistent conclusion cannot be made about this since the highest saturation values have been generally reported in alloys at around 30% Co, a content located significantly far from the compositions analyzed here. The lowest magnetization is observed in alloy F, in agreement with the widely reported decrease of the saturation with the addition of nickel [291, 297, 300, 301].

The temperatures of the main magnetic transition observed in the TM curves are in the range of 1100-1300 K, with the highest value found in the alloy with the highest Co content, in agreement with the general behavior reported [285, 286]. The alloy with nickel also shows a second magnetic transition at around 870 K related to Ni-rich environments.

6

Study of amorphous and nanocrystalline alloys produced by mechanical alloying (MA) of previously melt-spun (MS) ribbons

> *As long as the world is turning and spinning, we're gonna be dizzy and we're gonna make mistakes.*
>
> — **Mel Brooks**
> (Comedian)

Contents

Whereas chapters 4 and 5 have been focused on the production of soft-magnetic nanocrystalline powders produced by mechanical alloying (MA) from industrial precursors, this chapter deals with the production of powders by milling of previously melt-spun (MS) ribbons.

6.1 Introduction

As explained in chapter 2, melt spinning (MS) is one of the most used techniques to cast metallic glasses by rapidly cooling of molten alloys, but due to its intrinsic nature, the resulting alloys are generally limited to ribbon shapes with a maximum of 50μm [49]. This makes them not suitable for applications where a large volume of soft magnetic materials with intricate shapes is required [41, 302].

Mechanical alloying (MA) of previously melt-spun ribbons is a two-step route for the development of ferromagnetic alloys in powder form [9, 303–307]. It is widely known that this process usually can lead to a recrystallization of the previously amorphous matrix and a resulting nanocrystalline alloy [34, 49, 308, 309] in what has been often reported as a cyclic crystalline–amorphous transformation with the milling time [310–312] and thus can be considered as a suitable method for the production of both amorphous and nanocrystalline alloys, with the latter being an alternative path to the more common thermally-induced nanocrystallization [313–317].

Furthermore, there have been reported some cases of a superparamagnetic behavior in the resulting alloy due to the small particle size achieved by the milling [266, 318].

This method, however, has some shortcomings such as the limitation of the composition ranges to those of deep eutectics or the brittleness of the resulting alloys [49].

Their magnetic behavior can be improved by thermal treatments, but this often cause an unwanted further enbrittlement of the materials. In order to avoid the deterioration of their mechanical properties, recently magnetic anisotropies have been induced in amorphous magnetic ribbons by applying a magnetic field during the solidification process (field quenching technique) [319].

Co and Fe-based amorphous and nanocrystalline alloys generally show low coercivity, high magnetic permeability and zero magnetostriction [302, 320], which make them suitable for generators, sensors, actuators and power transformers [34, 321]. Some Co-based amorphous alloys also show a significant giant magnetoimpedance (GMI) effect and are candidates to be employed as a sensitive magnetic element for biosensors due to their very high sensitivity to magnetic fields [322–324].

According to the Random Anisotropy Model, introduced in section 1.3.1, when the grain size is reduced below the minimum exchange length ($D < L_{ex}$), the soft magnetic properties can be improved considerably [46, 50, 51]. The minimum exchange length in Fe-based amorphous/nanocrystalline alloys with a grain size of is around 5–20 nm is typically in the range 20–40 nm. However, the presence of regions of inhomogeneity with larger grain sizes may increase H_c and degrade the soft magnetic properties of the alloy [28].

One important variable in the control of grain size in these alloys is their chemical composition. The addition of most alloying elements generally disrupt crystallization and facilitates the creation of disordered phase by delaying the transformations [28, 325].

In the specific cases of boron and silicon, it has been widely reported that their addition to Fe-based amorphous or nanocrystalline alloys promote their glass forming ability or decrease their grain size although with the downside of reducing their magnetic saturation. The addition of silicon also improves the magnetic properties of the alloy at high temperatures. [28, 308, 326, 327].

6.2 Production of the alloys

Two Co-based and two Fe-based soft-magnetic amorphous alloys were produced in ribbon form by melt spinning (MS) and later processed by mechanical alloying (MA) for a relatively short time in order to produce samples in powder form. The composition of the alloys produced and studied are:

1. Co-based alloys:
    - Alloy G: $Co_{66}Fe_4Si_{15}B_{14}Ni_1$.
    - Alloy H: $Co_{69}Fe_4Si_{15}B_{12}$
2. Fe-based alloys:
    - Alloy I: $Fe_{80}B_{20}$
    - Alloy J: $Fe_{80}Si_{10}B_{10}$

The melt-spun ribbons (MS) were prepared by the single-rolled melt-spinning method. In this procedure, the molten alloys are quenched on the surface of a rapidly spinning copper roller, creating thin ribbon-shaped samples. The MS fundamentals and the specific details have been described previously in section 2.2.

The thickness of the resulting ribbons ranges between 25 and 130 μm and their width about 2.5 mm. An inert atmosphere (argon gas) was choosen in order to avoid undesirable reactions between the samples and the atmosphere.

For the production of the powder alloys, a fraction of these ribbons were cut into small pieces about 1 cm large and subsequently processed by MA (see section 2.1 for details) in a planetary ball mill under the milling conditions listed in table 6.1.

Several runs were executed with different milling times and the milled ribbons (now in powder form) sieved with a 50 μm mesh sieve after every single run until the proportion above this value was approximately lower than 5%. Figures 6.1 and 6.2 show SEM micrographs of the final alloys.

MS+MA milling conditions	
mill model	Fritsch Pulverisette 7 (see fig. 2.7)
type of mill	planetary ball mill
containers	hardened stainless steel vials (18% Cr, 10% Ni)
balls	same material as vials
raw materials	MS ribbons previously produced by the single-rolled melt-spinning method, cut into small pieces of ≈1 cm
milling atmosphere	Ar
process control agents (PCA)	1 ml of cyclohexane (C_6H_{12})
quantity of material to process	8 g
ball-to-powder mass ratio (BPR)	5:1
milling speed	700 rpm
milling times	variable
operation program	45-minute cycles (30 min running + 15 min pause) alternating clockwise and counter-clockwise rotation
procedure	The vials with the samples inside were placed in a vacuum vessel and then refilled with the argon gas. The procedure was repeated 3 times and the containers subsequently sealed with Teflon.

Tab. 6.1: *Milling conditions for the production of the MS+MA samples of alloys G, H, I and J*

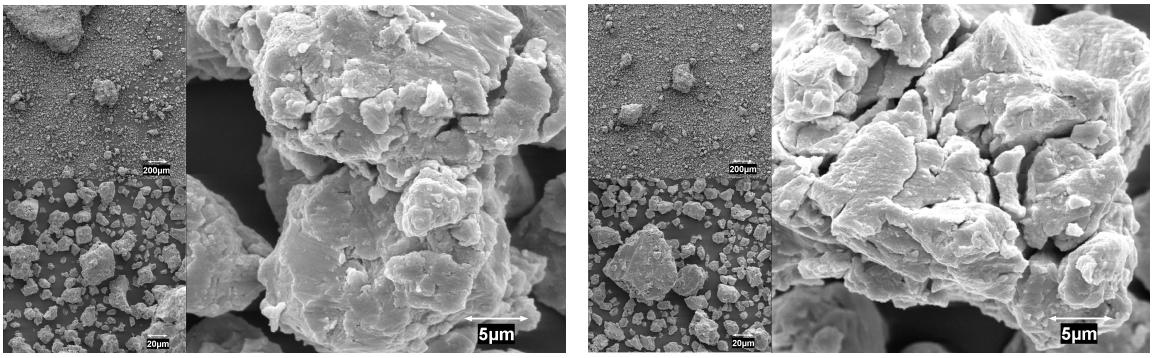

Fig. 6.1: *SEM micrographs of samples of the Co-based alloys after the MS+MA process. L: alloy G ($Co_{66}Fe_4Si_{15}B_{14}Ni_1$). R: alloy H ($Co_{69}Fe_4Si_{15}B_{12}$).*

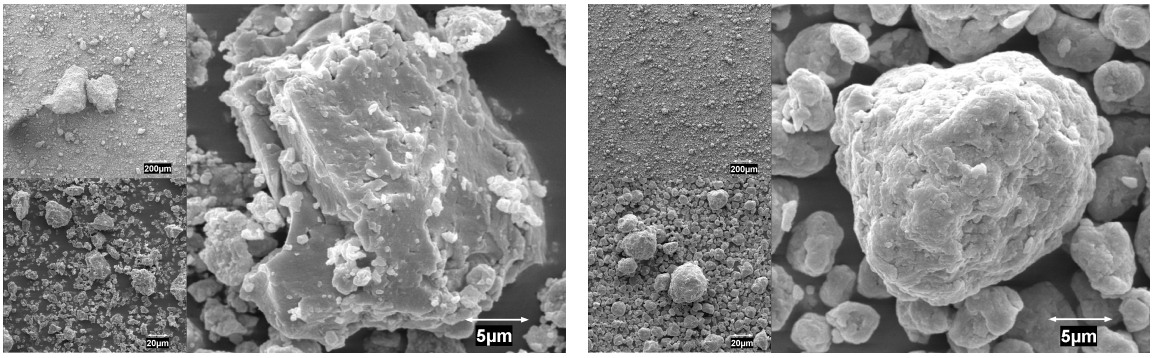

Fig. 6.2: *SEM micrographs of samples of the Fe-based alloys after the MS+MA process. L: alloy I ($Fe_{80}B_{20}$). R: alloy J ($Fe_{80}Si_{10}B_{10}$).*

As explained above, in addition to the MS ribbons and the MS+MA powders, an additional set of samples with identical compositions were produced directly by MA from industrial powders for comparison purposes. The milling processes were carried out in a Reitz PM400 planetary ball mill under the conditions shown in table 6.2.

MA milling conditions	
mill model	Reitz PM400 (see fig. 2.7)
type of mill	planetary ball mill
containers	Cr-Ni steel (18% Cr, 10% Ni)
balls	Cr-Ni steel (18% Cr, 10% Ni)
raw materials	Industrial powders of pure elemental B, Si, Fe, Co and Ni in stoichiometric proportions. Purity was >99% in all cases
milling atmosphere	Ar
process control agents (PCA)	1 ml of cyclohexane (C_6H_{12})
quantity of material to process	12 g
ball-to-powder mass ratio (BPR)	4:1 (7 balls of ≈7 g each)
milling speed	400 rpm
milling times	20, 50 and 80h
operation program	45-minute cycles (30 min running + 15 min pause) alternating clockwise and counter-clockwise rotation
procedure	The vials with the samples inside were placed in a vacuum vessel and then refilled with the argon gas. The procedure was repeated 3 times and the containers subsequently sealed with Teflon.

Tab. 6.2: *Milling conditions for the production of the MA samples of alloys G, H, I and J*

6.3 Analysis of the Co-based alloys

The structural, thermal and magnetic characterization of the alloys were analyzed using X-ray diffraction (XRD), differential scanning calorimetry (DSC) experiments and M-H hysteresis cycles, respectively. The specific equipment and working conditions have been previously detailed in the respective sections of chapter 3.

6.3.1 XRD analysis

Figure 6.3 shows the XRD patterns for the Co-based MS+MA powder alloys (G and H) and a comparison with the unmilled MS ribbons and the MA powder alloys.

A quick and general look to the figure shows that the patterns of the MS+MA powders seem to look much closer to those of the MS ribbons rather than to the MA powders, according to the following observed features:

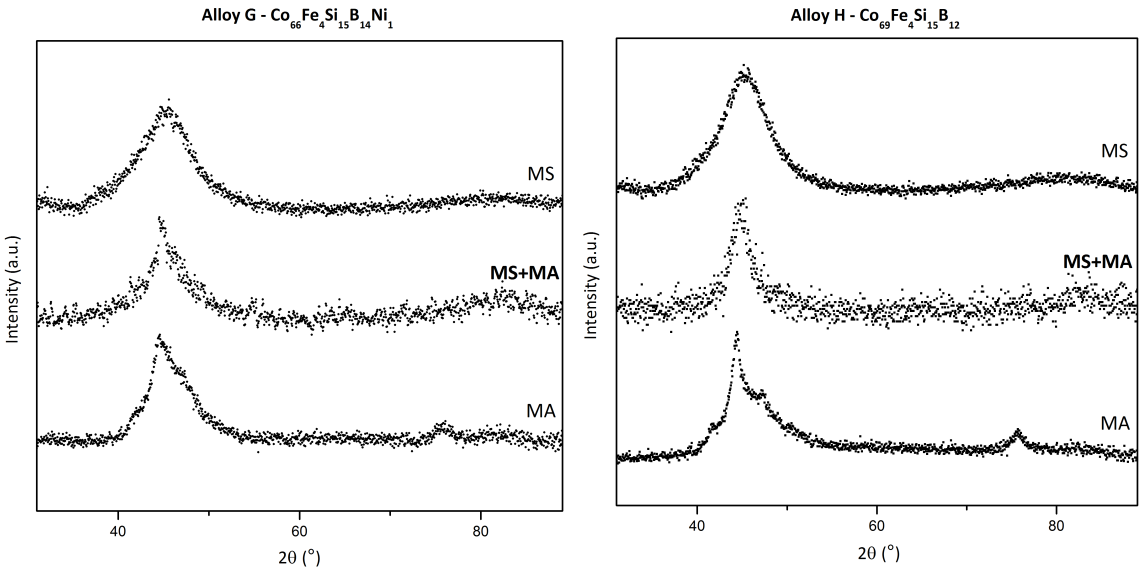

Fig. 6.3: *XRD spectra for MS+MA powder alloys G and H (middle) and comparison with the respective unmilled MS ribbons (top) and the MA powders (bottom).*

- The main peaks in the MS+MA cases look flatter than in the MA cases, where they are relatively sharp.
- The secondary peaks featured in the MA powders (at about 40, 50 and 75°) are not detected in the MS+MA counterparts.
- Typical secondary curves of patterns from amorphous materials are found, beyond 80°, in both the MS ribbons and MS+MA powders but not in the MA counterparts.

Although all these features seem to indicate that the MS+MA powders are mostly amorphous rather than nanocrystalline, it must be also taken into account that:

- The main peaks look significantly sharper than in the MS case, a possible indication of a certain degree of crystallization.
- A significant level of noise found in the MS+MA patterns (due to the low amount of material available for the analyses), which could have been hiding the presence of the undetected secondary peaks.

This introduces a significant uncertainty which do not allow the correct determination of the specific structure and forces the need for further experiments. The determination of the activation energies by DSC, for example, allows the identification of crystalline growth or nucleation processes and the possible structure from which is produced..

6.3.2 DSC analysis

DSC experiments were performed for each alloy under the three different processing paths. Several different constant heating rates were used in order to estimate the activation energies of the main transformations detected. The estimations have been carried out using again the Kissinger method

(see section 3.4.2) and are listed in table 6.3, with the DSC curves used shown in figure 6.4. As can be seen, some values -specially those of the MS alloys- show notably wide error bars due to some difficulties found in the exact determination of the peak temperatures along with a low number of experiments carried out. The magnitudes found, however, can be considered suitable for the main purpose of a simple comparison between the processing paths.

Estimated activation energies

processing method	temperature range (K)	activation energy E (kJ/mol)	R^2
alloy G ($Co_{66}Fe_4Si_{15}B_{14}Ni_1$)			
MS+MA	830 - 850	**490** ± 5	0.999
only MS	820 - 840	590 ± 10	0.998
only MA	790 - 825	330 ± 30	0.995
alloy H ($Co_{69}Fe_4Si_{15}B_{12}$)			
MS+MA	1070 - 1090	**550** ± 10	0.999
only MS	825 - 835	800 ± 150	0.941
only MA	790 - 830	290 ± 10	0.997

Tab. 6.3: *Estimated activation energies for alloys G and H under different processing methods*

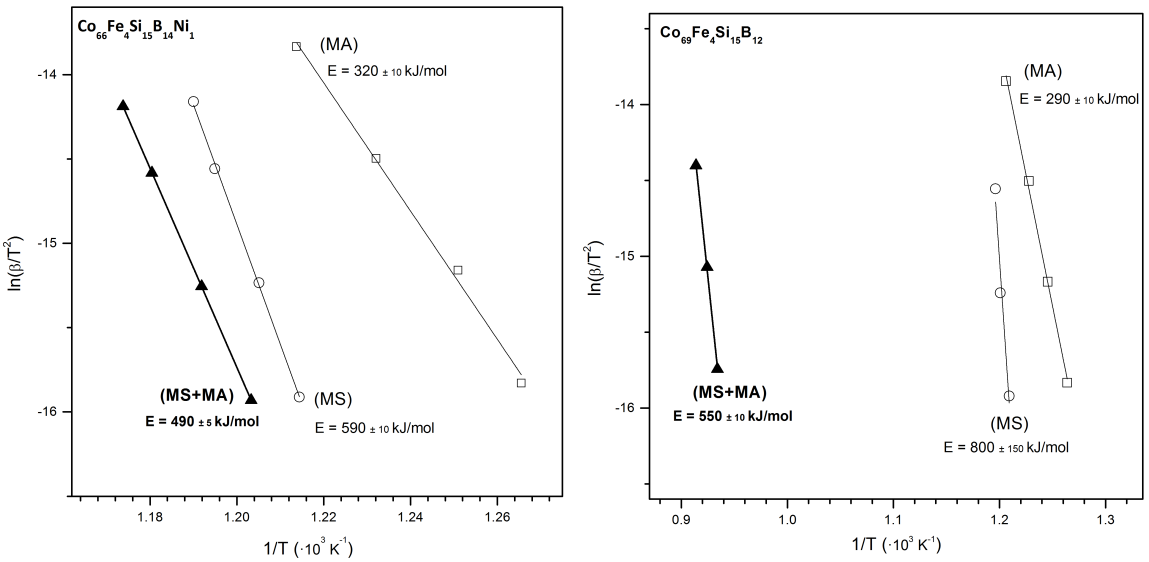

Fig. 6.4: *Kissinger plots for alloys G (left) and H (right)*

According to the estimated values, the highest activation energies are found in the MS alloys whereas the lowest are in the MA alloys, both results unsurprising and in agreement with the XRD results that revealed an amorphous structure for the former and a nanocrystalline one for the latter. The magnitudes estimated for alloy G seem to agree perfectly with the literature in both the amorphous MS [328] and the nanocrystalline MA [329] cases. In alloy H, the estimated value for the MS case is significantly higher than expected, although the extremely wide error bar -probably for the reasons mentioned above- includes values more in agreement.

The energy values for the MS+MA cases are significantly higher than their MA counterparts but still lower than the MS cases, which could be an indication of at least partial recrystallization of the alloys. It must be remember that the XRD spectra did not show a clear figure of either an amorphous or nanocrystalline structure, due to the high amount of noise in the signals. Alloy H shows a slightly higher energy value, probably due to its lower relative Fe-Co ratio. It has been reported that the clustering of Fe atoms can lower the potential barrier for nucleation and thus decrease the activation energy of crystallization [312].

6.3.3 Magnetic properties

The magnetic behaviors of the final powders have been studied by analyzing their respective M-H cycles, which are shown in figures 6.5 and 6.6.

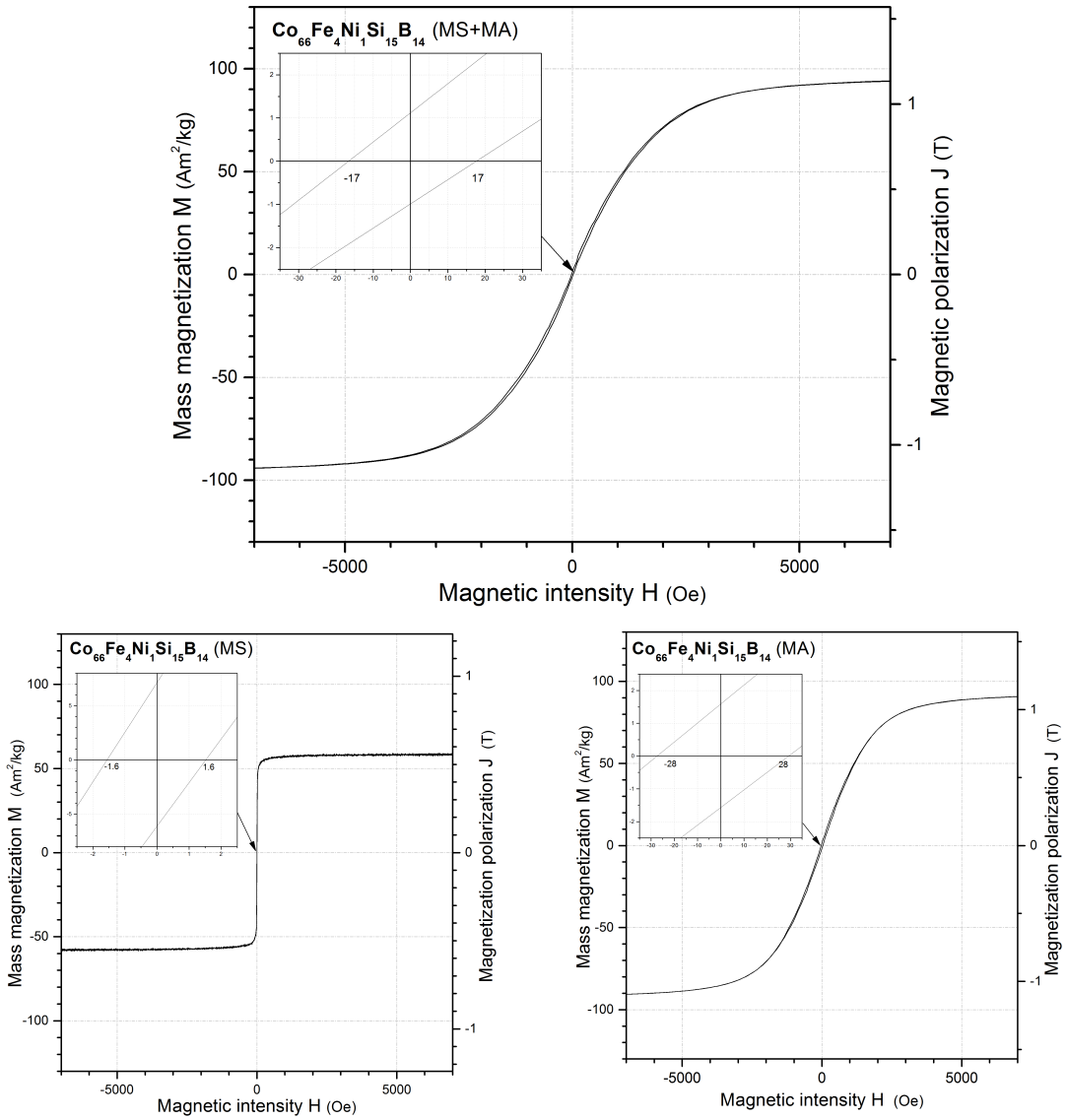

Fig. 6.5: *M-H hysteresis cycle for alloy G after the MS+MA process (top) and comparison with the unmilled MS ribbon (bottom left) and the MA-produced powder (bottom right)*

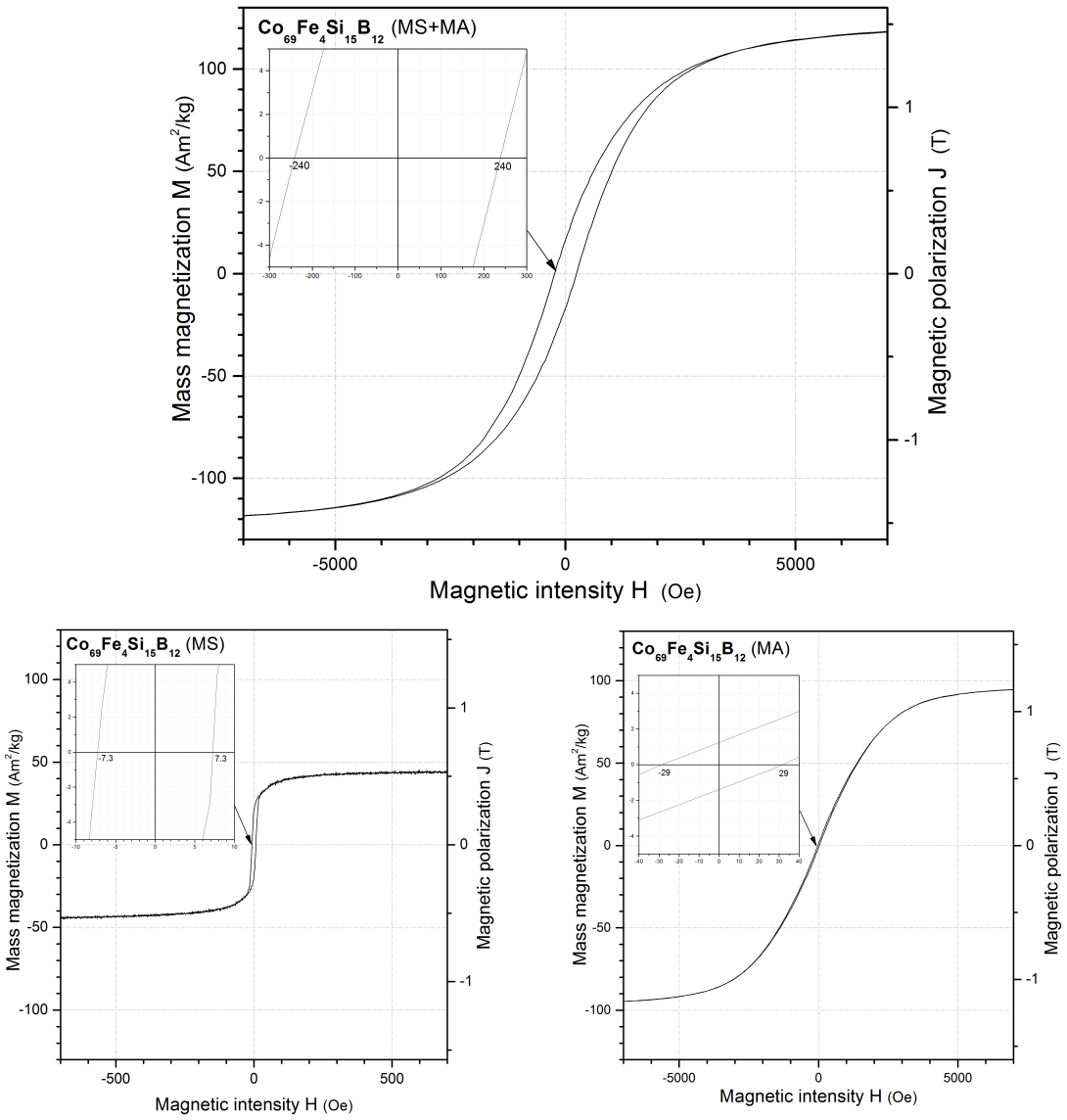

Fig. 6.6: *M-H hysteresis cycle for alloy H after the MS+MA process (top) and comparison with the unmilled MS ribbon (bottom left) and the MA-produced powder (bottom right)*

Like in the alloys studied in chapters 4 and 5, the analysis of the hysteresis loops allows the estimation of their respective magnetic properties, listed in table 6.4.

As can be seen in the table and the figures, the MS+MA alloys show magnetic properties closer to those of the MA alloys rather than to the unmilled MS ribbons.

- Coercivity H_c: All the milled alloys (MS+MA and MA) show higher coercivity than their unmilled MS counterparts, a commonly found behavior [302] which can be attributed to the increase in the internal strain and the absence of the grain boundary amorphous phase due to the milling process [318], both weakening the ferromagnetic exchange interaction between the nanograins.

Estimated magnetic properties			
	coercivity	magnetic saturation	
	H_c (Oe)	M_s (Am^2/kg)	J_s (T)
alloy G ($Co_{66}Fe_4Ni_1Si_{15}B_{14}$)			
MS+MA	**17**	**95**	1.16
MS	1.6	58	0.55
MA	28	92	1.12
alloy H ($Co_{69}Fe_4Si_{15}B_{12}$)			
MS+MA	**240**	**122**	1.51
MS	7.3	45	0.57
MA	50	97	1.21

Tab. 6.4: *Magnetic properties estimated from the M-H loops for alloys G and H*

Nevertheless, different trends are observed in the two compositions, with the MS+MA case of alloy G showing a lower value of the coercivity compared with its MA counterpart whereas alloy H featuring a significantly higher magnitude. The latter could be explained by a possible excessive grain growth due to the milling process, according to the D^6 dependence explained in chapter 1 (see figure 1.8 of section 1.3. A deeper XRD refinement should confirm or deny this, but due to the low amount of material available, this refinement has been proved unachievable, as explained in section 6.3.1.

- Saturation: The saturation magnitudes found in the milled alloys are in agreement with the literature [330] and, as expected, stand in significantly higher figures than their unmilled MS counterparts, which also show values in agreement with those reported from other amorphous alloys with the same compositions [331–333].

  The MS+MA cases seem to show an improvement compared to their MA counterparts, although the difference is only slight in alloy G.

6.4 Analysis of the Fe-based alloys

Like in the previous Co-based group, the Fe-based alloys have been also analyzed by XRD, DSC and M-H experiments.

6.4.1 XRD analysis

Figure 6.7 shows the XRD patterns for the Fe-based powder alloys (I and J). Like in the previous cases, the MS+MA curves show again a high degree of noise due to the low amount of material available for the XRD experiments.

The XRD patterns for these Fe-based alloys reveal a different behavior compared with the previous patterns observed for the Co-based alloys:

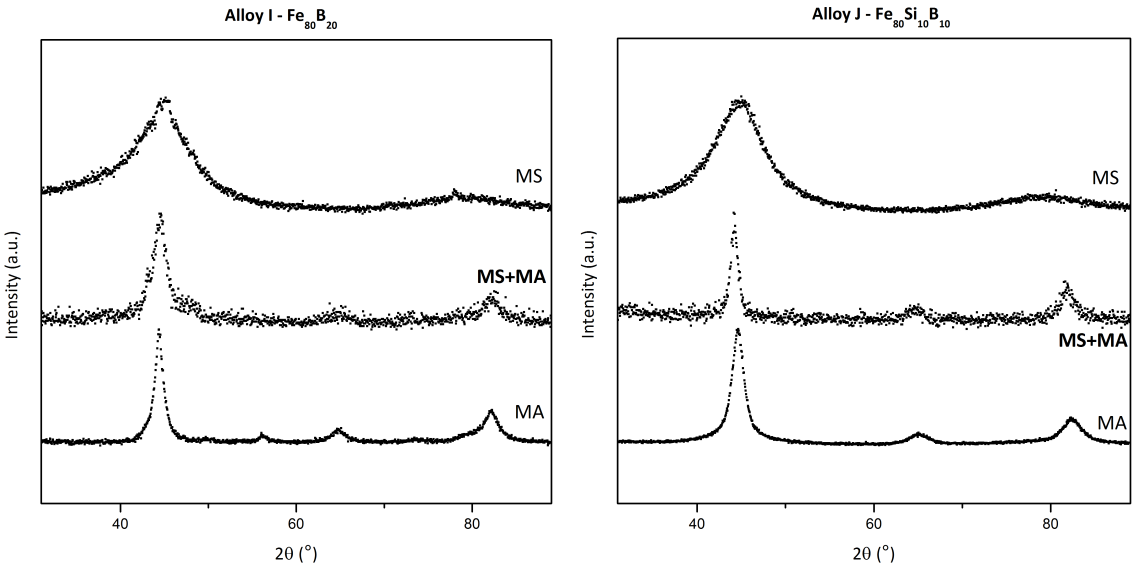

Fig. 6.7: *XRD patterns for the MS+MA powder alloys I and J (middle) and comparison with the respective unmilled MS ribbons (top) and the MA powders (bottom) counterparts.*

1. The shapes of the MS+MA peaks are closer to those of the nanocrystalline powders processed by MA rather than those of the amorphous ribbons processed by MS. Not only the primary peaks are sharper but also the secondary are clearly visible.

2. the peaks that appear in the MS pattern beyond the 80°, which correspond to the secondary neighbors of an amorphous pattern, are not shown here.

For all these reasons, the conclusion is that there is a significant degree of crystallization, enough for considering these alloys as nanocrystalline rather than amorphous.

6.4.2 DSC analysis

Like in the previous Co-based alloys, the Kissinger method was also used for the estimation of the activation energies of the Fe-based alloys, with the graphs shown in figure 6.8 and the results in table 6.5.

The estimated values of the activation energies for alloys I and J show notably lower values than in alloys G and H, probably due to being Fe-based alloys instead of Co-based.

Alloy J ($Fe_{80}Si_{10}B_{10}$) seems to follow the commonly reported behavior of a reduction in the thermal stability of the milled MS+MA powders compared to the unmilled MS ribbons due to the plastic deformation of the amorphous alloys induced by the milling process [334].

Alloy I ($Fe_{80}B_{20}$), however, shows the opposite, a behavior also found in other works involving low-energy milling of $Fe_{80}B_{20}$ ribbons [335].

Again, the highest activation energies are found in the MS samples and the lowest in the MA cases, with the alloys processed by the combined MS+MA method showing values generally averaging the other two.

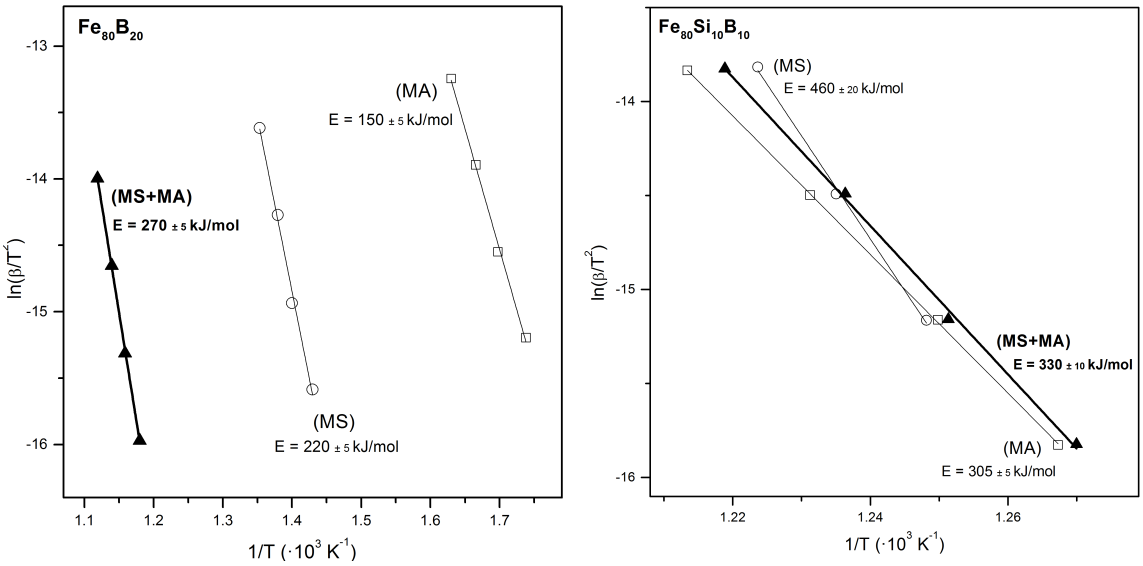

Fig. 6.8: *Kissinger plots for alloys I (left) and J (right)*

Estimated activation energies

processing method	temperature range (K)	activation energy E (kJ/mol)
alloy I ($Fe_{80}B_{20}$)		
MS+MA	845 - 895	**270** ±5
MS	700 - 740	220 ±10
MA	575 - 615	150 ±5
alloy J ($Fe_{80}Si_{10}B_{10}$)		
MS+MA	785 - 820	**330** ±10
MS	800 - 820	460 ±20
MA	790 - 825	305 ±5

Tab. 6.5: *Estimated activation energies for alloys I and J*

6.4.3 Magnetic properties

Like in the Co-based alloys, the magnetic properties of the Fe-based alloys have been also estimated by analyzing their respective M-H cycles (figures 6.9 and 6.10), with the results listed in table 6.6.

As can be seen in the figures and the table, the coercivity of the MS+MA powders are not only significantly higher than those of the unmilled MS ribbons but also even higher than their MA counterparts.

The higher coercivity of the milled alloys can be attributed to the increase in the internal strain and the absence of the grain boundary amorphous phase due to the milling process [318], both weakening the ferromagnetic exchange interaction between the nanograins.

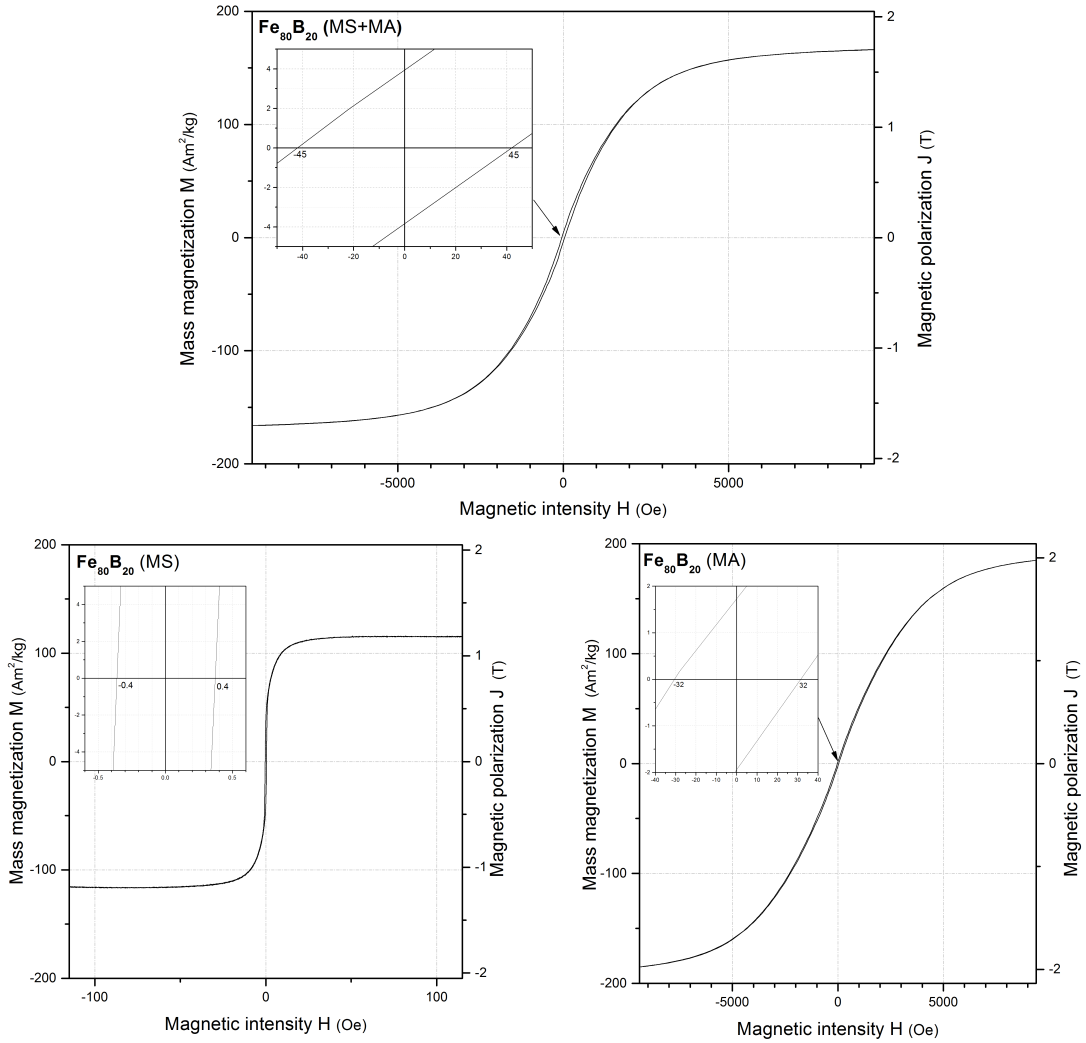

Fig. 6.9: *M-H hysteresis cycle for alloy I after the MS+MA process (top) and comparison with the unmilled MS ribbon (bottom left) and the MA-produced powder (bottom right)*

Estimated magnetic properties			
	coercivity	magnetic saturation	
	H_c (Oe)	M_s (Am^2/kg)	J_s (T)
alloy I ($Fe_{80}B_{20}$)			
MS+MA	**45**	**168**	1.72
MS	0.4	115	1.23
MA	32	193	1.95
alloy J ($Fe_{80}Si_{10}B_{10}$)			
MS+MA	**43**	**151**	1.60
MS	10	119	1.26
MA	25	176	1.87

Tab. 6.6: *Magnetic properties for alloys I and J, estimated from the respective M-H loops*

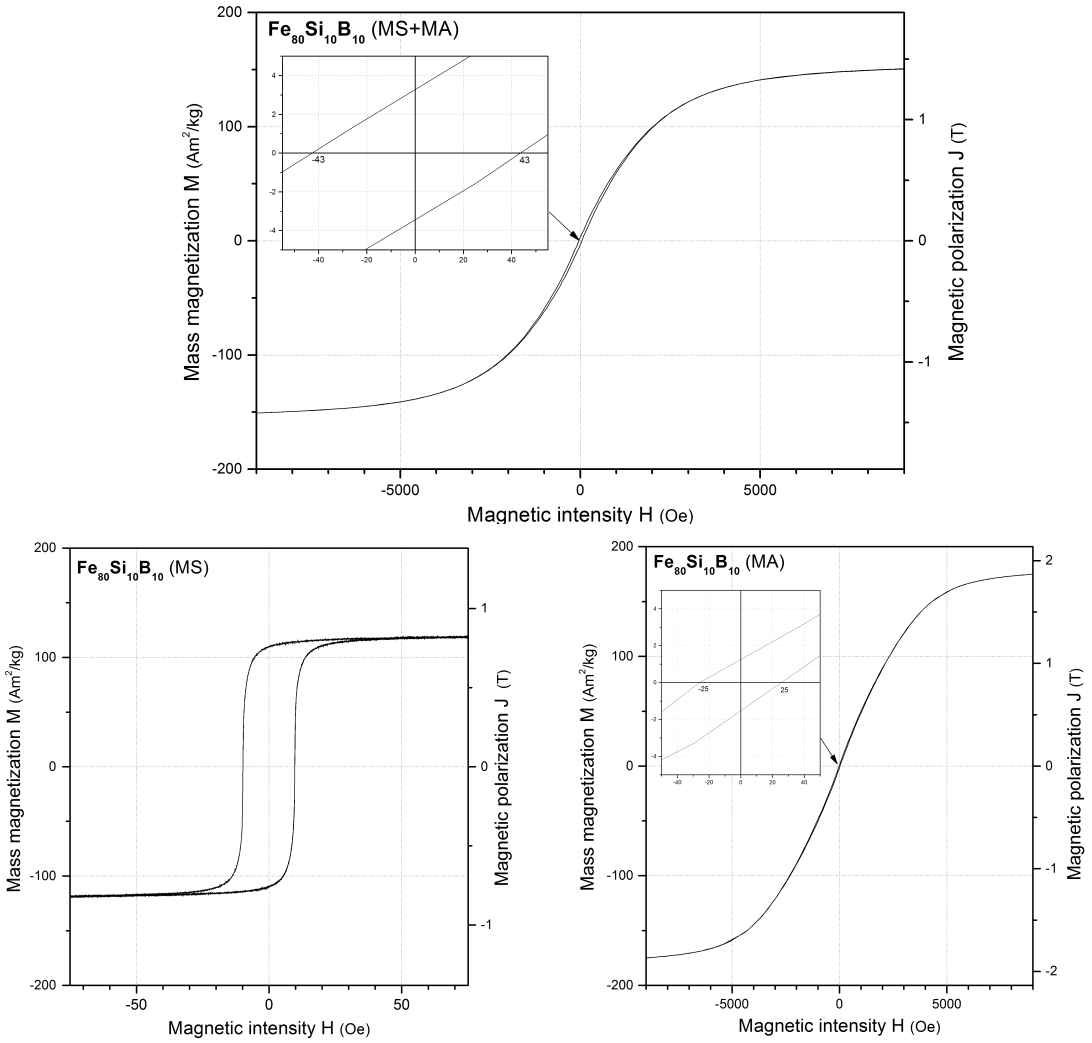

Fig. 6.10: *M-H hysteresis cycle for alloy I after the MS+MA process (top) and comparison with the unmilled MS ribbon (bottom left) and the MA-produced powder (bottom right)*

On the other hand, the saturation magnitudes are noticeable higher than in the MS ribbons, although they are still slightly lower than those found on the respective alloys processed directly by MA.

6.5 Summary

The structural and thermal analyses of the MS+MA alloys show significant differences between the Co-based and Fe-based alloys. Whereas the first group seem to retain some of the amorphous characteristics of their MS precursors and show only partial crystallization, the latter feature clear nanocrystalline properties [134, 266, 267, 328, 329].

All alloys (except the specific case of alloy H, discussed below) show soft magnetic properties but with the magnitudes involved closer to those found in MA processed powders (either when compared to the MA alloys of this study or to other reported works from the literature [241, 242, 245, 247, 287–289, 302]) rather than to their MS precursors. This can be explained by the increase in the internal strain due to the milling process [318], revealing that the milling process has indeed affected the resulting magnetic structure. In the Fe-based alloys, both the coercivity and the magnetic saturation are slightly inferior in comparison with the alloys processed directly by MA.

In the Co-based pair, alloy H ($Co_{69}Fe_4Si_{15}B_{12}$) features an unexpectedly high value of the coercivity after the milling process, with an order of magnitude of difference compared to alloy G ($Co_{69}Fe_4Si_{15}B_{12}$). This could reveal a possible excessive grain growth produced during the milling process, either due to the characteristics of the alloy itself or to the milling conditions used.

Much smaller differences have been found between the coercivities of the Fe-based pair of alloys, even though the MS precursors from which the powders were produced showed indeed values one order of magnitude apart. On the other hand, the saturation magnitudes, which were almost identical in both MS precursors, achieved a slightly higher value in the alloy without silicon content.

Figure 6.11 shows a visual comparison of the magnetic properties of all alloys, with the coercivity in the horizontal axis and the saturation in the vertical. An optimal soft ferromagnetic alloy should be located the closest possible to the upper left corner (low coercivity and high saturation).

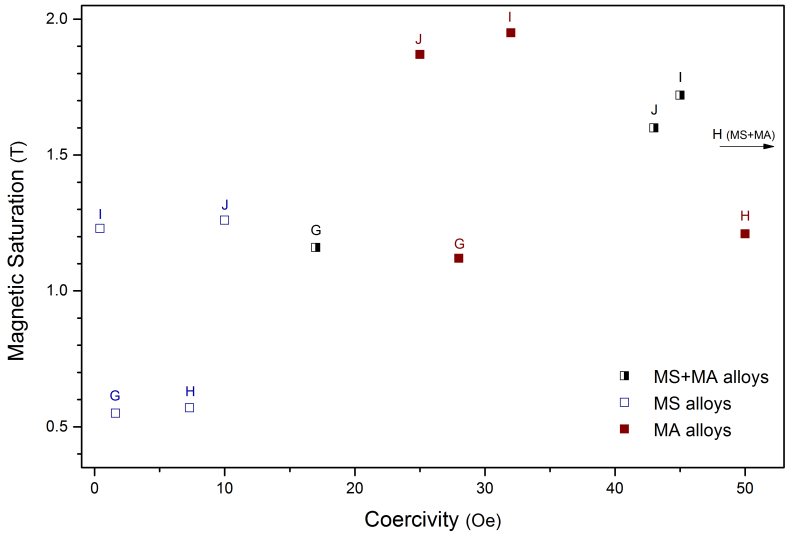

Fig. 6.11: *Comparison of the magnetic properties of alloys G-J.*

As can be seen in the graph, the MS ribbons feature the lowest coercivities but their magnetizations are generally lower than their powder counterparts. The milled ribbons (MS+MA) are in general shifted to the right (higher coercivities) compared to their MA counterparts, except in the particular case of alloy G, where the milled ribbons seems to feature lower coercivity and higher saturation.

7

Analysis of the effects of the application of a magnetic field during the MS quenching process

> *Do not quench your inspiration and your imagination; do not become the slave of your model.*
>
> **— Vincent Van Gogh**
> (Artist)

Contents

This chapter deals with the analysis of some specific samples of the alloys introduced in chapter 6 which were produced by MS under the presence of an external magnetic field during the quenching process. The study is focused on the anisotropy induced by this method and its subsequent effects on the properties of the resulting alloys.

7.1 Introduction

As explained in chapter 1, a low magnetic anisotropy is generally desired for the achievement of good soft magnetic properties. However, some magnetic anisotropies are interesting for specific applications related to the development of certain magnetic devices [336]. In amorphous alloys, their characteristic lack of long-range periodicity carries an almost zero magnetocrystalline anisotropy and, consequently, magnetoelastic and shape anisotropies, associated to the internal stresses produced during the fabrication process, are the main sources of magnetic anisotropy [337, 338]

In MS ribbons, one particular case is the presence of magnetic anisotropy in the direction transverse to the ribbon length, an interesting property for the development of magnetostrictive transducers [339]. This specific magnetic anisotropy can be induced in many ways such as annealing under the presence of an external magnetic field or stress [188, 340, 341], but this often leads to a decline in the soft-magnetic properties [342].

This can be avoided by forcing the presence of this magnetic field during the quenching process itself [319], a process commonly named *field quenching* (*fq*). It is known that the evolution of the melt during the fabrication process influences the resulting anisotropy of the material [343, 344]. The external magnetic field may produce slight displacements of the magnetic atoms or either determine the direction of bonding with their neighbors, even after considering the significantly short time the field is really acting during the cooling of the melt [338]. Therefore, it is expected to detect certain differences in the structural characterizations of the samples produced with and without this applied field, although their effects in the respective final properties might or might not be significant.

In order to test this method and their possible effects in the final properties of the alloys, some of the MS ribbons of two of the alloys of the previous chapter (alloy G, $Co_{66}Fe_4Si_{15}B_{14}Ni_1$, and alloy I, $Fe_{80}B_{20}$) were produced under the presence of a transverse 0.07 T magnetic field on the rotating wheel during the solidification process itself. The applied field was produced by an electromagnet incorporated into the vacuum chamber of the melt spinning device.

7.2 Determination of the magnetic anisotropy induced by the field-quenching process

As mentioned above, the production of the alloys under the presence of the transverse magnetic field is expected to induce the presence of some magnetic anisotropy which would produce some changes in the structural properties of the alloys.

DSC analysis

Figures 7.1 and 7.2 show DSC experiments performed on samples of alloy G ($Co_{66}Fe_4Si_{15}B_{14}Ni_1$) and I ($Fe_{80}B_{20}$), respectively. Two different samples were used for each alloy, one of them quenched under the presence of an external magnetic field (fq) and the other without it (aq).

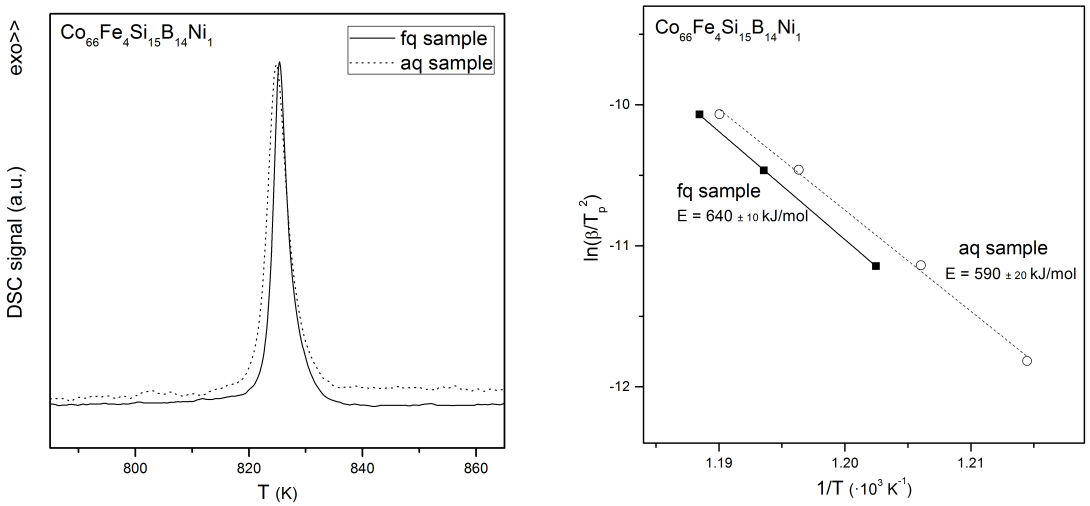

Fig. 7.1: *Comparison of the DSC curves (left) and activation energies (right) between samples of alloy G produced with (fq) and without (aq) the presence of an external magnetic field.*

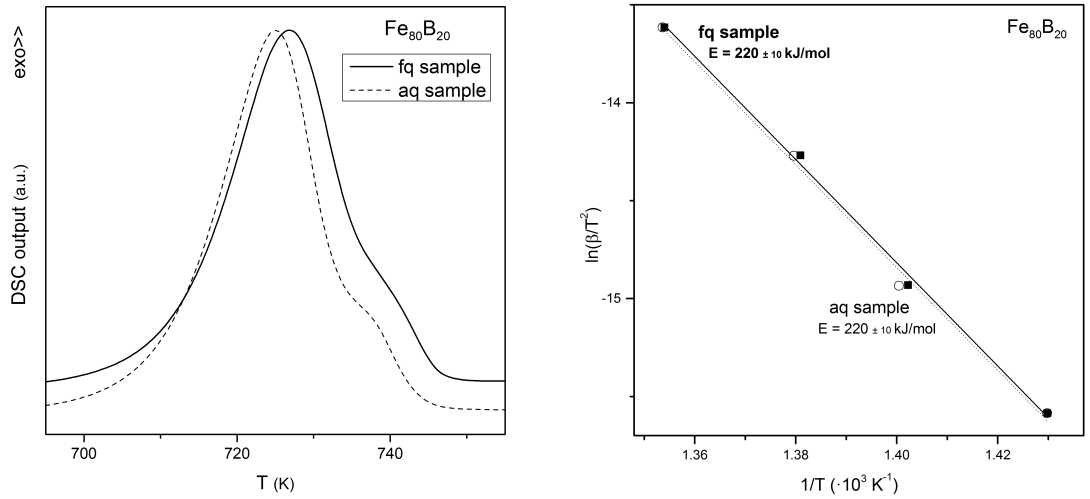

Fig. 7.2: *Comparison of the DSC curves (left) and activation energies (right) between samples of alloy I produced with (fq) and without (aq) the presence of an external magnetic field.*

As can be seen, the two DSC curves feature a relatively similar main crystallization peak with both the peak positions and the enclosed area having almost identical magnitudes in all cases.

However, different behaviors are observed between the two alloys when analyzing the respective estimations of the activation energies. Whereas in alloy G the fq sample features a significantly higher (50 kJ/mol) value than the aq sample, this difference is not observed between the samples of alloy I.

The difference detected in the Co-based alloy can be considered a likely indication of the magnetically induced anisotropy mentioned above, since its presence would expect the alloy to require additional energy for the reordering. For the Fe-based alloy, on the other hand, no conclusion can be made for the moment, requiring further complementary experiments, shown below.

TMS analysis

Due to these unexpectedly unclear results obtained in the DSC experiments performed on the samples of alloy I, a complementary TMS analysis was carried out for this particular Fe-based alloy, in order to get more detailed information about the possible presence of the induced anisotropy based on the differences on local electronic or atomic structure.

For the study, several TMS experiments were performed for both samples with the goal of estimate the spin relative number in each of the three axes:

N_x spin relative number in the x-axis, the direction corresponding to the *width* of the ribbon. This is also the direction of the external field applied during the quenching.

N_y spin relative number in the y-axis, the direction corresponding to the *length* of the ribbon.

N_z spin relative number in the z-axis, the direction corresponding to the *thickness* of the ribbon.

These individual relative numbers can be estimated by combining the information acquired by three independent measurements performed under different geometrical arrangements. The specific configurations used are based on a well-known procedure easily found in the literature [345, 346], with the respective settings shown in figure 7.3.

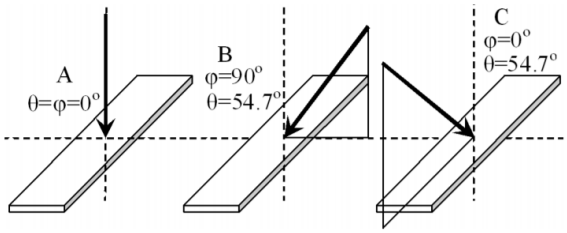

Fig. 7.3: *Geometrical arrangements used for the TMS experiments*[346].

As can be seen in the figure, two different angles were modified: angle θ, which is the angle of the beam with the z axis, and ϕ, which is the angle with the x axis.

1) $\theta = 0$, $\phi = 0$

2) $\theta = 54.7$, $\phi = 0$

3) $\theta = 54.7$, $\phi = 90°$

Figure 7.4 show the respective TMS spectra obtained under this three different settings for both the sample produced with the presence of the magnetic field (fq) and without it (aq).

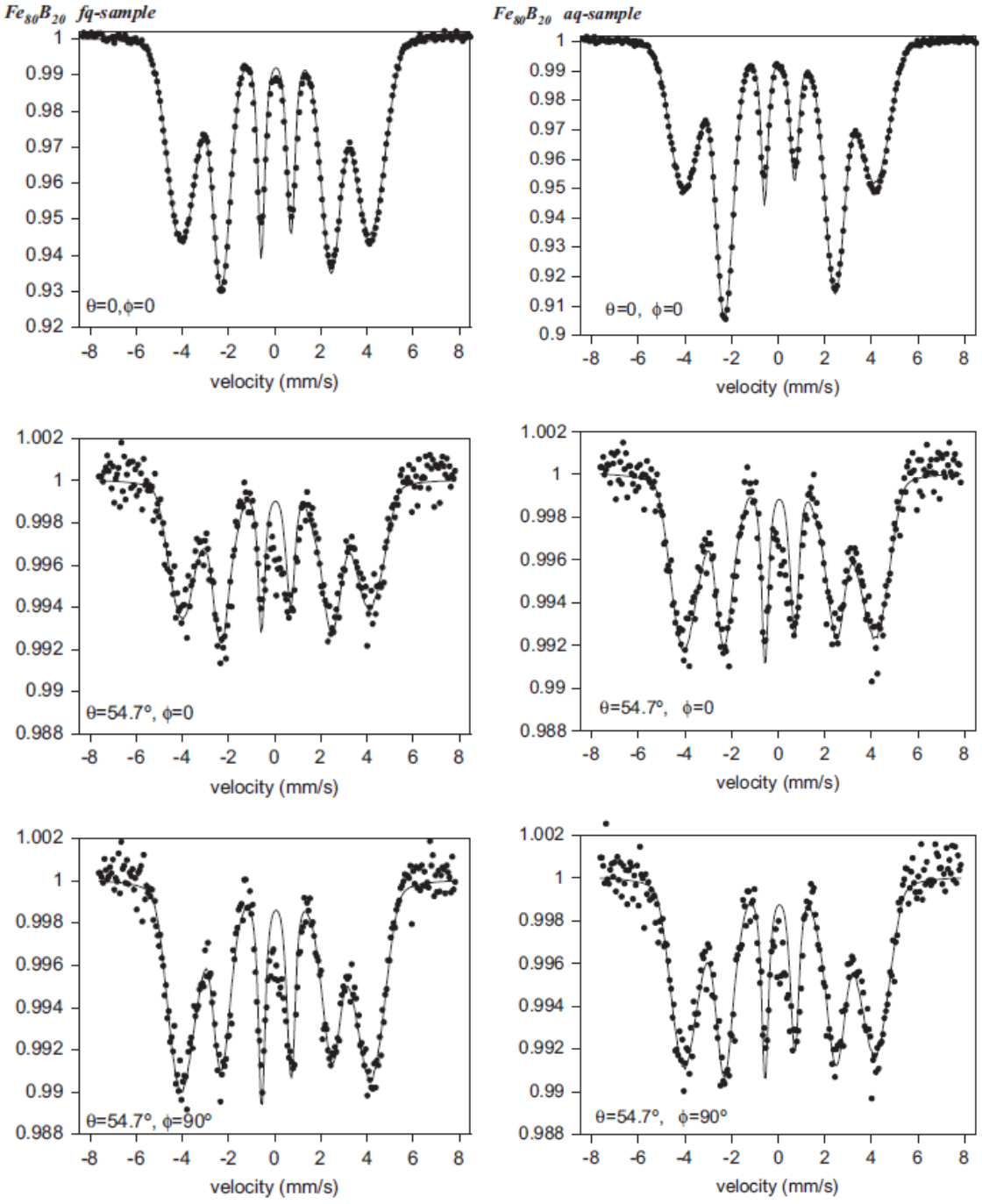

Fig. 7.4: *Comparison of the TMS of alloy I quenched with (left) and without (right) the presence of the external magnetic field.*

As can be seen in the graph, a simultaneous increase in the outermost peaks and a decrease in the second peaks are observed when comparing between the relative intensities of the different θ and ϕ configurations. The spin density values N_x, N_y and N_z were computed from the ratio between the intensities of the respective second and third Mössbauer lines in each of these angular configurations, with the estimated values listed in table 7.1.

Spin density anisotropy			
Sample	N_x	N_y	N_z
fq sample	48 ± 2	45 ± 1	6 ± 1
aq sample	28 ± 1	44 ± 1	27 ± 1

Tab. 7.1: *Comparison of the spin density values between the* fq *and the* aq *samples*

As can be seen in the table, in the *field-quenched* ribbon, the spin density is found to increase along the direction of the applied magnetic field (x-axis or width) and to decrease in the thickness axis (z-axis), an indication of the anisotropy induced by the magnetic field during the quenching process. It is important to note that all other processing parameters were the same in both sets of ribbons, since it is known that spin alignment in a ribbon plane is favored in ribbons produced with higher quenching rate [347].

Observation of the domain structure

For the Fe-based alloy studied (alloy I, $Fe_{80}B_{20}$), the domain structures of the two samples were observed via the Bitter technique and compared, with the results shown in figure 7.5.

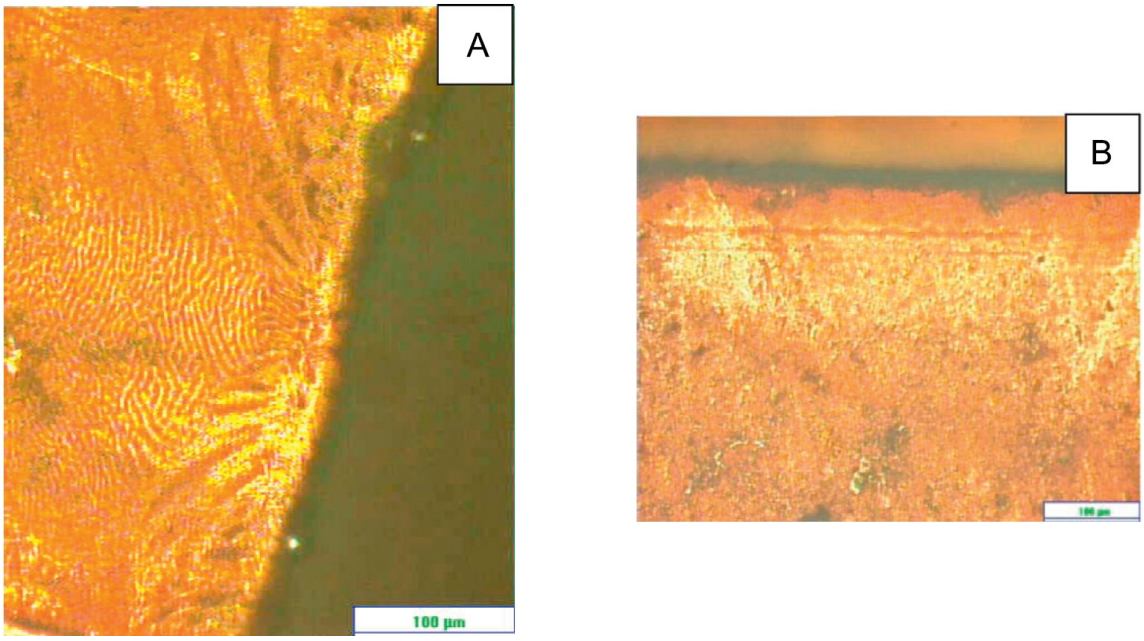

Fig. 7.5: *Comparison of the domain patterns in alloy I quenched with (B) and without (A) the presence of the external magnetic field.*

As can be seen in the figure, in the sample produced without the field, the domain patterns generally exhibit a maze configuration as well as zig-zag walls in regions with some anisotropy in the z-axis direction (thickness), surely due to the compression stresses developed during the quenching process. On the other hand, this does not seem to be observed in the *field-quenched* ribbon surface, with the

magnetization lying in the x (width) and y (length) axis all through the entire sample. This domain structure difference observed on the ribbons surface is again considered to be a consequence of the transverse anisotropy component induced on the *field-quenched* sample [348].

7.3 Effects of the induced anisotropy on the magnetic properties of the alloys

In order to study effects of this induced anisotropy in the magnetic properties of the alloy, M-H experiments were carried out in both samples, with the resulting hysteresis cycles shown in fig. 7.6.

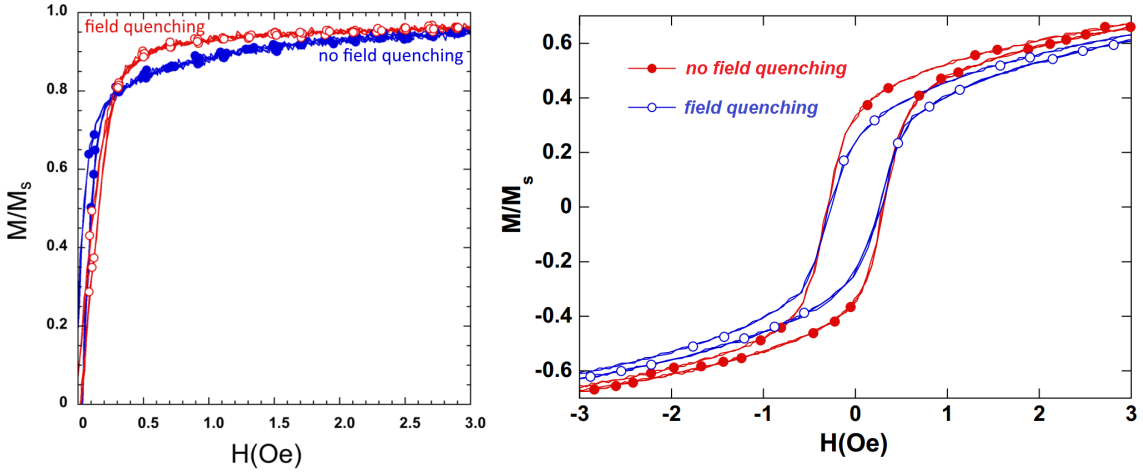

Fig. 7.6: *Comparison of M-H hysteresis cycles between samples produced with and without the presence of an external magnetic field, for alloys G (left) and I (right)* [338, 349].

In concordance with the previous DSC experiments, a slight different behavior is oberved when comparing the two cycles, mostly noticeable at the low H region. Like in the DSC case, this can be easily explained but the presence of the induced magnetic anisotropy due to the field quenching method.

Variations in the permeability due to different cooling procedures have been previously reported in other works with identical composition [350]. The relatively small magnitude of the difference detected here might be explained by the short time elapsed in the process due to the high cooling rates required in MS.

For the Co-based alloy, the effects of the anisotropy in the magnetoimpedance were also analyzed, since this alloy is part of a family showing giant magnetoimpedance (GMI) effect. The GMI effect is a large change in the electric impedance of a magnetic conductor when is under the presence of an external magnetic field and can be explained as the consequence of the change in the skin depth due to the presence of the applied field. Its study has been a topic of intensive research in the field of applied magnetism during the last few years, where it has been found to be higher in alloys with circular domain structure [322–324, 338]. Amorphous alloys showing GMI effect may easily achieve

up to 300% relative change of impedance, making them potentially suitable for applications where high sensitivities to magnetic fields are required, even though lower GMI ratios of around 60% have been observed for other amorphous magnetic materials without special treatment [351]. In any case, the analysis of the GMI effect has been shown also to be an effective tool in order to investigate the anisotropy of soft-magnetic materials [352].

Figure 7.7 shows a comparison of the magnetoimpedance between the samples produced with and without the presence of the external magnetic field, featuring noticeable differences due to the induced anisotropy confirmed by the previous DSC and M-H results.

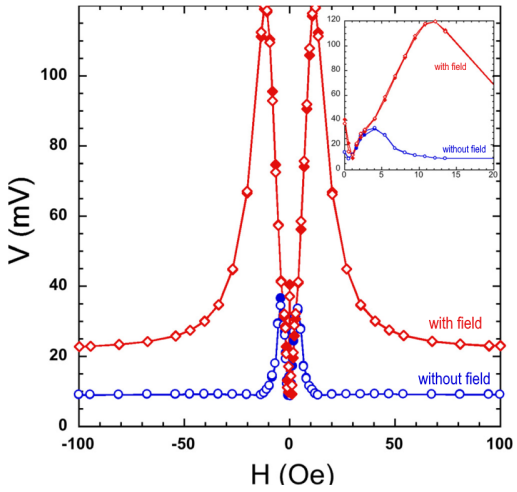

Fig. 7.7: *Comparison of the magnetoimpedance between samples quenched with and without the presence of an external magnetic field* [338].

7.4 Summary

Certain differences were detected in the alloys produced by quenching under the presence of an external magnetic field (field quenching) in comparison with the same alloys produced without the field, revealing the presence of some magnetic anisotropy, in agreement with previously reports [188, 340].

The analysis of the Co-based alloy (alloy G, $Co_{69}Fe_4Si_{15}B_{12}$) seems to confirm not only the presence of this induced anisotropy, denoted by the slightly higher activation energy found in the DSC experiments [338], but also its effects in the final magnetic properties, featuring both a slightly different M-H behavior and an enhancement of the GMI effect [332, 338].

A similar pattern has been observed in the Fe-based alloy (alloy I, $Fe_{80}B_{20}$), although the differences wthe anisotropy was not initially revealed in the DSC experiments but it was in initially is revealed by the differences in the estimated spin density between the different axes [336].

General discussion

8

> *If there is anything in the universe that can't stand discussion, let it crack.*
>
> — **Wendell Phillips**
> (Activist)

Contents

This chapter discusses the different analyses and procedures described throughout the experimental chapters of this work (chapters 4 to 7), focused on the following issues:

- Analysis of the MA process and its effects on nanocrystalline alloys in general and on the specific alloys studied here.
- Characterization of the final alloys produced, discussing the structural properties of the resulting alloys after the milling process.
- Analysis of the magnetic properties of the alloys and their suitability for soft magnetic applications.

8.1 Analysis of the MA process

The respective studies detailed in chapters 4, 5 and 6 have provided some clues about the effects of the MA process in different cases and provided information about:

- Process of formation of the solid solutions
- Evolution of the crystalline size
- Stress induced during the milling process
- Crystallization of the amorphous precursors (in the MS+MA alloys)

8.1.1 Formation of the solid solutions

The XRD analyses performed in chapters 4 and 5 seem to concur on the formation of a single solid solution phase after just a few hours of milling, in agreement with other previous reported works [247, 251].

The solid solution is considered to be started very early in the process but achieved at an uncertain stage. The absence of the secondary peaks in the XRD patterns of most of the 5h samples might be an indication that the solid solutions could have been achieved before this milling time. But in the case of the Fe-Cr alloys, for example, the TMS spectra and respective average hyperfine fields of this 5h samples (fig. 4.8) are still very similar to that of an unreacted α-Fe. As explained in section 4.3.3 (equation 8.2), the presence of Cr atoms in the neighborhood sites around the Fe atoms should have been produced a noticeable reduction in the average hyperfine field $\langle B_{hf} \rangle$, so this high average field possibly means that the diffusion of the Cr atoms in the Fe-rich matrix were still being produced at this stage. This apparent contradiction between the XRD and the TMS analyses of the 5h samples can be partially explained by the heterogeneity of the alloys, denoted by the existence of two main contributions in TMS: one with high hyperfine value, easily attributed to iron-rich environments with low number of Cr neighbors and a secondary with a lower average, attributed to environments with some Cr atoms [223–225].

The crystalline structure of the two Fe-Cr (A-B) and the three Fe-Co-B alloys (C-E) are found to be based in the bcc-Fe phase whereas the Fe-Co-Ni (F) features a different fcc crystal lattice.

In the specific case of alloys A-B, it is assumed that the Cr atoms were introduced into the initial α-Fe phase substitutionally, based on the fact that both Cr and Fe feature identical crystal structure and with similar cell parameters (0.291 nm and 0.287, respectively) and atomic radii (0.128 nm for Cr and 0.126 for Fe), and that Cr in Fe diffuses faster than Fe in Cr [190]. The boron atoms in alloy B ($Fe_{80}Cr_{10}B_{10}$), on the other hand, are considered to be introduced into the matrix interstitially rather than substitutionally, based on their lower atomic radius and the low solubility of B in Fe-Cr. This low solubility should also have favored the formation of Fe or Cr borides [212], but no indication of their presence seems to have been observed during the analysis.

The evolution of the lattice parameters a shown in figure 4.4 seems to feature a two-stage progress with an abrupt increase during the first hours and a roughly steady behavior at later stages. This increase is a consequence of the bcc-Cr phase having a slightly higher cell parameter than bcc-Fe (0.291 vs 0.287 nm, as mentioned above), and therefore it could be used as an indication of the degree of achievement of the bcc-(Fe,Cr) solid solution. However, it must be also taken into account that the increase of the cell parameter can be also due to the defects induced by the milling process and, in alloy B, to the interstitial introduction of boron atoms.

In the specific case of alloys C-F, the three Fe-Co-B alloys (C-E) also feature a main phase based on the initial bcc-Fe, even in the cases with high Co contents. This is concurrent with other reported works [268–272] and can be explained by the good diffusivity of Co into Fe [244, 262, 263]. The boron atoms are again considered to be introduced in the solid solution interstitially rather than substitutionally, but in this case with an excepcion in alloy E, for which both the XRD and TMS results seem to indicate that a significant part of the boron was introduced substitutionally.

The Fe-Co-Ni alloy (F), on the other hand, seems to depart from the other alloys and feature a fcc structure, in agreement with its hypothetical position in the ternary Fe-Co-Ni equilibrium phase diagram (fig. 5.20). This concords with other previous reports with similar compositions [273, 274, 298].

No specific analysis of the process of formation of the solid solution was carried out for alloys G-J.

8.1.2 Reduction of the crystalline size

Following the general behavior commonly reported in most Fe-based MA-produced alloys, a dramatic reduction in the grain size is observed during the very early stages of the process, with the alloys generally showing nanocrystalline properties after just 1h of milling in the Fe-Cr and Fe-Co-Ni alloys and after the 5h in the Fe-Co-B alloys (see figs. 4.5, 5.7 and 5.9). Later stages of the process seem to show a progressive moderation in the reduction rate and a subsequent stabilization of the crystalline size.

In the Fe-Cr alloys, the achieved crystalline size is about 5-6 nm. These values have been found to be relatively better in comparison with other similar works previously studied [237], revealing the importance of the specific working conditions in the characteristics of the resulting alloy.

In the Fe-Co alloys, the achieved magnitudes are in the range 5-15 nm, with the Co-rich alloys featuring the smallest sizes. Surprisingly, the lowest values have not been always found in the final

alloys but in some of the samples with a lower milling time, indicating a certain degree of crystalline grow during the final stages due to the milling process.

8.1.3 Stress induced by the milling process

The XRD analyses have been found to reveal an increase in the microstrain index and density of dislocations with the milling time in all alloys (figs. 4.6, 5.7 and 5.9), due to defects introduced by the milling process itself [235]. This induced strain is a common feature widely found in other MA-processed alloys [198, 199, 207, 219] and is confirmed again by the DSC experiments, where the curves corresponding to higher milling times feature more prominent peaks related to the structural relaxation and slightly higher peak temperatures in the main crystallization peaks.

8.1.4 Crystallization of the amorphous MS alloys

The study of the powder alloys in chapter 6 has been focused in the final alloys and does not include much information about the analysis of their evolution throughout the milling process. However, some noticeable differences have been found between the MA of the previously MS-produced amorphous ribbons and the direct MA of industrial powders.

According to the XRD and DSC analyses, the milling process of the MS amorphous ribbons seems to have induced the crystallization of the alloys, although some differences are observed between the Co-based and the Fe-based alloys studied, with the former showing mainly amorphous features with only a certain partial degree of crystallization and the latter generally revealing nanocrystalline features. This will be discussed in more detail in next section.

The alloys milled directly by MA from industrial crystalline powders, on the other hand, seems to show the same evolution as the previous Fe-Cr and Fe-Co based MA alloys described above, although no deeper analysis can be carried out due to the absence of samples processed with low milling times.

8.2 Characterization of the alloys produced

Alloys A-B

For the Fe-Cr based alloys (A-B), crystalline sizes around 5-6 nm are observed to having been achieved in the samples milled for several hours. This is a value noticeable lower than those found in other similar works, where sizes of around 12 nm have been reported [237], although the difference can be attributed to the dependence of the specific working conditions in the characteristics of the produced alloys.

The magnitudes of the estimated dislocation densities are in the order of 10^{16} m^{-2}, which are comparable to the edge dislocation densities limit in metal achieved by plastic deformation [89, 207, 220]. Alloy B shows a slightly higher value than alloy A, due to both the presence of boron and its lower Cr relative content.

Although the XRD patterns clearly show the presence of a single crystalline phase in the final alloys, both the TMS and the thermal analyses reveal a certain degree of heterogeneity. A deeper analysis of the TMS spectra (fig. 4.10 and table 4.3) reveals that the hyperfine field distributions do not seem to match those expected for a completely random distribution of the Cr atoms in the neighboring sites around the Fe nuclei, an indication that the total homogenization could have been not achieved after the 80h of milling. This is consistent with other MA-milled Fe-Cr alloys found in the literature [190, 230, 231], but not with the fact that no paramagnetic contribution has been detected when the presence of regions with higher relative Cr content should have produced it [136, 185]..

The TMS spectra seem to reveal low average hyperfine field $\langle B \rangle$ in both cases, although only the value found for alloy A ($Fe_{80}Cr_{20}$) agrees with the expected according to the well-known linear reduction with the Cr relative content (eq.) [136, 222]. Alloy B ($Fe_{80}Cr_{10}B_{10}$), on the other hand, seems to feature a significant lower value despite having less Cr content. This can be explained by the presence of boron in the alloy, since it has been widely reported that its addition generally favors the formation of nanocrystalline or amorphous alloys [171, 226, 236].

Alloys C-F

As explained above, the crystal structure observed in the three Fe-Co-B alloys (C-E) is based on the initial bcc-Fe, thanks to the good diffusivity of Co into Fe [244, 262, 263], and in agreement with other previously reported results [268–272]. The Fe-Co-Ni alloy (F), on the other hand, features a fcc structure, due to the presence of nickel and in concordance with the ternary Fe-Co-Ni phase diagram (fig. 5.20) and with other works [273, 274]. This different crystal structure is also the responsible of the high ductility of the alloy observed in the SEM micrographs.

The TMS spectra show some significant differences between the alloys. Alloys C and E feature a relatively wide distribution of hyperfine field values which could be an indication of the heterogeneity of the samples due to the presence of a wide variety of different iron-cobalt environments. The average values observed confirm the formation of the solid solution, although with a slightly lower magnitude compared with other similar works [251, 276], probably due to the presence of interstitial (C and E) and/or substitutional (E) boron [277]. Alloys D and F, on the other hand, seems to feature relatively homogeneous ferromagnetic environments but also the presence of minor oxide phases not detected previously in XRD either with paramagnetic (D) or ferromagnetic (F) behavior.

The thermal analyses reveal the significant presence of several processes associated to structural relaxation, easily explained by the high strain induced during the milling process. On the other hand, the $\alpha' \rightarrow \alpha$ transition (see fig. 5.1) is not detected in any alloy, although this is not entirely unexpected, since it is known that the MA process hinders the formation of highly ordered phases. At higher temperatures, a relatively high amount of processes detected and their wide distribution of activation energy values seems to confirm the heterogeneity found in the TMS analysis. Some of these processes are considered to be associated to the formation of borides, which would confirm their absence in the as-milled alloys mentioned before.

The temperatures of the main magnetic transition observed in the TM curves are in the range of 1100-1300 K, with the highest value found in the alloy with the highest Co content, in agreement

with the general behavior reported [285, 286]. The alloy with nickel also shows a second magnetic transition at around 870 K related to Ni-rich environments.

Alloys G-J

The structural and thermal analyses of the MS+MA alloys show significant differences between the Co-based and Fe-based alloys. Whereas the first group seem to retain some of the amorphous characteristics of their MS precursors and show only partial crystallization, the latter feature clear nanocrystalline properties [134, 266, 267, 328, 329].

Furthermore, some differences have been found between the samples produced by quenching under the presence of an external magnetic field (field quenching) in comparison with the other samples produced without the field, revealing the presence of some magnetic anisotropy, in agreement with previous reports [188, 340].

In the case of the Fe-based alloy, the anisotropy seems to be not revealed in the DSC experiments but it is deduced by the differences observed in the estimations of the spin densities between the three axes [336].

8.3 Soft-ferromagnetic behavior of the alloys

Good soft magnetic properties seem to be generally found in the final alloys, with the specific magnitudes shown in table 8.1.

The coercivity values of the powder alloys analyzed here are generally in the range of 15-50 Oe, magnitudes in concordance with other works on nanocrystalline alloys [241, 242, 245, 247, 287–289] but still significantly higher than those found in the MS ribbons of chapter 6 or in other works [49, 196, 207, 232, 233].

The saturation magnetizations are mostly in the range 140-180 Am^2/kg (equivalent to magnetic polarizations of roughly 1.4-1.8 T), also in agreement with the literature [190, 196, 207, 233, 241, 242, 245, 247, 287–289], with the exception of alloy G ($Co_{66}Fe_4Ni_1Si_{15}B_{14}$), which shows noticeable lower values.

Estimated magnetic properties

	coercivity	magnetic saturation	
	H_c (Oe)	M_s (Am^2/kg)	J_s (T)
alloy A ($Fe_{80}Cr_{20}$)	27	146	1.41
alloy B ($Fe_{80}Cr_{10}B_{10}$)	18	152	1.47
alloy C ($Fe_{80}Co_{10}B_{10}$)	44	176	1.79
alloy D ($Fe_{45}Co_{45}B_{10}$)	50	174	1.79
alloy E ($Co_{50}Fe_{30}B_{20}$)	32	161	1.75
alloy F ($Co_{50}Fe_{30}Ni_{20}$)	33	141	1.50
alloy G ($Co_{66}Fe_4Ni_1Si_{15}B_{14}$)			
MS+MA	17	95	1.16
MS	1.6	58	0.55
MA	28	92	1.12
alloy H ($Co_{69}Fe_4Si_{15}B_{12}$)			
MS+MA	240	122	1.51
MS	7.3	45	0.57
MA	50	97	1.21
alloy I ($Fe_{80}B_{20}$)			
MS+MA	45	168	1.72
MS	0.4	115	1.23
MA	32	193	1.95
alloy J ($Fe_{80}Si_{10}B_{10}$)			
MS+MA	43	151	1.60
MS	10	119	1.26
MA	25	176	1.87

Tab. 8.1: *Estimated magnetic properties of the alloys analyzed*

8.3.1 Effects of the MA process

Figure 8.1 shows the magnitudes of table 8.1 in a single plot for an easy visualization, with the coercivities in the horizontal axis and the saturations in the vertical. In this diagram, an optimal soft-ferromagnetic alloy should be located the closest possible to the upper left corner (low coercivity and high saturation).

As can be seen, the amorphous MS ribbons are all in the lower left half of the diagram, since they feature low coercivities and saturations, whereas the milled powder alloys are in the upper right half, due to their higher coercivities and saturations. It must be remembered that almost all the alloys showed nanocrystalline properties except the MS+MA of alloy G, which shows mostly amorphous features, explaining its location very close to the other amorphous alloys.

The different analyses carried out in the previous chapters show that the milling processes did not produce amorphisation of the alloys but did reduce the average crystalline size down to the nanoscale level. However, the coercivities observed are an order of magnitude higher than those expected for

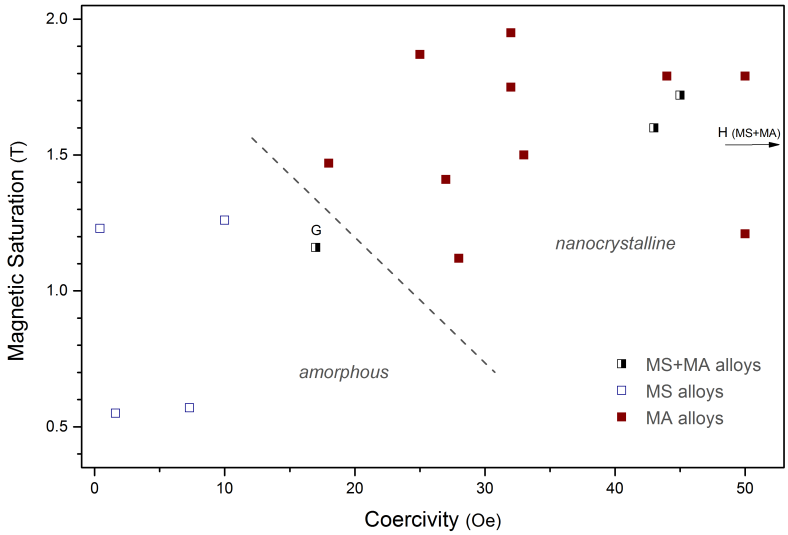

Fig. 8.1: *Comparison of the magnetic properties of all the alloys studied.*

the nanocrystalline sizes achieved, according to the D^6 relation explained in section 1.3 [28, 34, 46–48]. As mentioned above, this has been also found in other works dealing with nanocrystalline alloys produced by MA [241, 242, 245, 247, 287–289], and could be explained by the amount of stress introduced in the alloys during the MA process.

The respective DSC analyses carried out generally show the presence of a significant amount of low-temperature processes which have been attributed to structural relaxation processes, confirming the amount of stress mentioned above. This also means that further annealing of the alloys would produce a significant reduction of this induced stress and could mean a reduction in their coercivity. This hypothesis has not been tested yet in these alloys but proposed as future work in the next chapter (see section 9.2).

8.3.2 Effects of the alloying elements

Besides iron (Fe), which is present in the compositions of all the alloys studied in this work although in a wide range of relative contents, several other alloying elements are also included in some of the alloys in diverse numbers of cases and relative contents. Some approaches to possible analysis of the hypothetical effects of each of these elements can be extracted from certain comparisons between results.

Cobalt (Co) and nickel (Ni) are also, like iron, ferromagnetic elements and their additions modify the magnetic properties of the resulting alloy but generally do not remove them. A similar behavior has been also observed with the addition of chromium (Cr) in low relative contents, despite being an antiferromagnetic element.

Lastly, the additions of boron (B) and silicon (Si), which are not magnetically ordered elements, are indeed found to affect the microstructure of the resulting alloys by improving the glass forming ability or reducing the grain size, and therefore facilitate the achievement of optimal soft-magnetic properties.

Chromium (Cr)

A simple approach to the study of the possible effects of the Cr relative content can be made by comparing the properties of alloys A $Fe_{80}Cr_{20}$ and B $Fe_{80}Cr_{10}B_{10}$. Some of the common trends generally found in other Fe-Cr based nanocrystalline alloys such as an increase in the coercivity and a reduction in the saturation with the addition of Cr content have been observed also here. However, the results have been found to be partial and unfortunately inconclusive due to the additional presence of boron also affecting significantly the properties of one of the alloys, as it will be shown later.

Furthermore, some of the interesting features of the Fe-Cr systems, such as the wide miscibility gap and the transition from the ferromagnetic behavior of pure Fe to the antiferromagnetism of pure Cr with the possible presence of magnetic frustration, generally ocurr at higher Cr contents [174, 178, 179] and thus cannot be discussed with the information from the alloys studied here.

Cobalt (Co)

All the alloys studied in chapter 5 (C-F) and some of chapter 6 (G-H) contain cobalt either as the main or as a secondary alloying element.

The parallel analysis of alloys C ($Fe_{80}Co_{10}B_{10}$ and D ($Fe_{45}Co_{45}B_{10}$) gives a first approach to the possible effects of the Co relative content, which seems to be in concordance with the generally reported increase in the coercivity with the cobalt relative content up to near equiatomic compositions [290–293], although only a slight variation seems to be observed here. On the other hand, no consistent conclusion can be made about the effects on the saturation, due to the pair of alloys showing an apparent weak dependence with the Co content but unfortunately being too far away from the generally reported maximum at around 30% Co.

Alloys E ($Co_{50}Fe_{30}B_{20}$) and F ($Co_{50}Fe_{30}B_{20}$) could have given us some additional information about the effects of higher Co content, of which conflicting reports can be found in the literature [247, 253, 290, 294] due to the strong dependence of the coercivity with the microstructure [240, 295], but its higher boron content (E) and presence of nickel (F) makes them inconclusive, as will be shown later.

No particular conclusion about the effects of Co content can be neither made from the analysis of the Co-rich pair of alloys studied in chapter 6 (G-H), due to having several other alloying elements.

Boron (B)

A common behavior widely reported in the literature is that the addition of boron in the composition of an alloy generally lowers the coercivity of the resulting alloy [125, 165, 189, 193, 194, 235, 272, 296]. This can be found also here when comparing the coercivities of alloy A and B and D and E, respectively, from table 8.1 and fig. 8.1.

In the Fe-Cr group, the alloy with boron content (B) features the lowest coercivity. Although this fact can be partially explained by its lowest Cr content [196], it could be an indication of the effects of the addition of boron.

In the Fe-Co-B group, a less ambiguous result is found, since the alloy with the highest boron content (E) shows the lowest coercivity even when its highest Co should have meant an increase in its magnitude [292].

Nickel (Ni)

The parallel analyses of alloys E ($Co_{50}Fe_{30}B_{20}$) and F ($Co_{50}Fe_{30}Ni_{20}$) in chapter 5 allow a comparison between the effects of the presence of nickel and boron.

The most noticeable difference observed is in their crystalline structure, with the alloy with boron showing the same bcc structure than the other Fe-Co alloys but the alloy with nickel showing a different fcc structure. Although strange at first sight, it is indeed an expected result according to the ternary Fe-Co-Ni equilibrium diagram (fig. 5.20). One of the consequences of this is the higher ductility of the samples confirmed in the SEM analysis in chapter 5, since it is widely known that materials based on the fcc crystalline structure generally show higher ductility than bcc-based due to the fcc being a closely packed structure [275].

Regarding the magnetic properties, although both alloys have almost identical coercivities, their respective magnetic hysteresis cycles do show significant differences, with the alloy with Ni featuring lower saturation and susceptibility magnitudes. This is considered to be more a consequence of the Ni atoms introduced substitutionally in the fcc structure rather than to the nature of the fcc itself.

Silicon (Si)

In a similar way than for the previous pair, a quick comparison of the magnetic properties of alloys I ($Fe_{80}B_{20}$) and J ($Fe_{80}Si_{10}B_{10}$) allows the analysis of the possible differences between the addition of Si and B to the alloys.

The two alloys show almost identical coercivities and only slight differences in the saturation magnitudes. As explained in chapter 6, both the addition of B and Si to Fe-based nanocrystalline alloys decrease their grain size and therefore improves the coercivity but at the same time tend to reduce their magnetic saturation [28, 308, 326, 327]. Comparing the two alloys, it seems that the alloy with Si (J) features a higher reduction.

9 Conclusions

> *Finally, in conclusion, let me say just this.*
>
> — **Peter Sellers**
> (Actor)

Contents

9.1 Conclusions

Some conclusions can be drawn about the MA process of the Fe-Cr and Fe-Co based powder alloys produced:

- The milling process seems to favor the formation of solid solutions, which are observed to have been started very early in the process and generally achieved at around 5 hours of milling. In the Fe-Cr and Fe-Co-B alloys, the resulting phases are based on the bcc-Fe crystal structure with the Cr or Co atoms being introduced substitutionally in the matrix and the B atoms mostly interstitially, except in the case of the alloy with the higher boron content, where they seem to have been introduced both interstitially and substitutionally. The Fe-Co-Ni alloy, on the other hand, features a fcc structure due to the presence of Ni.

- The early stages of the process seems to have produced a dramatic reduction of the average crystalline size, but later stages feature a softer decrease until the achievement of a roughly steady state. The crystalline size achieved are in all the range 5-15 nm, with the lower values found in the Fe-Cr alloys, although some alloys show an increment of the crystalline size during the final stages.

- The milling process also seems to have introduced a large amount of crystalline defects which seems to have increased the stress in the alloys.

- A certain degree of heterogeneity has been found in all alloys, albeit with some differences between them. No presence of borides has been detected in the alloys with boron at any stage of the process.

Regarding the alloys produced by a combined MS+MA process, the following conclusions can be drawn:

- The milling process seems to have produced some degree of crystallization on the previously amorphous alloys, although some differences have been observed between the Co-based and the Fe-based alloys.

- The analyses of the Co-based alloys show only a certain degree of crystallization and some of the amorphous features of their MS precursors are found to be still retained.

- On the other hand, the Fe-based alloys seem to have been highly recrystallized during the milling process.

About the magnetic properties of the alloys produced,

- Almost all the alloys produced feature good soft ferromagnetic properties.

- The measured coercivities are generally in the range 15-50 Oe. These magnitudes are in agreement with most other works about nanocrystalline similar alloys but still significantly higher than those of amorphous alloys.

- The presence of boron in the compositions of the alloys seems to have allowed the achievement of lower coercivities, due to this element generally favoring the reduction of the crystalline size.

- Furthermore, the coercivity magnitudes do not agree with the expected for the crystalline sizes achieved, which is inferred to be due to the stress induced by the milling process. This, on the other hand, means that a controlled annealing of the alloys could further reduce their coercivity.

- The alloys produced by the MA of amorphous ribbons previously produced by MS do not retain the low coercivities of the latter but show values closer to the alloys produced directly by MA. This could be a consequence of the powder alloys mostly showing nanocrystalline features, although the alloy that showed the lowest degree of crystallization also showed the lowest increase in the coercivity.

- The magnetic saturations of the milled amorphous ribbons also achieved the higher values of the powder counterparts produced directly by MA rather than the low magnitudes of the ribbons themselves.

- The samples produced with the application of an external magnetic field during the MS quenching process do show magnetic anisotropy, the effects of which are noticeable in the respective magnetic hysteresis and magnetoimpedances.

9.2 Future Work

Several complementary analysis and procedures have been considered to be approached for this work but discarded due to time restrictions or logistic difficulties.

- *Analysis of the possible effects of certain changes in the milling conditions.*

  As explained in section 2.1, the change in the milling conditions in MA process can produce a dramatic change in the properties of the resulting alloys. Arguably two of the most relevant parameters are the milling energy and the milling time, with the former comprising several different specific controllable parameters such as the specific mill model or the rotation speed.

  An increase in the milling time could help reducing the heterogeneity in the samples, although it could also mean a significant modification of the properties of the alloy, either due to amorphization of the alloy or to the opposite behavior.

- *Study of the possible consequences of small and/or huge changes in the composition of the alloys.*

  As explained above, some groups of alloys have allowed a first approach to the analysis of the effects of some specific variations in the compositions, such as the increase or decrease in the relative content of boron, nickel, etc.

  A further deeper study could be made by analyzing several different alloys with slight variations in the relative contents of some of their alloying elements in order to find optimal compositions.

Another path to be also considered is the inclusion of other alloying elements not described in this work but widely used in other similar works.

- *Controlled annealing of the alloys and analysis of its possible effects on the resulting properties.*

  Due to time restrictions, the analyses carried out in this work, including the thermal analysis, have been limited only to the study of the as-milled samples. However, the DSC and TM experiments already performed have provided some interesting information about the expected behavior of these alloys at certain temperatures.

  One particular desired behavior observed during these experiments is the reduction of the residual strain from the microstructure of the alloys. It has been made clear in this work that the density of crystalline defects in the as-milled samples is generally high, and that low-temperature annealing treatments generally trigger the structural relaxation of the alloys and helps reducing them. However, it has been also shown here that annealing at excessively high temperatures could trigger crystalline growth or nucleation processes and thus increase the average crystalline size.

  A complete study of the structural properties of the alloys after being submitted to several different controlled annealing treatments could help determine the optimal temperature programs and conditions for the achievement of the desired microstructure.

  As explained in chapter 1, one of the main goals to target at when researching for a good soft magnetic material is to achieve a low coercivity value. It is well-known that coercivity is a heavily structurally sensitive property and its specific magnitude strongly depends on the internal defects [249, 353]. Therefore, a complete knowledge of the thermal behavior of the alloys is crucial for the achievement of its lowest possible value.

  The immediate effect of a low-temperature annealing of an alloy is generally a decrease in the coercivity value [196, 242], thanks to the structural relaxation mentioned above. However, without the complete knowledge of the optimal temperature program this could be counterproductive, since further annealing could force excessive crystallization of the alloys and thus produce an undesired increase in the coercivity, limiting their suitability for soft magnetic applications.

  Therefore, a complete analysis of the magnetic properties of the alloys after several different annealing conditions could help finding the optimal procedures for the achievement of the lowest coercivities and the enhancement of the soft magnetic properties of the alloys.

- *Sintering of the alloys.*

  The study of the specific details of sintering -i.e. the process of compacting and forming a solid mass of material by heat or pressure without reaching its melting point- of powder alloys is a component of a wider field known as powder metallurgy, and is beyond the scope of this work.

  However, a complementary characterization of some of the alloys produced for this work after being sintered could bring us some interesting information about their potential properties and possible suitability for certain specific applications.

Bibliography

[1] SL Sass, ed. *The substance of civilization*. Arcade Publishing, 1998.

[2] D Bloor, RJ Brook, MC Flemings, and S Mahajan. *The encyclopedia of advanced materials*. Oxford, UK: Pergamon Press, 1994.

[3] C Suryanarayana, ed. *Non-equilibrium processing of materials*. Oxford, UK: Pergamon Press, 1999.

[4] TR Anantharaman and C Suryanarayana. *Rapidly solidified alloys - a technological overview*. Aedermannsdorf, CH: Trans Tech Publications, 1987.

[5] HH Liebermann, ed. *Rapidly solidified alloys: Processes, structures, properties, applications*. New York, NY: Marcel Dekker, 1993.

[6] CC Koch. *Processing of metals and alloys*. Ed. by Cahn RW. Vol. 15. Weinheim, DE: VCH Verlagsgesellschaft GmbH, 1991.

[7] C Suryanarayana. *Bibliography on mechanical alloying and milling*. Cambridge, UK: Cambridge International Science Publishing, 1995.

[8] L Lu and MO Lai. *Mechanical alloying*. Kluwer Academic Publishers, 1998.

[9] BS Murty and S Ranganathan. "Novel materials synthesis by mechanical alloying/milling". In: *Int. Mater. Rev.* 43.3 (1998), pp. 101–141.

[10] K Upadhya, ed. *Plasma synthesis and processing of materials*. Warrendale, PA: TMS, 1993.

[11] RL Bickerdike, D Clark, JN Easterbrook, G Hughes, WN Mair, PG Partridge, and HC Ranson. "Microstructures and tensile properties of vapor-deposited aluminum alloys - 1. Layered microstructures". In: *Intern. J Rapid Solidif.* 1.4 (1985), pp. 305–325.

[12] D Turnbull. "Metastable structures in metallurgy". In: *Met. Trans* 12.5 (1981), pp. 695–708.

[13] G Martin and P Bellon. "Driven alloys". In: *Solid State Phys.* 50 (1997), pp. 189–331.

[14] H Gleiter. "Nanocrystalline Materials". In: *Advanced Structural and Functional Materials: Proceedings of an International Seminar Organized by Deutsche Forschungsanstalt für Luft- und Raumfahrt (DLR), Köln, June 1991*. Ed. by Wolfgang G J Bunk. Berlin, Heidelberg: Springer Berlin Heidelberg, 1991, pp. 1–37. ISBN: 978-3-642-49261-7.

[15] S Schumacher, R Birringer, R Strauss, and H Gleiter. "Diffusion of silver in nanocrystalline copper between 303 and 373 K". In: *Acta Metallurgica* 37.9 (1989), pp. 2485–2488.

[16] H Gleiter. "Nanostructured materials: basic concepts and microstructure". In: *Acta Materialia* 48.1 (2000), pp. 1–29.

[17] J Torrens. "Preparation and characterization of FeNbB-based metallic glasses and nanostructured materials for soft magnetic applications". PhD thesis. Autonomous University of Barcelona, 2009.

[18] SJ Takayama. "Amorphous structures and their formation and stability". In: *Journal of Materials Science* 11.1 (1976), pp. 164–185.

[19] MW Grinstaff, MB Salamon, and KS Suslick. "Magnetic properties of amorphous iron". In: *Physical Review B* 48.1 (1993), pp. 269–273.

[20] A Russell and KL Lee. *Structure-Property Relations in Nonferrous Metals*. John Wiley & Son, 2005.

[21] XJ Gu, SJ Poon, and GJ Shiflet. “Mechanical properties of iron-based bulk metallic glasses”. In: *Journal of Materials Research* 22.2 (2007), pp. 344–351.

[22] SF Guo, JL Qiu, P Yu, SH Xie, and W Chen. “Fe-based bulk metallic glasses: Brittle or ductile?” In: *Applied Physics Letters* 105 (2014).

[23] A Inoue and JS Gook. “Effect of additional elements (M) on the thermal stability of supercooled liquid in Fe(72-x)Al(5)Ga(2)P(11)C(6)B(4)M(x) glassy alloys”. In: *Materials Transactions JIM* 37.1 (1996), pp. 32–38.

[24] A Inoue, A Takeuchi, A Makino, and T Matsumoto. “Soft and hard magnetic properties of nanocrystalline Fe-M-B (M=Zr,Nd) base alloys containing intergranular amorphous phase”. In: *Science Reports of the Research Institutes Tohoku University Series A -Physics Chemistry and Metallurgy* 42.1 (1996), pp. 143–156.

[25] A Inoue. “Stabilization of metallic supercooled liquid and bulk amorphous alloys”. In: *Acta Materialia* 48 (2000), pp. 279–306.

[26] A Takeuchi and A Inoue. “Mixing enthalpy of liquid phase calculated by miedema’s scheme and approximated with sub-regular solution model for assessing forming ability of amorphous and glassy alloys”. In: *Intermetallics* 18.9 (2010), pp. 1779–1789.

[27] S Vincent, DR Peshwe, BS Murty, and Jatin Bhatt. “Thermodynamic prediction of bulk metallic glass forming alloys in ternary Zr–Cu–X (X= Ag, Al, Ti, Ga) systems”. In: *Journal of Non-Crystalline Solids* 357.19 (2011), pp. 3495–3499.

[28] HR Lashgari, D Chu, S Xie, H Sun, M Ferry, and S Li. *Composition dependence of the microstructure and soft magnetic properties of Fe-based amorphous/nanocrystalline alloys: A review study*. 2014. DOI: 10.1016/j.jnoncrysol.2014.03.010.

[29] K Klement, R Willens, and P Duwez. “Non-crystalline structure in solidified gold-silicon alloys”. In: *Nature* 187.4740 (1960), p. 869.

[30] BD Cullity. *Introduction to Magnetic Materials*. 1st Ed. Addison-Wesley, 1972.

[31] Nobelprize.org. *Pierre Curie - Biographical*. 2014. URL: http://www.nobelprize.org/nobel_prizes/physics/laureates/1903/pierre-curie-bio.html (visited on 09/20/2016).

[32] C Kittel. “Physical theory of ferromagnetic domains”. In: *Reviews of modern Physics* 21.4 (1949), p. 541.

[33] Wikimedia Commons. *Curie temperature*. 2016. URL: https://en.wikipedia.org/w/index.php?title=Curie_temperature (visited on 10/04/2016).

[34] ME McHenry, MA Willard, and DE Laughlin. “Amorphous and nanocrystalline materials for applications as soft magnets”. In: *Prog. Mat. Sci.* 44.4 (1999), pp. 291–433.

[35] DA DeAntonio. “Soft magnetic ferritic stainless steels”. eng. In: *Advanced Materials & Processes* 161.10 (2003), pp. 29–32. ISSN: 0882-7958. URL: http://cat.inist.fr/?aModele=afficheN%7B%5C&%7Dcpsidt=15211459.

[36] Merriam Webster. *Bloch Wall*. 2016. URL: http://www.merriam-webster.com/dictionary/Bloch%20wall (visited on 10/05/2016).

[37] BA Lilley. “LXXI. Energies and widths of domain boundaries in ferromagnetics”. In: *The London, Edinburgh, and Dublin Philosophical Magazine and Journal of Science* 41.319 (1950), pp. 792–813.

[38] Wikimedia Commons. *Domain wall (magnetism)*. 2016. URL: https://en.wikipedia.org/w/index.php?title=Domain_wall_(magnetism) (visited on 10/05/2016).

[39] LK Metlov. “Cross-Tie Domain Wall Ground State in Thin Films”. In: *Journal of Low Temperature Physics* 139.1 (2005), pp. 207–219.

[40] Wikimedia Commons. *The magnetic moments configuration in three types of domain wall*. 2016. URL: https://commons.wikimedia.org/w/index.php?title=File:DWconfiguration.png&oldid=131429854 (visited on 10/05/2016).

[41] T Gheiratmand and HRM Hosseini. “Finemet nanocrystalline soft magnetic alloy - Investigation of glass forming ability, crystallization mechanism, production techniques, magnetic softness and the effect of replacing the main constituents by other elements”. In: *Journal of Magnetism and Magnetic Materials* 408 (2016), pp. 177–192. ISSN: 03048853. DOI: 10.1016/j.jmmm.2016.02.057.

[42] R Skomski and J Zhou. “Nanomagnetic Models”. In: *Advanced Magnetic Nanostructures*. Ed. by D Sellmyer and R Skomski. Boston, MA: Springer US, 2006, pp. 41–90. ISBN: 978-0-387-23316-1. DOI: 10.1007/0-387-23316-4_3. URL: http://dx.doi.org/10.1007/0-387-23316-4%7B%5C_%7D3.

[43] O Fruchart. *Lecture notes on Nanomagnetism*. Grenoble, 2011.

[44] G Herzer. “Nanocrystalline soft magnetic materials”. In: *Journal of Magnetism and Magnetic Materials* 157 (1996), pp. 133–136.

[45] ME McHenry and DE Laughlin. “Nano-scale materials development for future magnetic applications”. In: *Acta Materialia* 48.1 (2000), pp. 223–238. ISSN: 13596454. DOI: 10.1016/S1359-6454(99)00296-7.

[46] G Herzer. “Grain structure and magnetism of nanocrystalline ferromagnets”. In: *IEEE Trans. Magn.* 25.5 (1989), p. 3327.

[47] G Herzer. “Grain-size dependence of coercivity and permeability in nanocrystalline ferromagnets”. In: *IEEE Transactions on Magnetics* 26.5 (1990), pp. 1397–1402.

[48] KHJ Buschow and FR De Boer. *Physics Of Magnetism And Magnetic Materials*. New York, NY: Kluwer Academic Publishers, 2003.

[49] TD Shen, RB Schwarz, and JD Thompson. “Soft magnetism in mechanically alloyed nanocrystalline materials”. In: *Physical Review B* 72.1 (2005).

[50] R Alben, J Becker, and M Chi. “Random anisotropy in amorphous ferromagnets”. In: *Journal of Applied Physics* 49.3 (1978), pp. 1653–1658.

[51] T Bitoh, A Makino, A Inoue, and T Masumoto. “Random anisotropy model for nanocrystalline soft magnetic alloys with grain-size distribution”. In: *Materials Transactions* 44.10 (2003), pp. 2011–2019.

[52] S Bedanta, O Petracic, and W Kleemann. “Supermagnetism”. In: *Handbook of Magnetic Materials, vol. 15*. Ed. by KHJ Buschow. Amsterdam, NL: Elsevier Science, 2003. ISBN: 978-0-444-63528-0.

[53] S Chikazumi, S Taketomi, M Ukita, Miyajima Mizukami, H Miyajima, M Setogawa, and Y Kurihara. “Physics of magnetic fluids”. In: *Journal of Magnetism and Magnetic Materials* 65.2-3 (1987), pp. 245–251.

[54] AH Lu, EL Salabas, and F Schüth. “Magnetic nanoparticles: synthesis, protection, functionalization, and application”. In: *Angewandte Chemie International Edition* 46.8 (2007), pp. 1222–1244. DOI: 10.1002/anie.200602866.

[55] CC Berry and ASG Curtis. “Functionalisation of magnetic nanoparticles for applications in biomedicine”. In: *Journal of physics D: Applied physics* 36.13 (2003), R198.

[56] PP Freitas and HA Ferreira. “Spintronic biochips for biomolecular recognition”. In: *Handbook of Magnetism and Advanced Magnetic Materials* (2007).

[57] FE Luborsky. *Amorphous metallic alloys*. 1st Ed. Butterworths Monographs in Materials, 1983.

[58] P Duwez and SCH Lin. “Amorphous ferromagnetic phase in iron-carbon-phosporus alloys”. In: *J. Appl. Phys.* 38.10 (1967), p. 4096.

[59] Y Yoshizawa, S Oguma, and K Yamauchi. “New Fe-based soft-magnetic alloys composed of ultrafine grain structure”. In: *J. Appl. Phys.* 64.10 (1988), p. 6044.

[60] A Kojima, H Horikiri, Y Kawamura, A Makino, A Inoue, and T Masumoto. “Production of nanocrystalline Fe-Nb-B bulk alloys by warm extrusion and their magnetic properties”. In: *Materials Science & Engineering A* 179 (1994), pp. 511–515.

[61] M Willard, D Laughlin, M McHenry, D Thoma, K Sickafus, J Cross, and V Harris. “Structure and magnetic properties of (Fe0.5Co0.5)(88)Zr7B4Cu1 nanocrystalline alloys”. In: *J. Appl. Phys.* 84.12 (1998), pp. 6773–6777.

[62] A Makino, K Suzuki, A Inoue, and T Masumoto. “Magnetic properties and core losses of nanocrystalline Fe-M-B (M = Zr, Hf or Nb) alloys”. In: *Mater. Sci. Eng. A* 179 (1994), pp. 127–131.

[63] A Calka, AP Radlinski, and R Shanks. “Thermal properties of nanocrystalline and amorphous Fe-B alloys made by mechanical alloying”. In: *Materials Science and Engineering A* 133 (1991), pp. 555–559.

[64] A Calka and AP Radlinski. “Universal high-performance ball-milling device and its application for mechanical alloying”. In: *Materials Science and Engineering A* 134 (1991), pp. 1350–1353.

[65] A Calka and AP Radlinski. “Formation of amorphous Fe-B alloys by mechanical alloying”. In: *Applied Physics Letters* 58.2 (1991), pp. 119–121.

[66] S Roth, M Stoica, J Degmova, U Gaitzsch, J Eckert, and L Schultz. “Fe-based bulk amorphous soft magnetic materials”. In: *J. Magn. Magn. Mater.* 304.2 (2006), pp. 192–196.

[67] M Stoica. “Casting and characterization of Fe-(Cr,Mo,Ga)-(P,C,B) soft magnetic bulk metallic glasses”. PhD thesis. IFW-Dresden, 2005.

[68] A Inoue. “Bulk amorphous and nanocrystalline alloys with high functional properties”. In: *Mat. Sci. Eng. A* 304 (2001), pp. 1–10.

[69] A Makino, T Kubota, C Chang, M Makabe, and A Inoue. “FeSiBP bulk metallic glasses with high magnetization and excellent magnetic softness”. In: *J. Magn. Magn. Mater.* 320.20 (2008), pp. 2499–2503.

[70] C Y Lin, H Y Tien, and T S Chin. “Soft magnetic ternary iron-boron-based bulk metallic glasses”. In: *Appl. Phys. Lett.* 86.16 (2005).

[71] V Franco, J S Blazquez, C F Conde, and A Conde. “A FINEMET-type alloy as a low-cost candidate for high-temperature magnetic refrigeration”. In: *Appl. Phys. Lett.* 88.4 (2006).

[72] A Makino, T Hatanai, A Inoue, and T Masumoto. “Nanocrystalline soft magnetic Fe-M-B (M=Zr, Hf, Nb) alloys and their applications”. In: *Mater. Sci. Eng. A* 226 (1997), pp. 594–602.

[73] R Boll. *Weichmagnetische Werkstoffe: Einf{ü}hrung in den Magnetismus ; VAC-Werkstoffe und ihre Anwendungen*. John Wiley & Sons Canada, Limited, 1990. ISBN: 9783800915460.

[74] A Makino, K Suzuki, A Inoue, and T Masumoto. “Low core loss of a bcc Fe86Zr7B6Cu1 alloy with nanoscale grain size”. In: *Mater. Trans. JIM* 32.6 (1991), pp. 551–556.

[75] G Herzer. “Modern soft magnets: Amorphous and nanocrystalline materials”. In: *Acta Materialia* 61.3 (Feb. 2013), pp. 718–734. ISSN: 1359-6454. DOI: 10.1016/j.actamat.2012.10.040.

[76] A Moser, K Takano, DT Margulies, M Albrecht, Y Sonobe, Y Ikeda, S Sun, and EE Fullerton. “Magnetic recording: advancing into the future”. In: *Journal of Physics D: Applied Physics* 35.19 (2002), R157. URL: stacks.iop.org/JPhysD/35/R157.

[77] BD Terris and T Thomson. “Nanofabricated and self-assembled magnetic structures as data storage media”. In: *Journal of Physics D: Applied Physics* 38.12 (2005), R199. URL: http://stacks.iop.org/0022-3727/38/i=12/a=R01.

[78] EC Stoner and EP Wohlfarth. “A mechanism of magnetic hysteresis in heterogeneous alloys”. In: *Philosophical Transactions of the Royal Society of London A: Mathematical, Physical and Engineering Sciences* 240.826 (1948), pp. 599–642.

[79] C Suryanarayana. “Mechanical alloying and milling”. In: *Prog. Mater. Sci.* 46 (2001), pp. 1–184.

[80] JS Benjamin. “Mechanical Alloying”. In: *Sci. Am.* 234.5 (1976), pp. 40–49.

[81] HKDH Bhadeshia. “Recrystallisation of practical mechanically alloyed iron-base and nickel-base superalloys”. In: *Materials Science and Engineering A - Structural Material Properties, Microstructre and Processing* 223.1-2 (1997), pp. 64–77.

[82] JS Benjamin. *New materials by mechanical alloying techniques*. Ed. by Arzt E and Schultz L. Oberursel, DE: DGM Informationgesellschaft, 1989.

[83] JS Benjamin. “Mechanical alloying - A perspective”. In: *Met. Powder Rep.* 45.2 (1990), pp. 122–127.

[84] AE Ermakov, EE Yurchikov, and VA Barinov. “Magnetic Properties of Amorphous Y–Co Powders Prepared by Mechanical Milling”. In: *Physics of Metals and Metallography* 52.6 (1981), pp. 1184–1193.

[85] CC Koch, OB Cavin, CG McKamey, and JO Scarbrough. “Preparation of amorphous Ni60Nb40 by mechanical alloying”. In: *Appl Phys Lett.* 43.11 (1983), pp. 1017–1019.

[86] C Suryanarayana, E Ivanov, and V V Boldyrev. “The science and technology of mechanical alloying”. In: *Materials Science and Engineering A* 304 (2001), pp. 151–158.

[87] Shaw KP. *The Hand Book on Mechanical Maintenance*. 2017. URL: practicalmaintenance.net/wp-content/uploads/Diffusion-Mechanisms.jpg (visited on 01/10/2017).

[88] RB Schwarz and WL Johnson. "Formation of an amorphous alloy by solid-state reaction of the pure polycrystalline metals". In: *Phys. Rev. Lett.* 51.5 (1983), pp. 415–418.

[89] HJ Fetch. "Nanophase Materials by Mechanical Attrition: Synthesis and Characterization". In: *Nanophase Materials: Synthesis - Properties - Applications*. Ed. by GC Hadjipanayis and RW Siegel. Netherlands: Kluwer Academic Publisher, 1994, pp. 125–144.

[90] C Suryanarayana. "Nanocrystalline titanium-magnesium alloys through mechanical alloying". In: *Journal of Materials Research* 5.9 (1990), pp. 1880–1886.

[91] PY Lee, JL Yang, and HM Lin. "Amorphization behaviour in mechanically alloyed Ni-Ta powders". In: *Journal of Materials Science* 33.1 (1998), pp. 235–239.

[92] JS Benjamin and TE Volin. "Mechanism of mechanical alloying". In: *Metall. Trans.* 5.8 (1974), pp. 1929–1934.

[93] P R Soni. *Mechanical Alloying: Fundamentals and Applications*. Cambridge International Science Publishing, 2000. ISBN: 9781898326564. URL: https://books.google.es/books?id=25M6AcDumycC.

[94] M L Mahlatji, S Chikosha, HK Chikwanda, WE Stumpf, and CW Siyasiya. "Formation of amorphous Ti-50Pt by solid-state reactions during mechanical alloying". In: *Journal of the Southern African Institute of Mining and Metallurgy* 114.2 (2014), pp. 167–172.

[95] CC Harris. "A method for determining the parameters of the Gaudin-Meloy distribution". In: *Trans. Soc. Mining. Eng.* 238.17 (1967), p. 7.

[96] RM Davis and CC Koch. "Mechanical alloying of brittle components - silicon and germanium". In: *Scr. Met.* 21.3 (1987), pp. 305–310.

[97] RM Davis, B McDermott, and CC Koch. "Mechanical alloying of brittle materials". In: *Metall. Trans. A* 19.12 (1988), pp. 2867–2874.

[98] PY Lee and CC Koch. "Formation of amorphous Ni-Zr alloys by mechanical alloying of mixtures of the intermetallic compounds Ni11Zr9 and NiZr2". In: *Appl. Phys. Lett.* 50.22 (1987), pp. 1578–1580.

[99] iPAT Institut für Partikeltechnik. *Stress processes in planetary ball mills and their application to mill scale-up and transfer*. 2015. URL: http://www.ipat.tu-bs.de/en/forschung/arbeitsgruppen/zerkleinern/beanspruchungsvorgaenge-in-planetenkugelmuehlen-und-deren-anwendung-auf-die-massstabs-und-muehlenuebertragungstress-events-in-planetary-ball-mills-and-their-application-on-scaling-and-mill-changing-b (visited on 09/14/2016).

[100] SD Kaloshkin, IA Tomilin, GA Andrianov, UV Baldokhin, and EV Shelekhov. "Phase transformations and hyperfine interactions in mechanically alloyed Fe-Cu solid solutions". In: *Mater Sci Forum* 235 (1997), pp. 565–570.

[101] LM Di and H Bakker. "No Title". In: *J Phys C Condens Matter* 3 (1991), pp. 3427–3432.

[102] CR Clark, C Wright, C Suryanarayana, EG Baburaj, and FH Froes. "Synthesis of Mg2X (X = Si, Ge, Sn) intermetallics by mechanical alloying". In: *Mater. Lett.* 33.1-2 (1997), pp. 71–75.

[103] T Tanaka, KN Ishihara, and PH Shingu. "Formation of metastable phases of Ni-C and Co-C systems by mechanical alloying". In: *Met. Trans A* 23.9 (1992), pp. 2431–2435.

[104] M Miki, T Yamasaki, and Y Ogino. "Preparation of nanocrystalline NbN and (Nb,Al)N powders by mechanical alloying under nitrogen atmosphere". In: *Mater. Trans. JIM* 33.9 (1992), pp. 839–844.

[105] A Calka and TS Williams. "Synthesis of nitrides by mechanical alloying". In: *Int. symp Mech. Alloy.* Vol. 88. 1992, pp. 787–794.

[106] Y Chen and JS Williams. "Hydriding reactions induced by ball milling". In: *Mater. Sci. Forum* 225-227 (1996). Ed. by R Schulz, pp. 881–888.

[107] AM Harris, GB Schaffer, and NW Page. "The Evolution of Microstructure and Particle Morphology During Mechanical Alloying of Ductile Metals". In: *Mechanical Alloying for Structural Applications* (1993), pp. 15–19.

[108] R Juárez, JJ Suñol, R Berlanga, J Bonastre, and L Escoda. “The effects of process control agents on mechanical alloying behavior of a Fe–Zr based alloy”. In: *Journal of Alloys and Compounds* 434.2 (2007), pp. 472–476. DOI: 10.1016/j.jallcom.2006.08.108.

[109] P Bhattacharya, P Bellon, RS Averback, and SJ Hales. “Nanocrystalline TiAl powders synthesized by high-energy ball milling: effects of milling parameters on yield and contamination”. In: *Journal of Alloys and Compounds* 368.1-2 (2004), pp. 187–196.

[110] RB Schwarz, PB Desch, and SR Srinivasan. “Mechanical properties and microstructure of mechanically alloyed Al-10At-Percent-X (X=Ti,Zr,Hf) alloys”. In: *Mechanical alloying for structural applications*. 1993, pp. 227–235.

[111] JS Byun, JH Shim, and YW Cho. “Influence of stearic acid on mechanochemical reaction between Ti and BN powders”. In: *Journal of Alloys and Compounds* 365.1-2 (2004), pp. 149–156.

[112] A Palacios-Lazcano, JG Cabanas-Moreno, and F Cruz-Gandarilla. “On the formation of a mixed carbide (MgNi3Cx) during production of nanocrystalline Mg2Ni by mechanical alloying”. In: *Scripta Materialia* 52.7 (2005), pp. 571–575.

[113] G Adamek. “Influence of Type of Alcohol as the Process Control Agent on Ti-20Ta-20Nb Alloy Preparation by Mechanical Alloying”. In: *Acta Physica Polonica A* 126.4 (2014), pp. 875–878.

[114] YF Zhang, L Lu, and SM Yap. “Prediction of the amount of PCA for mechanical milling”. In: *Journal of Materials Processing Technology* 90 (1999), pp. 260–265.

[115] V Arnhod and K Hummert. “New materials by MA techniques”. In: 1988.

[116] H Kimura and M Kimura. “Solid-state amorphization of NiTi by reaction ball milling”. In: *Solid State Powder Processing*. Ed. by AH Clauer and JJ de Barbadillo. 1990, pp. 365–377.

[117] CH Lee, M Mori, and T Fukunaga. “Structural evidence for the amorphization of mechanically alloyed Cu-Ta powders studied by neutron-diffraction and exafs”. In: *Mechanical alloying* 88 (1992), pp. 399–406.

[118] Y Chen, R Le Hazif, and G Martin. “Influence of milling conditions on the formation of metastable phases: the crystal to amorphous transition”. In: *Solid State Phenomena*. Vol. 23. Trans Tech Publ. 1992, pp. 271–283.

[119] E Gaffet and L Yousfi. “Crystal to Non-Equilibrium Phase Transition Induced by Ball-Milling”. In: *Materials Science Forum*. Vol. 88. Trans Tech Publ. 1992, pp. 51–58.

[120] Fritsch. *Planetary Micro Mill Pulverisette 7 - classic line*. 2017. URL: http://www.fritsch-international.com/sample-preparation/milling/planetary-mills/details/product/pulverisette-7-classic-line/ (visited on 05/19/2017).

[121] Retsch. *Planetary Ball Mill PM 400*. 2017. URL: http://www.retsch.com/products/milling/ball-mills/planetary-ball-mill-pm-400/function-features/ (visited on 05/19/2017).

[122] Wikimedia Commons. *Scanning electron microscope*. 2016. URL: https://en.wikipedia.org/w/index.php?title=Scanning_electron_microscope (visited on 09/13/2016).

[123] ETH Zurich. *Scanning Electron Microscopy (SEM)*. 2016. URL: http://www.microscopy.ethz.ch/sem.htm (visited on 09/14/2016).

[124] University of Glasgow. *Scanning Electron Microscopy (SEM)*. 2016. URL: http://www.gla.ac.uk/schools/ges/research/researchfacilities/isaac/services/scanningelectronmicroscopy/ (visited on 09/14/2016).

[125] González, A. “Desenvolupament i caracterització d’aliatges de base ferro produïts per Aliatge Mecanic i Solidificació Rapida”. PhD thesis. University of Girona, 2005.

[126] W Zhou and LW Zhong. *Scanning Microscopy for Nanotechnology*. New York, NY: Springer New York, 2007.

[127] University of Girona. *Microscopy Unit (UM)*. 2017. URL: http://www2.udg.edu/serveis/STRUM/Presentaci%C3%B3/tabid/13256/language/en-US/Default.aspx (visited on 05/19/2017).

[128] Nobelprize.org. *Max von Laue - Nobel Lecture: Concerning the Detection of X-ray Interferences*. 2014. URL: http://www.nobelprize.org/nobel%7B%5C_%7Dprizes/physics/laureates/1914/laue-lecture.html.

[129] WH Bragg and WL Bragg. “The Reflexion of X-rays by Crystals”. In: *Proc R. Soc. Lond. A* 88.605 (1913).

[130] Nobelprize.org. *The Nobel Prize in Physics 1915*. 2014. URL: http://www.nobelprize.org/nobel%7B%5C_%7Dprizes/physics/laureates/1915/ (visited on 09/14/2016).

[131] University of Girona. *Chemical Analysis Unit (UAQiE)*. 2017. URL: http://www.udg.edu/serveis/STRUAQ/Presentaci%C3%B3/tabid/13176/language/en-US/Default.aspx (visited on 01/17/2017).

[132] JCPDS - International Centre for Diffraction Data. *The International Centre for Diffraction Data*. 2017. URL: http://www.icdd.com/ (visited on 01/17/2017).

[133] T Bitoh, A Makino, T Hatanai, A Inoue, and T Masumoto. “The relationship between the crystallization process and the soft magnetic properties of nanocrystalline Fe–M–B–Cu (M= Zr, Nb) alloy”. In: *Journal of applied physics* 81.8 (1997), pp. 4634–4636.

[134] BE Warren. *X-ray Diffraction*. Addison-Wesley series in metallurgy and materials engineering (1969). Dover Publications, 1990. ISBN: 9780486663173. URL: https://books.google.es/books?id=wfLBhAbEYAsC.

[135] HM Rietveld. “Line profiles of neutron powder-diffraction peaks for structure refinement”. In: *Acta Cryst.* 22 (1967), p. 151.

[136] FZ Bentayeb, S Alleg, B Bouzabata, and JM Greneche. “Study of alloying mechanisms of ball milled Fe-Cr and Fe-Cr-Co powders”. In: *J. Magn. Magn. Mater.* 288 (2005).

[137] L Lutterotti, S Matthies, and HR Wenk. “MAUD: a friendly Java program for material analysis using diffraction”. In: *IUCr Newsl. CPD* 21 (2000).

[138] RL Mossbauer. “Kernresonanzfluoreszenz von Gammastrahlung in Ir-191”. In: *Zeitschrift für Phys.* 151.2 (1958), pp. 124–143.

[139] Nobelprize.org. *Rudolf Mossbauer - Nobel Lecture: Recoilless Nuclear Resonance Absorption of Gamma Radiation*. 2014. URL: http://www.nobelprize.org/nobel_prizes/physics/laureates/1961/mossbauer-lecture.html (visited on 09/14/2016).

[140] RV Pound and GA Revka. “Variation with temperature of the energy of recoil-free gamma-rays from solids”. In: *Phys. Rev. Lett.* 4.6 (1960), pp. 274–275.

[141] International Board on the Applications of the Mossbauer Effect IBAME and Mossbauer Effect Data Center MEDC. *What is the Mossbauer Effect?* 2014. URL: http://www.mossbauer.info/mossbauer.html (visited on 09/14/2016).

[142] R A Brand, J Lauer, and D M Herlach. “The evaluation of hyperfine field distributions in overlapping and asymmetric Mossbauer spectra: a study of the amorphous alloy Pd77.5-xCu6Si16.5Fex”. In: *Journal of Physics F: Metal Physics* 13.3 (1983), p. 675.

[143] J Hesse and A Rubartsch. “Model independent evaluation of overlapped Mössbauer spectra”. In: *Journal of Physics E: Scientific Instruments* 7.7 (1974), pp. 526–532.

[144] Universitat Politècnica de Catalunya. *Mössbauer spectroscopy*. 2016. URL: http://www.upc.edu/sct/en/equip/152/mossbauer-spectroscopy.html (visited on 10/07/2016).

[145] IUPAC. *Compendium of Chemical Terminology*. 2nd ed. Oxford, UK: Blackwell Scientific Publications, 1985.

[146] University of Girona. *Thermal Analysis Unit (UAT)*. 2017. URL: http://www.udg.edu/serveis/STRUAT/Presentaci%C3%B3/tabid/13395/language/en-US/Default.aspx (visited on 01/17/2017).

[147] H Kissinger. “Reaction kinetics in differential thermal analysis”. In: *Analytical Chemistry* 29.11 (1957), pp. 1702–1706.

[148] T Ozawa. “Kinetic analysis of derivative curves in thermal analysis”. In: *Journal of Thermal Analysis* 2 (1970), pp. 301–324.

[149] B Carroll and EP Manche. “Kinetic analysis of chemical reactions for non-isothermal procedures”. In: *Thermochimica acta* 3.6 (1972), pp. 449–459.

[150] C Wagner. *Pittsburgh International Conference on Surface Reactions*. 1948.

[151] G Valensi. “Kinetics of the oxidation of metallic wires”. In: *Compt. Rend* 201 (1935), pp. 602–604.

[152] RE Carter. “Kinetic Model for Solid-State Reactions”. In: *The Journal of Chemical Physics* 34.6 (1961), pp. 2010–2015.

[153] R E Carter. “Addendum: Kinetic Model for Solid-State Reactions”. In: *The Journal of Chemical Physics* 35.3 (1961), pp. 1137–1138.

[154] J Sestak. “Non-isothermal kinetics”. In: *Proc. 3rd Intl. Conf. Therm. Anal. Davos*. Vol. 2. 1971, pp. 3–30.

[155] M Avrami. “Kinetics of phase change - I. General theory”. In: *Journal of Chemical Physics* 7.12 (1939), pp. 1103–111.

[156] M Avrami. “Kinetics of Phase Change - II. Transformation-Time Relations for Random Distribution of Nuclei”. In: *Journal of Chemical Physics* 8.2 (1940), pp. 212–224.

[157] M Avrami. “Kinetics of Phase Change - III. Granulation, Phase Change, and Microstructure”. In: *Journal of Chemical Physics* 9.2 (1941), pp. 177–184.

[158] WA Johnson and RF Mehl. “Reaction kinetics in processes of nucleation and growth”. In: *Transactions of the Amrican Institute of Mining and Metallurgical Engineers* 135 (1939), pp. 416–442.

[159] P Germain, K Zellama, S Squelard, JC Bourgoin, and A Gheorghiu. “Crystallization in amorphous germanium”. In: *Journal of Applied Physics* 50.11 (1979), pp. 6986–6994.

[160] JJ Suñol. “Contribució a l’estudi d’aliatges metall-metaloide obtinguts per aliatge mecànic i per solidificació ràpida”. PhD thesis. Autonomous University of Barcelona, 1996.

[161] UPV/EHU. *Equipment SGIker - UPV/EHU*. 2017. URL: https://investigacion.us.es/scisi/sgi/servicios/caracterizacion-funcional/equipamiento-scf (visited on 01/17/2017).

[162] University of Sevilla. *Caracterización funcional: equipamiento*. 2017. URL: https://investigacion.us.es/scisi/sgi/servicios/caracterizacion-funcional/equipamiento-scf (visited on 01/17/2017).

[163] PK Gallagher. “Thermoanalytical Methods”. In: *Materials Science and Technology: A Comprehensive Treatment - Vol 2A: Characterization of materials*. Ed. by Cahn, RW and Haasen, P and Kramer, EJ and Lifshin, E. VCH, 1992. Chap. 7. ISBN: 9783527268139.

[164] PK Gallagher. “Aspects of thermal analysis and calorimetry”. In: *Thermochim. Acta* 121 (1987), pp. 1–19.

[165] J Bonastre. “Desenvolupament i caracterització d’aliatges de base Fe-Co produïts per aliatge mecànic”. MA thesis. University of Girona, 2006.

[166] U Hartmann and HH Mende. “Ferrohydrodynamical fundamentals of ferrofluid Bitter pattern evolution”. In: *Zeitschrift f{ü}r Physik B Condensed Matter* 61.1 (1985), pp. 29–32.

[167] S Porthun, P ten Berge, and JC Lodder. “Bitter colloid observations of magnetic structures in perpendicular magnetic recording media”. In: *Journal of magnetism and magnetic materials* 123.1-2 (1993), pp. 199–208.

[168] DJ Craik. “Magnetic fields from subdivided surfaces”. In: *British Journal of Applied Physics* 17.7 (1966), p. 873.

[169] W Xiong, M Selleby, Q Chen, J Odqvist, and Y Du. “Phase Equilibria and Thermodynamic Properties in the Fe-Cr System”. In: *Critical Reviews in Solid State and Materials Sciences* 35.2 (2010), pp. 125–152.

[170] SM Dubiel and J Żukrowski. “Fe-rich border and activation energy of phase decomposition in a Fe-Cr alloy”. 2013.

[171] HH Yao, Z Zhou, YM Wang, DY He, K Bobzin, L Zhao, M Öte, and T Königstein. “Microstructure and Properties of FeCrB Alloy Coatings Prepared by Wire-Arc Spraying”. In: *Journal of Thermal Spray Technology* (), pp. 1–9.

[172] V Franco, A Conde, and L F Kiss. “Magnetocaloric response of Fe-Cr-B amorphous alloys: Predicting the magnetic entropy change from the Arrot-Noakes equation of state”. In: *J. Appl. Phys.* 104.3 (2008).

[173] P Alvaredo, S Tsipras, and E Gordo. “Influence of carbon content on the sinterability of an FeCr matrix reinforced with TiCN”. In: *Journal of Applied Physics* 36 (2013).

[174] T P C Klaver, R Drautz, and M W Finnis. “Magnetism and thermodynamics of defect-free Fe-Cr alloys”. In: 74.9 (2006), p. 94435.

[175] P Olsson, I A Abrikosov, and J Wallenius. “Electronic origin of the anomalous stability of Fe-rich bcc Fe-Cr alloys”. In: *Phys. Rev. B* 73.10 (2006), p. 104416.

[176] A Hishinuma, A Kohyama, R.L Klueh, D.S Gelles, W Dietz, and K Ehrlich. “Current status and future R&D for reduced-activation ferritic/martensitic steels”. In: *Journal of Nuclear Materials* 258 (1998), pp. 193–204.

[177] F.A Garner, M.B Toloczko, and B.H Sencer. “Comparison of swelling and irradiation creep behavior of fcc-austenitic and bcc-ferritic/martensitic alloys at high neutron exposure”. In: *Journal of Nuclear Materials* 276.1 (2000), pp. 123–142.

[178] SM Dubiel and J Cieslak. “Short-range order in iron-rich Fe-Cr alloys as revealed by Mössbauer spectroscopy”. In: *Phys. Rev. B* 83.18 (2011).

[179] SM Dubiel, C Sauer, and W Zinn. “Mössbauer effect sutdy of a nearly homogeneous Cr75Fe25 alloy doped with 0.6 at% 119Sn”. In: *Physical Review B* 30.11 (1984), pp. 6285–6291.

[180] I Mirebeau, M Hennion, and G Parette. “1st Measurement of short-range order inversion as a function of concentration in a transition alloy”. In: *Physical Review Letters* 53.7 (1984), pp. 687–690.

[181] Martínez, E and Senninger, O and Fu, CC and Soisson, F. “Decomposition kinetics of Fe-Cr solid solutions during thermal aging”. In: *Physica Review B* 86.22 (2012).

[182] B Fultz, H Kuwano, and H Ouyang. “Average Widths of grain-boundaries in nanophase alloys by mechanical attrition”. In: *Journal of Applied Physics* 77.7 (1995), pp. 3458–3466.

[183] G LeCaer, P Delcroix, TD Shen, and B Malaman. “Mössbauer investigation of intermixing during ball milling of Fe0.3Cr0.7 and Fe0.5W0.5 powder mixtures”. In: *Physical Review B* 54.18 (1996), pp. 12775–12786.

[184] A Otmani, B Bouzabata, A Djekoun, and S Alleg. “Preparation by mechanical alloying and study of the FeCr compound”. In: *Annales de chimie-science des materiaux* 22.3-4 (1997), pp. 201–206.

[185] C Lemoine, A Fridiki, D Lemarchand, and J Teillet. “Mössbauer and TEM study of Fe-Cr powcers elaborated by mechanical alloying”. In: *J. Magn. Magn. Mater.* 203 (1999).

[186] C Lemoine, A Fnidiki, D Lemarchand, and J Teillet. “Grain core study of Fe(1-x)Cr(x) nanograins obtained by mechanical alloying”. In: *Journal of Physics - Condensed matter* 11.42 (1999), 8341–8350.

[187] SK Xia, E Baggiosaitovitch, and FCR Assuncao. “The structural relaxation of Cr65Fe35 amorphous powder obtained by mechanical milling”. In: *Journal of Alloys and Compounds* 196.1-2 (1993), 177–181.

[188] J He, L Zhou, DL Zhao, and XL Wang. “Hysteresis loop shift behavior of CoFeSiB amorphous ribbons”. In: *J. Mater. Res.* 24.4 (2009), pp. 1607–1610.

[189] G Cui and Z Kou. “The effect of boron on mechanical behavior and microstructure for Fe-Cr matrix alloy prepared by PM”. In: *Journal of Alloys and Compounds* 586 (2014), pp. 699–702. ISSN: 09258388. DOI: 10.1016/j.jallcom.2013.10.110. URL: http://www.sciencedirect.com/science/article/pii/S0925838813025255.

[190] T Koyano, T Takizawa, T Fukunaga, U Mizutani, S Kamizuru, E Kita, and A Tasaki. “Mechanical alloying process of Fe-Cr powders studied by magnetic measurements”. In: *J. Appl. Phys.* 73 (1993).

[191] JJ Suñol, R Berlanga, MT Clavaguera-Mora, and N Clavaguera. “Modeling crystallization processes: transformation diagrams”. In: *Acta Mater.* 50.19 (2002), pp. 4783–4790.

[192] JJ Suñol, A González, T Pradell, P Bruna, MT Clavaguera-Mora, and N Clavaguera. “Thermal and structural changes induced by mechanical alloying in melt-spun Fe-Ni based amorphous alloys”. In: *Mater. Sci. Eng. A* 375 (2004), pp. 881–887.

[193] J.J. Suñol, A Gonzalez, J Bonastre, MT Clavaguera-Mora, and B Arcondo. “Synthesis and characterization of nanocrystalline FeNiZrB developed by mechanical alloying”. In: *Journal of Alloys and Compounds* 434-435 (2005), pp. 415–419. DOI: 10.1016/j.jallcom.2006.08.319.

[194] A González, JJ Suñol, J Bonastre, L Escoda, and J Caleya. “Thermal behavior of several Fe-Ni alloys prepared by mechanical alloying and rapid solidification”. In: *Journal of Thermal Analysis and Calorimetry* 80.2 (2005), pp. 253–256. DOI: 10.1007/s10973-005-0644-3.

[195] SM Dubiel, BFO Costa, J Cieslak, and AC Batista. “Debye temperature of nanocrystalline Fe-Cr alloys obtained by mechanical alloying”. In: *Journal of Alloys and Compounds* 649 (2015), pp. 1246–1252. ISSN: 09258388. DOI: 10.1016/j.jallcom.2015.07.067.

[196] RA Rastabi, A Ghasemi, M Tavoosi, and T Sodaee. “Magnetic characterization of nanocrystalline Fe(80-x)Cr(x)Co20 (15<=x<=35) alloys during milling and subsequent annealing”. In: *Journal of Magnetism and Magnetic materials* 416 (2016), pp. 174–180.

[197] JJ Suñol, A González, J Saurina, L Escoda, and L Fernández Barquín. “Thermal and magnetic behavior of a nanocrystalline Fe(Ni, Co) based alloy”. In: *Journal of Non-Crystalline Solids* 353.8-10 (2007), pp. 865–868.

[198] YH Zhao, HW Sheng, and K Lu. “Microstructure evolution and thermal properties in nanocrystalline Fe during mechanical attrition”. In: *Acta Materialia* 49 (2001), pp. 365–375.

[199] IUH Toor, J Ahmed, MA Hussein, F Patel, and N Al-Aqeeli. “Phase evolution studies during mechanical alloying of Fe(82-x)-Cr-18-Si-x (x=0,1,2,3) alloy”. In: *Journal of Alloys and Compounds* 683 (2016), pp. 463–469.

[200] WD Wang, SH Zhang, and XL He. “Diffusion of boron in alloys”. In: *Acta Metallurgica et Materialia* 43.4 (1995), pp. 1693–1699.

[201] T Van Rompaey, KCH Kumar, and P Wollants. “Thermodynamic optimization of the B-Fe system”. In: *Journal of Alloys and Compounds* 334 (2002), pp. 173–181.

[202] PE Busby and C Wells. “Diffusion of boron in alpha-iron”. In: *Journal of Metals* 6.9 (1954), p. 972.

[203] PM Strocchi, BA Melandri, and A Tamba. “On nature of boron solid solution in alpha-iron”. In: *Nuovo Cimento B* 51.1 (1967), p. 1.

[204] WR Thomas and GM Leak. “Condition of boron in alpha-iron”. In: *Nature* 176.4470 (1955), pp. 29–31.

[205] DHR Fors and G Wahnstrom. “Nature of boron solution and diffusion in alpha-iron”. In: *Physical Review B* 77.13 (2008).

[206] U Patil, S H Hong, and C Suryanarayana. “An unusual phase transformation during mechanical alloying of an Fe-based bulk metallic glass composition”. In: *Journal of Alloys and Compounds* 389.1-2 (2005), pp. 121–126.

[207] N Ammouchi, A Otmani, Z Bensebaa, S Azzaza, M Bououdina, A Djekoun, L Bechiri, and J M Grénèche. “Structural, Microstructural and Magnetic Characterizations of Mechanically Alloyed Fe65Si20Cr15 Powders Mixture”. In: *Journal of Superconductivity and Novel Magnetism* 28.12 (2015), pp. 3651–3661.

[208] H Okumura, KN Ishihara, PH Shingu, HS Park, and S Nasu. “Mechanical alloying of Fe-B alloys”. In: *Journal of materials science* 27.1 (1992), pp. 153–160.

[209] VI Dybkov, W Lengauer, and K Barmak. “Formation of boride layers at the Fe-10% Cr alloy-boron interface”. In: *Journal of Alloys and Compounds* 398.1 (2005), pp. 113–122.

[210] MM Rico, JM Greneche, and GA Pérez Alcázar. “Effect of boron on structural and magnetic properties of the Fe60Al40 system prepared by mechanical alloying”. In: *Journal of Alloys and Compounds* 398.1 (2005), pp. 26–32. ISSN: 09258388. DOI: 10.1016/j.jallcom.2005.02.029.

[211] JD Santos, J Olivera, P Gorria, MJ Pérez, ML Sánchez, B Hernando, VM Prida, A Fernández-Martínez, and G Cuello. “Structural evolution and magnetic properties in Fe70Cr10B20 ribbons”. In: *Journal of Magnetism and Magnetic Materials* 294.2 (2005), e155–e158. ISSN: 03048853. DOI: 10.1016/j.jmmm.2005.03.074.

[212] C Guo and PM Kelly. “Boron solubility in Fe–Cr–B cast irons”. In: *Materials Science and Engineering: A* 352.1 (2003), pp. 40–45.

[213] VD Mote, Y Purushotham, and BN Dole. “Williamson-Hall analysis in estimation of lattice strain in nanometer-sized ZnO particles”. In: *Journal of Theoretical and Applied Physics* 6.1 (2012), pp. 1–8.

[214] SW Du and RV Ramanujan. “Mechanical alloying of Fe-Ni based nanostructured magnetic materials”. In: *Journal of magnetism and magnetic materials* 292 (2005), pp. 286–298.

[215] M Ferrari and L Lutterotti. “Method for the simultaneous determination of anisotropic residual-stresses and texture by X-ray diffraction”. In: *Journal of Applied Physics* 76.11 (1994), pp. 7246–7255.

[216] GK Williamson and RE Smallman. “Dislocation densities in some annealed and cold-worked metals from measurements on the X-Ray Debye-Scherrer spectrum”. In: *Philosophical magazine* 1.1 (1956), pp. 34–46.

[217] RE Smallman and KH Westmacott. “Stacking faults in face-centered cubic metals and alloys”. In: *Philosophical magazine* 2.17 (1957), pp. 669–683.

[218] KJ Van Vliet. *Mechanical Behavior of Materials*. 2006.

[219] R Amini, M J Hadianfard, E Salahinejad, M Marasi, and T Sritharan. “Microstructural phase evaluation of high-nitrogen Fe-Cr-Mn alloy powders synthesized by the mechanical alloying process”. In: *Journal of Materials Science* 44.1 (2008), p. 136. ISSN: 1573-4803. DOI: 10.1007/s10853-008-3117-9. URL: http://dx.doi.org/10.1007/s10853-008-3117-9.

[220] HJ Fecht. “Nanostructure formation by mechanical attrition”. In: *Nanostructured Materials* 6.1-4 (1995), pp. 33–42.

[221] F Hadef, A Otmani, A Djekoun, and J M Greneche. “Mossbauer effect study of fine atomic structure of Fe50Al40Ni10 powders”. In: *SUPERLATTICES AND MICROSTRUCTURES* 51.6 (2012), pp. 952–958.

[222] H Kuwano. “Mössbauer-effect study on the miscibility gap of the iron-chromium binary systems”. In: *Transactions of the Japan Institute of Metals* 26.7 (1985), pp. 473–481.

[223] SM Dubiel and J Zükrowski. “Mössbauer-effect study of charge and spin transfer in Fe-Cr”. In: *Journal of Magnetism and Magnetic materials* 23.2 (1981), pp. 214–228.

[224] H Moumeni, S Alleg, and JM Greneche. “Structural properties of Fe50Co50 nanostructured powder prepared by mechanical alloying”. In: *Journal of Alloys and Compounds* 386.1-2 (2005), pp. 12–19.

[225] SM Dubiel. “Relationship between the magnetic hyperfine field and the magnetic moment”. In: *Journal of Alloys and Compounds* 488.1 (2009), pp. 18–22.

[226] N Ito, K Suzuki, JS Garitaonandia, and JD Cashion. “Effect of boron on the field-induced magnetic anisotropy in Fe-based soft magnetic nanostructures”. In: *Journal of Applied Physics* 105.7 (2009), 07A321.

[227] M Multigner, A Hernando, P Crespo, C Stiller, J Eckert, and L Schultz. “Structural and magnetic properties of mechanically alloyed (FexCu1-x)(93)Zr(7) (x=0.5, 0.7) solid solutions”. In: *Journal of Magnetism and Magnetic materials* 196 (1999), pp. 214–215.

[228] M T Clavaguera-Mora, J J Sunol, and N Clavaguera. “Relaxation kinetics of mechanically alloyed powders. Fe-Ni-Si-P: A case study”. In: *Metastable, mechanically alloyed and nanocrystalline materials, ISMANAM-2000*. Vol. 360-3. Zurich, 2001, pp. 459–466.

[229] SM Dubiel and K Krop. “Influence of neighbouring chromium atoms on hyperfine fields at 57Fe nuclei and isomer shifts in Fe-Cr alloys”. In: *Le Journal de Physique Colloques* 35.C6 (1974), pp. C6–459.

[230] A Fnidiki, C Lemoine, J Teillet, and JJ Malandain. “Mixing at micrometric and nanometric scale in mechanically alloyed Fe60Cr40”. In: *Physica B: Condensed Matter* 327.2-4 (2003), pp. 140–143. ISSN: 09214526. DOI: 10.1016/S0921-4526(02)01713-1.

[231] G Shen, DM Jiang, F Lin, WZ Shi, and XM Ma. “Mössbauer study on the disordered Fe60Cr40 alloys prepared by mechanical alloying”. In: *Physica B: Condensed Matter* 367.1 (2005), pp. 137–141. ISSN: 09214526. DOI: 10.1016/j.physb.2005.06.008.

[232] D Fiorani, H Romero, L Suber, A M Testa, J L Dormann, J Maknani, and N Sparvieri. “Magnetic properties of amorphous Fe(80-x)Cr(x)B20 particles”. In: *Journal of Magnetism and Magnetic Materials* 140 (1995), pp. 411–412. ISSN: 0304-8853. DOI: http://dx.doi.org/10.1016/0304-8853(94)01348-9. URL: http://www.sciencedirect.com/science/article/pii/0304885394013489.

[233] N Bensebaa, S Alleg, N Loudjani, and JM Greneche. “Effect of the milling conditions on the amorphisation of Fe77Cr4P8C11 alloy”. In: *Annales de chimie-science des materiaux* 35.3 (2010), pp. 177–186.

[234] RS Turtelli, T Krenicky, A Penton-Madrigal, R Groessinger, I Skorvanek, H Sassik, E Estevez-Rams, M Schoenhart, and CD Barbatti. “Magnetic and structural characterization of as-cast and annealed melt-spun Fe(80-x)Si(20)Cr(x)”. In: *Journal of Magnetism and Magnetic Materials* 304.2 (2006), E687–E689.

[235] JJ Suñol, JM Güell, J Bonastre, and S Alleg. “Structural study of nanocrystalline Fe-Co-Nb-B alloys prepared by mechanical alloying”. In: *Journal of Alloys and Compounds* 483 (2009). DOI: 10.1016/j.jallcom.2008.07.212.

[236] H Iwanabe, B Lu, ME McHenry, and DE Laughlin. “Thermal stability of the nanocrystlline Fe-Co-Hf-B-Cu alloy”. In: *J. Appl. Phys.* 85 (1999).

[237] S Hendi, SK Deni, U Pudji, SM Husin, and S Darwin. “Determination of nanocrystalline Fe80Cr20 powder based alloys using Williamson-Hall method”. In: *Mater. Manuf. Technol. B. Ser. Adv. Mater. Res.* 129-131 (2010).

[238] A Fnidiki, C Lemoine, and J Teillet. “Properties of mechanically alloyed Fe(100-x)Cr(x) powder mixtures: Mössbauer study”. In: *Physica B: Condensed Matter* 357.3 (2005), pp. 319–325. ISSN: 09214526. DOI: 10.1016/j.physb.2004.11.083.

[239] T Sourmail. “Near equiatomic FeCo alloys: Constitution, mechanical and magnetic properties”. In: *Progress in Materials Science* 50.7 (2005), pp. 816–880.

[240] S Azzaza, S Alleg, H Moumeni, AR Nemamcha, JL Rehspringer, and JM Greneche. “Magnetic properties of nanostructured ball-milled Fe and Fe50Co50 alloy”. In: *Journal of Physics - Condensed matter* 18.31 (2006), pp. 7257–7272.

[241] M. Khajepour and S. Sharafi. “Structural and magnetic properties of nanostructured (Fe50Co50)-6.5Si powder prepared by high energy ball milling”. In: *Journal of Alloys and Compounds* 509.29 (2011), pp. 7729–7737.

[242] MD Chermahini, MR Rahimipour, and AH Pakseresht. “Microstructure and magnetic properties of nanostructured Fe-Co powders prepared by series of milling and annealing treatments”. In: *Advanced Powder Technology* 25.1 (2014), pp. 462–466.

[243] ZL Caamaño-De Avila, MA Consuegra-Peña, MD Baró, and S Surinach. “Synthesis and characterization of nanostructured materials based on Fe50Co50 and Fe75Co25”. In: *CTyF-Ciencia, Tecnología y Futuro* 6 (2015), pp. 33–44.

[244] R Bruning, K Samwer, C Kuhrt, and L Schultz. “The mixing of iron and cobalt during mechanical alloying”. In: *Journal of Applied Physics* 72.7 (1992).

[245] A Sharifati and S Sharafi. “Structural and magnetic properties of nanostructured (Fe70Co30)(100-x)Cu(x) alloy prepared by high energy ball milling”. In: *Materials and Design* 41 (2012), pp. 8–15.

[246] Kyung-Hwan Kim, Sok-Hyun Kong, and Shigeki Nakagawa. “Control of magnetic anisotropy in Fe-Co-B soft magnetic underlayer for perpendicular magnetic recording media”. In: *Journal of electroceramics* 23.2-4 (2009), p. 191.

[247] H Shokrollahi. “The magnetic and structural properties of the most important alloys of iron produced by mechanical alloying”. In: *Materials and Design* 30.9 (2009), pp. 3374–3387.

[248] S. Bergheul, F. Otmane, and M. Azzaz. “Structural and microwave absorption properties of nanostructured Fe-Co alloys”. In: *Advanced Powder Technology* 23.5 (2012), pp. 580–582.

[249] M Yousefi and S Sharafi. “The effect of simultaneous addition of Si and Co on microstructure and magnetic properties of nanostructured iron prepared by mechanical alloying”. In: *Materials and Design* 37 (2012), pp. 325–333.

[250] J Kim, M Kim, F Herrault, J Park, and MG Allen. “Highly laminated soft magnetic electroplated CoNiFe thick films”. In: *IEEE Magnetics Letters* 4 (2013), p. 5000204.

[251] S Alleg, FZ Bentayeb, R Bensalem, C Djebbari, L Bessais, and JM Greneche. “Effect of the milling conditions on the formation of nanostructured Fe-Co powders”. In: *Physica Status Solidi A* 205.7 (2008), pp. 1641–1646.

[252] C Kuhrt and L Schultz. “Formation and magnetic properties of nanocrystalline mechanically alloyed Fe-Co”. In: *Journal of Applied Physics* 71.4 (1992), pp. 1896–1900.

[253] Young Do Kim, Jin Youl Chung, Jongryoul Kim, and Hyeongtag Jeon. “Formation of nanocrystalline Fe-Co powders produced by mechanical alloying”. In: *Materials Science and Engineering: A* 291.1 (2000), pp. 17–21.

[254] T Nishizawa and K Ishida. *Binary alloy phase diagrams*. 2nd ed. Vol. 2. ASM International, OH, 1990.

[255] I Ohnuma, H Enoki, O Ikeda, R Kainuma, H Ohtani, B Sundman, and K Ishida. "Phase equilibria in the Fe–Co binary system". In: *Acta Materialia* 50.2 (2002), pp. 379–393.

[256] N E Fenineche, O El Kedim, and Eric Gaffet. "Magnetic Properties Study Of Nanocrystalline Cobalt and Cobalt-Based Alloys". In: *Journal of Metastable and Nanocrystalline Materials: e-Volume 2000*. Vol. 7. Journal of Metastable and Nanocrystalline Materials. Trans Tech Publications, 1999, pp. 41–48.

[257] J Löffler and J Weissmüller. "Grain-boundary atomic-structure in nanocrystalline palladium from X-ray atomic distribution functions". In: *PHYSICAL REVIEW B* 52.10 (1995), pp. 7076–7093.

[258] M Matsuda, K Yamashita, R Sago, K Akamine, K Takashima, and M Nishida. "Development of Ductile B2-Type Fe-Co Based Alloys". In: *Materials Transactions* 53.10 (2012), pp. 1826–1828.

[259] K Kawahara. "Structures and mechanical properties of an FeCo-2V alloy". In: *Journal of Materials Science* 18.11 (1983), pp. 3427–3436. ISSN: 1573-4803. DOI: 10.1007/BF00544171. URL: http://dx.doi.org/10.1007/BF00544171.

[260] MJ Marcinkowski and J Larsen. "The effect of atomic order on fracture surface morphology". In: *Metallurgical Transactions* 1.4 (1970). DOI: 10.1007/BF02811791.

[261] M Matsuda, R Sago, K Akamine, S Tsurekawa, K Takashima, and M Nishida. "Enhancement of ductility in Fe-Co based alloys by substitution of Pd". In: *Journal of Alloys and Compounds* 682 (2016), pp. 124–131.

[262] K Hirano and M Cohen. "Diffusion of cobalt in iron-cobalt alloys". In: *Transactions of the Japan Institute of Metals* 13.2 (1972), p. 96.

[263] AD LeClaire and G Neumann. "3.2.8 Iron group metals". In: *Diffusion in Solid Metals and Alloys*. Springer-Verlag, pp. 124–130.

[264] F Cardellini and G Mazzone. "Thermal and structural study of the hcp-to-fcc transformation in cobalt". In: *Philosophical Magazine A* 67.6 (1993), pp. 1289–1300.

[265] J Y Huang, Y K Wu, H Q Ye, and K Lu. "Allotropic transformation of cobalt induced by ball milling". In: *NANOSTRUCTURED MATERIALS* 6.5-8 (1995), pp. 723–726.

[266] J.Y JY Yang, J.S JS Wu, TJ T.J Zhang, and K Cui. "Multicomponent mechanical alloying of Fe–Cu–Nb–Si–B". In: *Journal of Alloys and Compounds* 265.1 (1998), pp. 269–272. ISSN: 09258388. DOI: 10.1016/S0925-8388(97)00308-3.

[267] A Grabias, M Kopcewicz, and D Oleszak. "Phase transformations in the Fe (Co, Ni) ZrB alloys induced by ball milling". In: *Journal of alloys and compounds* 339.1 (2002), pp. 221–229.

[268] T Nishizawa and K Ishida. "The Co-Fe (Cobalt-Iron) system". In: *Bulletin of Alloy Phase Diagrams* 5.3 (1984), p. 250.

[269] TB Massalski, H Okamoto, and PR Subramanian. *Binary Alloy Phase Diagrams*. ASM International, 1990. ISBN: 9780871704030.

[270] Computational Thermodynamics. *Iron-Cobalt (Fe-Co) Phase Diagram*. 2016. URL: http://www.calphad.com/iron-cobalt.html (visited on 10/13/2016).

[271] V Raghavan. "B-Co-Fe (Boron-Cobalt-Iron)". In: *Journal of Phase Equilibria and Diffusion* 33.5 (2012), pp. 392–394.

[272] Y Han, A Inoue, FL Kong, CT Chang, SL Shu, E Shalaan, and F Al-Marzouki. "Softening and good ductility for nanocrystal-dispersed amorphous Fe-Co-B alloys with high saturation magnetization above 1.7 T". In: *Journal of Alloys and Compounds* 657 (2016), pp. 237–245.

[273] S U Jen, H P Chiang, C M Chung, and M N Kao. "Magnetic properties of Co-Fe-Ni films". In: *Journal of Magnetism and Magnetic Materials* 236.3 (2001), pp. 312–319.

[274] E Jartych. "On the magnetic properties of mechanosynthesized Co-Fe-Ni ternary alloys". In: *Journal of Magnetism and Magnetic Materials* 323.2 (2011), pp. 209–216.

[275] NDT - Resource Center. *Solid State Structure*. 2017. URL: https://www.nde-ed.org/EducationResources/CommunityCollege/Materials/Structure/solidstate.htm/ (visited on 06/14/2017).

[276] B DeMayo, DW Forester, and S Spooner. “Effects of atomic configurational changes on hyperfine interactions in concentrated iron-cobalt alloys”. In: *Journal of Applied Physics* 41.3 (1970), p. 1319.

[277] J Foct, JP Senateur, JM Dubois, and G Le Caer. “Mössbauer Spectroscopy of Different Interstitial Compounds and Solid Soltuions Containing 57Fe”. In: *Le Journal de Physique Colloques* 40.C2 (1979), pp. 647–649.

[278] H Moumeni, S Alleg, C Djebbari, FZ Bentayeb, and JM Grenèche. “Synthesis and characterisation of nanostructured FeCo alloys”. In: *Journal of Materials Science* 39.16 (2004), pp. 5441–5443.

[279] YJ Liu, ITH Chang, and P Bowen. “Amorphization and microstructural evolution in multicomponent (FeCoNi)70Zr10B20 alloy system by mechanical alloying”. In: *Materials Science and Engineering A* (2001).

[280] T.R Malow and C.C Koch. “Grain growth in nanocrystalline iron prepared by mechanical attrition”. In: *Acta Materialia* 45.5 (1997), pp. 2177–2186. ISSN: 13596454. DOI: 10.1016/S1359-6454(96)00300-X.

[281] PV Krakhmalev, D Yi, L Nyborg, and Y Yao. “Isothermal grain growth in mechanically alloyed nanostructured Fe80Ti8B12 alloy”. 2003.

[282] F Johnson, P Hughes, R Gallagher, DE Laughlin, ME McHenry, MA Willard, and VG Harris. “Structure and thermomagnetic properties of new FeCo-based nanocrystalline ferromagnets”. In: *IEEE Transactions on Magnetics* 37.4 (2001), pp. 2261–2263. ISSN: 0018-9464. DOI: 10.1109/20.951142.

[283] F Ye and K Lu. “Crystallization kinetics of Al-La-Ni amorphous alloy”. In: *Journal of Non-Crystalline Solids* 262.1 (2000), pp. 228–235.

[284] RS De Biasi and MLN Grillo. “FMR study of crystallization in the amorphous alloy Fe67Co18B14Si1 (Metglas 2605CO)”. In: *Journal of alloys and compounds* 279.2 (1998), pp. 233–236.

[285] T Gheiratmand, HRM Hosseini, P Davami, M Gjoka, G Loizos, and H Aashuri. “Effect of annealing on soft magnetic behavior of nanostructured (Fe0.5Co0.5)73.5Si13.5B9Nb3Cu1 ribbons”. In: *Journal of Alloys and Compounds* 582 (2014), pp. 79–82. ISSN: 09258388. DOI: 10.1016/j.jallcom.2013.08.038.

[286] HA Shivaee, M Samadi, H Alihosseini, and HRM Hosseini. “Nanocrystallization kinetics and magnetic properties of the melt spun amorphous (Fe0.5Co0.5)77Si11B9Cu0.6Nb2.4 alloy”. In: *Thermochimica Acta* 575 (2014), pp. 64–69. ISSN: 00406031. DOI: 10.1016/j.tca.2013.10.022.

[287] NE Fenineche, R Hamzaoui, and O El Kedim. “Structure and magnetic properties of nanocrystalline Co-Ni and Co-Fe mechanically alloyed”. 2003.

[288] HF Li and RV Ramanujan. “Synthesis of Fe-Co based nanomagnetic materials”. In: *Transactions of the Indian Institute of Metals* 58.6 (2005), pp. 965–970.

[289] S Alleg, S Azzaza, R Bensalem, JJ Suñol, S Khene, and G Fillion. “Magnetic and structural studies of mechanically alloyed (Fe50Co50)62Nb8B30 powder mixtures”. In: *Journal of Alloys and Compounds* 482.1 (2009), pp. 86–89. ISSN: 09258388. DOI: 10.1016/j.jallcom.2009.03.189.

[290] S Bergheul, A Haddad, A Tafat, and M Azzaz. “Magnetic microwave and absorbing properties of Fe-Co alloy synthesised by mechanical alloying process”. In: *International journal of microstructure and materials properties* 1.3-4 (2006), pp. 334–340.

[291] RC Kambale, PA Shaikh, SS Kamble, and YD Kolekar. “Effect of cobalt substitution on structural, magnetic and electric properties of nickel ferrite”. In: *Journal of Alloys and Compounds* 478.1 (2009), pp. 599–603.

[292] F Sánchez-De Jesús, AM Bolarín-Miró, CA Cortés Escobedo, G Torres-Villaseñor, and P Vera-Serna. “Structural Analysis and Magnetic Properties of FeCo Alloys Obtained by Mechanical Alloying”. In: *Journal of Metallurgy* 2016 (2016).

[293] L Xue, W Yang, H Liu, H Men, A Wang, C Chang, and B Shen. “Effect of Co addition on the magnetic properties and microstructure of FeNbBCu nanocrystalline alloys”. In: *Journal of Magnetism and Magnetic Materials* 419 (2016), pp. 198–201.

[294] AN Popova, YA Zaharov, and VM Pugachev. “Chemical synthesis, structure and magnetic properties of nanocrystalline Fe-Co alloys”. In: *Materials Letters* 74 (2012), pp. 173–175.

[295] E Suharyadi, A Riyanto, K Abraha, H Susanto, R Suryana, and K Triyana. “The annealing temperature dependences of microstructures and magnetic properties in electro-chemical deposited CoNiFe thin films”. In: *AIP Conference Proceedings*. Vol. 1725. 1. AIP Publishing. 2016, p. 020082.

[296] E Jartych, J K Zurawicz, D Oleszak, and M Pekekala. “Hyperfine interactions, structure and magnetic properties of nanocrystalline Co-Fe-Ni alloys prepared by mechanical alloying”. In: *Hyperfine Interactions* 168.1 (2006), pp. 989–994.

[297] K Chokprasombat, S Pinitsoontorn, and S Maensiri. “Effects of Ni content on nanocrystalline Fe-Co-Ni ternary alloys synthesized by a chemical reduction method”. In: *Journal of Magnetism and Magnetic Materials* 405 (2016), pp. 174–180.

[298] Xingguo Li and Seiki Takahashi. “Synthesis and magnetic properties of Fe-Co-Ni nanoparticles by hydrogen plasma-metal reaction”. In: *Journal of Magnetism and Magnetic Materials* 214.3 (2000), pp. 195–203. ISSN: 03048853. DOI: 10.1016/S0304-8853(00)00081-0.

[299] YQ Liu, XS Zhao, J Yang, and JY Shen. “Thermodynamic optimization of the boron–cobalt–iron system”. In: *Journal of alloys and Compounds* 509.14 (2011), pp. 4805–4810.

[300] FJ Humphreys and M Hatherly. *Recrystallization and related annealing phenomena*. Elsevier, 2004.

[301] T Sourmail. “Evolution of strength and coercivity during annealing of FeCo based alloys”. In: *Scripta materialia* 51.6 (2004), pp. 589–591.

[302] Saksl, K and Bednarčík, J and Nicula, R and Burkel, E and Roth, S and Franz, H. “The influence of short-time ball-milling on the stability of amorphous CoFeB alloys”. In: *Journal of Physics: Condensed Matter* 19.17 (2007), p. 176215.

[303] M López, P Marín, P Agudo, I Carabias, J de la Venta, and A Hernando. “Nanocrystalline FeSiBNbCu alloys: Differences between mechanical and thermal crystallization process in amorphous precursors”. In: *Journal of Alloys and Compounds* 434 (2007), pp. 199–202. ISSN: 09258388. DOI: 10.1016/j.jallcom.2006.08.127.

[304] J. Bonastre, L. Escoda, J. Saurina, J.J. Suñol, J.D. Santos, M.L. Sánchez, and B. Hernando. “Non-isothermal approach to crystallization process of a Co-rich alloy”. In: *Journal of Non-Crystalline Solids* 354.47 (2008), pp. 5126–5128. DOI: 10.1016/j.jnoncrysol.2008.05.060.

[305] J Bonastre, L Escoda, B Hernando, JM Sánchez-Llamazares, and JJ Suñol. “Amorphous metal nanocrystallization changes due to mechanical alloying”. In: *Physica Status Solidi (C)* 7.11-12 (2010), pp. 2660–2662. DOI: 10.1002/pssc.200983790.

[306] T Gheiratmand, HRM Hosseini, P Davami, M Gjoka, and M Song. “The effect of mechanical milling on the soft magnetic properties of amorphous FINEMET alloy”. In: *Journal of Magnetism and Magnetic Materials* 381 (2015), pp. 322–327. ISSN: 03048853. DOI: 10.1016/j.jmmm.2015.01.016.

[307] T Gheiratmand, HRM Hosseini, P Davami, G Ababei, and M Song. “Mechanism of Mechanically Induced Nanocrystallization of Amorphous FINEMET Ribbons During Milling”. In: *Metallurgical and Materials Transactions A* 46.6 (2015), pp. 2718–2725. ISSN: 1543-1940. DOI: 10.1007/s11661-015-2848-x. URL: http://dx.doi.org/10.1007/s11661-015-2848-x.

[308] G Herzer. “Chapter 3 Nanocrystalline soft magnetic alloys”. In: *Handbook of Magnetic Materials*. Vol. 10. 1997, pp. 415–462. ISBN: 9780444825995. DOI: 10.1016/S1567-2719(97)10007-5.

[309] K. Lu. “Nanocrystalline metals crystallized from amorphous solids: nanocrystallization, structure, and properties”. In: *Materials Science and Engineering: R: Reports* 16.4 (1996), pp. 161–221. ISSN: 0927796X. DOI: 10.1016/0927-796X(95)00187-5.

[310] MS El-Eskandarany, K Akoi, K Sumiyama, and K Suzuki. “Cyclic crystalline-amorphous transformations of mechanically alloyed Co75Ti25”. In: *Applied physics letters* 70.13 (1997), pp. 1679–1681.

[311] S Sharma and C Suryanarayana. “Mechanical crystallization of Fe-based amorphous alloys”. In: *Journal of Applied Physics* 102.8 (2007), p. 83544.

[312] VV Muhgalin, GA Dorofeev, MA Eremina, VI Lad’yanov, and IV Sapegina. “Nanocrystallization of the amorphous Co-B-Si alloys formed by melt spinning and mechanical alloying”. In: *The Physics of Metals and Metallography* 112.6 (2011), pp. 596–602.

[313] G Herzer. “Nanocrystalline soft magnetic materials”. In: *Physica Scripta* 1993.T49A (1993), p. 307.

[314] K Lu. “Synthesis of nanocrystalline materials from amorphous solids”. In: *Advanced Materials* 11.13 (1999), pp. 1127–1128.

[315] AL Greer. “From metallic glasses to nanocrystalline solids”. In: *Proc. of 22nd Ris{ø} Int. Symp. on Materials Science: Science of Metastable and Nanocrystalline Alloys Structure, Properties and Modelling (Ris{ø} National Laboratory Roskilde Denmark 2001)*. 2001, pp. 461–466.

[316] AI Gusev. *Nanomaterials, Nanostructures and Nanotechnologies*. Moscow: Fizmatlit, 2005.

[317] M Ohta and Y Yoshizawa. “Effect of heating rate on soft magnetic properties in nanocrystalline Fe80. 5Cu1. 5Si4B14 and Fe82Cu1Nb1Si4B12 alloys”. In: *Applied physics express* 2.2 (2009), p. 023005.

[318] MM Raja, K Chattopadhyay, B Majumdar, and A Narayanasamy. “Structure and soft magnetic properties of FINEMET alloys”. In: *Journal of Alloys and Compounds* 297.1 (2000), pp. 199–205. ISSN: 09258388. DOI: 10.1016/S0925-8388(99)00565-4.

[319] M Tejedor, JA García, J Carrizo, L Elbaile, and JD Santos. “Induced magnetic anisotropy in amorphous ribbons by applying a magnetic field during the quenching process”. In: *Applied Physics Letters* 82.6 (2003), p. 937. ISSN: 00036951. DOI: 10.1063/1.1542675. URL: http://scitation.aip.org/content/aip/journal/apl/82/6/10.1063/1.1542675.

[320] S Roth, A R Ferchmin, and S Kobe. *Landolt-Brnstein: Numerical Data and Functional Relationships in Science and Technology, vol. III/19 of Magnetic Properties of Metals, ed: HPJ Wijn*. 1994.

[321] RB Schwarz, TD Shen, U Harms, and T Lillo. “Soft ferromagnetism in amorphous and nanocrystalline alloys”. In: *Journal of Magnetism and Magnetic Materials* 283.2 (2004), pp. 223–230.

[322] LV Panina and K Mohri. “Magneto-impedance effect in amorphous wires”. In: *Applied Physics Letters* 65.9 (1994), pp. 1189–1191.

[323] RS Beach and AE Berkowitz. “Giant magnetic field dependent impedance of amorphous FeCoSiB wire”. In: *Applied Physics Letters* 64.26 (1994), pp. 3652–3654.

[324] K Mohri, T Uchiyama, and LV Panina. “Recent advances of micro magnetic sensors and sensing application”. In: *Sensors and Actuators A: Physical* 59.1-3 (1997), pp. 1–8.

[325] ASM Handbook. “Heat treating”. In: *vol* 4 (1991), p. 744.

[326] B Yao, L Si, H Tan, Y Zhang, and Y Li. “Effects of high boron content on crystallization, forming ability and magnetic properties of amorphous Fe91-x Zr5 Bx Nb4 alloy”. In: *Journal of non-crystalline solids* 332.1 (2003), pp. 43–52.

[327] M Ohta and Y Yoshizawa. “Recent progress in high Bs Fe-based nanocrystalline soft magnetic alloys”. In: *Journal of Physics D: Applied Physics* 44.6 (2011), p. 064004.

[328] Rohit Jain, Deepika Bhandari, N S Saxena, S K Sharma, and A Tripathi. “Effect of high-energy heavy ion irradiation on the crystallization kinetics of Co-based metallic glasses”. In: *Bulletin of Materials Science* 24.1 (2001), pp. 27–33. ISSN: 0973-7669. DOI: 10.1007/BF02704836. URL: http://dx.doi.org/10.1007/BF02704836.

[329] RS Sundar and SC Deevi. “Soft magnetic FeCo alloys: alloy development, processing, and properties”. In: *International materials reviews* 50.3 (2005), pp. 157–192.

[330] A Makino, T Hatanai, Y Naitoh, T Bitoh, A Inoue, and T Masumoto. “Applications of nanocrystalline soft magnetic Fe-MB (M= Zr, Nb) alloys "NANOPERM"”. In: *IEEE Transactions on Magnetics* 33.5 (1997), pp. 3793–3798.

[331] G. Bordin, G. Buttino, A. Cecchetti, and M. Poppi. “Hall effect and magnetoresistance in Co-based amorphous and crystallized alloys”. In: *Journal of Magnetism and Magnetic Materials* 172.3 (1997), pp. 291–300. ISSN: 03048853. DOI: 10.1016/S0304-8853(97)00078-4.

[332] T Sánchez, V Vega, J D Santos, M J Pérez, V M Prida, M L Sánchez, Ll Escoda, J J Suñol, and B Hernando. “Off-diagonal magnetoimpedance effect in field quenched Co69Fe4Si15B12 amorphous ribbons”. In: *Physica Status Solidi A* 208.10 (2011), pp. 2265–2268.

[333] METGLAS. *Metglas 2714A Magnetic Alloy*. 2016. URL: http://www.metglas.com/products/magnetic_materials/2714a.asp (visited on 11/30/2016).

[334] RJ Hebert and JH Perepezko. “Effect of cold-rolling on the crystallization behavior of amorphous Al88Y7Fe5 alloy”. In: *Materials Science and Engineering: A* 375 (2004), pp. 728–732.

[335] GJ Fan, MX Quan, and ZQ Hu. “Deformation-enhanced thermal stability of an amorphous Fe80B20 alloy”. In: *Journal of applied physics* 80.10 (1996), pp. 6055–6057.

[336] J Bonastre, JJ Suñol, P Bruna, Kiminori Sato, JD Santos, and B Hernando. “Influence of a magnetic field applied during the quenching process on the spin density and nanoscale structure of an amorphous Fe-B ribbon”. In: *Materials letters* 87 (2012), pp. 131–134. DOI: 10.1016/j.matlet.2012.07.072.

[337] H Fujimori and FE Luborsky. “Amorphous metallic alloys”. In: *edited by FE Luborsky, Butterworths Monographs in Materials* (1983), p. 300.

[338] T Sánchez, J Bonastre, JD Santos, ML Sánchez, A Chizhik, J González, JJ Suñol, and B Hernando. “The effect of field-quenching fabrication on the magnetoimpedance response in Co66Fe4Ni1Si15B14 amorphous ribbons”. In: *Journal of Applied Physics* 111.5 (2012), p. 053913. DOI: 10.1063/1.3687417.

[339] JD Livingston, WG Morris, and T Jagielinsky. “Effects of anisotropy on domain-structures in amorphous ribbons”. In: *IEEE Trans Magn* 19.5 (1983), pp. 1916–1918.

[340] A Chaturvedi, N Laurita, A Leary, MH Phan, ME McHenry, and H Skrikanth. “Giant magnetoimpedance and field sensitivity in amorphous and nanocrystalline (Co1-xFex)(89)Zr7B4 (x=0, 0.025, 0.05, 0.1) ribbons”. In: *J. Appl. Phys.* 109.7 (2011), pp. 479–482.

[341] JS Blázquez, J Marcin, F Andrejka, V Franco, A Conde, and I Skorvanek. “Study of the Induced Anisotropy in Field Annealed Hitperm Alloys by Mössbauer Spectroscopy and Kerr Microscopy”. In: *Metallurgical and Materials Transactions A* 47.8 (2016), pp. 4301–4305.

[342] M Ohnuma, G Herzer, P Kozikowski, C Polak, V Budinsky, and S Koppoju. “Structural anisotropy of amorphous alloys with creep-induced magnetic anisotropy”. In: *Acta Materialia* 60.3 (2012), pp. 1278–1286.

[343] JM Riveiro, V Madurga, and A Hernando. “Structure-related induced anisotropy in metallic glasses”. In: *Physical Review B* 39.16 (1989), p. 11950.

[344] GS Mogilny, BD Shanina, VV Maslov, VK Nosenko, AD Shevchenko, and VG Gavriljuk. “Structure and magnetic anisotropy of rapidly quenched FeSiB ribbons”. In: *Journal of Non-Crystalline Solids* 357.16 (2011), pp. 3237–3244.

[345] JM Greneche and F Varret. “On the texture problem in Mossbauer spectroscopy”. In: *J Phys C Solid State Phys* 15.25 (1982), pp. 5333–5344.

[346] Brzózka, K and Sovák, P and Górka, B and Szumiata, T and Gawronski, M. “Mössbauer Study of Magnetic Texture of Finemet-Type Ribbons”. In: *Acta Physica Polonica A* 119.1 (2011), pp. 33–36.

[347] T Kulik and M Kopcewicz. “Effect of quenching rate on magnetic properties and local magnetic anisotropy in Fe78Si9B13 glass”. In: *J. Magn. Magn. Mater.* 215 (2000), pp. 455–458.

[348] T Sánchez, J Garcia, JD Santos, L Escoda, VM Prida, ML Sánchez, JJ Sunol, and B Hernando. “Off-diagonal Magnetoimpedance Dependence of Magnetostriction and Anisotropy in Co-Based and Fe-Based Amorphous Ribbons”. In: *Acta Phys. Pol. A* 118.5 (2010), pp. 756–758.

[349] Sánchez, ML and Sánchez, T and Ribot, I and Pérez, MJ and Santos, JD and Sánchez-Llamazares, JL and Prida, VM and Álvarez, P and Hernando, B and Escoda, Ll and Suñol, JJ. “Off-diagonal magnetoimpedance effect in Fe80B20 amorphous ribbons”. In: *Journal of Non-Crystalline Solids* 354.47 (2008), pp. 5147–5149.

[350] H Lee, YK Kim, and YB Kim. “Soft Magnetic Properties of Co-Based Amorphous Alloy by Two-Step Cooling Method”. In: *Physica Status Solidi A* 189.3 (2002), pp. 1073–1076.

[351] JP Sinnecker, EHCP Sinnecker, A Zhukov, JM Garcia-Beneytez, MJ Garcia Prieto, and M Vázquez. “Giant magneto-impedance in glass covered microwires”. In: *Le Journal de Physique IV* 8.PR2 (1998), Pr2–225.

[352] M Knobel, M Vázquez, and L Kraus. “Giant Magnetoimpedance”. In: *Handbook of Magnetic Materials, vol. 15*. Ed. by KHJ Buschow. Amsterdam, NL: Elsevier Science, 2003. ISBN: 978-0-444-63528-0.

[353] B Chitsazan, H Shokrollahi, A Behvandi, and M Ghaffari. “Magnetic, structural and micro-structural properties of mechanically alloyed nano-structured Fe48Co48V4 powder containing inter-metallic Co3V”. In: *Journal of Magnetism and Magnetic Materials* 323.9 (2011), pp. 1128–1133.

This thesis was typeset with LaTeX using the *Clean Thesis* style[1].

[1] http://cleanthesis.der-ric.de/